INTERACTION OF HEATED FILAMENTS WITH A BLUNT BODY IN SUPERSONIC FLOW

BY KELLIE ANDERSON

A thesis submitted to the

Graduate School—New Brunswick

Rutgers, The State University of New Jersey

in partial fulfillment of the requirements

for the degree of

Master of Science

Graduate Program in Mechanical and Aerospace Engineering

Written under the direction of

Doyle D. Knight

and approved by

New Brunswick, New Jersey

JANUARY, 2010

© 2010
KELLIE ANDERSON
ALL RIGHTS RESERVED

ABSTRACT OF THE THESIS

Interaction of Heated Filaments with a Blunt Body in Supersonic Flow

by KELLIE ANDERSON

Thesis Director: Doyle D. Knight

Two computational studies are performed to examine the influence of energy deposition on a blunt body in supersonic flow. The first objective is to determine the effect of increasing filament diameter on the efficiency and effectiveness of drag reduction to a blunt body. The second objective is to evaluate the influence of the energy filaments on the heat transfer to the blunt body. The energy deposition is modeled as a low density, high temperature filament that is injected in the freestream and interacts with the blunt body. A code is written to solve the compressible Navier Stokes equations to evaluate these effects.

Keywords: blunt body, stand–off distance, bow shock, recompression shock, expansion fan, microwave filament, contact discontinuity, heat transfer, viscous, Richtmeyer–Meshkov instability, lensing effect, vortex region, recirculation area, drag reduction, CFD

Acknowledgements

I am sincerely indebted to my advisor, Professor Doyle Knight for his guidance, expertise and extraordinary patience. Without his kind encouragement, graduate school would not be nearly as rewarding.

I am indebted to Kevin Anderson, who has been my boyfriend, fiance and husband through my graduate career. I am constantly bewildered by his patience and unyielding support.

And to my family, who have always supported my endeavors.

Dedication

To my Nana, Marge Norton. The strongest person I know.

Table of Contents

List of Tables

List of Figures

Chapter 1

Introduction

1.1 Motivation

Two of the greatest impediments to high speed aircraft today are high drag and heat loads. From fighter jets to space shuttles, drag forces and heat loads limit vehicle speed, range, fuel efficiency and performance [1]. One way to mitigate heat loads in hypersonic flows is to use blunt body vehicle designs. A disadvantage of blunt body designs is a higher pressure drag on the vehicle. Developing viable techniques to reduce drag on high speed blunt body vehicles is necessary to design more sophisticated air and space vehicles.

One effective means of drag reduction for blunt bodies is the use of energy deposition. Energy deposition is the injection of heat to the flow in front of the blunt body shock by means of laser, microwave, electron beam, glow discharge or plasma arcs. The mechanism behind the drag reduction is the creation of high temperature, low density filaments that interact with the shock wave to create vortices behind the shock. The vortices generate a lower pressure region at the front of the body. Energy deposition has been widely studied for shock wave modification [2, 3].

Microwave energy deposition, in particular, is an effective means of drag reduction for blunt bodies. Microwave induced plasmas can be created at distances from the microwave generator [4]. Because the wavelength of the microwave is on the same order as the plasma length of interest, the plasma shape and size can be manipulated more than other plasma generation techniques [4].

1.2 Literature Survey

Flow control by means of energy deposition has a long history. Microwave energy deposition is attractive because energy deposition can be created at a distance from the energy generating source. Successes with microwave generation have been accomplished fairly recently. Preceeding microwave energy deposition, a bounty of research was performed using laser energy deposition. Though the physical mechanisms by which breakdown is achieved is fundamentally different between microwave and laser induced plasma generation, drag reduction is primarily a thermal phenomenon [5]. Thus the mechanism by which the plasma is created has a secondary effect on the plasma-shock interaction. Both microwave and laser induced energy deposition research is presented here to illustrate the flow physics and to demonstrate the strong agreement between computational modeling and experiments of the filament/shock interaction.

Computational modeling of microwave energy filaments in supersonic flows has received significant attention in the past few years. Computational results can provide physical data difficult to measure in laboratory tests and is a means of obtaining quick results prior to performing experiments. Previous computational studies by Azarova *et al* [6], Georgivsky and Levin [7], and Farzan *et al* [8] have shown microwave energy deposition to reduce pressure drag. Farzan's [8] investigation showed the effect on the aerodynamic drag characteristics of varying the nondimensional filament length.

The research summary presented in this section is by no means comprehensive. Summaries are provided of selected research in recent years. Both computational and experimental research is discussed. Surveys in this area are Knight *et al* [2], Fomin *et al* [9], Knight *et al* [10], Bletzinger *et al* [11] and Knight [12].

Adelgren *et al* 2001

Adelgren, Elliot, Knight, Zheltodov and Beutner [13] performed experiments using laser energy deposition upstream of a sphere in Mach 3.45 flow. Their research showed momentary reduction in surface pressure on the surface of the sphere. The intent of the experiments was to evaluate the capability of laser energy deposition to reduce surface pressure induced by an Edney IV shock-shock interaction. An Edney Type IV shock-shock interaction is an oblique shock which crosses a blunt body shock at the body centerline, as illustrated in Figure 1.1.

Four tests were performed, the first two in quiescent air, the second two in Mach 3.45 flow. The quiscent air tests were performed with an Nd:YAG laser with a wavelength of 532 nm. The laser was focused through a lens to initiate breakdown in air. The first test studied energy deposition in quiescent air. The second test investigated microwave energy deposition in the presence of an under-expanded jet. Rayleigh scattering images were used to visualize the flow in each test. The images show an initial blast wave generated by the energy deposition. For the under-expanded jet test, the interaction of the energy deposition and the Mach disc show significant alteration of the Mach disk, which resulted in a vortex ring behind the Mach disc.

The third and fourth tests were performed on a sphere in Mach 3.45 air. For these tests an Nd:YAG laser was focused through a lens to generate the energy deposition. The laser had a pulse duration of 10 nanoseconds, and was capable of energy levels up to 150-200 milli-Joules per pulse. The tests were performed in a Mach 3.45 wind tunnel, with a stagnation pressure of 1.4 MPa, a stagnation temperature of 290 K, a test section area of 15 cm by 15 cm, with a test section length of 30 cm. The third test showed the effect of laser induced energy deposition on the shock structure of the sphere. The fourth test was a study on a Edney Type IV shock-shock interation. An Endevco $8530C - 100$ pressure transducer measured pressure within the 25.4 mm sphere behind a 1.32 mm diameter port, 1.78 mm behind the sphere front surface.

In the third experiment, the laser energy deposition reduced the surface pressure on the sphere by 40%. For the case of the shock-shock interaction, surface pressure was momentarily reduced by 30%. These results indicated the excellent potential of energy deposition for the purpose of shock control.

Exton *et al* 2001

Exton *et al* [14] demonstrated the capability to generate a microwave plasma upstream of a Mach 6 bow shock by an on-board Ku-band horn. The intent of the research was to

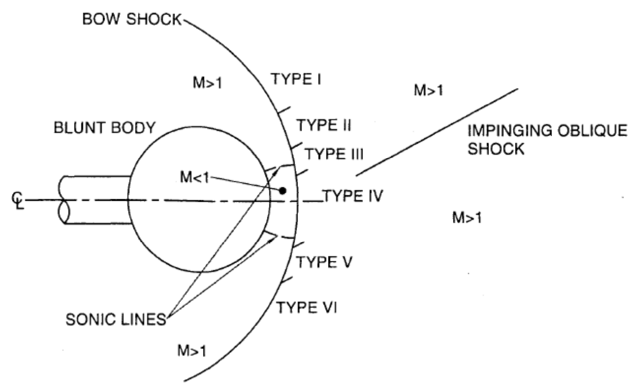

Figure 1.1: Types of Edney Shock-Shock Interactions

demonstrate the capability of generating a plasma from microwaves at the surface of the test body.

Experiments were performed in the Langley 15 inch High Temperature Wind Tunnel. The tunnel has a cylindrical test section with an internal diameter of 1.5 m and is 1.8 m long. The model was an 8.26 cm diameter aluminum cylinder. The model was affixed with Ku-band horn, as is shown in Figure 1.2.

A time-averaged schlieren image is shown from these experiments in Figure 1.3. The primary plasma is shown just upstream of the bow shock. Subsidiary plasmas form upstream of the main plasma. The primary plasma is overexposed in the photo; in real time it was much thinner. The thin plasma was not sufficiently large to affect the shape of the shock and alter the flow structure. The research succesfully generated a precurser plasma ahead of the shock. In order to reduce surface pressure on the cylinder, however, the plasma region would have needed to be spatially and temporally larger.

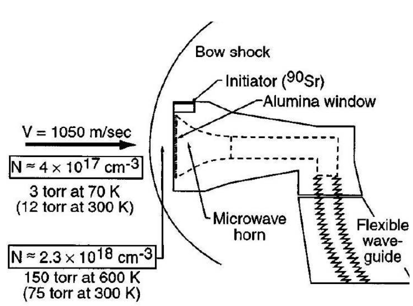

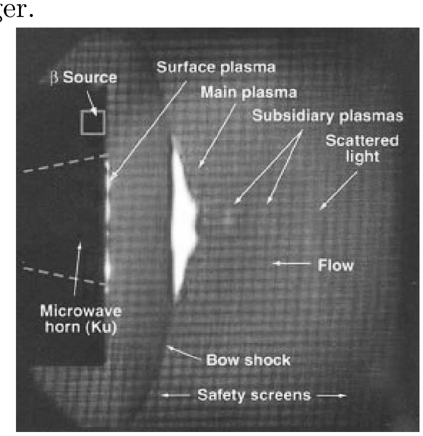

Figure 1.2 : Schematic diagram of a Ku-band microwave horn on-board a model in Mach 6 flow field. [14]

Figure 1.3 : Time-averaged schlieren image of precurser plasma at Mach 6. [14]

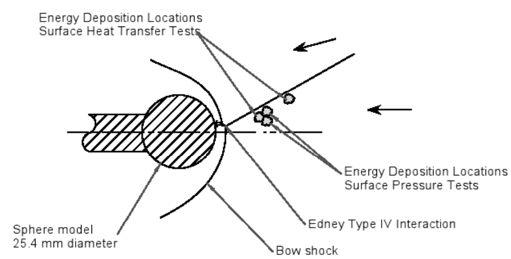

(a) Edney Type IV Shock-Shock Configuration

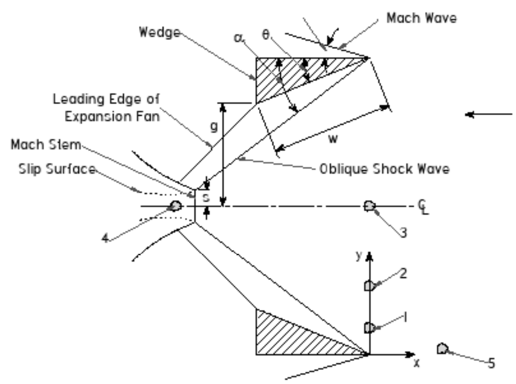

(b) Oblique Shock-Shock Configuration

Figure 1.4: Shock Crossing Configurations Studied in Adelgren *et at* 2003

Adelgren *et al* 2003

Adelgren, Yan, Elliot, Knight and Beutner [15] performed both experimental and computational experiments to study the effect of energy deposition on wave structures in Mach 3.45 flow. Three configuractions were studied. The first case studied the interaction of energy deposited upstream of a sphere. The second case evaluated the interaction of laser energy deposition on an Edney type IV configuration, as illustrated in Figure 1.4(a). The final configuration studied the effect of laser energy deposition on crossing oblique shocks generated by two wedges in Mach 3.45 flow. The oblique shock crossing configuration is shown in Figure 1.4(b). The stagnation pressure was 1.4 MPa and the stagnation temperature was 290 K.

The experiments were performed in a Mach 3.45 wind tunnel at Rutgers University. The laser used to create the energy deposition was a Nd:YAG 532 wavelength laser beam, with a 10 nanosecond duration and pulsed at a frequency of 10 Hz. The energy deposition was applied at both one diameter and 0.6 diameters upstream of the sphere. The test model was a 25.4 mm diameter sphere. The crossing shock was created by a 15 degree wedge mounted at the top of the test section. Heat transfer and temperature were measured along the surface of the sphere using thin film gauges made from platinum. The pressure was measured by a single Endevco 8560C-100 pressure transducer located in the center of the sphere, mounted 1.78 mm from the front of the sphere, behind a port with a 1.32 mm diameter.

The computations were performed with a three-dimensional Euler code. The General Aerodynamic Simulation Program (GASP) was used to perform the computations. The laser was modeled through an energy source term with an initially Gaussian temperature distribution.

The computed stagnation pressure agreed with the experimental stagnation pressure to within the experimental uncertainty for the steady state condition as well as the Edney IV blunt body shock- oblique shock configuration. For the case of the sphere in the Mach 3.45 flow without the crossing shock, the stagnation pressure was reduced 40% during the 50 microseconds of the thermal spot interaction with the sphere. During that time, the heat transfer rate and temperature at the surface of the sphere increased dramatically. In the Edney IV case, the peak surface pressure was reduced by 30%, but the heat transfer rate and temperature at the surface of the sphere was not reduced. The heat transfer rates for the surface of the sphere, with energy deposition applied at one diameter upstream of the model, for both sphere and Edney IV interaction can be found in Figures 1.5 and 1.6, respectively. The oblique shock crossing configuration demonstrated a 80% reduction in Mach stem. The numerical and experimental results were similar on a quantitative basis.

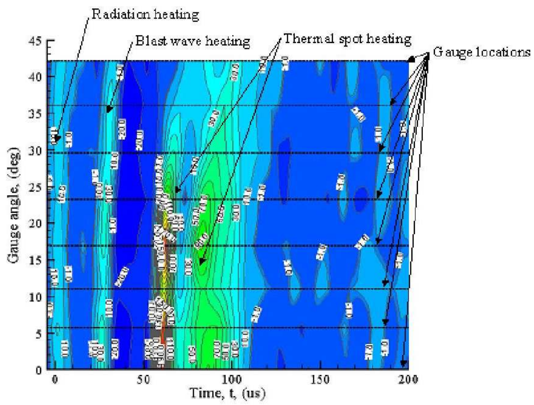

Figure 1.5 : Heat Transfer at Surface of Sphere for Case of Energy Deposition Applied One Diameter Upstream of Cylinder [15].

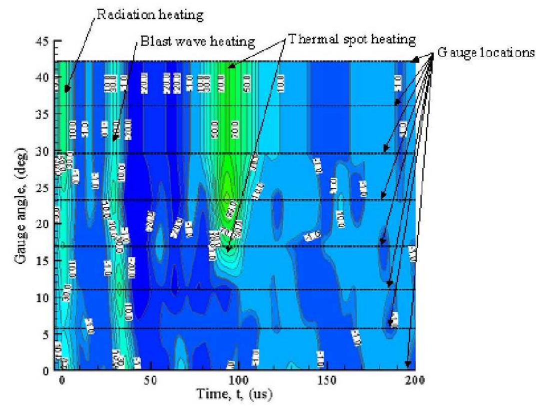

Figure 1.6 : Heat Transfer at Surface of Sphere for Case of Energy Deposition Applied One Diameter Upstream of Cylinder, Edney IV Type Shock Crossing Configuration [15].

Zaidi *et al* 2004

Zaidi, Shneider and Miles [16] performed a computational and experimental study of a wedge in Mach 2.4 flow with laser energy deposition. The study was performed to evaluate the surface pressure effects of the laser energy deposition, primarily for sonic boom reduction. Reduced shock strength and near-field pressure is an indication of reduction in wave drag.

The experiments were performed in a blow-down type wind tunnel with free stream Mach number 2.4. The laser energy deposition was obtained with a YAG laser pulsed at 10 Hz, capable of 350 mJ/pulse. The energy deposition was applied 10 mm upstream and 10 mm below the model centerline axis. The stagnation pressure in the tunnel is one atmosphere and the stagnation temperature was 136 K, using air as the test gas. The model was a 15 mm length 20 degree wedge. To avoid flow instabilities at the trailing edge, an inclined rear region was used, such that the test section was more diamond shaped. Schlieren and shadowgraph images were used to visualize the flow. The computational code was a two-dimensional Euler solver using a second order MacCormack scheme.

The computational and experimental flow structures were qualitatively very similar. The computational results showed similar shock bending and weakening as the experimental results. A numerical case was run modeling the blast wave from the laser energy deposition and a separate case was run without modeling the blast wave. The case with the energy deposition blast wave modeled showed much higher pressure peaks than the case in the absense of the blast wave, as seen in Figure 1.7. This result is an indicator that energy deposition must be generated far enough upstream of the body shock that the blast wave from the energy deposition generation has sufficiently dissipated.

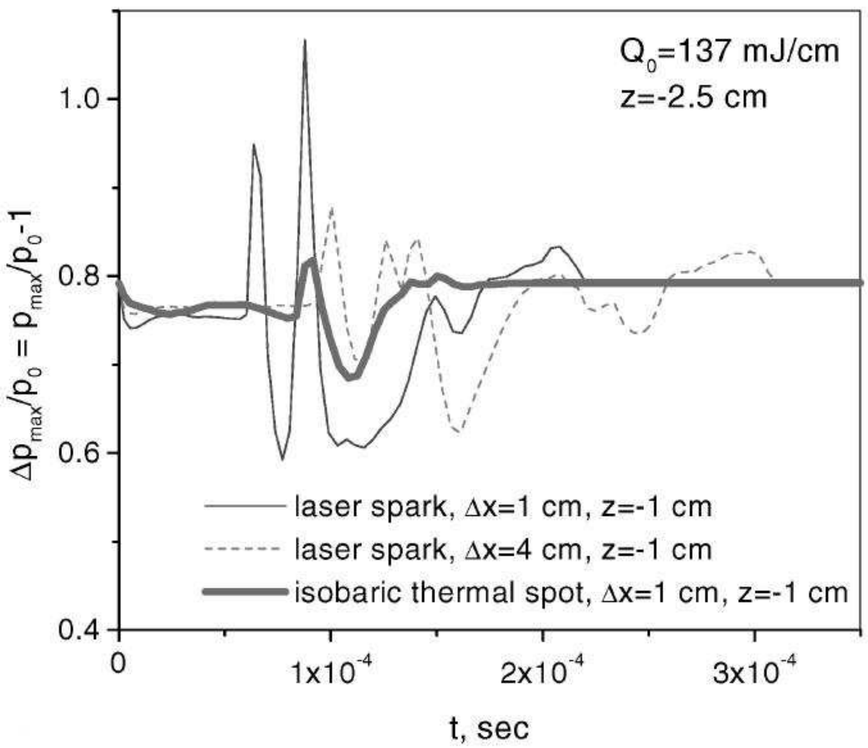

Figure 1.7 : Computational Prediction of Maximum Relative Pressures at Bottom of Test Section [16]

Kolesnichenko *et al* 2007

Kolesnichenko, Khmara, Brovkin and Afansas'ev evaluated different types of laser pulses in combination with microwave fields to generate a more efficient drag reducing energy deposition shape [17]. The most efficient energy deposition geometry for flow control is a long hot cylindrical filament. The shape of the laser induced plasmas, however are more spherical, and the microwave induced filaments are very irregular in shape. The article sought to combine the two technologies to create an optimally shaped energy deposition filament. Both experimental and computational analyses were performed.

For the experiments, sparks were generated with an Nd:YAG laser with a wavelength of

532 nanometers, pulse energy up to 130 mJ, with a pulse duration of 15 ns. The microwaves were generated at a pulse rate of 13.5 GHz, a pulse power of 500 kW and a pulse duration of $3-70$ microseconds. The laser in this experiment was aligned with electric field vector of the electromagnetic waves. Previous research had microwaves perpendicular to the flow. It was found that sparks could be initiated at lower microwave fields with the parallel orientation.

Computational simulations modeled both thermal and non-equilibrium laser plasmas as initiators for the microwave breakdown. The thermal mode model demonstrated decay rates independent of air pressure. Also, the spark transparency only existed for a distinct period of time, which decreased as ambient air pressure increased. It was shown that the non-equilibrium laser initiator achieved a thermal filament along the path of the laser. However, to achieve this configuration, simultaneous application of the microwave and the laser would be necessary. Additionally, an electric field would have to be present to prevent recombination and attachment, which would otherwise rapidly decay the energy deposition filament.

Lashkov ***et al*** 2007

Lashkov, Mashek, Anisimov, Ivanov, Kolesnichenko and Azarova [18] investigated the effect of microwave energy deposition in combination with an aerodynamic spike generated by counterflow at the front of a body. Both experimental and computational methods were employed in this study.

In the computational study, a sphere in Mach 3 flow was evaluated for different filament densities relative to the freestream density, and length of filament. The reduction in pressure upon interaction of the shock wave was greater for the lower density filament and longer length filament. The reduction in force on the front of the body was shown to be insensitive to the filament density. This was thought to be a sign that the distance between data points sampled on the front face of the sphere was not small enough to capture differences. The computational study illustrated the presence of a standing shock wave in the stagnation region after the microwave energy deposition had passed through the flow domain.

The experiments investigated a 25 mm diameter sphere in Mach 1.2 flow with a stagnation pressure of 40 Torr. The experimental apparatus can be seen in Figure 1.8. A 1 mm diameter spike was placed at the front of the sphere. The first experiment injected microwave energy deposition to the flow in front of the sphere with the spike, but no air injection. In this case, the microwave energy deposition increased the pressure at the front of the sphere. The second case was run with air injected through the spike at a flow rate of $4 \cdot 10^{-5}$ kg/s. The interaction of the microwave energy deposition and the spike/shock increased the pressure on the sphere, but far less than the case without air injection. The pressure on the sphere is shown in Figure 1.9.

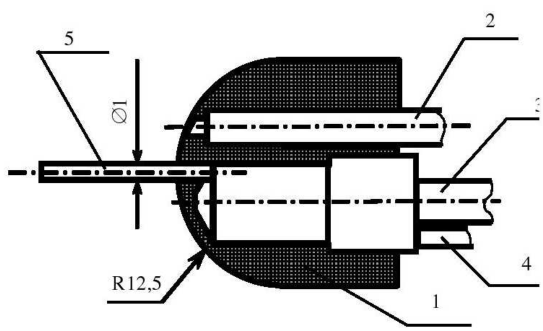

Figure 1.8 : Apparatus of Spike on Sphere

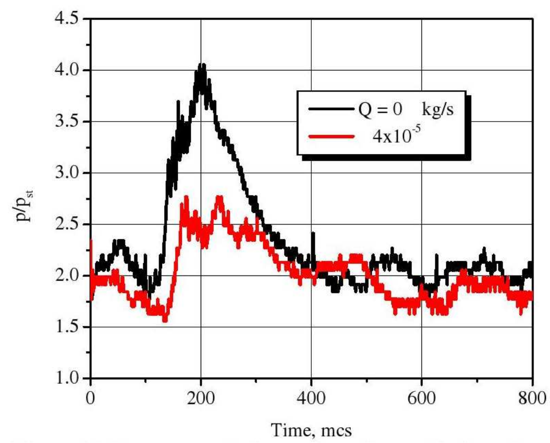

Figure 1.9 : Relative Pressure on Surface of Sphere With and Without Air Injection Through the Spike

Knight, Azarova, Kolesnichenko 2009

A computational study of microwave energy deposition in supersonic flow was presented for axially symmetrically applied and asymmetrically applied energy deposition [19]. The configuration was a right cylinder in Mach 1.89 and Mach 3 flow, for various filament geometries. The ratio of filament diameter to cylinder diameter ranged from 0.1 to 0.26, the length of pulsed filament nondimensionalized by the cylinder diameter varied from 3 to infinitely long, and the off-axis location was varied for the different configurations.

The computational study used two codes, both of which solved the Euler equations. One code solved the Euler equations in cylindrical coordinates, while the other solved the Euler equations in plane coordinates. Both codes were second order accurate in both space and time.

The symmetrically located filament reduced the drag on the cylinder, while the asymmetrically located filament cases increased the drag on the cylinder. The mechanism by which the drag increased was described as a heat piston. The asymmetrically located filament induced an asymmetric vortex, which collided with the cylinder and compressed the air near the cylinder face. The result was an increase in drag on the cylinder. The flow field around the heat piston is illustrated in Figure 1.10.

The off-axis filaments were shown to induce a pitching moment on the cylinder. The pitching moment was a function of how far off axis the energy deposition is positioned.

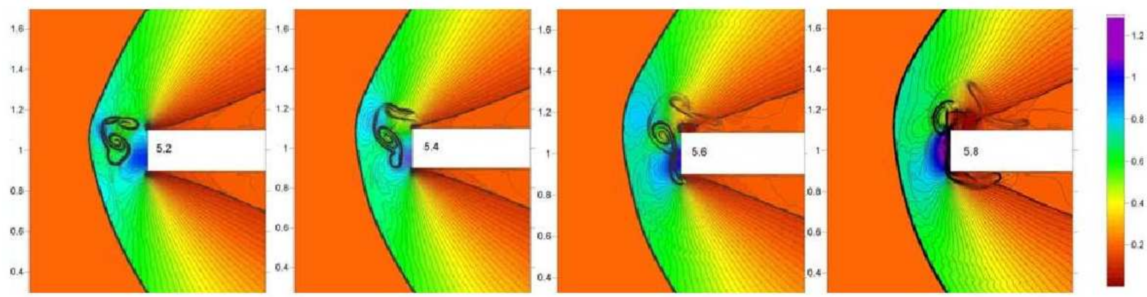

Figure 1.10 : Asymmetrically Located Filament / Shock Layer Interaction Density Isochors and Pressure Contours [19]

1.3 Statement of Objectives

There are two objectives of this research. The first objective is to investigate how variations in the energy deposition filament diameter affect aerodynamic drag. This work extends the research of Farzan *et al* [8]. Their work demonstrated that a pulsed energy filament in the region of the bow shock generates a sustained vortex region that reduces drag on the body in inviscid supersonic flow [8]. It was concluded that shorter pulses generated a higher efficiency and lower effectiveness than longer pulses, which generated the converse. This research will show the relations between filament radius and drag reduction efficiency and effectiveness. The drag reduction efficiency is the ratio of the power saved due to drag reduction by introduction of the microwave filament to the power necessary to create the microwave filament. The effectiveness is the ratio of the average frontal drag reduction due to the presence of the filament to the frontal drag in the absence of the filament.

The second objective of this research is to study the viscous effects of energy deposition. Inviscid computational studies of energy deposition have shown that microwave energy deposition can be effective and efficient for drag reduction. The viscous effects of energy deposition, so far, have been limited to experimental work [15]. This research solves the Navier Stokes equations to compute the heat transfer rate to the front of the blunt body with and without energy deposition.

Chapter 2

Problem Definition

Two problems are solved in this research. The first problem is an inviscid study of energy deposition in Mach 1.89 flow past a right cylinder. This study looks at the effect of a varying energy deposition filament diameter. The second problem is a study of the heat transfer effects of microwave energy deposition to blunt bodies in supersonic flow. The same flow configuration is used in both studies.

2.1 Inviscid Simulations

The problem of a cylinder of diameter D in supersonic flow with continuous energy deposition is solved in this research. The energy deposition is applied along the axis of symmetry of the cylinder. One wedge of the axisymmetric problem is solved. The energy deposition is modeled by a lower density than the freestream. The ratio of energy deposition density to freestream density will be referred to as the reduced density and denoted by α. The problem dimensions are depicted in Figure 2.1. The flow and energy deposition filament parameters are defined in Table 2.1. The flow parameters and filament density ratio match those of Farzan *et al* [8]. The dimensionless filament diameter is varied to study the effect on drag efficiency and effectiveness. The filament diameters versus case numbers are shown in Table 2.2. The filaments are chosen to be infinitely long. The effect of the filament pulse frequency on drag reduction was previously studied by Farzan *et al* [8].

2.1.1 Solution Domain

The problem of a cylinder in supersonic flow with energy deposition is axisymmetric. The geometry of the computational domain is shown in Figure 2.1. A cylindrical control volume is used to evaluate the flow around the cylinder. The energy deposition is applied along

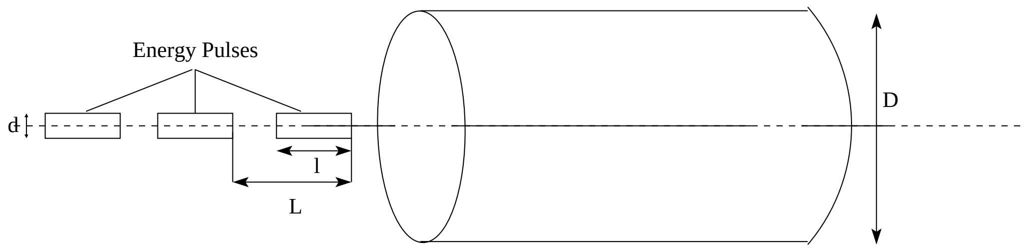

Figure 2.1: Computational domain

Table 2.1: Dimensionless Flow Parameters for Filament Diameter Study

Type	Description	Definition	Value
Flow	Mach	M_∞	1.89
	Specific heat ratio	γ	1.4
Filament	Density ratio	α	0.5
	Diameter	$\frac{d}{D}$	varies
	Length (Duration)	$\frac{l}{D}$	infinitely long

the centerline of the cylinder in the freestream flow. The solution domain and boundary conditions are axisymmetric. The problem can be reduced to a wedge of the solution domain shown in Figure 2.2.

2.1.2 Boundary Conditions

The compressible Euler equations represent a hyperbolic system of equations requiring initial and boundary conditions. The steady state solution to flow over the body (at the same freestream conditions as the energy deposition problem) is used for the initial condition. Each face that corresponds to a flow domain boundary is given a unique number as shown in Figure 2.2. The boundary condition applied at each boundary face is listed in Table 2.3. Symmetry boundary conditions are applied on azimuthal boundaries to ensure that the flow maintains axisymmetry. The inflow boundary condition is modeled as uniform supersonic

Table 2.2: Filament Diameters for Three Cases of Filament Diameter Study

Case	Filament Diameter $\frac{d}{D}$
1	0.25
2	0.50
3	1.0

flow with energy deposition imposed via a reduced density. The reduced density is modeled as $\alpha = \rho_{filament}/\rho_{\infty}$. Pressure in the filament is the freestream pressure and temperature is increased by $\frac{1}{\alpha}$, where α is less than one. The velocity of the filament is equal to the freestream velocity. The reduced density reduces the Mach number in the filament by a factor of $\sqrt{\alpha}$.

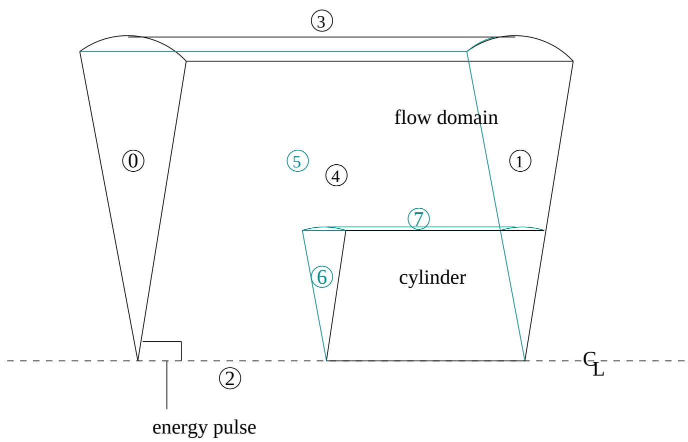

Figure 2.2: Axisymmetric wedge solution domain

Table 2.3: Boundary Conditions for Inviscid Filament Diameter Study

Boundary	Boundary Condition
0	Freestream flow and energy deposition
1	Outflow (zero-gradient)
2	Axisymmetric
3	Symmetry
4	Symmetry
5	Symmetry
6	Symmetry
7	Symmetry

2.1.3 Details of Computation

Each calculation was performed with three processors, with uniform grid cells in each direction. The grid spacing in the axial direction was uniform with $\Delta x/D$=0.02. The radial spacing was uniform with $\Delta r/D$=0.02. The chosen cell size ensures 23 cells between the cylinder face and the normal shock and 5 cells across the diameter of the heated filament. The computations were run on prigogine, a 24 node Linux cluster with two single-core processors per node at 2.2 GHz, 1MByte RAM per processor, Debian Linux. Each computation ran for 92 hours wall clock time, 276 hours processor time (92 hours on 3 processors).

2.2 Viscous Simulation

The problem of a blunt cylinder in supersonic flow with periodic energy deposition with viscous effects is solved for this research. One wedge of the axisymmetric problem is solved. The flow and energy deposition filament parameters are defined in Table 2.4. The problem dimensions are depicted in Figure 2.1. The flow parameters match those of Farzan *et al* [8]. The freestream Reynolds number is chosen to approximate experiments performed by Kolesnichenko *et at* [20]. Typical experimental values are listed in Table 2.4. Sutherland's law was used to approximate freestream viscosity. The pulse period, L/D is varied from 4/3 to infinitely long, as was done in Farzan *et al* [8]. The effect of the filament on the heat transfer to the face is evaluated.

2.2.1 Solution Domain

The flow domain used to compute the viscous cases is shown in Figure 2.2. The blunt body is taken to be a perfect cylinder. The effect of the microwave pulses is known to have the greatest effect at the front of the cylinder body. Therefore, only the first two cylinder diameters in length of the body are included in the flow domain. The height of the domain extends two diameters above the body. The inviscid computations provided verification that this height is sufficient to capture the effect of the microwave filaments on the flow. The blunt body shock is expected to lense forward upon interaction with the microwave filaments based on previous inviscid cases. To include the lensing, the flow

Table 2.4: Flow Parameters for Heat Transfer Study

Type	Description	Definition	Value
Dimensionless Flow	Mach	M_∞	1.89
	Specific heat ratio	γ	1.4
	Reynolds number	Re	$7.0 \cdot 10^4$
Dimensional Flow	Freestream Pressure	P_∞	25-50 Torr
	Freestream Temperature	T_∞	155 K
	Freestream Viscosity	μ_∞	$1.06 \cdot 10^{-5} \frac{kg}{m \cdot s}$
Dimensionless Filament	Density ratio	α	0.5 all cases
	Diameter	$\frac{d}{D}$	0.1 all cases
	Length	$\frac{l}{D}$	1.0, 1.0, 1.0, ∞
	Pulse (Period)	$\frac{L}{D}$	$\frac{4}{3}$, 2.0, 4.0, n/a
Cylinder	Temperature	T_w/T_∞	2.0 all cases
	Cylinder Diameter	D	20-40 mm

domain is chosen to begin two cylinder diameters in length before the front of the body. Because the microwave filaments are applied along the axis of symmetry of the flow domain, both the domain and the boundary conditions are axisymmetric about the x-axis. Thus it is feasible to compute only a 1/32 wedge of the flow domain to reduce computation times.

2.2.2 Boundary Conditions

The compressible Navier Stokes equations represent a parabolic system of equations requiring initial and boundary conditions. The steady state solution to flow over the body (at the same freestream conditions as the pulsed energy deposition problem) is used for the initial condition. Each face that corresponds to a flow domain boundary is given a unique number as shown in Figure 2.2. The boundary condition applied at each boundary face is listed in Table 2.5. Symmetry boundary conditions are applied on the boundary tangent to the radial direction of the cylinder to ensure that the wedge maintains axisymmetry to the remaining domain. The inflow boundary condition is modeled as uniform supersonic flow with pulsed energy imposed via a reduced density. The reduced density is modeled as $\alpha = \rho_{filament}/\rho_\infty$. Pressure in the filament is the freestream pressure and temperature is increased by $\frac{1}{\alpha}$, where α is less than one. The velocity of the filament is equal to the freestream velocity. The reduced density reduces the Mach number in the filament by a factor of $\sqrt{\alpha}$. The outflow boundary condition is modeled as a zero gradient condition. In supersonic flow, disturbances do not propagate upstream, thus the outflow boundary does not affect the upstream flow field. The dimensionless surface temperature of the cylinder is chosen to be $T_w/T_\infty = 2.0$ to ensure a hot cylinder. The adiabatic wall temperature would be $T_w/T_\infty = 1.7$ at the stagnation point.

Table 2.5: Boundary Conditions for Heat Transfer Study

Boundary	Boundary Condition
0	Freestream flow and pulsed energy
1	Outflow (zero-gradient)
2	Axisymmetric
3	Symmetry
4	Symmetry
5	Symmetry
6	No slip, $T/T_\infty = 2.0$
7	No slip, $T/T_\infty = 2.0$

2.2.3 Details of Computation

The grid spacing was chosen to ensure at least five cells in the boundary layer at the front face of the cylinder. The boundary layer at the front face of the cylinder was calculated using the boundary layer thickness calculation for stagnation flows [21]. For Hiemenz flow, the boundary layer thickness, δ, is given by

$$\delta = 2.4\sqrt{\frac{\nu}{\epsilon}} \tag{2.1}$$

where $\epsilon = \frac{U}{D}$ The quantities are taken from the conditions behind the shock, using the normal shock relations.

The boundary layer height is nondimensionalized by the diameter of the cylinder, which, for this calculation is chosen to be unity. The nondimensional boundary layer height is

$$\frac{\delta}{D} = 2.4\sqrt{\frac{\mu}{\rho U D}} = 0.011 \tag{2.2}$$

Thus the grid spacing in the direction normal to the front face of the cylinder is $\frac{\Delta x}{D} = 0.002$. Therefore, there are six cells in the boundary layer at the front face of the cylinder.

The grid spacing in the radial direction was chosen to be $\frac{\Delta r}{D} = 0.00175$. This ensured twenty nine cells within the radius of the energy deposition filament.

If the shock wave left the upper boundary, it would reflect back and affect the calculation. The height of the domain was chosen by evaluating the inviscid computation to determine the height such that the bow shock exits the domain at the back corner. The nondimensional height of the computed domain is 3.1.

The grid above the cylinder is stretched in the radial direction at a stretching rate of 1.01. Stretching in the radial direction significantly reduces computing times by reducing the number of cells.

To further reduce computing time, the computational domain was divided into twenty-five zones. Each zone was run on a separate processor. The zones in front of the cylinder face, with uniform grid spacing in each direction are 100x286x1 cells in the axial, radial and azimuthal directions, respectively. The remaining fifteen zones which are stretched in the radial direction are 100x89x1 cells in the axial, radial and azimuthal directions, respectively.

The grid is shown in Figure 2.3. Each zone is outlined in the figure. The cylinder body, which is not included in the computational flow domain, is shaded. The lengths are shown in terms of the cylinder diameter.

Each computation required 25 processors, one for each zone. The total run time of each computation varied from approximately 272-388 hours for the transient cases.

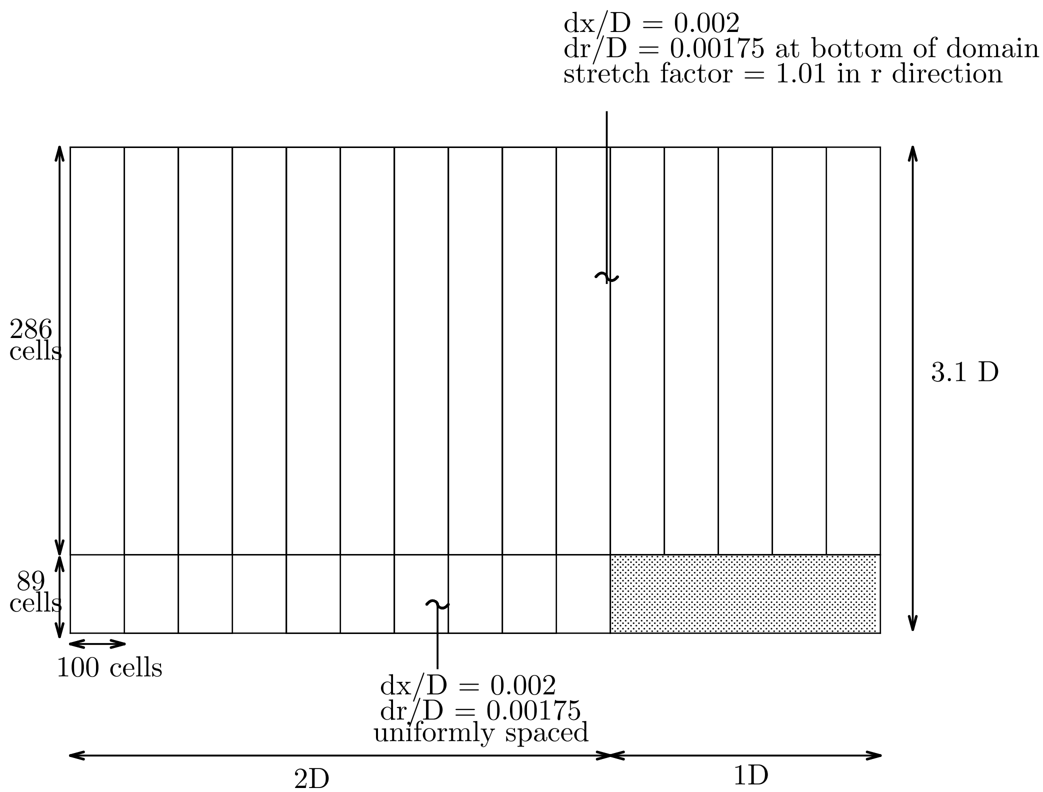

Figure 2.3: Computational Domain

Chapter 3

Methodology

3.1 Governing Equations

The fluid motion is described by the conservation of mass, momentum and energy. The dimensional governing equations are described by equations (3.1) to (3.3), where the Einstein summation notation is used. The viscous terms are included in this section; however, these terms were deactivated for the inviscid computations.

Conservation of Mass

$$\frac{\partial \rho}{\partial t} + \frac{\partial \rho u_j}{\partial x_j} = 0 \tag{3.1}$$

Conservation of Momentum

$$\frac{\partial \rho u_i}{\partial t} + \frac{\partial \rho u_i u_j}{\partial x_j} = -\frac{\partial p}{\partial x_i} + \frac{\partial \tau_{ij}}{\partial x_j} \tag{3.2}$$

Conservation of Energy

$$\frac{\partial \rho e}{\partial t} + \frac{\partial (\rho e + p) u_j}{\partial x_j} = \frac{\partial q_j}{\partial x_j} + \frac{\partial \tau_{ij} u_j}{\partial x_i} \tag{3.3}$$

For a Newtonian fluid, the stress tensor is written as

$$\tau_{ij} = \mu \left[\frac{\partial u_i}{\partial x_j} + \frac{\partial u_j}{\partial x_i} \right] - \frac{2}{3} \mu \delta_{ij} \frac{\partial u_k}{\partial x_k} \tag{3.4}$$

The heat flux, is given by Fourier's Law

$$q_j = c_p \frac{\mu}{Pr} \frac{\partial T}{\partial x_j} \tag{3.5}$$

The total energy per unit mass is given by

$$e = c_v T + \frac{1}{2} u_j u_j \tag{3.6}$$

The total enthalpy is

$$H = h + \frac{1}{2}u_i u_i \tag{3.7}$$

where h is the static enthalpy, defined as

$$h = e + \frac{p}{\rho} \tag{3.8}$$

3.1.1 Nondimensionalization

The governing equations are rewritten in dimensionless form. The dimensional variables are denoted with a starred superscript * in the following definitions. The indices represent the component of a vector.

$$\rho = \frac{\rho^*}{\rho_\infty} \tag{3.9}$$

$$u_i = \frac{u_i^*}{u_\infty} \tag{3.10}$$

$$e = \frac{e^*}{u_\infty^2} \tag{3.11}$$

$$p = \frac{p^*}{\rho_\infty u_\infty^2} \tag{3.12}$$

$$\tau_{ij} = \frac{\tau_{ij}^*}{\rho_\infty u_\infty^2} \tag{3.13}$$

$$q_i = \frac{q_i^*}{\rho_\infty u_\infty^3} \tag{3.14}$$

$$x_i = \frac{x_i^*}{L} \tag{3.15}$$

$$t = \frac{t^*}{\frac{L^*}{u_\infty}} \tag{3.16}$$

$$\mu = \frac{\mu^*}{\mu_\infty} \tag{3.17}$$

$$T = \frac{T^*}{T_\infty} \tag{3.18}$$

$$h = \frac{h^*}{u_\infty^2} \tag{3.19}$$

$$H = \frac{H^*}{u_\infty^2} \tag{3.20}$$

3.1.2 Nondimensional Governing Equations

The governing equations in terms of the non-dimensional parameters are as follows.

$$\frac{\partial \rho}{\partial t} + \frac{\partial \rho u_j}{\partial x_j} = 0 \tag{3.21}$$

$$\frac{\partial \rho u_i}{\partial t} + \frac{\partial \rho u_i u_j}{\partial x_j} = -\frac{\partial p}{\partial x_i} + \frac{\partial \tau_{ij}}{\partial x_j} \tag{3.22}$$

$$\frac{\partial \rho e}{\partial t} + \frac{\partial (\rho e + p) u_j}{\partial x_j} = \frac{\partial q_j}{\partial x_j} + \frac{\partial \tau_{ij} u_j}{\partial x_i} \tag{3.23}$$

Where the dimensionless auxiliary relations become

$$p = \frac{\rho T}{\gamma M_\infty^2} = \frac{a^2 \rho}{\gamma} \tag{3.24}$$

$$\tau_{ij} = \frac{\mu}{Re_\infty} \left(\frac{\partial u_j}{\partial x_j} + \frac{\partial u_j}{\partial x_i} - \frac{2}{3} \frac{\partial u_j}{\partial x_j} \delta_{ij} \right) \tag{3.25}$$

$$q_i = \frac{\mu}{M_\infty^2} \frac{1}{(\gamma - 1) Pr Re_\infty} \frac{\partial T}{\partial x_i} \tag{3.26}$$

$$a^2 = \frac{T}{M_\infty^2} \tag{3.27}$$

$$e = \frac{1}{\gamma(\gamma - 1)} \frac{T}{M_\infty^2} + \frac{u_j u_j}{2} = \frac{a^2}{\gamma(\gamma - 1)} + \frac{u_j u_j}{2} \tag{3.28}$$

$$Re_\infty = \frac{\rho_\infty u_\infty L}{\mu_\infty} \tag{3.29}$$

$$Pr = \frac{c_p \mu_\infty}{k_\infty} \tag{3.30}$$

3.1.3 Conservative Form of Governing Equations

A coordinate transformation is performed from the x, y, z basis to general coordinates ξ, η, ζ. The general coordinates describe the directions of the cell faces, as shown in Figure 3.1. The general coordinates are not necessarily orthogonal, but each cell is restricted to a parallelepiped.

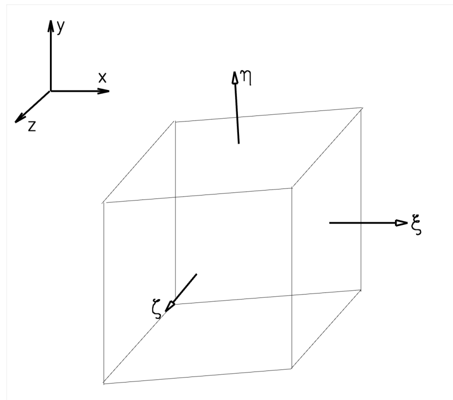

Figure 3.1: General Coordinate Axes

The strong form of the differential governing equations is

$$\frac{\partial \hat{Q}}{\partial t} + \frac{\partial(\hat{E} - \hat{E}_v)}{\partial \xi} + \frac{\partial(\hat{F} - \hat{F}_v)}{\partial \eta} + \frac{\partial(\hat{G} - \hat{G}_v)}{\partial \zeta} = 0 \tag{3.31}$$

where

$$\hat{Q} = J^{-1}Q = J^{-1} \begin{pmatrix} \rho \\ \rho u \\ \rho v \\ \rho w \\ \rho e \end{pmatrix} \tag{3.32}$$

$$\hat{E} = J^{-1} \begin{pmatrix} \rho U' \\ \rho u U' + \xi_x p \\ \rho v U' + \xi_y p \\ \rho w U' + \xi_z p \\ (\rho e + p) U' \end{pmatrix}, \quad \hat{F} = J^{-1} \begin{pmatrix} \rho V' \\ \rho u V' + \eta_x p \\ \rho v V' + \eta_y p \\ \rho w V' + \eta_z p \\ (\rho e + p) V' \end{pmatrix}, \quad \hat{G} = J^{-1} \begin{pmatrix} \rho W' \\ \rho u W' + \zeta_x p \\ \rho v W' + \zeta_y p \\ \rho w W' + \zeta_z p \\ (\rho e + p) W' \end{pmatrix} \tag{3.33}$$

$$U' = \xi_x u + \xi_y v + \xi_z w$$

$$V' = \eta_x u + \eta_y v + \eta_z w$$

$$W' = \zeta_x u + \zeta_y v + \zeta_z w$$

where

$$\begin{aligned}
\xi_x &= \frac{\partial \xi}{\partial x}, \quad \xi_y = \frac{\partial \xi}{\partial y}, \quad \xi_z = \frac{\partial \xi}{\partial z} \\
\eta_x &= \frac{\partial \eta}{\partial x}, \quad \eta_y = \frac{\partial \eta}{\partial y}, \quad \eta_z = \frac{\partial \eta}{\partial z} \\
\zeta_x &= \frac{\partial \zeta}{\partial x}, \quad \zeta_y = \frac{\partial \zeta}{\partial y}, \quad \zeta_z = \frac{\partial \zeta}{\partial z}
\end{aligned} \tag{3.34}$$

Integrating over a cell volume, we find the conservative form of the governing equations in integrated form.

$$\frac{\partial}{\partial t}\int_V Q dxdydz + (E - E_v)|_{i-\frac{1}{2}}^{i+\frac{1}{2}} + (F - F_v)|_{j-\frac{1}{2}}^{j+\frac{1}{2}} + (G - G_v)|_{k-\frac{1}{2}}^{k+\frac{1}{2}} = 0 \tag{3.35}$$

where the fluxes are evaluated at the cell faces, $i + \frac{1}{2}$ and $i = \frac{1}{2}$, as shown in Figure 3.2 where the inviscid fluxes are

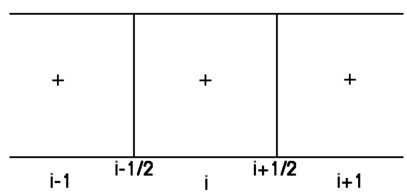

Figure 3.2: Cell Face Location

$$E = \left\{ \begin{array}{c} \rho U \\ \rho u U + l_x p \\ \rho v U + l_y p \\ \rho w U + l_z p \\ (\rho e + p) U \end{array} \right\} \quad F = \left\{ \begin{array}{c} \rho V \\ \rho u V + m_x p \\ \rho v V + m_y p \\ \rho w V + m_z p \\ (\rho e + p) V \end{array} \right\} \quad G = \left\{ \begin{array}{c} \rho W \\ \rho u W + n_x p \\ \rho v W + n_y p \\ \rho w W + n_z p \\ (\rho e + p) W \end{array} \right\} \tag{3.36}$$

where

$$U = \vec{v} \cdot \vec{l}, \quad V = \vec{v} \cdot \vec{m}, \quad W = \vec{v} \cdot \vec{n} \tag{3.37}$$

The vectors l, m and n are defined as normals to the ξ,η, and ζ faces, respectively, with magnitudes equal to the surface area.

$$\vec{l} \quad = \quad J^{-1}\,\overrightarrow{\nabla\xi}\; d\eta d\zeta = \hat{n}\, dA|_{\xi\text{-face}},$$

$$
\begin{aligned}
\vec{m} &= J^{-1}\,\overrightarrow{\nabla\eta}\,d\xi d\zeta = \hat{n}\,dA|_{\eta\text{-face}}, \\
\vec{n} &= J^{-1}\,\overrightarrow{\nabla\zeta}\,d\xi d\eta = \hat{n}\,dA|_{\zeta\text{-face}},
\end{aligned} \tag{3.38}
$$

and the viscous fluxes are

$$
E_v = \left\{ \begin{array}{c} 0 \\ l_x\tau_{xx} + l_y\tau_{xy} + l_z\tau_{xz} \\ l_x\tau_{yx} + l_y\tau_{yy} + l_z\tau_{yz} \\ l_x\tau_{zx} + l_y\tau_{zy} + l_z\tau_{zz} \\ l_x\beta_x + l_y\beta_y + l_z\beta_z \end{array} \right\} \quad F_v = \left\{ \begin{array}{c} 0 \\ m_x\tau_{xx} + m_y\tau_{xy} + m_z\tau_{xz} \\ m_x\tau_{yx} + m_y\tau_{yy} + m_z\tau_{yz} \\ m_x\tau_{zx} + m_y\tau_{zy} + m_z\tau_{zz} \\ m_x\beta_x + m_y\beta_y + m_z\beta_z \end{array} \right\} \tag{3.39}
$$

$$
G_v = \left\{ \begin{array}{c} 0 \\ n_x\tau_{xx} + n_y\tau_{xy} + n_z\tau_{xz} \\ n_x\tau_{yx} + n_y\tau_{yy} + n_z\tau_{yz} \\ n_x\tau_{zx} + n_y\tau_{zy} + n_z\tau_{zz} \\ n_x\beta_x + n_y\beta_y + n_z\beta_z \end{array} \right\}
$$

The heat flux terms are written as

$$
\begin{aligned}
q_x &= \frac{\mu}{M_\infty^2}\frac{1}{(\gamma-1)Pr_\infty Re_\infty}\frac{\partial T}{\partial x} \\
q_y &= \frac{\mu}{M_\infty^2}\frac{1}{(\gamma-1)Pr_\infty Re_\infty}\frac{\partial T}{\partial y} \\
q_z &= \frac{\mu}{M_\infty^2}\frac{1}{(\gamma-1)Pr_\infty Re_\infty}\frac{\partial T}{\partial z}
\end{aligned} \tag{3.40}
$$

and β terms in the energy conservation equation are defined as follows

$$
\begin{aligned}
\beta_x &= q_x + \tau_{xx}u + \tau_{xy}v + \tau_{xz}w \\
\beta_y &= q_y + \tau_{yx}u + \tau_{yy}v + \tau_{yz}w \\
\beta_z &= q_z + \tau_{zx}u + \tau_{zy}v + \tau_{zz}w
\end{aligned} \tag{3.41}
$$

3.2 Numerical Algorithm

3.2.1 Inviscid Flux Formulation

The inviscid flux terms are solved using Van Leer's flux vector splitting method [22]. A three-dimensional Van Leer scheme is proposed following [23]. The scheme is validated by showing the scheme is equivalent to the integrated equations of motion, Equation (3.36). The scheme is evaluated for the flux component perpendicular to the ξ face. A similar evaluation holds for the flux components perpendicular to the η and ζ faces.

$$E = \begin{cases} E_l & \text{for} \quad \overline{\mathrm{M}} > 1 \\ \left(f^+ + f^-\right) dA_{\xi\text{-face}} & \text{for} \quad -1 \leq \overline{\mathrm{M}} \leq 1 \\ E_r & \text{for} \quad \overline{\mathrm{M}} < -1 \end{cases} \tag{3.42}$$

where $\hat{n} = (\hat{n}_x, \hat{n}_y, \hat{n}_z)$ is the unit normal to the face, $\overline{\mathrm{M}} = (\vec{v} \cdot \hat{n})/a$, $\overline{U} = \vec{v} \cdot \hat{n}$, and

$$f^{\pm} = f_m^{\pm} \begin{cases} \rho \\ \rho u + \rho \hat{n}_x \left(-\overline{U} \pm 2a\right)/\gamma \\ \rho v + \rho \hat{n}_y \left(-\overline{U} \pm 2a\right)/\gamma \\ \rho w + \rho \hat{n}_z \left(-\overline{U} \pm 2a\right)/\gamma \\ \rho f_e^{\pm} \end{cases}$$

where

$$f_m^{\pm} = \pm \frac{a}{4}\left(\overline{\mathrm{M}} \pm 1\right)^2$$

$$f_e^{\pm} = \pm h_o - \frac{\left(-\overline{U} \pm a\right)^2}{\gamma + 1}$$

$$h_o = e + \frac{p}{\rho}$$

The system is evaluated to demostrate that it is equivalent to the integrated form of the laminar Navier Stokes equations, Equation (3.36). The cases of $\overline{\mathrm{M}} < -1$ and $\overline{\mathrm{M}} > 1$ are the flux evaluated at the flow conditions taken from the appropriate side of the cell face. For example, E_l indicates that the flux vector E is evaluated using the flow conditions on the left side of the cell. The equivalence to Equation (3.36) is therefore inherent to the definition of these. The subsonic cases, $-1 \leq \overline{\mathrm{M}} \leq 1$, are proven below.

The mass equation, from Van Leer's scheme, Equation (3.42), evaluated for the subsonic case, is

$$\rho\left(\frac{a}{4}\left(\overline{\mathrm{M}}+1\right)^2-\frac{a}{4}\left(\overline{\mathrm{M}}-1\right)^2\right)dA_{\xi\text{-face}}$$
$$\rho\frac{a}{4}\left(\left(\overline{\mathrm{M}}^2+2\overline{\mathrm{M}}+1\right)-\left(\overline{\mathrm{M}}^2-2\overline{\mathrm{M}}+1\right)\right)dA_{\xi\text{-face}}$$
$$\rho a\overline{\mathrm{M}}dA_{\xi\text{-face}}$$
$$\rho a\frac{(\vec{v}\cdot\hat{n})}{a}dA_{\xi\text{-face}}$$
$$\rho\vec{v}\cdot\hat{n}dA_{\xi\text{-face}}$$
$$\rho\vec{v}\cdot\vec{l}$$
$$\rho U \tag{3.43}$$

which is identical to the first term in E in Equation (3.36). The momentum equation, from Van Leer's scheme, evaluated for $-1\leq\overline{\mathrm{M}}\leq 1$ is

$$\begin{aligned}
&= \frac{a}{4}\left(\overline{\mathrm{M}}+1\right)^2\left(\rho u+\rho\hat{n}_x\frac{-\overline{U}+2a}{\gamma}\right)-\frac{a}{4}\left(\overline{\mathrm{M}}-1\right)^2\left(\rho u+\rho\hat{n}_x\frac{-\overline{U}-2a}{\gamma}\right)dA_{\xi\text{-face}}\\
&= \frac{a}{4}\left[\left(\overline{\mathrm{M}}^2+2\overline{\mathrm{M}}+1\right)\left(\rho u+\rho\hat{n}_x\frac{-\overline{U}+2a}{\gamma}\right)-\left(\overline{\mathrm{M}}^2-2\overline{\mathrm{M}}+1\right)\left(\rho u+\rho\hat{n}_x\frac{-\overline{U}-2a}{\gamma}\right)\right]dA_{\xi\text{-face}}\\
&= \frac{a}{4}\left[\overline{\mathrm{M}}^2\frac{4a}{\gamma}\rho\hat{n}_x+\overline{\mathrm{M}}\rho u-\overline{\mathrm{M}}\frac{\rho\hat{n}_x\overline{U}}{\gamma}+\frac{a}{\gamma}\rho\hat{n}_x\right]dA_{\xi\text{-face}}
\end{aligned}$$

where $\overline{\mathrm{M}}a=\overline{U}$

$$\begin{aligned}
&= \left(\frac{\overline{U}^2\rho\hat{n}_x}{\gamma}+\overline{U}\rho u-\frac{\overline{U}^2\rho\hat{n}_x}{\gamma}+\frac{a^2\rho\hat{n}_x}{\gamma}\right)dA_{\xi\text{-face}}\\
&= \left(\overline{U}\rho u+\frac{a^2\rho\hat{n}_x}{\gamma}\right)dA_{\xi\text{-face}}
\end{aligned}$$

and, from Equation (3.39),

$$\hat{n}=\frac{\vec{\nabla}\xi}{J}=\frac{1}{J}\left(\frac{\partial\xi}{\partial x}\hat{i}+\frac{\partial\xi}{\partial y}\hat{j}+\frac{\partial\xi}{\partial z}\hat{k}\right)$$

implies

$$\hat{n}_x=\hat{n}\cdot\hat{i}=\frac{1}{J}\frac{\partial\xi}{\partial x}=\frac{\xi_x}{J}$$

Additionally, in dimensionless form, $p = a^2\rho/\gamma$, thus the momentum equation in the x direction for the flux in the ξ direction is

$$\begin{aligned} &= \left(\overline{U}\rho u + \frac{p\xi_x}{J}\right) dA_{\xi\text{-face}} \\ &= \rho u U + p l_x \\ &= \rho u U + l_x p \end{aligned} \tag{3.44}$$

The derivation for the y and z momentum parallels this derivation, and is omitted here.

The energy equation is

$$\begin{aligned}
\left(f^+ + f^-\right) dA_{\xi\text{-face}} &= \rho\frac{a}{4}\left(\overline{\mathrm{M}}+1\right)^2\left(h_o - \frac{\left(-\overline{U}+a\right)^2}{\gamma+1}\right) - \rho\frac{a}{4}\left(\overline{\mathrm{M}}-1\right)^2\left(h_o - \frac{\left(-\overline{U}-a\right)^2}{\gamma+1}\right) dA_{\xi\text{-face}} \\
&= \rho\frac{a}{4}\left[\left(\overline{\mathrm{M}}^2+2\overline{\mathrm{M}}+1\right)\left(h_o - \frac{\left(-\overline{U}+a\right)^2}{\gamma+1}\right) - \left(\overline{\mathrm{M}}^2-2\overline{\mathrm{M}}+1\right)\left(h_o - \frac{\left(-\overline{U}-a\right)^2}{\gamma+1}\right)\right] dA_{\xi\text{-face}} \\
&= \frac{\rho a}{4}\left[4\overline{\mathrm{M}}h_o - \left(\overline{\mathrm{M}}^2+2\overline{\mathrm{M}}+1\right)\left(\frac{\left(-\overline{U}+a\right)^2}{\gamma+1}\right) + \left(\overline{\mathrm{M}}^2-2\overline{\mathrm{M}}+1\right)\left(\frac{\left(-\overline{U}-a\right)^2}{\gamma+1}\right)\right] dA_{\xi\text{-face}} \\
&= \frac{\rho a}{4}\left[4\overline{\mathrm{M}}h_o - \left(\overline{\mathrm{M}}^2+2\overline{\mathrm{M}}+1\right)\left(\frac{\overline{U}^2-2\overline{U}a+a^2}{\gamma+1}\right) + \left(\overline{\mathrm{M}}^2-2\overline{\mathrm{M}}+1\right)\left(\frac{\overline{U}^2+2\overline{U}a+a^2}{\gamma+1}\right)\right] dA_{\xi\text{-face}} \\
&= \frac{\rho a}{4}\left[4\overline{\mathrm{M}}h_o + \frac{4\overline{\mathrm{M}}^2\overline{U}a}{\gamma+1} - \frac{4\overline{\mathrm{M}}\,\overline{U}^2}{\gamma+1} - \frac{4\overline{\mathrm{M}}a^2}{\gamma+1} + \frac{4\overline{\mathrm{U}}a}{\gamma+1}\right] \\
&= \rho a\left[\overline{\mathrm{M}}h_o + \frac{\overline{\mathrm{M}}\overline{U}^2}{\gamma+1} - \frac{\overline{\mathrm{M}}\,\overline{U}^2}{\gamma+1} - \frac{\overline{\mathrm{M}}a^2}{\gamma+1} + \frac{\overline{\mathrm{M}}a^2}{\gamma+1}\right] \\
&= \rho a\overline{\mathrm{M}}h_o dA_{\xi\text{-face}} \\
&= \rho\overline{\mathrm{U}}h_o dA_{\xi\text{-face}} \\
&= \mathrm{U}h_o \\
&= \mathrm{U}\left(\rho e + p\right)
\end{aligned} \tag{3.45}$$

Putting together Equations (3.43), (3.44) and (3.47), the following is obtained, for $-1 \leq \overline{\mathrm{M}} \leq 1$

$$E = \left\{\begin{array}{c} \rho U \\ \rho u U + l_x p \\ \rho v U + l_y p \\ \rho w U + l_z p \\ U\left(\rho e + p\right) \end{array}\right\}$$

3.2.2 Viscous Flux Formulation

The viscous flux terms in equations (3.39) can be written as

$$E_v = \widetilde{T} \cdot l \quad F_v = \widetilde{T} \cdot m \quad G_v = \widetilde{T} \cdot n \tag{3.46}$$

where we define $\widetilde{T}$ as

$$\widetilde{T} = \left\{ \begin{array}{ccc} 0 & 0 & 0 \\ \tau_{xx} & \tau_{xy} & \tau_{xz} \\ \tau_{yx} & \tau_{yy} & \tau_{yz} \\ \tau_{zx} & \tau_{zy} & \tau_{zz} \\ \beta_x & \beta_y & \beta_z \end{array} \right\} \tag{3.47}$$

Thus it remains only to find the components of $\widetilde{T}$ at each face. From equation (3.24),

$$\tau_{ij} = \frac{\mu}{Re_\infty} \left(\frac{\partial u_i}{\partial x_j} + \frac{\partial u_j}{\partial x_i} - \frac{2}{3} \frac{\partial u_k}{\partial x_k} \delta_{ij} \right)$$

The derivatives are evaluated with a second order approximation at each face. The chain rule is used to evaluate the derivatives in terms of the grid parameters.

$$\frac{\partial u_i}{\partial x_j} = \frac{\partial u_i}{\partial \xi} \frac{\partial \xi}{\partial x_j} + \frac{\partial u_i}{\partial \eta} \frac{\partial \eta}{\partial x_j} + \frac{\partial u_i}{\partial \zeta} \frac{\partial \zeta}{\partial x_j} \tag{3.48}$$

The derivatives $\frac{\partial \eta}{\partial x}$ are expressed in terms the Jacobian, $J = J(\frac{\xi,\eta,\zeta}{x,y,z})$ as $\frac{\partial \eta_i}{\partial x_j} = \frac{1}{J} \frac{\partial x_j}{\partial \eta_i}$. The velocity gradients are evaluated by the central difference scheme evaluated at each face.

For the fluxes in the ξ direction, the velocity gradients are computed as follows,

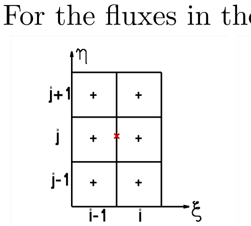

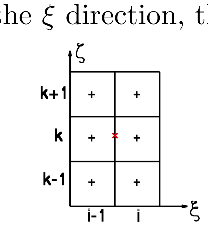

$$\frac{\partial u}{\partial \xi}_{i-1/2} = u_{i,j,k} - u_{i-1,j,k}$$
$$\frac{\partial u}{\partial \eta}_{i-1/2} = \frac{1}{4} \left(u_{i,j+1,k} + u_{i-1,j+1,k} - u_{i-1,j-1,k} - u_{i,j-1,k} \right)$$
$$\frac{\partial u}{\partial \zeta}_{i-1/2} = \frac{1}{4} \left(u_{i,j,k+1} + u_{i-1,j,k+1} - u_{i-1,j,k-1} - u_{i,j,k-1} \right)$$

For the fluxes in the η direction, the velocity gradients are computed as follows,

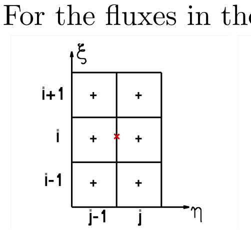

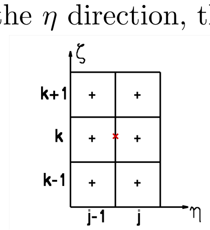

$$\frac{\partial u}{\partial \xi}_{j-1/2} = \frac{1}{4} \left(u_{i+1,j,k} + u_{i+1,j-1,k} - u_{i-1,j-1,k} - u_{i-1,j,k} \right)$$
$$\frac{\partial u}{\partial \eta}_{j-1/2} = u_{i,j,k} - u_{i,j-1,k}$$
$$\frac{\partial u}{\partial \zeta}_{j-1/2} = \frac{1}{4} \left(u_{i,j,k+1} + u_{i,j-1,k+1} - u_{i,j-1,k-1} - u_{i,j,k-1} \right)$$

For the fluxes in the ζ direction, the velocity gradients are computed as follows,

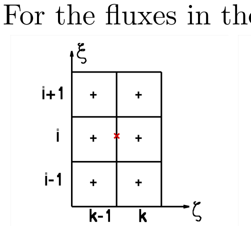

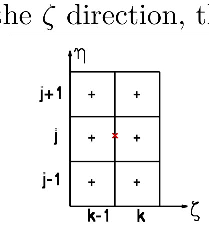

$$\frac{\partial u}{\partial \xi}_{k-1/2} = \frac{1}{4} \left(u_{i+1,j,k} + u_{i+1,j,k-1} - u_{i-1,j,k-1} - u_{i-1,j,k} \right)$$
$$\frac{\partial u}{\partial \eta}_{k-1/2} = \frac{1}{4} \left(u_{i,j+1,k} + u_{i,j+1,k-1} - u_{i,j-1,k} - u_{i,j-1,k-1} \right)$$
$$\frac{\partial u}{\partial \zeta}_{k-1/2} = u_{i,j,k} - u_{i,j,k-1}$$

The derivatives are centered at the cell face perpendicular to the direction of the flux being computed and at the center of the cell in the remaining two directions. The derivative center is indicated by a red cross in the figures above.

The temperature gradients for the heat flux are evaluated similarly with a second order central difference scheme evaluated at each face.

3.2.3 Reconstruction

Essentially Non-Oscillatory Method

For the viscous computations, a third order accurate Essentially Non-Oscillatory (ENO) Method is to reconstruct the conserved variables, Q defined in Equation (3.35). As proposed by Harten and Chakravarthy [24], the ENO method reduces the number of oscillations near the shock, by satisfying three conditions:

$$Q(x) = \mathcal{Q}(x) + \mathcal{O}(\Delta x^3) \tag{3.49}$$

$$Q_i = \int_{x_{i-\frac{1}{2}}}^{x_{i+\frac{1}{2}}} Q_i(x)dx \tag{3.50}$$

$$TV(Q_i(x)) \leq TV(\mathcal{Q}) + \mathcal{O}(\Delta x^3) \tag{3.51}$$

where TV is the Total Variation of a function, as defined in [25] :

$$TV(Q) = \int_{x_{i+\frac{1}{2}}}^{x_{i+\frac{1}{2}}} \left|\frac{dQ}{dx}\right| dx \tag{3.52}$$

The primitive function is used to integrate the conserved variables, Q, from $x_{i-\frac{1}{2}}$ to an arbitrary x within a given cell according to

$$I(x) = \int_{x_{i-a-\frac{1}{2}}}^{x} \mathcal{Q}dx \tag{3.53}$$

for $x_{i-a-\frac{1}{2}} \leq x \leq x_{i-a+\frac{5}{2}}$. The cell locations are shown in Figure 3.3.

The integer a moves a stencil of three cells to the region that minimizes oscillation, by the following method. The one-dimensional formulation is shown here, however, an extension to three-dimensions for a non-uniform grid is utilized in the code.

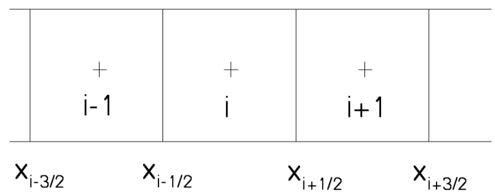

Figure 3.3: Location of Cell Faces

The integrated quantity is interpolated to third order accuracy by a polynomial interpolation with Newton basis. The interpolation scheme is

$$P(x) = a_0 + a_1(x - x_{i-a-\frac{1}{2}}) + a_2(x - x_{i-a-\frac{1}{2}})(x - x_{i-a+\frac{1}{2}}) \tag{3.54}$$

$$+a_3(x - x_{i-a-\frac{1}{2}})(x - x_{i-a+\frac{1}{2}})(x - x_{i-a+\frac{3}{2}}) \tag{3.55}$$

where the coefficients, a_0,a_1,a_2 and a_3 are found via divided differences [24].

The reconstruction of $\mathcal{Q}$ is obtained by differentiating the interpolated integral with respect to x :

$$Q_i(x) = \frac{dP}{dx} \tag{3.56}$$

for $x_{i-\frac{1}{2}} \leq x \leq x_{i+\frac{1}{2}}$ and

$$\begin{aligned} Q_i(x) = \; & a_1 + a_2\left[(x - x_{i-a+\frac{1}{2}}) + (x - x_{i-a-\frac{1}{2}})\right] + \\ & a_3\left[(x - x_{i-a+\frac{1}{2}})(x - x_{i-a+\frac{3}{2}}) + (x - x_{i-a-\frac{1}{2}})(x - x_{i-a+\frac{3}{2}})\right. \\ & \left.(x - x_{i-a-\frac{1}{2}})(x - x_{i-a+\frac{1}{2}})\right] \end{aligned} \tag{3.57}$$

The variable a is chosen to minimize oscillations within the cell. The Total Variation of the derivitive of Q is minimized to ensure minimum oscillations, as defined in equation 3.54. The derivative of Q can be interpreted as the following,

$$\frac{dQ_i}{dx} = \frac{\alpha}{\Delta x} + \frac{\beta}{\Delta x^2}\left(x - x_{i+k-\frac{1}{2}}\right) \tag{3.58}$$

α,β and k are defined in Table 3.1

Table 3.1: Constants of Derivative of Q for Determination of Parameter a

a	α	β	k
0	$\Delta Q_{i+1/2}$	$\Delta Q_{i+3/2} - \Delta Q_{i+1/2}$	1
1	$\Delta Q_{i+1/2}$	$\Delta Q_{i+1/2} - \Delta Q_{i-1/2}$	1
1	$\Delta Q_{i-1/2}$	$\Delta Q_{i+1/2} - \Delta Q_{i-1/2}$	0
2	$\Delta Q_{i-1/2}$	$\Delta Q_{i+1/2} - \Delta Q_{i-3/2}$	0

Thus,

$$\begin{aligned} TV(Q_i(x)) &= \int_{x_{i-1/2}}^{x_{i+1/2}} \|\frac{dQ_i}{dx}\| dx \\ &\leq \int_{x_{i-1/2}}^{x_{i+1/2}} \frac{|\alpha|}{\Delta x} + \int_{x_{i-1/2}}^{x_{i+1/2}} \frac{|\beta|}{\Delta x^2} |(x - x_{i+k-1/2})| dx \\ &= |\alpha| + \frac{1}{2}|\beta| \end{aligned} \tag{3.59}$$

Then, a is selected to minimize α and β in turn, as shown in Table 3.2

Table 3.2: Criteria for Selection of Parameter a

1st Criterion	2nd Criterion	k	a
$\lvert\Delta Q_{i+1/2}\rvert \leq \lvert\Delta Q_{i-1/2}\rvert$	$\lvert\Delta Q_{i+3/2} - \Delta Q_{i+1/2}\rvert \leq \lvert\Delta Q_{i+1/2} - \Delta Q_{i-1/2}\rvert$	1	0
	$\lvert\Delta Q_{i+3/2} - \Delta Q_{i+1/2}\rvert > \lvert\Delta Q_{i+1/2} - \Delta Q_{i-1/2}\rvert$	1	1
$\lvert\Delta Q_{i+1/2}\rvert > \lvert\Delta Q_{i-1/2}\rvert$	$\lvert\Delta Q_{i+1/2} - \Delta Q_{i-1/2}\rvert \leq \lvert\Delta Q_{i-1/2} - \Delta Q_{i-3/2}\rvert$	0	1
	$\lvert\Delta Q_{i+1/2} - \Delta Q_{i-1/2}\rvert > \lvert\Delta Q_{i-1/2} - \Delta Q_{i-3/2}\rvert$	0	2

The different stencils with which Q_i are determined for the different values of a are shown in Figure 3.4.

Modified Upwind Scheme for Conservation Laws

For the inviscid computation, a second order accurate Modified Upwind Scheme for Conservation Laws (MUSCL) scheme is used to reconstruct the conserved variable vector, Q. As proposed by Anderson *et al* [26], the MUSCL scheme is an upwind scheme that minimizes oscillations at discontinuities by limiting the reconstructed values based on the following conditions :

$$\min(Q_{i-1}, Q_i, Q_{i+1}) \leq Q^l_{i+\frac{1}{2}} \leq \max(Q_{i-1}, Q_i, Q_{i+1}) \tag{3.60}$$

$$\min(Q_{i-1}, Q_i, Q_{i+1}) \leq Q^r_{i-\frac{1}{2}} \leq \max(Q_{i-1}, Q_i, Q_{i+1}) \tag{3.61}$$

The one-dimensional formulation is shown here; an extension to three dimensions is utilized in the code.

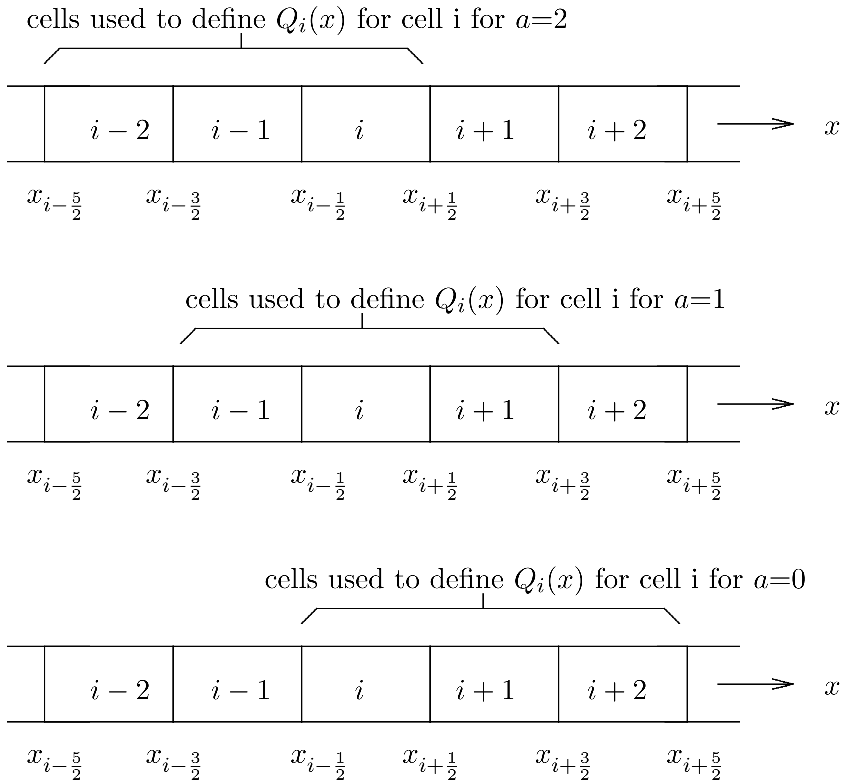

Figure 3.4: Possible Cell Stensils to Construct $Q_i(x)$

The primitive function is used to integrate the conserved variables, Q, from $x_{i-\frac{3}{2}}$ to an arbitrary x within a given cell.

$$I(x) = \int_{x_{i-\frac{3}{2}}}^{x} \mathcal{Q}\ dx \tag{3.62}$$

for $x_{i-\frac{3}{2}} \leq x \leq x_{i+\frac{1}{2}}$

The integrated quantity is interpolated to second order accuracy by a polynomial interpolation with Newton Basis. The interpolation scheme is

$$P(x) = a_0 + a_1(x - x_{i-\frac{3}{2}}) + a_2(x - x_{i-\frac{1}{2}})(x - x_{i-\frac{3}{2}}) \tag{3.63}$$

where the coefficients, a_0, a_1, and a_2 are found via divided differences [27].

The reconstruction of $\mathcal{Q}$, then, is obtained by differentiating the interpolated integral with respect to x :

$$Q_i(x) = \frac{dP}{dx} \tag{3.64}$$

for $x_{i-\frac{1}{2}} \leq x \leq x_{i+\frac{1}{2}}$ and

$$Q_i(x) \quad = \quad a_1 + a_2 \left[(x - x_{i-\frac{1}{2}}) + (x - x_{i-\frac{3}{2}}) \right] \tag{3.65}$$

The reconstruction values for the Q at the cell face are

$$Q^l_{i+\frac{1}{2}} = Q_i + \frac{1}{4} \left[(1-\kappa)\widehat{\Delta Q}_{i-\frac{1}{2}} + (1+\kappa)\widehat{\Delta Q}_{i+\frac{1}{2}} \right] \tag{3.66}$$

$$Q^r_{i+\frac{1}{2}} = Q_i - \frac{1}{4} \left[(1-\kappa)\widehat{\Delta Q}_{i+\frac{1}{2}} + (1+\kappa)\widehat{\Delta Q}_{i-\frac{1}{2}} \right] \tag{3.67}$$

For a value of $\kappa = \frac{1}{3}$ the following values of $\widehat{\Delta Q}_{i+\frac{1}{2}}$ are used where $b = (3-\kappa)/(1-\kappa)$.

When $\Delta Q_{i+\frac{1}{2}} \geq 0$ and $\Delta Q_{i-\frac{1}{2}} \geq 0$

$$\widehat{\Delta Q}_{i-\frac{1}{2}} = \begin{cases} \Delta Q_{i-\frac{1}{2}} & \text{if} \quad \Delta Q_{i-\frac{1}{2}} \leq b\Delta Q_{i+\frac{1}{2}} \\ b\Delta Q_{i+\frac{1}{2}} & \text{if} \quad \Delta Q_{i-\frac{1}{2}} > b\Delta Q_{i+\frac{1}{2}} \end{cases} \tag{3.68}$$

$$\widehat{\Delta Q}_{i+\frac{1}{2}} = \begin{cases} \Delta Q_{i+\frac{1}{2}} & \text{if} \quad \Delta Q_{i+\frac{1}{2}} \leq b\Delta Q_{i-\frac{1}{2}} \\ b\Delta Q_{i-\frac{1}{2}} & \text{if} \quad \Delta Q_{i+\frac{1}{2}} > b\Delta Q_{i-\frac{1}{2}} \end{cases} \tag{3.69}$$

When $\Delta Q_{i+\frac{1}{2}} \geq 0$ and $\Delta Q_{i-\frac{1}{2}} \leq 0$

$$\widehat{\Delta Q}_{i-\frac{1}{2}} = \begin{cases} \Delta Q_{i-\frac{1}{2}} & \text{if} \quad \Delta Q_{i-\frac{1}{2}} \geq -2\Delta Q_{i+\frac{1}{2}} \\ -2\Delta Q_{i+\frac{1}{2}} & \text{if} \quad \Delta Q_{i-\frac{1}{2}} < -2\Delta Q_{i+\frac{1}{2}} \end{cases} \tag{3.70}$$

$$\widehat{\Delta Q}_{i+\frac{1}{2}} = \begin{cases} \Delta Q_{i+\frac{1}{2}} & \text{if} \quad \Delta Q_{i+\frac{1}{2}} \leq -2\Delta Q_{i-\frac{1}{2}} \\ -2\Delta Q_{i-\frac{1}{2}} & \text{if} \quad \Delta Q_{i+\frac{1}{2}} > -2\Delta Q_{i-\frac{1}{2}} \end{cases} \tag{3.71}$$

When $\Delta Q_{i+\frac{1}{2}} \leq 0$ and $\Delta Q_{i-\frac{1}{2}} \leq 0$

$$\widehat{\Delta Q}_{i-\frac{1}{2}} = \begin{cases} \Delta Q_{i-\frac{1}{2}} & \text{if} \quad \Delta Q_{i-\frac{1}{2}} \geq b\Delta Q_{i+\frac{1}{2}} \\ b\Delta Q_{i+\frac{1}{2}} & \text{if} \quad \Delta Q_{i-\frac{1}{2}} < b\Delta Q_{i+\frac{1}{2}} \end{cases} \tag{3.72}$$

$$\widehat{\Delta Q}_{i+\frac{1}{2}} = \begin{cases} \Delta Q_{i+\frac{1}{2}} & \text{if} \quad \Delta Q_{i+\frac{1}{2}} \geq b\Delta Q_{i-\frac{1}{2}} \\ b\Delta Q_{i-\frac{1}{2}} & \text{if} \quad \Delta Q_{i+\frac{1}{2}} < b\Delta Q_{i-\frac{1}{2}} \end{cases} \tag{3.73}$$

When $\Delta Q_{i+\frac{1}{2}} \leq 0$ and $\Delta Q_{i-\frac{1}{2}} \geq 0$

$$\widehat{\Delta Q}_{i-\frac{1}{2}} = \begin{cases} \Delta Q_{i-\frac{1}{2}} & \text{if} \quad \Delta Q_{i-\frac{1}{2}} \leq -2\Delta Q_{i+\frac{1}{2}} \\ -2\Delta Q_{i+\frac{1}{2}} & \text{if} \quad \Delta Q_{i-\frac{1}{2}} > -2\Delta Q_{i+\frac{1}{2}} \end{cases} \tag{3.74}$$

$$\widehat{\Delta Q}_{i+\frac{1}{2}} = \begin{cases} \Delta Q_{i+\frac{1}{2}} & \text{if} \quad \Delta Q_{i+\frac{1}{2}} \geq -2\Delta Q_{i-\frac{1}{2}} \\ -2\Delta Q_{i-\frac{1}{2}} & \text{if} \quad \Delta Q_{i+\frac{1}{2}} < -2\Delta Q_{i-\frac{1}{2}} \end{cases} \tag{3.75}$$

3.2.4 Time Integration

The two-stage explicit Runge-Kutta scheme [28] is used to march forward in time. The scheme is applied as follows:

$$\begin{aligned} Q_i^0 &= Q_i^n \\ Q_i^1 &= Q_i^0 + \frac{\Delta t}{2} R_i^0 \\ Q_i^2 &= Q_i^0 + \Delta t R_i^1 \\ Q_i^{n+1} &= Q_i^2 \end{aligned} \tag{3.76}$$

where R_i^0 is the flux evaluated at Q_i^0 and R_i^1 is the flux evaluated at Q_i^1.

Computing Q_i^1 is an intermediate step that ensures second order accuracy of the scheme. The time step is determined by the Courant-Friedrichs-Lewy (CFL) condition for viscous flows. The inviscid timestep criterion is given by Equation (3.79) in terms of dimensionless variables. The viscous timestep criterion in terms of dimensionless variables is given by Equation (3.80).

$$\Delta t_x = \frac{\text{CFL } \Delta x}{u + a}, \quad \Delta t_y = \frac{\text{CFL } \Delta y}{v + a}, \quad \Delta t_x = \frac{\text{CFL } \Delta z}{w + a} \tag{3.77}$$

$$\Delta t_x = \frac{\text{CFL } \Delta x^2 \rho}{\mu}, \quad \Delta t_y = \frac{\text{CFL } \Delta y^2 \rho}{\mu}, \quad \Delta t_z = \frac{\text{CFL } \Delta z^2 \rho}{\mu} \tag{3.78}$$

where CFL<1. The final timestep is the minimum timestep required by the inviscid and viscous criteria in every direction.

3.2.5 Parallelization

The code has been parallelized to handle large grids. The Message Passing Interface (MPI) has been used to run jobs on parallel computers.

The message passing scheme in this software is limited to only pass information between zone faces of the same size. Zones are limited to hexahedrons that pass to zones with adjacent faces of the same size (number of cells). A two dimensional depiction is shown in Figure 3.5.

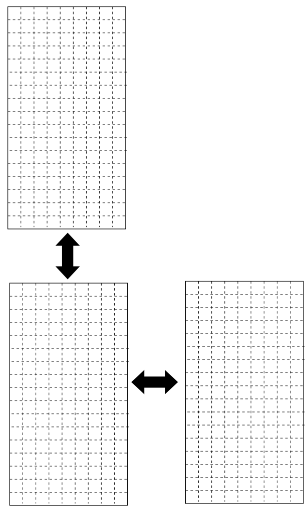

Figure 3.5: Adjacent Zones Must Have Faces of Equal Sizes

The fluid cells are updated by the finite volume scheme. The ghost cells are updated during after each stage of the Runge-Kutta time iteration scheme (twice for each time step). The ghost cells across zone boundaries are swapped at the time the ghost cells are updated internally to each zone. A depiction of the cell updating is shown in Figure 3.6. Fluid cells from the upstream (closer to (x, y, z)=(0,0,0)) zone provide flow data to the ghost cells in the adjacent zone in each direction (ξ, η, ζ) simultaneously. Then the higher (farther from (x, y, z)=(0,0,0)) provide flow data to the ghost cells in the adjacent zones in all three directions (ξ, η, ζ).

3.2.6 Corner Corrections

Entropy Fix

The cylinder edge (Figure 2.1) creates a local singularity in the flow. Near regions of high gradients, such as quickly accelerating flow, the ENO scheme chooses $a = 1$, which equates the ENO scheme to an upwind scheme, specifically, MUSCL with $k = \frac{1}{3}$. Upwind schemes

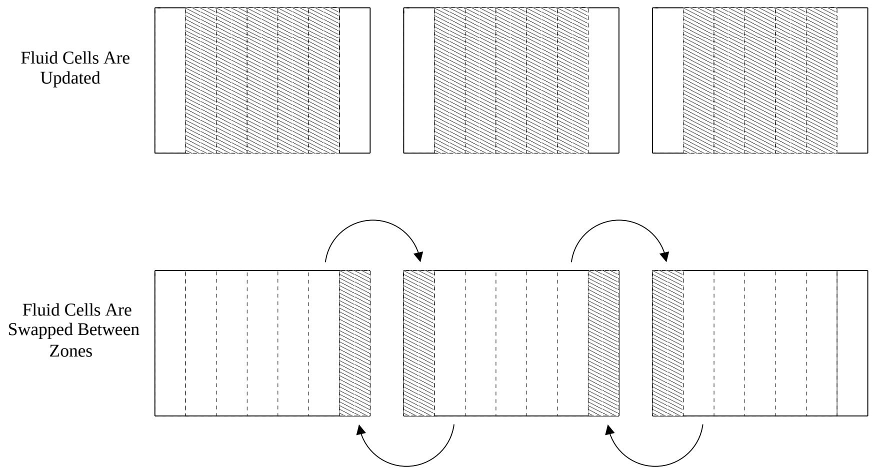

Figure 3.6: Transfer of Ghost Cells Between Three Zones

are not required to conserve entropy. Any numerical entropy production near the expansion is made further unstable by the singularity. Woodward and Collela introduced an imposed entropy fix near the step [29], which was later summarized by Marquina and Donat [30]. The entropy is first corrected in six cells in the vicinity of the step, as shown in Figure 3.7.

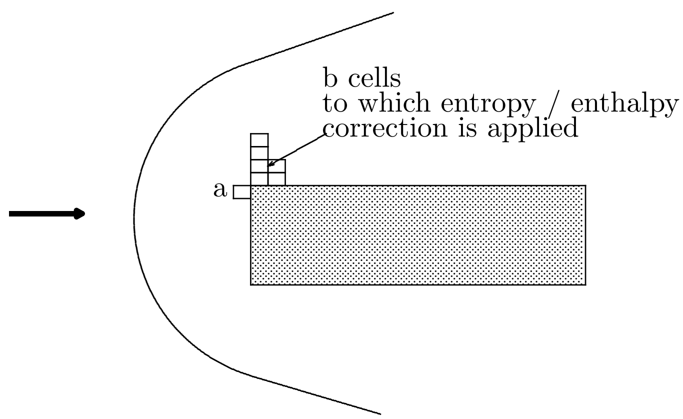

Figure 3.7: Cells Used to Correct Entropy and Enthalpy Around Corner Singularity

The following equation makes use of the isentropic relations for a perfect gas:

$$\rho_b = \rho_a (\frac{p_b}{p_a})^{\frac{1}{\gamma}} \tag{3.79}$$

The enthalpy is corrected for the same cells using the following relation for the conservative vector:

$$\hat{\alpha} = \frac{\frac{1}{2}q_a^2 + \frac{\gamma}{\gamma-1}A(\rho_a^{\gamma-1} - \rho_b^{\gamma-1})}{\frac{1}{2}q_b^2} \tag{3.80}$$

$$= \left(\frac{q_a}{q_b}\right)^2 \left(1 + \frac{2}{M_a^2(\gamma-1)}\right) - \frac{2}{(\gamma-1)M_b^2} \tag{3.81}$$

where q_b^2 is the sum of squares of velocities from cell b.

$$Q = \begin{pmatrix} \rho_b \\ \hat{\alpha}^{\frac{1}{2}}(q_b)_x \\ \hat{\alpha}^{\frac{1}{2}}(q_b)_y \\ \hat{\alpha}^{\frac{1}{2}}(q_b)_z \\ \frac{1}{\gamma-1}\rho_b + \frac{1}{2}\rho_b\hat{\alpha}q_b^2 \end{pmatrix} \tag{3.82}$$

where Q is vector of dependant variables from equation 3.32. The quantity $\hat{\alpha}$ is dimensionless, thus vector of dependant variables, Q, is represented in terms of dimensionless variables.

It is shown in Marquina and Donat [30] that the adiabatic constant, A=$\frac{p}{\rho^\gamma}$, is conserved over the step with this correction, and thus entropy is conserved over the step.

Density and Pressure Relaxing

In the vicinity of the corner, singularity can create computational errors despite the entropy fix. For the larger period cases of the viscous computation ($L = 2$ and $L = 4$), the density and pressure were relaxed in time in the event that the density in one of the cells in the viscinity of the corner was computed to be negative. An average density between the current computed density and the density from the previous Runge Kutta stage. This fix was only implemented for the two closest cells the corner.

Chapter 4

Code Validation

4.1 Comparison to Blasius Flat Plate Boundary Layer

To verify the accuracy of the viscous algorithms in the code, computations of known solutions are performed for comparison. The Dorodnistyn-Howarth transformation is utilized to find an ODE that is the same as the Blasius flat plate boundary layer incompressible case. The derivation is provided in Appendix A. The solution to the Blasius flat plate boundary layer case is well documented (for instance, [31]).

To gauge the accuracy of every viscous and heat transfer term, twelve cases are computed. For both isothermal and adiabatic flat plate in Mach 2 flow three cases of plates aligned with the three axes, and three plates at 10 degree inclements to the three axes are computed. The six different geometries are shown in Figure 4.1. Each axis refers to one of the six faces of the cell, as is shown in Figure 4.2.

The flat plate is modelled with a no-slip condition on the velocity, and either a constant heat flux or temperature, depending on the case. The isothermal wall is a hot wall, T_w/T_∞=2.0, as the adiabatic wall is approximately T_w/T_∞=1.8.

All cases are run with non-uniform ENO reconstruction and Van Leer's flux algorithm. Each case was run on one processor.

The grid for each case was stretched in the direction perpendicular to the plate, with a stretching factor of 1.01. At the plate, the $\Delta x/L$ was 0.01, where L is the length of the plate and x is taken to be the direction of the flow, parallel to the plate. The smallest cell occurs at the bottom of the domain, just above the plate, with a $\Delta y/L$ of 0.0005, where y is taken to be the direction perpendicular to the plate. At the back of the plate, x/L=1, there would be approximately 44 cells in the boundary layer.

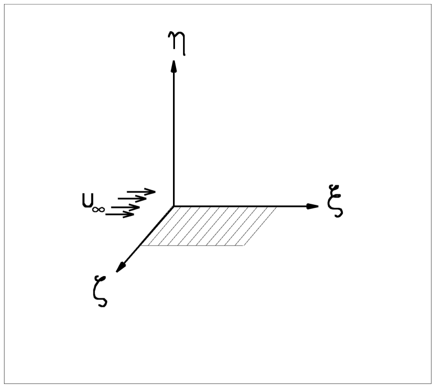

(a) Flat Plate Aligned with ξ Axis

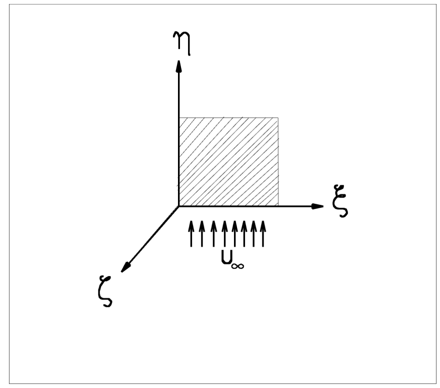

(b) Flat Plate Aligned with η Axis

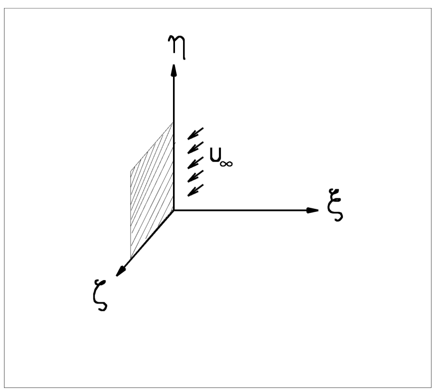

(c) Flat Plate Aligned with ζ Axis

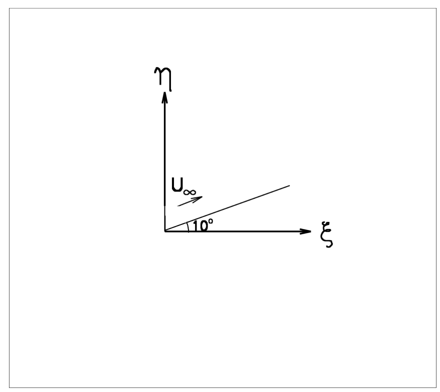

(d) Flat Plate at 10 degree angle with ξ Axis

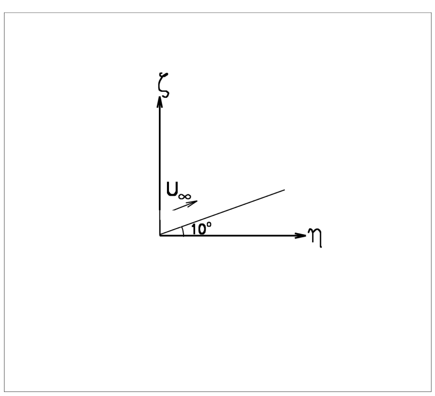

(e) Flat Plate at 10 degree angle with η Axis

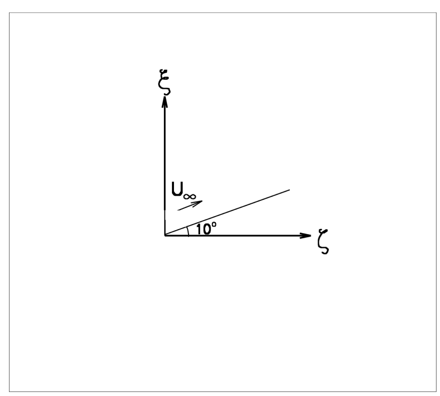

(f) Flat Plate at 10 degree angle with ζ Axis

Figure 4.1: Six Geometries Run to Verify Viscous and Heat Transfer Terms

The freestream parameters for the calculations are displayed in Table 4.1.

Table 4.1: Dimensionless Flow Parameters for Blasius Flat Plate Case

Description	Definition	Value
Mach	M_∞	2.0
Specific heat ratio	γ	1.4
Reynolds number	Re_L	100,000
Prandtl number	Pr	1

4.1.1 Skin Friction Calculation

The skin friction is defined as

$$C_f = \frac{\tau_w^*}{\frac{1}{2}\rho_e^* U_e^{*2}} = \frac{\tau_w}{\frac{1}{2}\rho_e U_e^2} \tag{4.1}$$

where ρ_e is the dimensionless density at the edge of the boundary layer and U_e is the dimensionless velocity at the edge of the boundary layer. In the subsonic case, the freestream and edge conditions are the same. Because of the weak leading edge shock wave caused by the boundary layer displacement thickness, the edge and freestream conditions are not exactly the same. The stress term is non-dimensionalized by $\rho_\infty U_\infty^2$, and thus the skin friction equation is the same in terms of its non-dimensional parameters.

The skin friction from the computation was calculated from the stress term, as calculated in the viscous terms in the flow solver. The height of the boundary layer cannot be determined exactly, and thus edge conditions were taken at a location qualitatively selected where the velocity gradient had dropped nearly to zero.

The Blasius skin friction was calculated with the following equation :

$$C_f = \frac{2f''(\eta)}{\sqrt{Re_x}} \tag{4.2}$$

where Re_x is the Reynolds number taken at the edge of the boundary layer, and $f''(\eta)$ refers to the solution of the Blasius equation, which was taken from White [31].

$$Re_x = \frac{\rho_e^* U_e^* x^*}{\mu^*} = \frac{\rho_e U_e x}{\mu} Re_\infty \tag{4.3}$$

4.1.2 Stanton Number Calculation

The Stanton Number is defined as

$$St = \frac{q_w^*}{\rho_e^* U_e^* C_p^* (T_w^* - T_{ad}^*)} \tag{4.4}$$

where T_{ad}^* is the dimensional adiabatic wall temperature. In terms of nondimensional variables, this becomes

$$St = \frac{-\frac{\partial T}{\partial y}_w}{Pr_\infty Re_\infty \rho_e U_e C_p (T_w - T_{ad})} \tag{4.5}$$

where the subscript e refers to the edge condition, at the edge of the boundary layer.

The adiabatic wall temperature was determined from the equation derived by Crocco for a $Pr = 1$,

$$T_{ad} = T_e(x) \left(1 + \frac{\gamma - 1}{2} M_e^2 \right) \tag{4.6}$$

The Stanton number from the code is calculated using the heat transfer rate, as calculated in the viscous terms in the flow solver, and the conditions at the edge of the boundary layer, as described above. The Stanton number was only computed for the isothermal cases.

The Stanton number in terms of the Blasius solution is calculated as half the skin friction, by the Reynolds' analogy, derived in Appendix B.

4.1.3 Results

The profiles of velocity are shown in Figures 4.3 through 4.14. Subfigures (a) - (c) show the velocity parallel to the plate, u/U_∞. The computed parallel velocities are within 1% of the Blasius predicted velocities. The profiles of velocity perpendicular to the flat plate, v/U_∞, are shown in Figures 4.3 through 4.14, subfigures (d)-(f). The magnitude of the velocity perpendicular to the plate is very small compared to velocity parallel to the plate. Thus, the perpendicular velocities, v, are highly sensitive to perturbations in the flow. The ENO scheme minimizes oscillations across the shock; however, it does not entirely prevent all numerical oscillations. Due to small numerical perturbations, the perpendicular velocities oscillate very slightly in time. The oscillations of velocity perpendicular to the plate are shown in Figure 4.15. The velocity is taken from the $x/L = 0.4$ location on the plate at $\eta = 6$, near the edge of the boundary layer. The mean of velocity in the dimensionless time range shown, is $v_{mean} = 0.00495$. The Blasius solution at $\eta = 6$ is $v_{Blasius} = 0.0045$. It is shown that the mean of the oscillations is 10% lower than the Blasius solution. The 10% difference can be attributed to small oscillations in the expansion fan at the leading edge of the plate.

The temperature profiles, nondimensionalized by the freestream temperature, are shown in Figures 4.16 through 4.27 plotted against the Blasius temperature in the boundary layer. It can be seen that the temperatures agree very well.

The skin friction coefficient is graphed in Figures 4.28 through 4.31. The calculated skin friction is within 2% of the Blasius skin friction. This indicates the viscous terms in the code are accurate.

The Stanton number is graphed for the isothermal cases in Figures 4.32 and 4.33. The Stanton number falls within the 2% of the Blasius predicted Stanton number in each case. This is lower than the error that can be expected from experimental measurement of heat transfer.

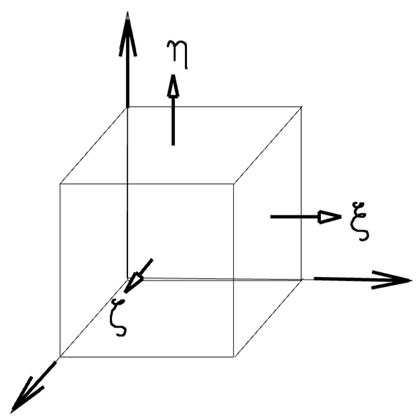

Figure 4.2: Direction of Axes Determined by Cell Geometry

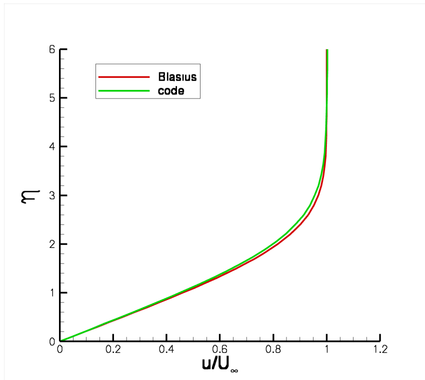

(a) $x/L = 0.4$

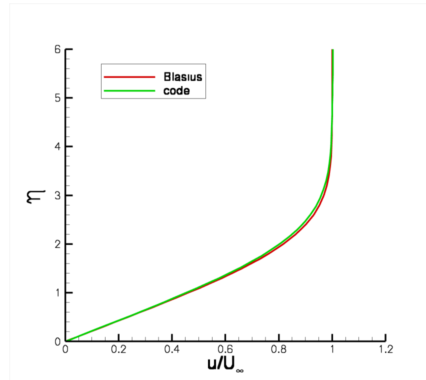

(b) $x/L = 0.6$

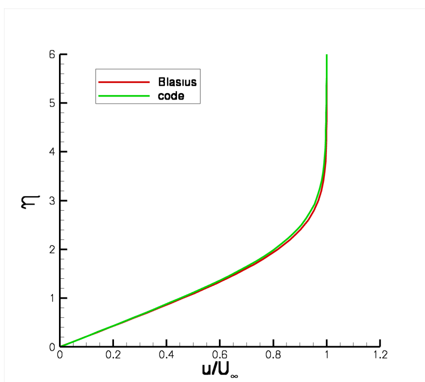

(c) $x/L = 0.8$

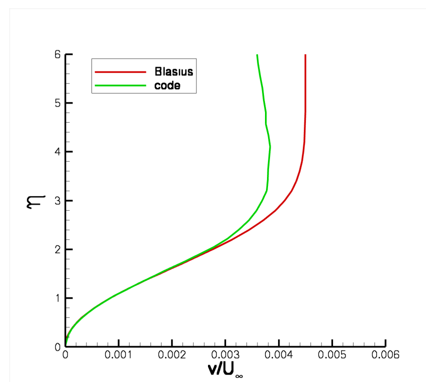

(d) $x/L = 0.4$

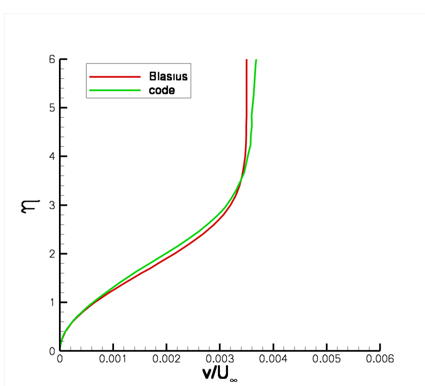

(e) $x/L = 0.6$

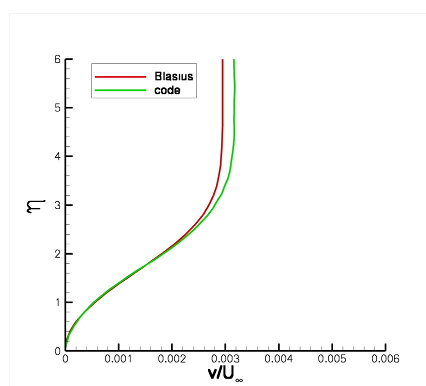

(f) $x/L = 0.8$

Figure 4.3: Adiabatic Flat Plate Perpendicular to η Axis.

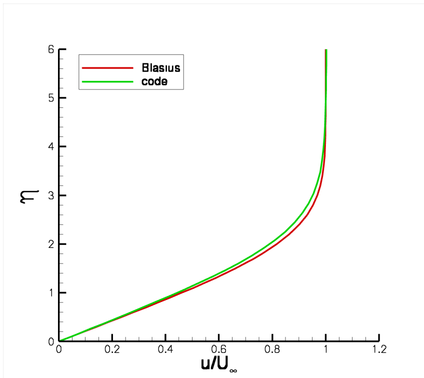

(a) $x/L = 0.4$

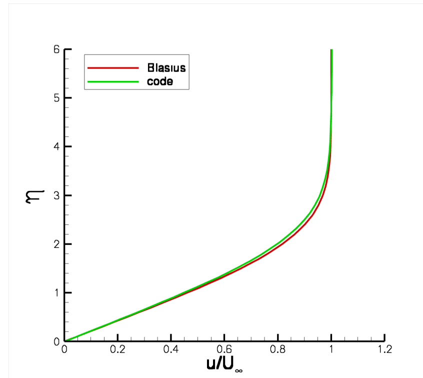

(b) $x/L = 0.6$

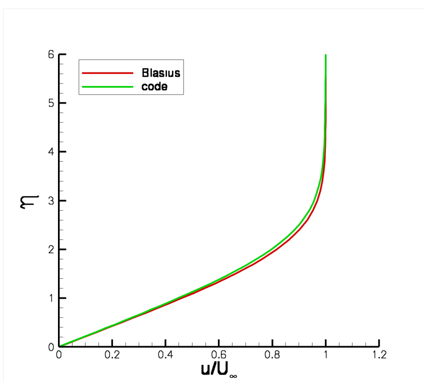

(c) $x/L = 0.8$

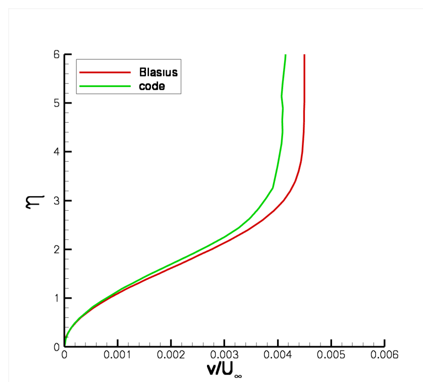

(d) $x/L = 0.4$

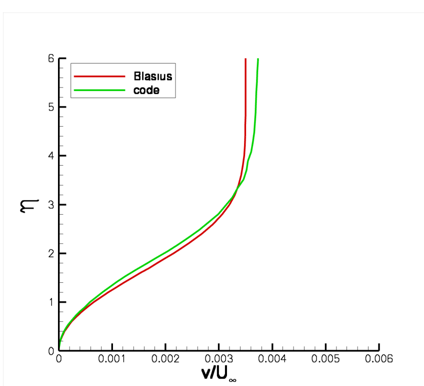

(e) $x/L = 0.6$

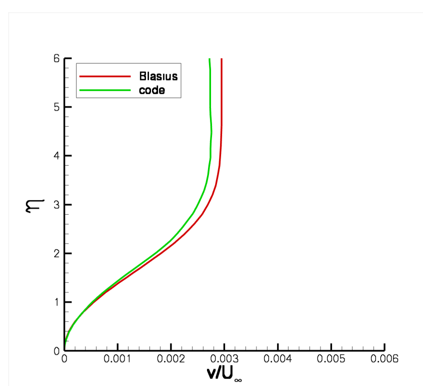

(f) $x/L = 0.8$

Figure 4.4: Adiabatic Flat Plate Perpendicular to ζ Axis.

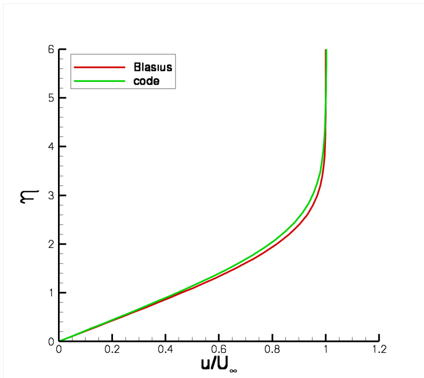

(a) $x/L = 0.4$

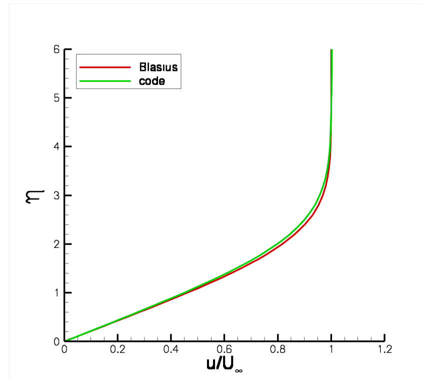

(b) $x/L = 0.6$

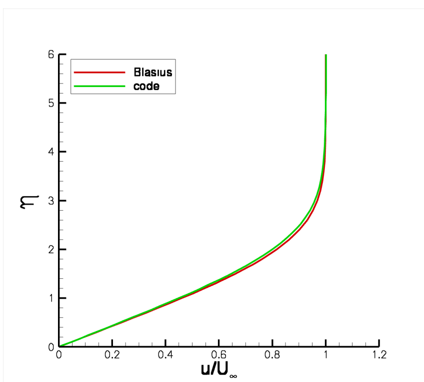

(c) $x/L = 0.8$

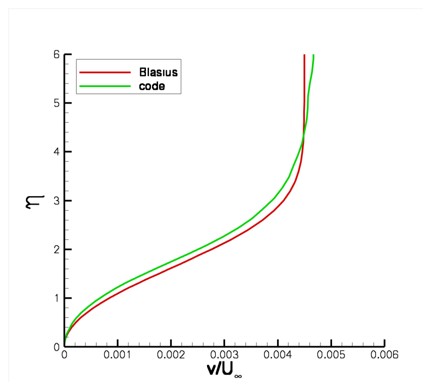

(d) $x/L = 0.4$

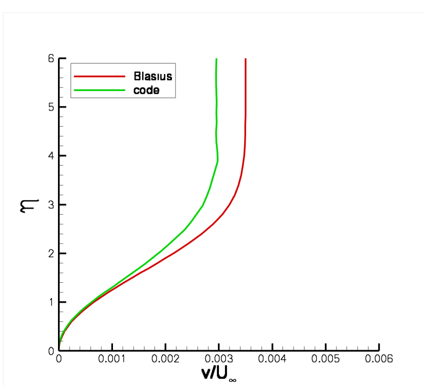

(e) $x/L = 0.6$

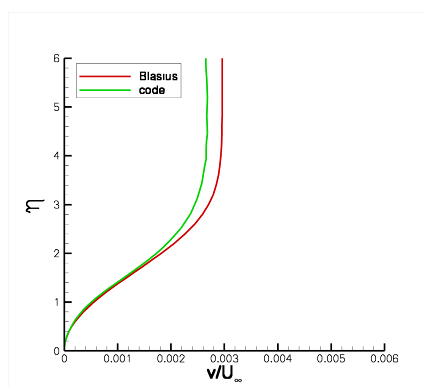

(f) $x/L = 0.8$

Figure 4.5: Adiabatic Flat Plate Perpendicular to ξ Axis.

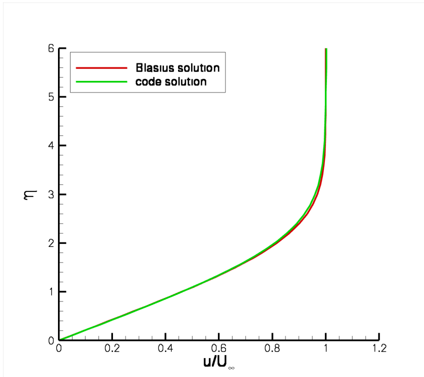

(a) $x/L = 0.4$

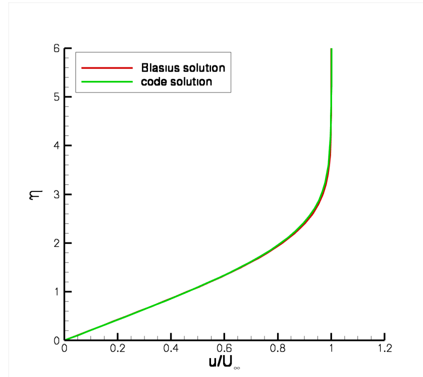

(b) $x/L = 0.6$

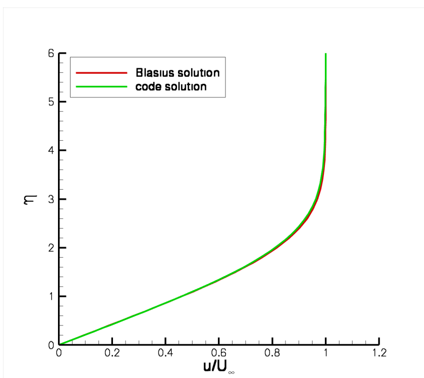

(c) $x/L = 0.8$

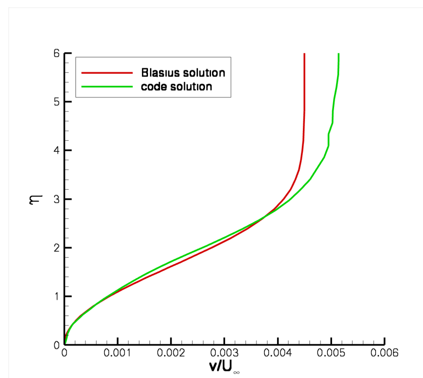

(d) $x/L = 0.4$

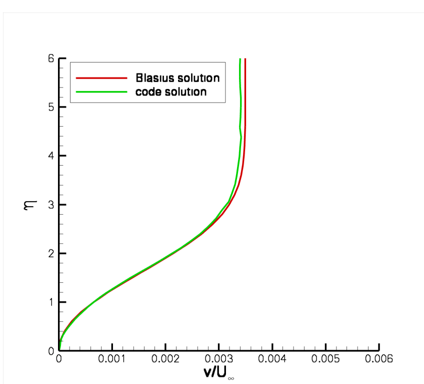

(e) $x/L = 0.6$

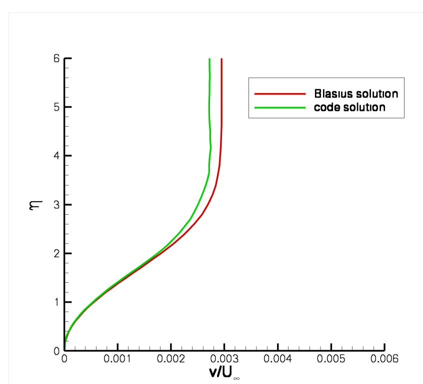

(f) $x/L = 0.8$

Figure 4.6: Isothermal Flat Plate Perpendicular to η Axis.

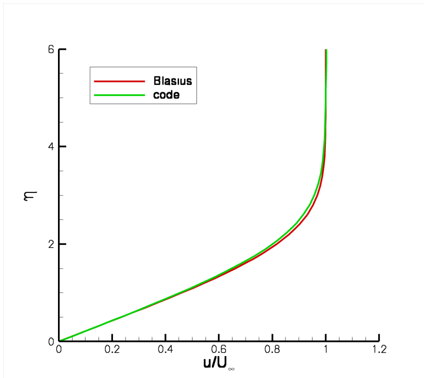

(a) $x/L = 0.4$

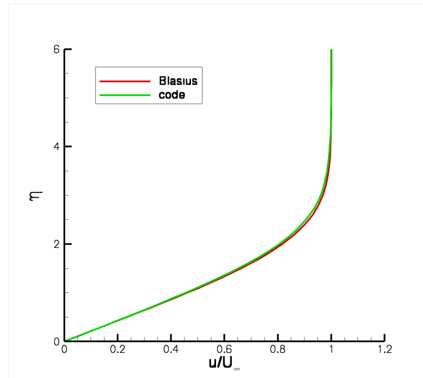

(b) $x/L = 0.6$

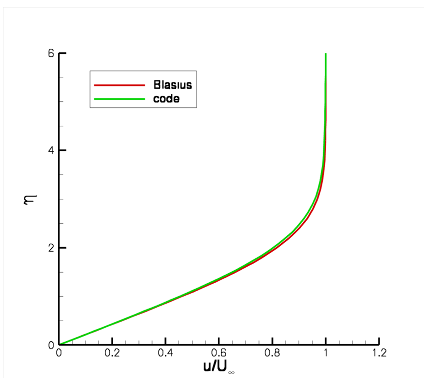

(c) $x/L = 0.8$

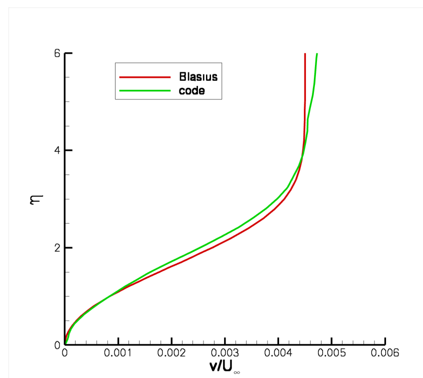

(d) $x/L = 0.4$

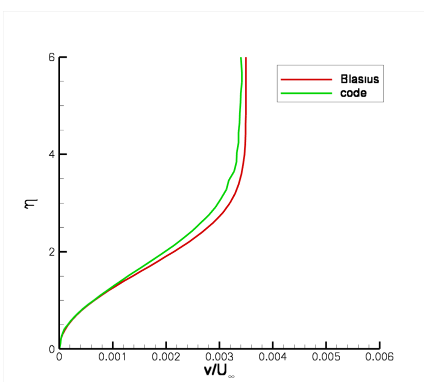

(e) $x/L = 0.6$

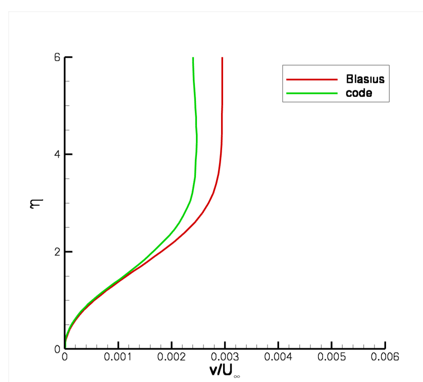

(f) $x/L = 0.8$

Figure 4.7: Isothermal Flat Plate Perpendicular to ζ Axis.

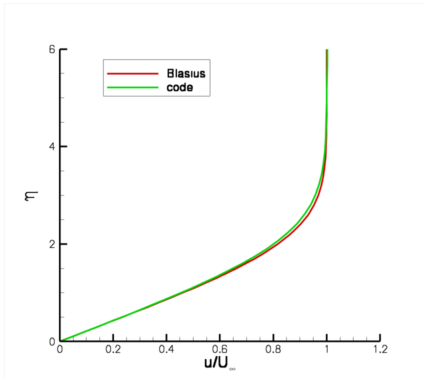

(a) $x/L = 0.4$

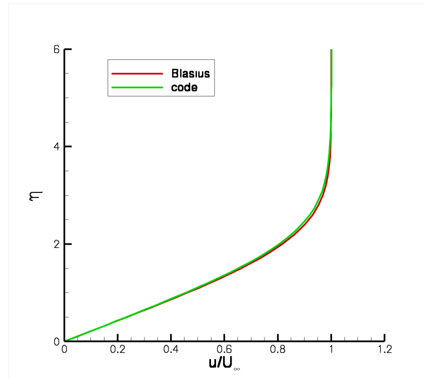

(b) $x/L = 0.6$

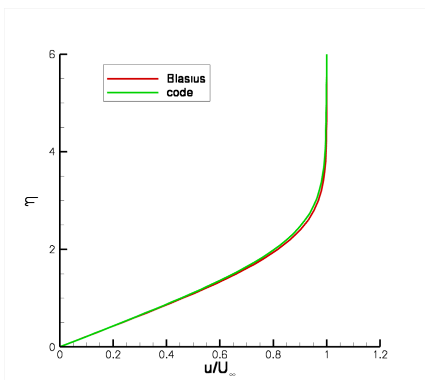

(c) $x/L = 0.8$

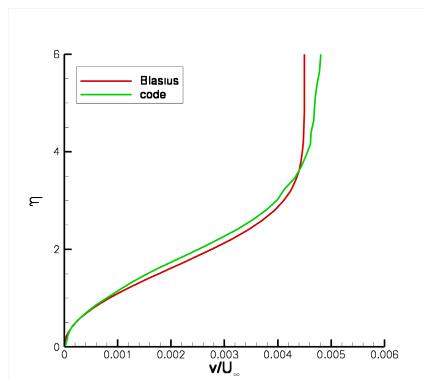

(d) $x/L = 0.4$

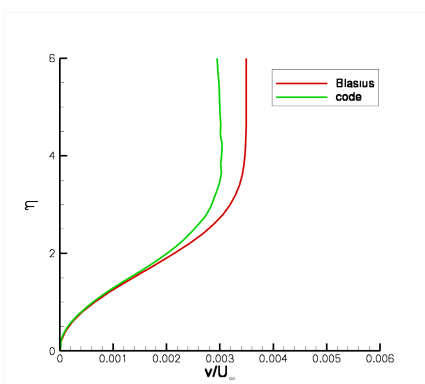

(e) $x/L = 0.6$

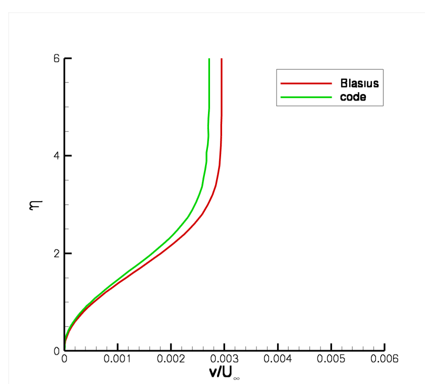

(f) $x/L = 0.8$

Figure 4.8: Isothermal Flat Plate Perpendicular to ξ Axis.

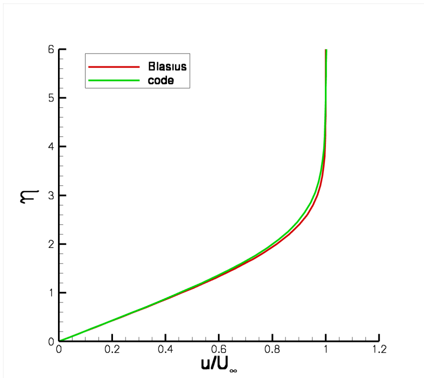

(a) $x/L = 0.4$

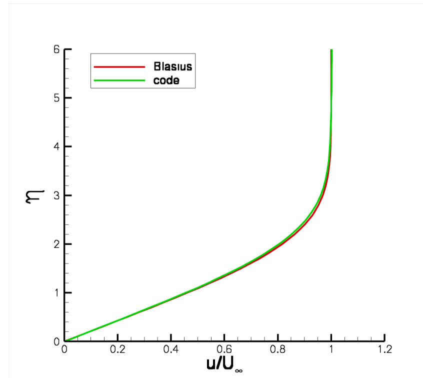

(b) $x/L = 0.6$

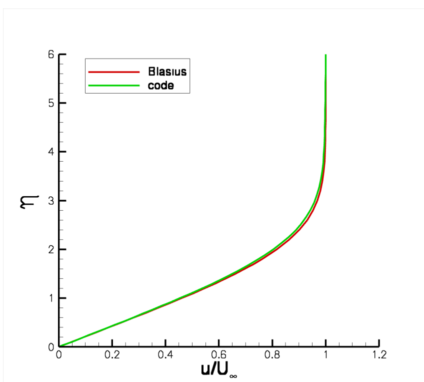

(c) $x/L = 0.8$

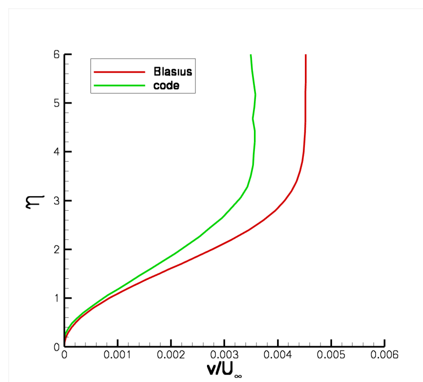

(d) $x/L = 0.4$

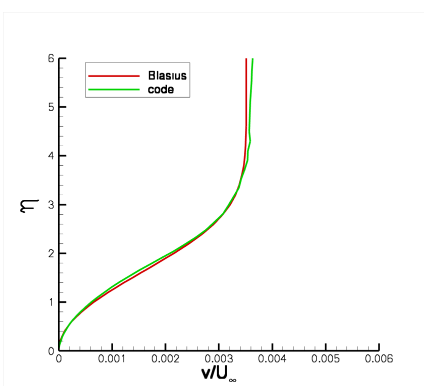

(e) $x/L = 0.6$

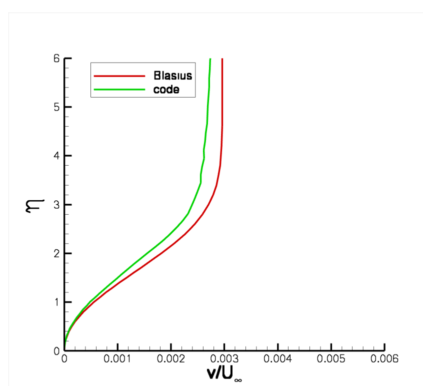

(f) $x/L = 0.8$

Figure 4.9: Adiabatic Flat Plate At Ten Degree Incline from ξ Axis.

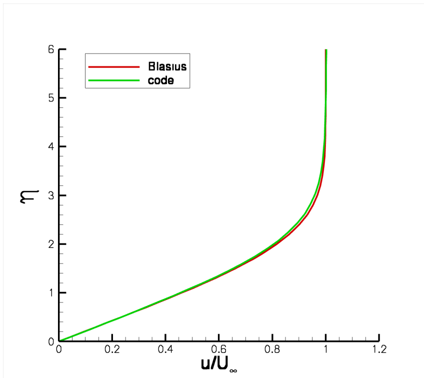

(a) $x/L = 0.4$

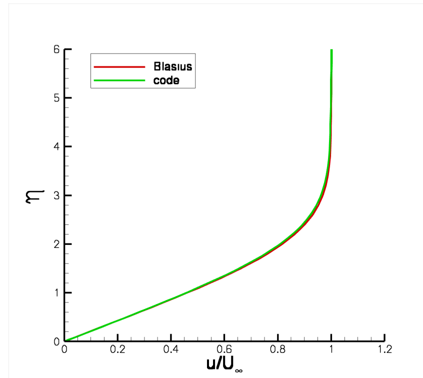

(b) $x/L = 0.6$

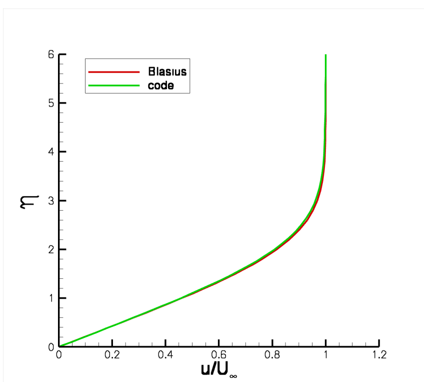

(c) $x/L = 0.8$

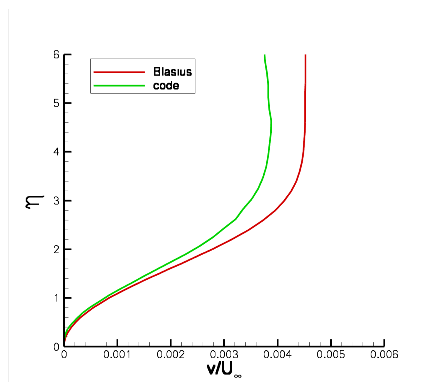

(d) $x/L = 0.4$

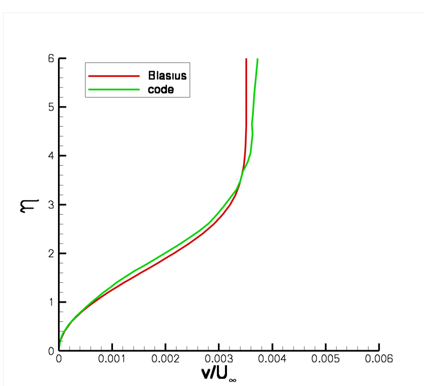

(e) $x/L = 0.6$

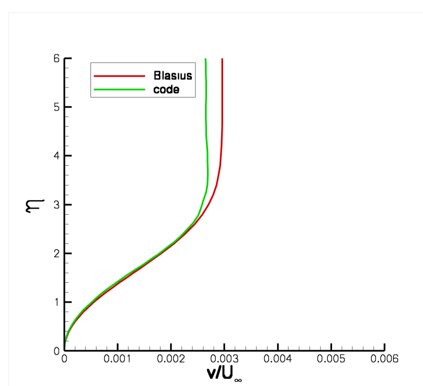

(f) $x/L = 0.8$

Figure 4.10: Adiabatic Flat Plate At Ten Degree Incline from η Axis.

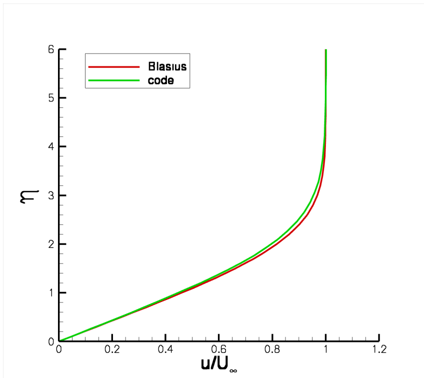

(a) $x/L = 0.4$

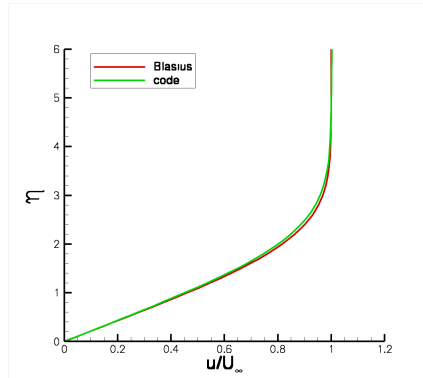

(b) $x/L = 0.6$

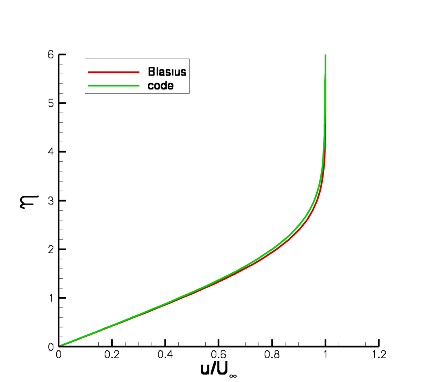

(c) $x/L = 0.8$

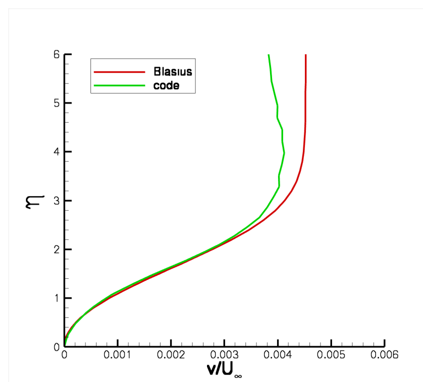

(d) $x/L = 0.4$

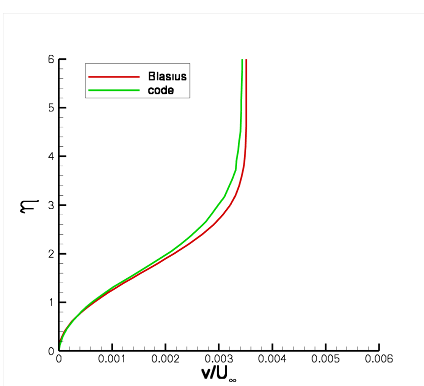

(e) $x/L = 0.6$

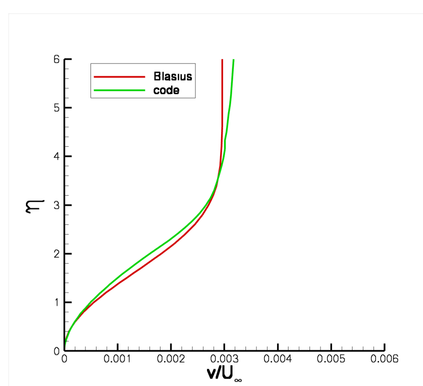

(f) $x/L = 0.8$

Figure 4.11: Adiabatic Flat Plate At Ten Degree Incline from ζ Axis.

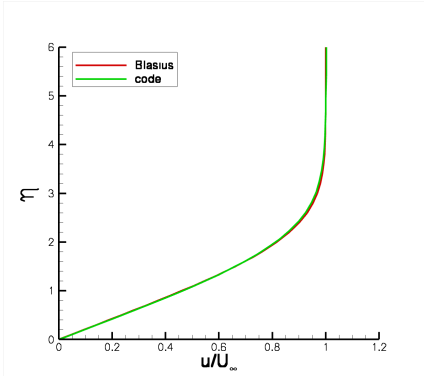

(a) $x/L = 0.4$

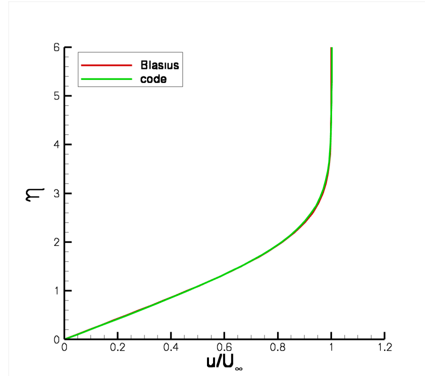

(b) $x/L = 0.6$

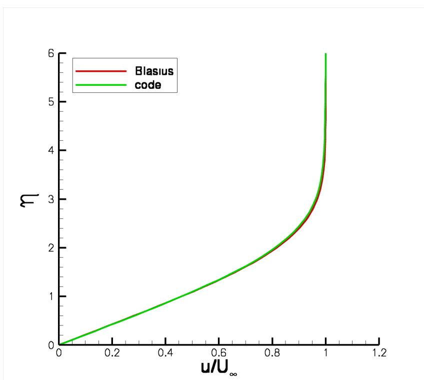

(c) $x/L = 0.8$

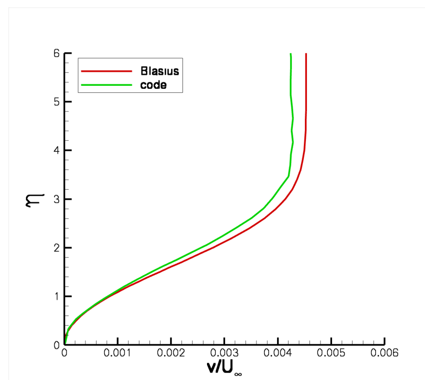

(d) $x/L = 0.4$

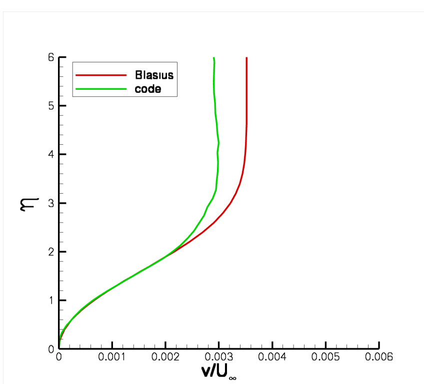

(e) $x/L = 0.6$

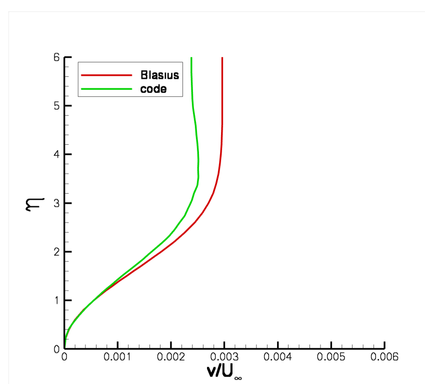

(f) $x/L = 0.8$

Figure 4.12: Isothermal Flat Plate At Ten Degree Incline to ξ Axis.

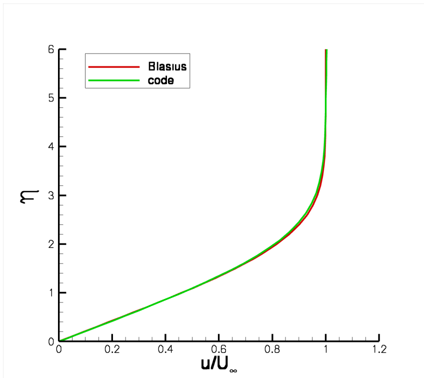

(a) $x/L = 0.4$

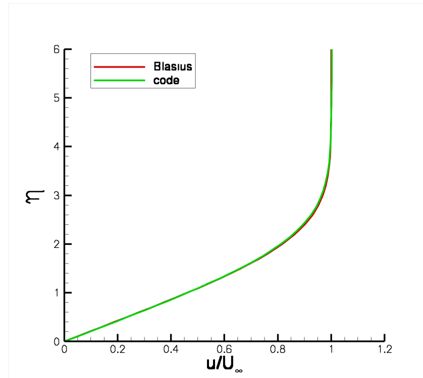

(b) $x/L = 0.6$

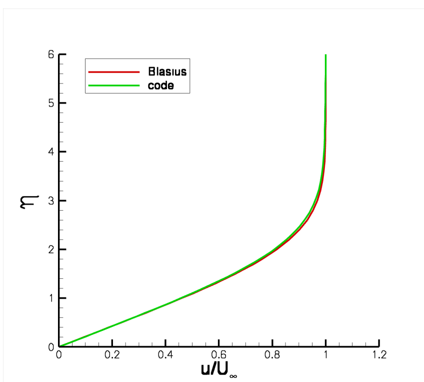

(c) $x/L = 0.8$

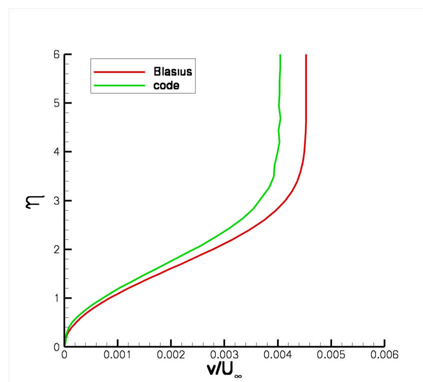

(d) $x/L = 0.4$

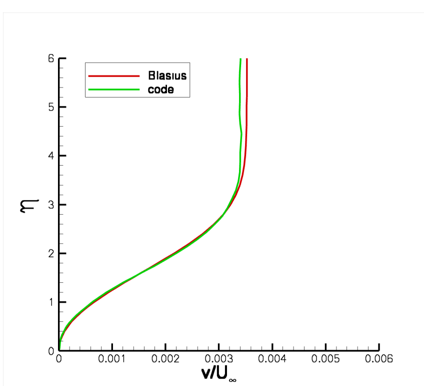

(e) $x/L = 0.6$

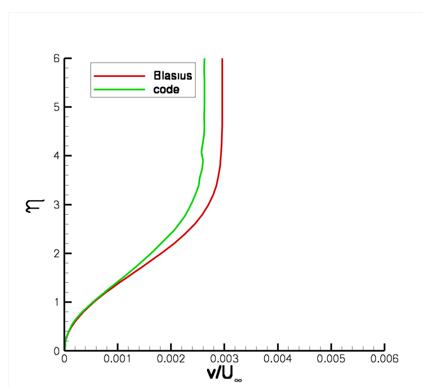

(f) $x/L = 0.8$

Figure 4.13: Isothermal Flat Plate At Ten Degree Incline to η Axis.

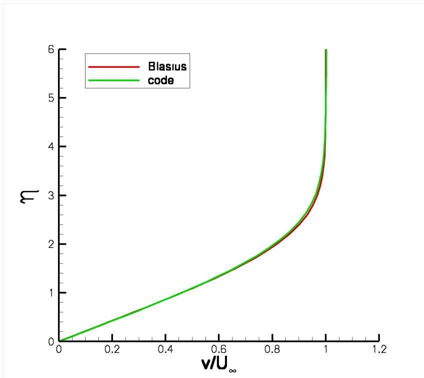

(a) $x/L = 0.4$

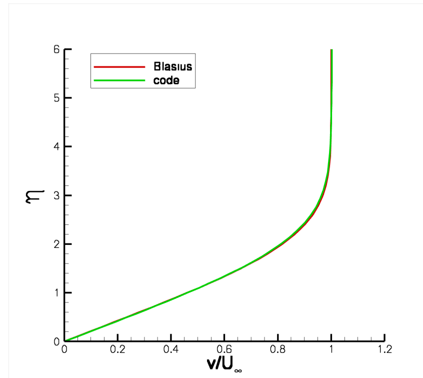

(b) $x/L = 0.6$

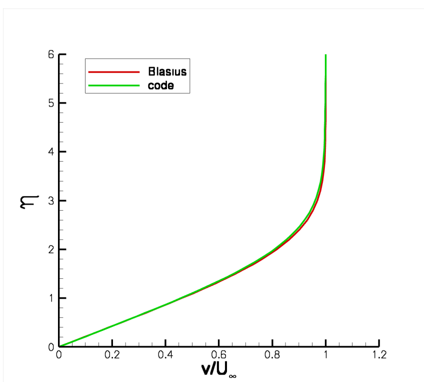

(c) $x/L = 0.8$

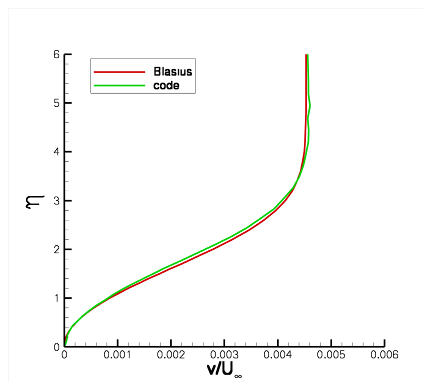

(d) $x/L = 0.4$

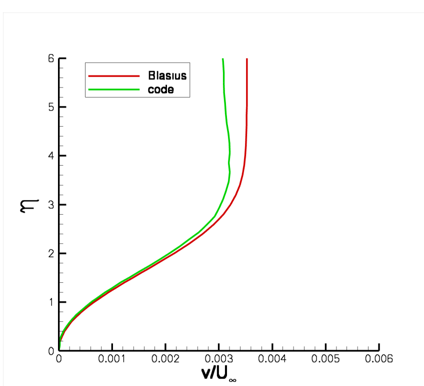

(e) $x/L = 0.6$

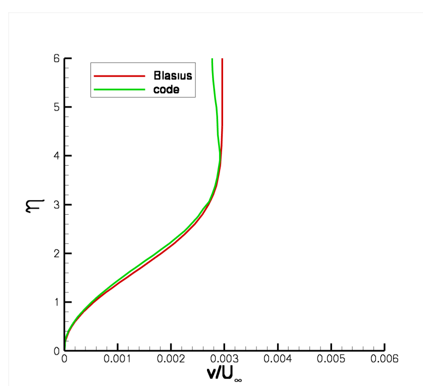

(f) $x/L = 0.8$

Figure 4.14: Isothermal Flat Plate At Ten Degree Incline to ζ Axis.

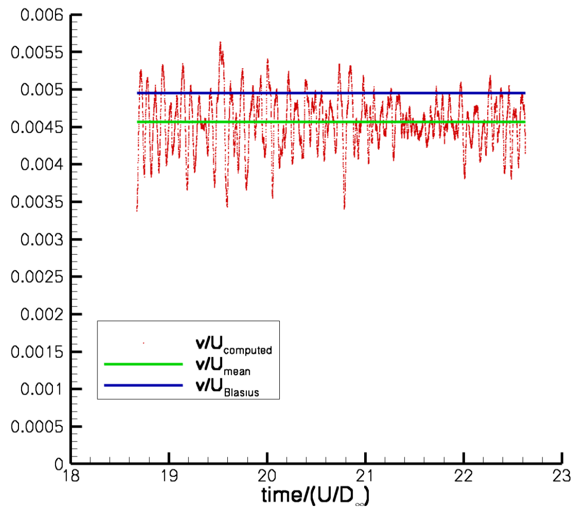

Figure 4.15: Oscillations in Time of Velocities Perpendicular to Flat Plate at $\eta = 6$, at $x/L = 0.4$ on the Plate

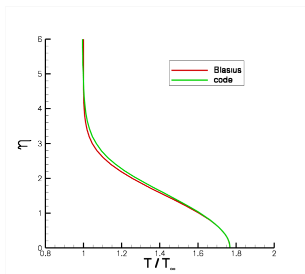

(a) $x/L = 0.4$

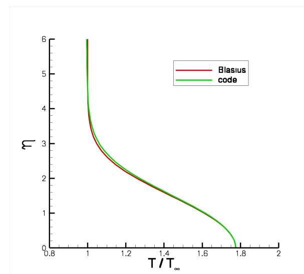

(b) $x/L = 0.6$

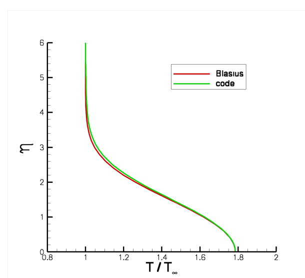

(c) $x/L = 0.8$

Figure 4.16: Temperature in Boundary Layer for Adiabatic Flat Plate Perpendicular to η Axis

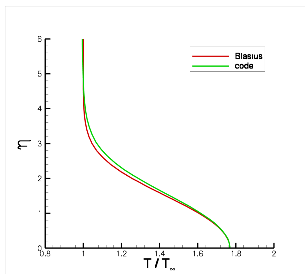

(a) $x/L = 0.4$

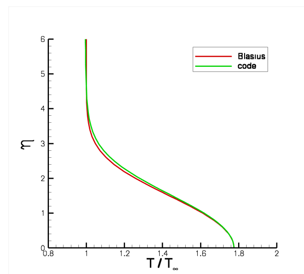

(b) $x/L = 0.6$

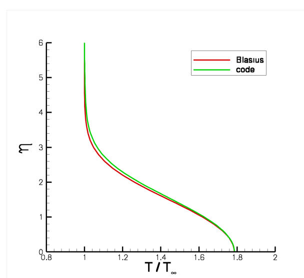

(c) $x/L = 0.8$

Figure 4.17: Temperature in Boundary Layer For Adiabatic Flat Plate Perpendicular to ζ Axis

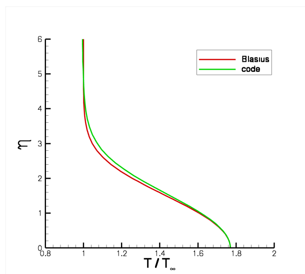

(a) $x/L = 0.4$

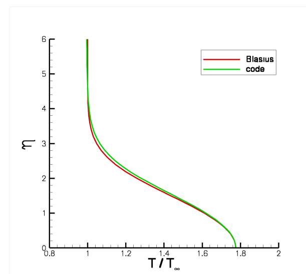

(b) $x/L = 0.6$

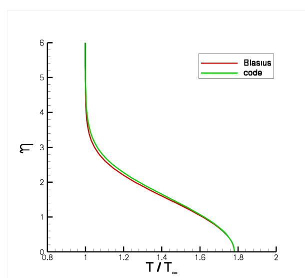

(c) $x/L = 0.8$

Figure 4.18: Temperature in Boundary Layer For Adiabatic Flat Plate Perpendicular to ξ Axis

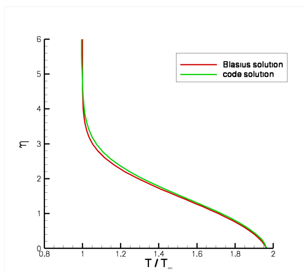

(a) $x/L = 0.4$

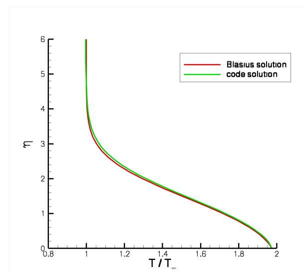

(b) $x/L = 0.6$

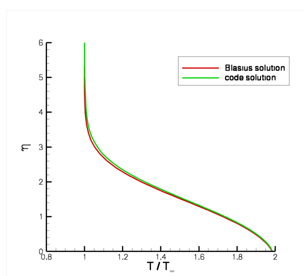

(c) $x/L = 0.8$

Figure 4.19: Temperature in Boundary Layer For Isothermal Flat Plate Perpendicular to η Axis

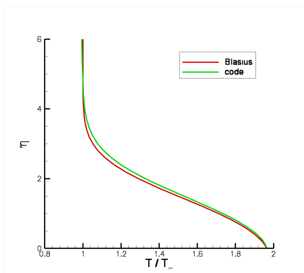

(a) $x/L = 0.4$

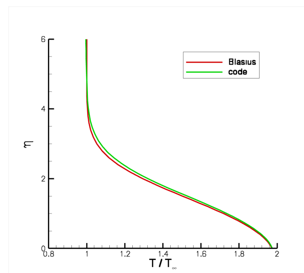

(b) $x/L = 0.6$

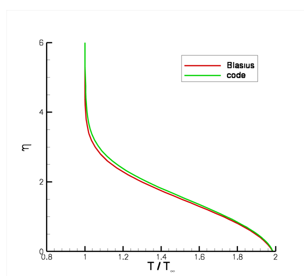

(c) $x/L = 0.8$

Figure 4.20: Temperature in Boundary Layer For Isothermal Flat Plate Perpendicular to ζ Axis

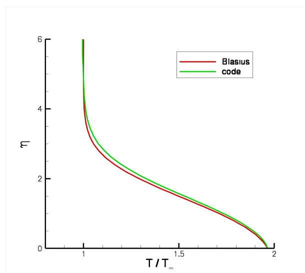

(a) $x/L = 0.4$

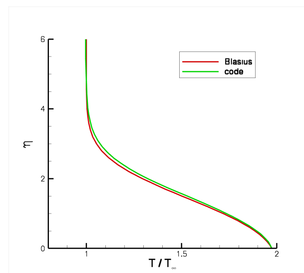

(b) $x/L = 0.6$

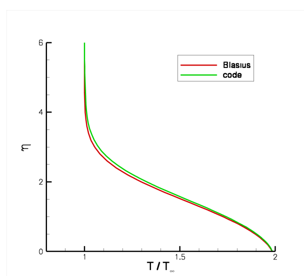

(c) $x/L = 0.8$

Figure 4.21: Temperature in Boundary Layer For Isothermal Flat Plate Perpendicular to ξ Axis

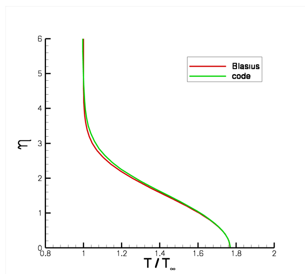

(a) $x/L = 0.4$

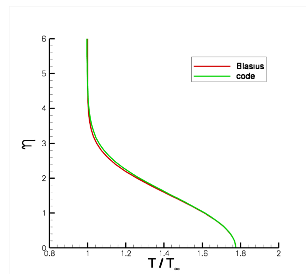

(b) $x/L = 0.6$

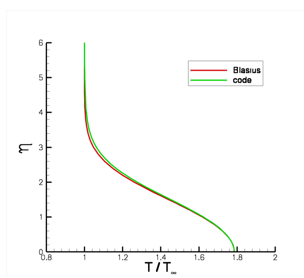

(c) $x/L = 0.8$

Figure 4.22: Temperature in Boundary Layer for Adiabatic Flat Plate At Ten Degree Incline from η Axis

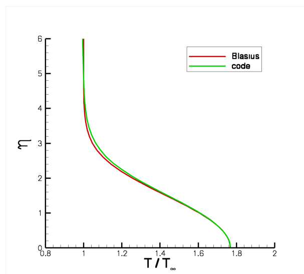

(a) $x/L = 0.4$

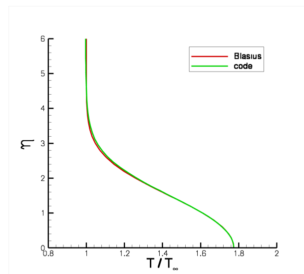

(b) $x/L = 0.6$

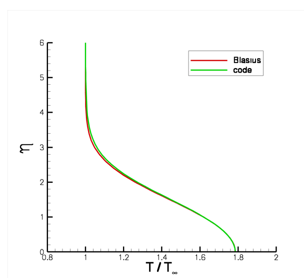

(c) $x/L = 0.8$

Figure 4.23: Temperature in Boundary Layer For Adiabatic Flat Plate At Ten Degree Incline from ζ Axis

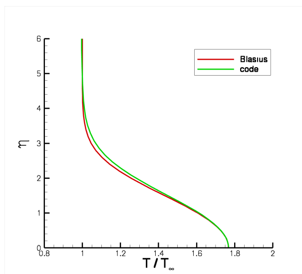

(a) $x/L = 0.4$

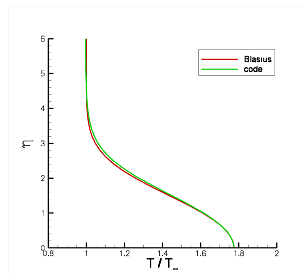

(b) $x/L = 0.6$

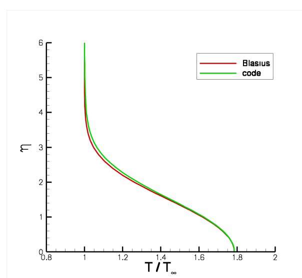

(c) $x/L = 0.8$

Figure 4.24: Temperature in Boundary Layer For Adiabatic Flat Plate At Ten Degree Incline from ξ Axis

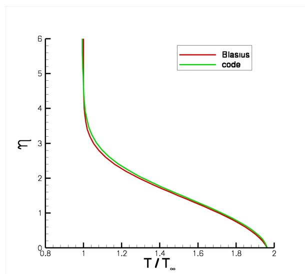

(a) $x/L = 0.4$

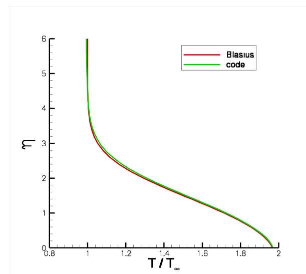

(b) $x/L = 0.6$

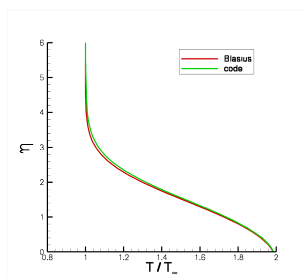

(c) $x/L = 0.8$

Figure 4.25: Temperature in Boundary Layer For Isothermal Flat Plate At Ten Degree Incline to η Axis

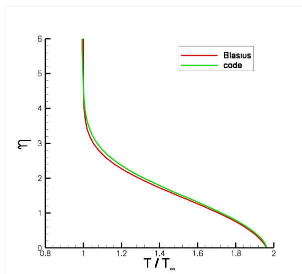

(a) $x/L = 0.4$

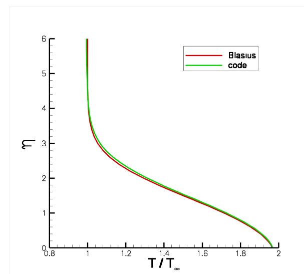

(b) $x/L = 0.6$

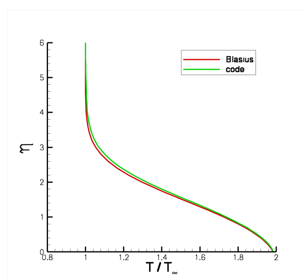

(c) $x/L = 0.8$

Figure 4.26: Temperature in Boundary Layer For Isothermal Flat Plate At Ten Degree Incline to ζ Axis

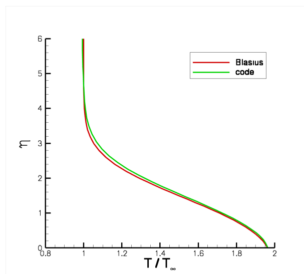

(a) $x/L = 0.4$

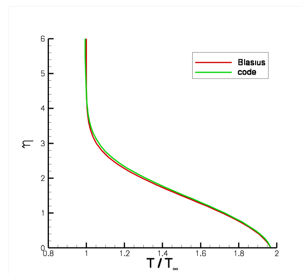

(b) $x/L = 0.6$

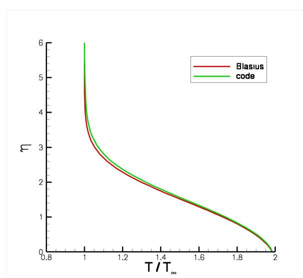

(c) $x/L = 0.8$

Figure 4.27: Temperature in Boundary Layer For Isothermal Flat Plate At Ten Degree Incline to ξ Axis

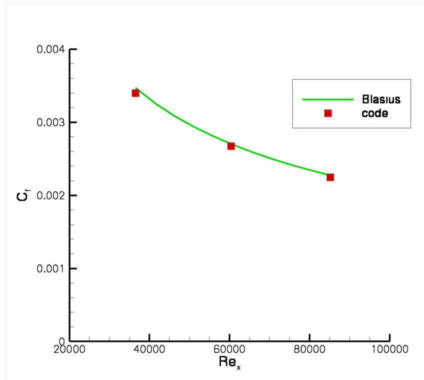

(a) Flat Plate Perpendicular to η Axis

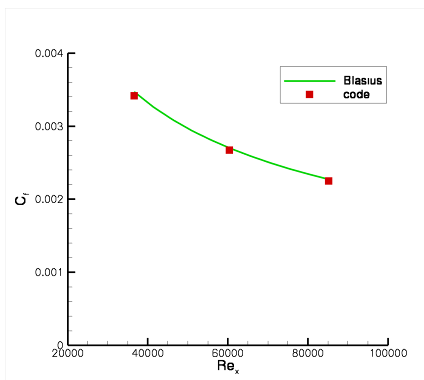

(b) Flat Plate Perpendicular to ζ Axis

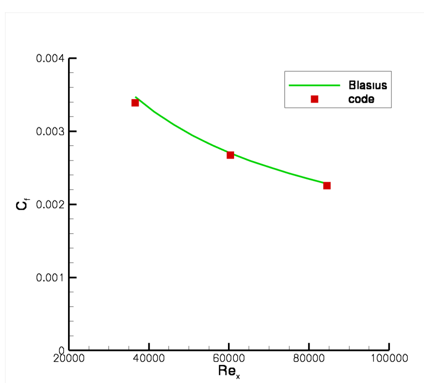

(c) Flat Plate Perpendicular to ξ Axis

Figure 4.28: Skin Friction Versus Re for Adiabatic Flat Plate Cases

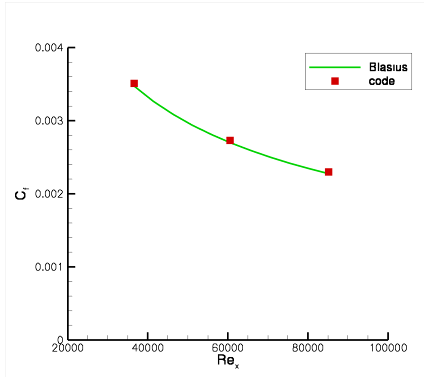

(a) Flat Plate Perpendicular to η Axis

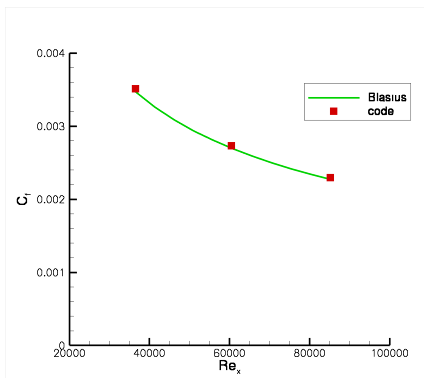

(b) Flat Plate Perpendicular to ζ Axis

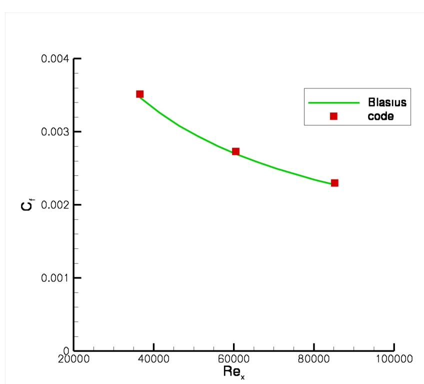

(c) Flat Plate Perpendicular to ξ Axis

Figure 4.29: Skin Friction Versus Re for Isothermal Flat Plate Cases

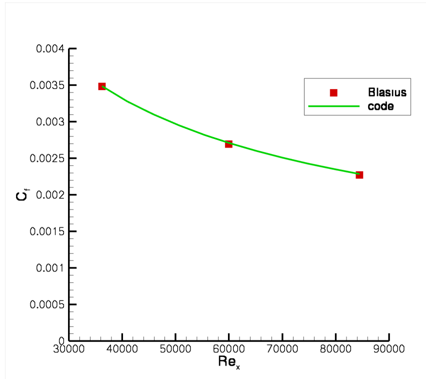

(a) Flat Plate 10 Degree Incline to ξ Axis

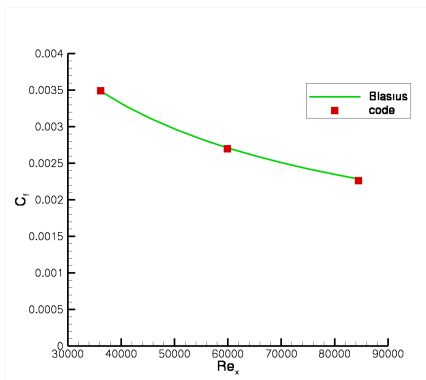

(b) Flat Plate 10 Degree Incline to η Axis

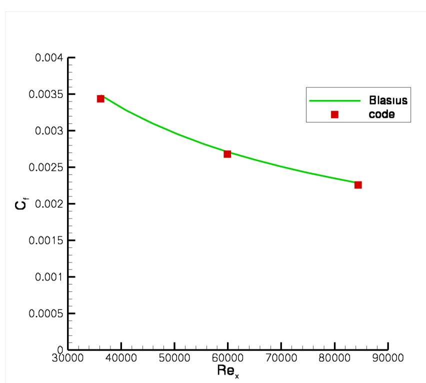

(c) Flat Plate 10 Degree Incline to ζ Axis

Figure 4.30: Cf Versus Re for Adiabatic Inclinded Flat Plate Cases

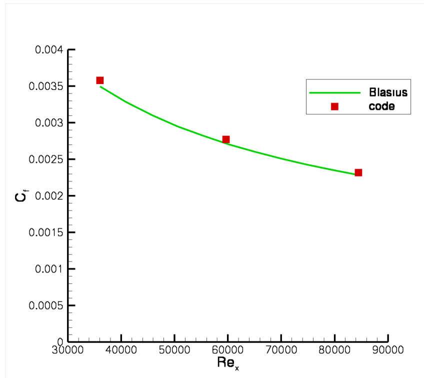

(a) Flat Plate 10 Degrees from ξ Axis

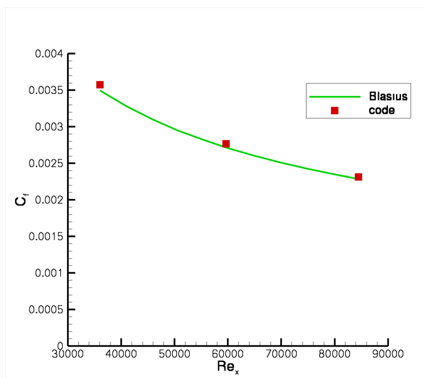

(b) Flat Plate 10 Degrees from η Axis

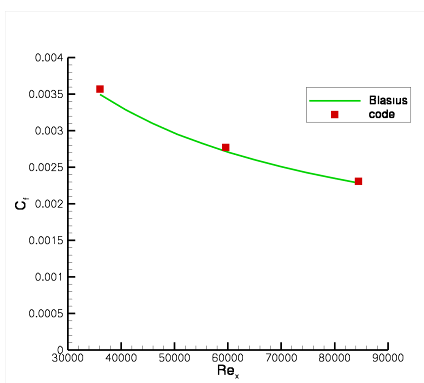

(c) Flat Plate 10 Degrees from ζ Axis

Figure 4.31: Skin Friction Versus Re for Inclined Isothermal Flat Plate Cases

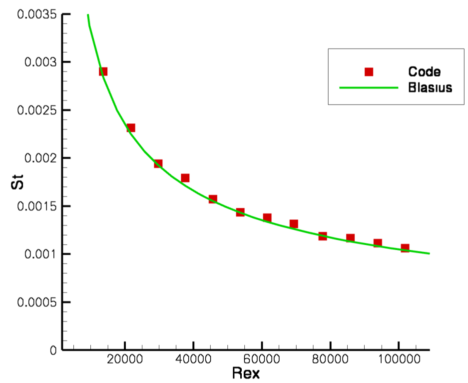

(a) Flat Plate Perpendicular to η Axis

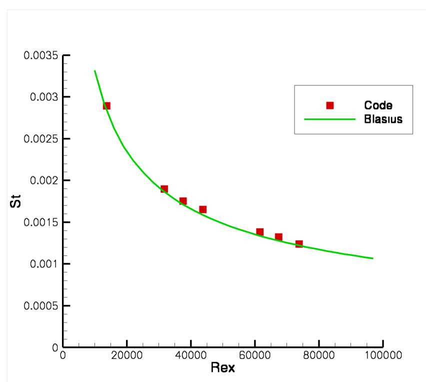

(b) Flat Plate Perpendicular to ζ Axis

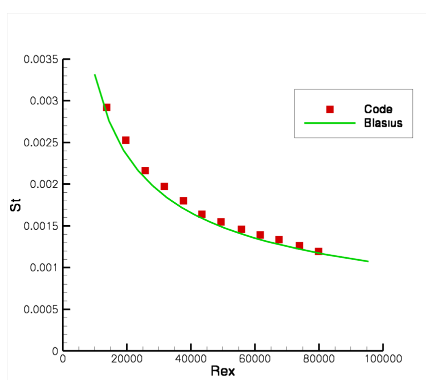

(c) Flat Plate Perpendicular to ξ Axis

Figure 4.32: Stanton Number Versus Re for Isothermal Flat Plate Cases

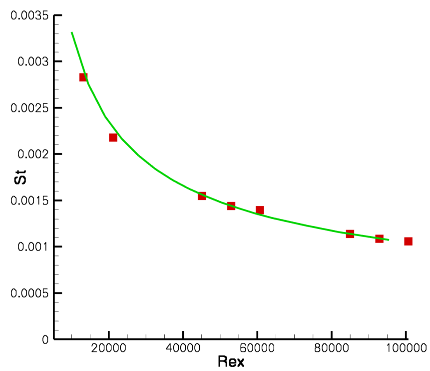

(a) Flat Plate 10 Degrees from ξ Axis

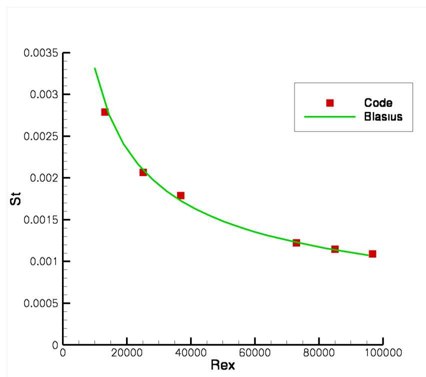

(b) Flat Plate 10 Degrees from η Axis

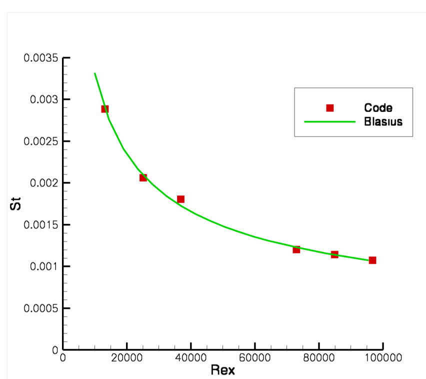

(c) Flat Plate 10 Degrees from ζ Axis

Figure 4.33: Stanton Number Versus Re for Isothermal Flat Plate Cases

4.2 Second Order Accuracy Check

The following method shows second order accuracy of the code independent of the exact solution. The following derivation follows the second order accuracy based on the skin friction; however, the same argument applies for the Stanton number.

For a second order scheme,

$$\mathrm{C}_f^h - \mathrm{C}_f^0 = a_1 (\Delta y)^2 + \text{h.o.t.} \tag{4.7}$$

$$\mathrm{C}_f^m - \mathrm{C}_f^0 = a_1 (\Delta y_m)^2 + \text{h.o.t.} \tag{4.8}$$

where the superscripts indicate the following

$$\begin{aligned} h &= \text{grid cell size} \\ 0 &= \text{exact solution} \\ m &= \text{minimum grid size} \end{aligned}$$

and h.o.t. indicates higher order terms.

Subtracting Equation (4.8) from (4.7),

$$\mathrm{C}_f - \mathrm{C}_f^m = a_1 \left[(\Delta y)^2 - (\Delta y_m)^2\right] + \text{h.o.t.} \tag{4.9}$$

$$= a_1 (\Delta y_m)^2 \left[\left(\frac{\Delta y}{\Delta y_m}\right)^2 - 1\right] + \text{h.o.t.} \tag{4.10}$$

Taking the logarithm of the absolute value of each side,

$$log_{10} \left|\mathrm{C}_f^h - \mathrm{C}_f^m\right| = log_{10} \left|a_1 (\Delta y_m)^2\right| + log_{10} \left|\left(\frac{\Delta y}{\Delta y_m}\right)^2 - 1\right| + \text{h.o.t.} \tag{4.11}$$

Defining

$$\Delta y = \Delta y_m (1 + \Lambda) \tag{4.12}$$

$$\left(\frac{\Delta y}{\Delta y_m}\right)^2 = 1 + 2\Lambda + \Lambda^2 \tag{4.13}$$

where $\Lambda \geq 0$. Thus,

$$log_{10} \left|\mathrm{C}_f^h - \mathrm{C}_f^m\right| = log_{10} \left|a_1 (\Delta y_m)^2\right| + log_{10} \left|2\Lambda + \Lambda^2\right| + \text{h.o.t.} \tag{4.14}$$

Evaluating (4.14) at $\Delta y = 1.25\,(\Delta y_m)$ and thus $\Lambda = 0.25$, also, replacing superscript m with $\Lambda = 0$,

$$log_{10}\left|C_f^{\Lambda=0.25} - C_f^{\Lambda=0}\right| = log_{10}\left|a_1\,(\Delta y)^2_{min}\right| + log_{10}\left|2\cdot 0.25 + 0.25^2\right| + \text{h.o.t.} \tag{4.15}$$

Subtracting (4.15) from (4.14),

$$log_{10}\left|\frac{C_f^h - C_f^{\Lambda=0}}{C_f^{\Lambda=0.25} - C_f^{\Lambda=0}}\right| = log_{10}\left|\frac{2\Lambda + \Lambda^2}{2\cdot 0.25 + 0.25^2}\right| \tag{4.16}$$

Thus, if the left hand side of equation (4.16), using values from the computation, and it matches the right hand side, the computation is second order accurate. For larger grid cell sizes, error in the higher order terms are significant. However, if the code converges to the second order values as the grid cell size is reduced, then the code achieves second order accuracy. Figures 4.34 and 4.35 show that second order accuracy is achieved. The code calculated values converge to the second order accurate expected solution for small enough values of Λ.

The approximate number of cells in the boundary layer is calculated by the following method. The boundary layer height is approximated by the analytical solution using the Dorodnitsyn-Howarth Transformation, using the freestream parameters instead of the edge of the boundary layer parameters.

For the adiabatic case :

$$\frac{\delta(x)}{L} = \frac{1}{Re_x}\left[5 + 1.19(\gamma - 1)M_\infty^2\right] \tag{4.17}$$

For the isothermal case :

$$\frac{\delta(x)}{L} = \frac{1}{Re_x}\left[5 + 1.19(\gamma - 1)M_\infty^2\right] + \frac{1.717\Delta T_{wall}}{\sqrt{Re_x}T_\infty} \tag{4.18}$$

The number of cells in the largest grid case, n, is found for the stretched grid with the following equation. The smaller grids divide the cells of the largest grid equally. The stretch factor, s, of the largest grid case is 1.01.

$$n = log_{sf}\left[1 + (s-1)\left(\frac{\delta}{\Delta y_0}\right)\right] \tag{4.19}$$

Δy	Λ	Cells in Boundary Layer
0.001	4.0	20
0.0005	1.5	40
0.000333	0.6650	60
0.00025	0.25	80
0.0002	0	100

Table 4.2. Calculation Details of C_f 2nd Order Study.

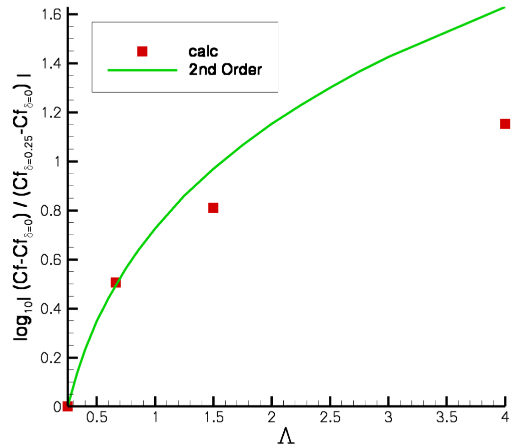

Figure 4.34: 2nd Order Study of C_f, Adiabatic Wall

Δy	Λ	Cells in Boundary Layer
0.001	4	21
0.0005	1.5	42
0.000333	0.67	63
0.00025	0.25	84
0.0002	0	105

Table 4.3. Calculation Details of St 2nd Order Study.

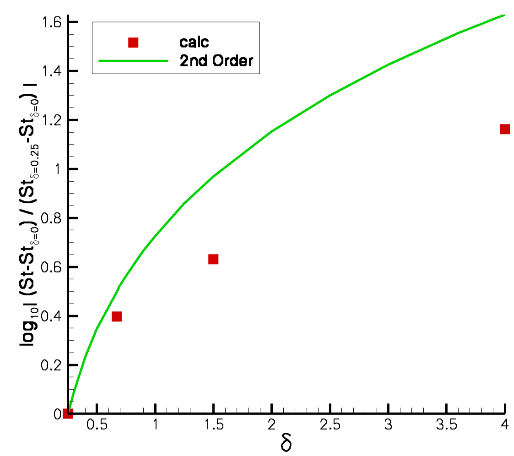

Figure 4.35: 2nd Order Study of St, Isothermal Wall

4.3 Performance

The code's performance is evaluated by the fixed grid speedup and the scaled grid efficiency. The fixed grid speedup is a measure of the speedup of the code attained by using more processors for a fixed grid size.

$$Speedup_{fixedgrid} = \frac{wallclocktime_{1processor}}{wallclocktime_{nprocessors}} \tag{4.20}$$

The scaled grid efficiency, η, is a measure of the efficiency of increasing the code using n processors, for the same number of grid cells for each processor.

$$\eta_{scaledgrid} = \frac{1}{n}\frac{wallclocktime_{1processor}}{wallclocktime_{nprocessors}} \cdot 100 \tag{4.21}$$

The results of this study are shown in Figures 4.36(a) and 4.36(b) for speedup and efficiency respectively. The fixed grid speedup, Figure 4.36(a), shows a 20% loss of speedup at 16 processors. The inability to speed up the calculation linearly with increased number of processors is due to communication time between the processors. The greater the number of processors, the cells involved in data transfer to cells involved in calculation time increases. This limits the speedup from added processors. The scaled grid efficiency shows a 25% drop in efficiency at 16 processors. This is also due to the increases data transfer to calculation ratio.

4.4 Residual

The residual is defined by the difference between a quantity the prediction of that quantity. This accomplished, in this code by the difference of the predictor and corrector step in the Runga Kutta scheme. This difference represents the

$$\begin{aligned}
\rho^{corrector} - \rho^{predictor} &= residual[0] \\
\rho u^{corrector} - \rho u^{predictor} &= residual[1] \\
\rho v^{corrector} - \rho v^{predictor} &= residual[2] \\
\rho w^{corrector} - \rho w^{predictor} &= residual[3]
\end{aligned}$$

$$\rho e^{corrector} - \rho e^{predictor} \quad = \quad = residual[4] \tag{4.22}$$

where nondimensional values are used. To ensure the residual represents a gauge of the all variables in all cells, the residual at timestep, n, is calculated by a sum over all dependant variables in all cells,

$$residual^n = \sum_{cell} \sum_{k=0}^{4} (residual_k^i)^2 \tag{4.23}$$

The total residual is normalized by the residual at the first timestep,

$$residual = \frac{residual^n}{residual^0} \tag{4.24}$$

Figure 4.37 shows the residual for the adiabatic flat plate perpendicular to the η axis. The residual drops to 10^{-6}. The smallest dimensionless parameter evaluated in the Blasius cases is the perpendicular velocity, which is of order 10^{-3}, thus the error in the code has converged sufficiently to resolve the flow variables.

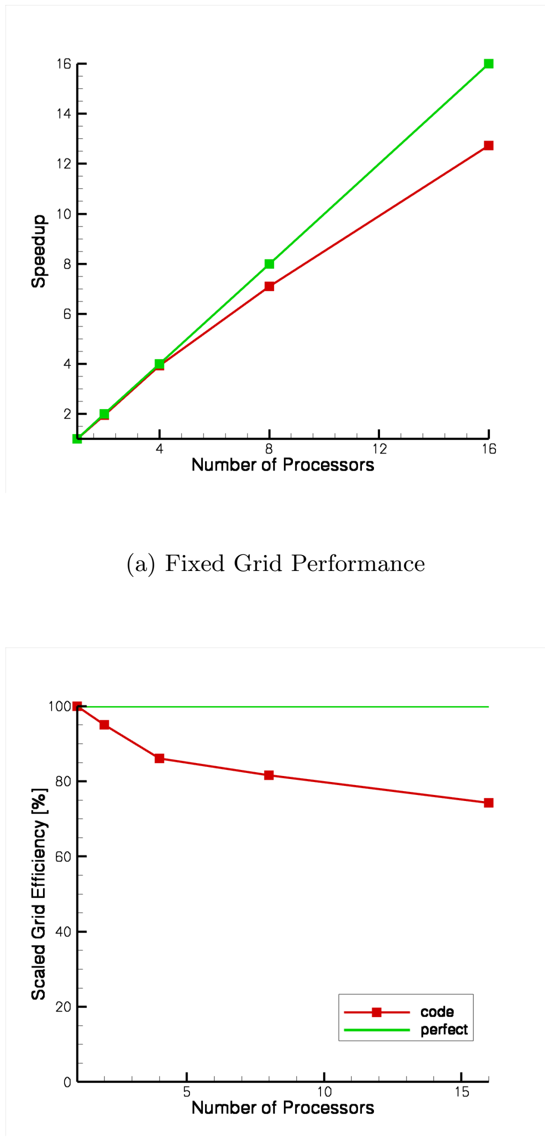

(a) Fixed Grid Performance

(b) Scaled Grid Efficiency

Figure 4.36: Scaled Grid Efficiency Versus Number of Processors

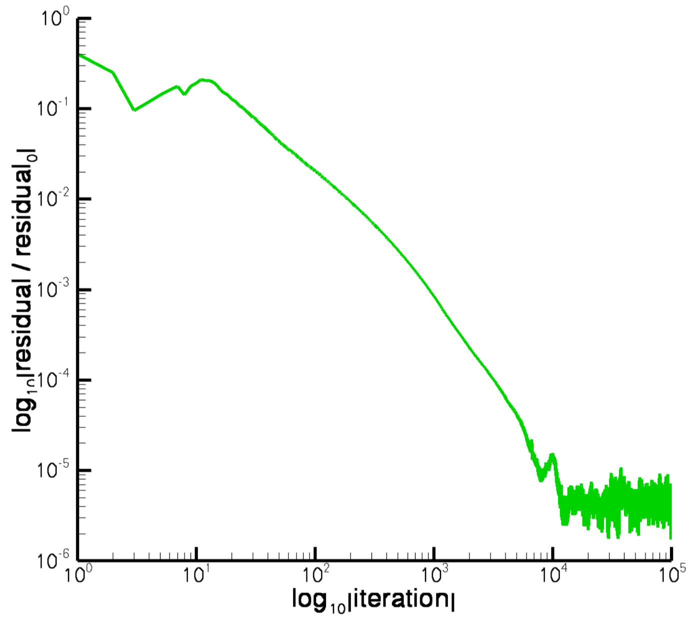

Figure 4.37: Residual for Adiabatic Flat Plate Perpendicular to Zeta Axis.

Chapter 5

Results

5.1 Inviscid Simulations

5.1.1 Steady State

The steady state contours are shown in Figure 5.1. The cylinder body is shown in dark blue. The the distance between the cylinder face and the blunt body shock, or standoff distance, is within 5% of the experimental results [32]. The stagnation pressure on the centerline at the front of the body is compared to the theoretical results obtained from the Rankine-Hugoniot conditions. A comparison between the calculated conditions and the aforementioned predictions is shown in Table 5.1. The axial cell size $\Delta x/D = 0.02$ and thus the standoff distance is one cell off from the experimentally obtained standoff distance. The nondimensional stagnation pressure is within one percent of the theoretical result.

Table 5.1: Steady State Values Compared to Known Results

	Standoff Distance / D	Stagnation Pressure / $\rho_\infty U_\infty^2$
Computation	0.42	1.01
Predicted	0.40	1.02

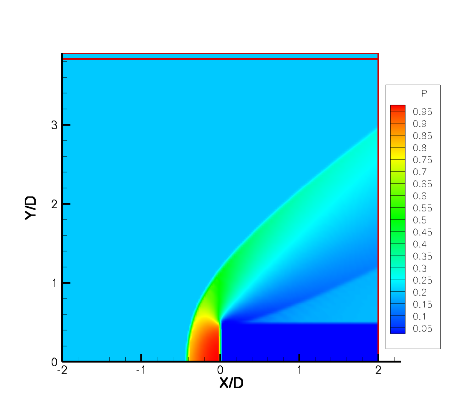

(a) Pressure Contours

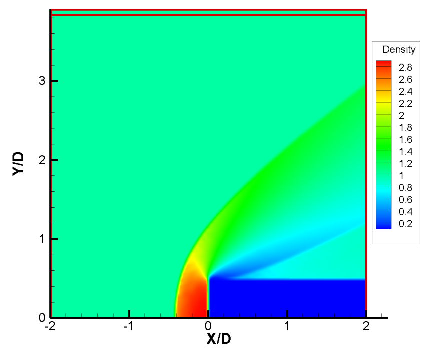

(b) Density Contours

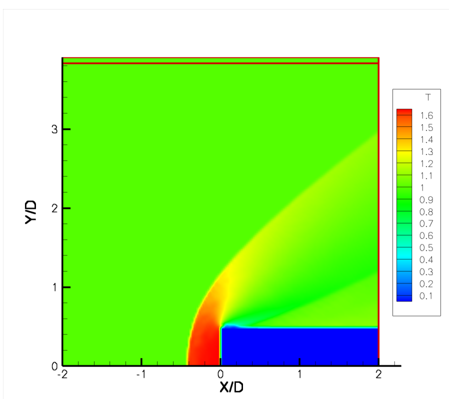

(c) Temperature

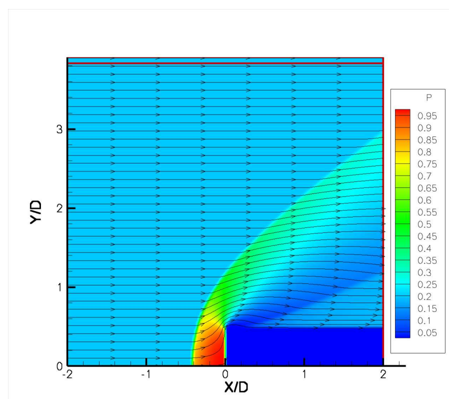

(d) Pressure Contours with Streamlines

Figure 5.1: Steady State Contours

5.1.2 Energy Deposition Results

The problem of an infinitely long filament with varying filament diameters is considered. The filament parameters are shown in Table 5.2. The flow contours are shown in Figures 5.2, 5.3 and 5.4 for d/D=0.25, 0.5, and 1.0, respectively. The distances are nondimensionalized by the cylinder diameter, D. The pressure, density and temperature are shown in terms of their dimensionless parameters, $p/\rho_\infty U_\infty^2$, ρ/ρ_∞ and T/T_∞, respectively. The nondimensional freestream pressure is $1/\gamma M_\infty^2$, and the nondimensional freestream density and temperature are equal to one. The case of nondimensional filament diameter of 0.25 shows a sustained eddy behind the shock. The other two cases do not demonstrate this behavior. The larger diameter filament cases create a large enough density variation that the flow just before the body encounters a uniform density and temperature region. The smaller diameter filament cases create a large density gradient which generates instability in the flow in front of the body. The result is an eddy that remains in front of the body.

Table 5.2: Dimensionless Flow Parameters for Filament Diameter Study

Type	Description	Definition	Value
Flow	Mach	M_∞	1.89
	Specific heat ratio	γ	1.4
Filament	Density ratio	α	0.5
	Diameter	$\frac{d}{D}$	0.25, 0.5, 1.0
	Length (Duration)	$\frac{l}{D}$	infinitely long

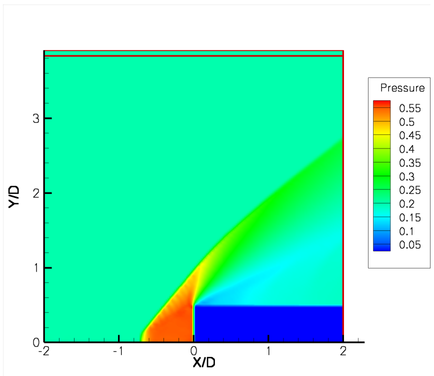

(a) Pressure Contours

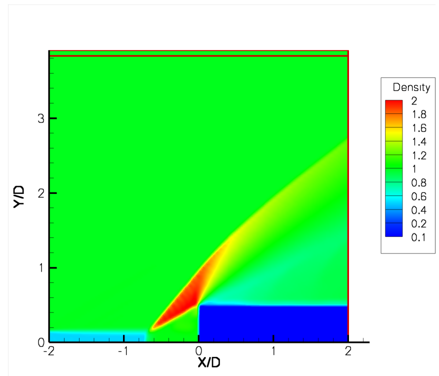

(b) Density Contours

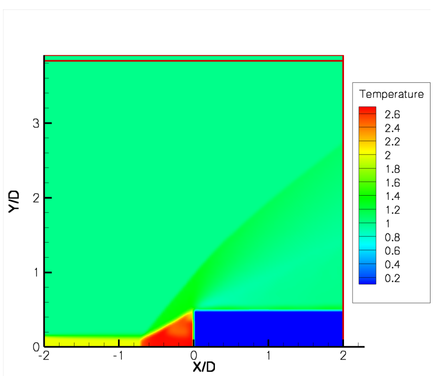

(c) Temperature

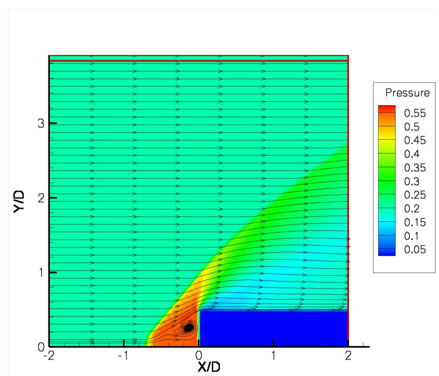

(d) Pressure Contours with Streamlines

Figure 5.2: $d/D = 0.25$ Contours After 45 Nondimensional Time Units

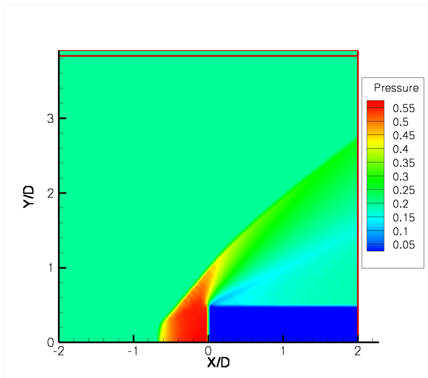

(a) Pressure Contours

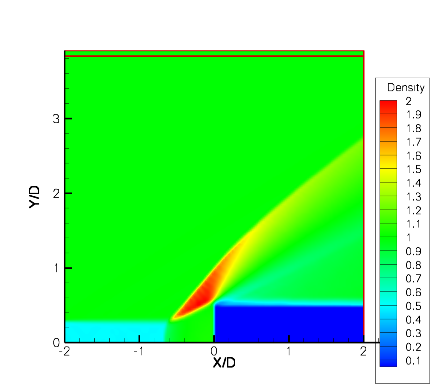

(b) Density Contours

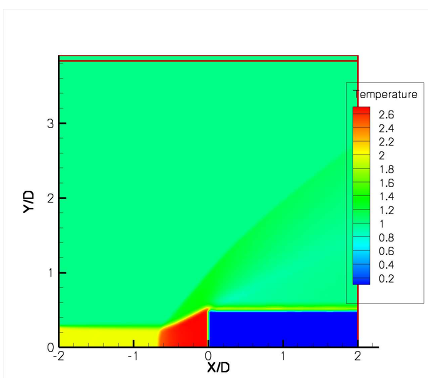

(c) Temperature

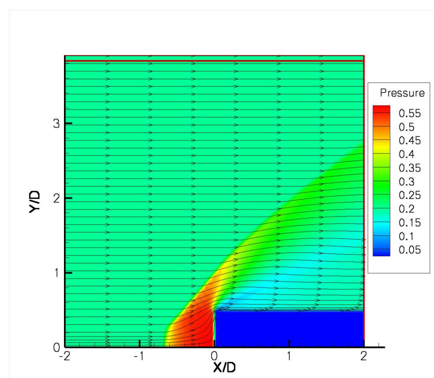

(d) Pressure Contours with Streamlines

Figure 5.3: $d/D = 0.50$ Contours After 34 Nondimensional Time Units

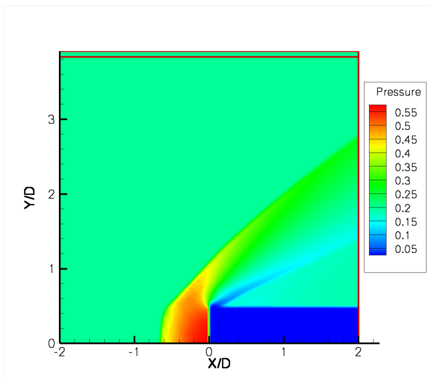

(a) Pressure Contours

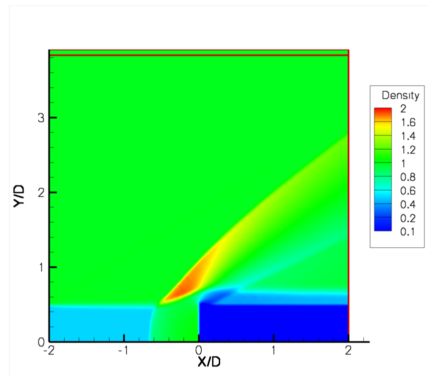

(b) Density Contours

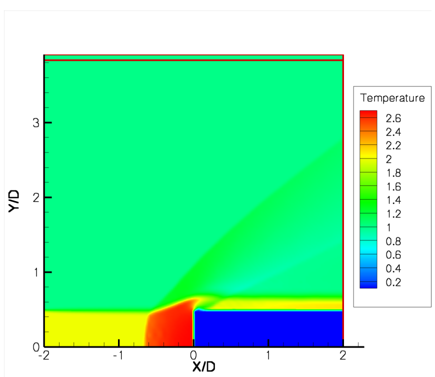

(c) Temperature

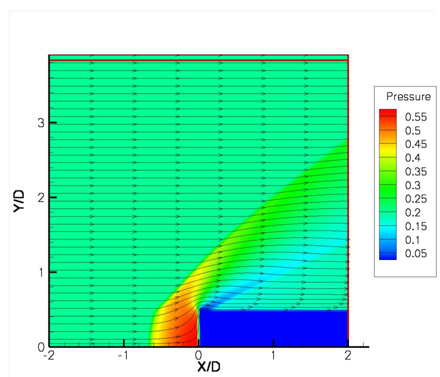

(d) Pressure Contours with Streamlines

Figure 5.4: $d/D = 1.0$ Contours After 48 Nondimensional Time Units

The pressure at the center of the cylinder face of the three cases, nondimensionalized by $\rho_\infty U_\infty^2$, is graphed in Figure 5.5. The d/D=0.25 case is periodic in time. The interaction of the low density filament and the bow shock generates a vortex. The vortex convects toward the corner. This vortex generation and convection was also observed by Farzan *et al* [8] for the $d/D = 0.25$ case. The vortex creation and convection is periodic in time. This periodicity can be seen in the graphs of pressure at the centerline in Figure 5.5. The nondimensional pressure variation due to this eddy is on the order of 0.01. The d/D=0.5 and 1.0 cases show oscillatory behavior that is much smaller in magnitude, with a much higher frequency, as can be seen in Figure 5.5. The vortex creation and convection phenomenon does not occur for these cases.

Numerical Schlieren images are presented in Figures 5.6, 5.7 and 5.8. The filament, bow shock, reattachment shock, cylinder body and lensing area of the shock are labeled on the graphs. The numerical Schlieren is computed by the density magnitude gradient plotted on a gray scale.

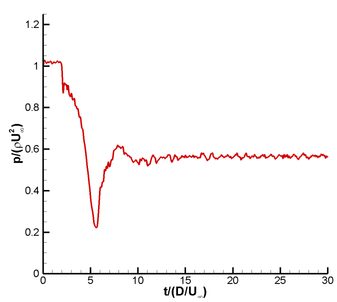

(a) d/D=0.25

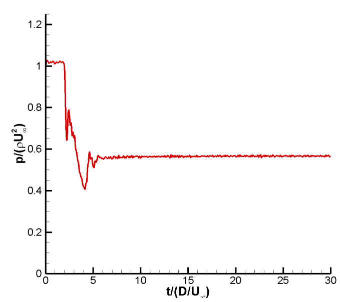

(b) d/D=0.50

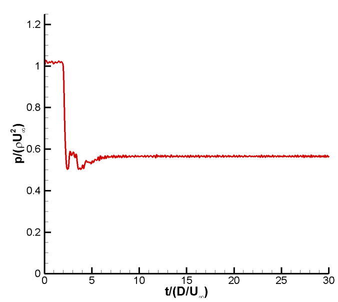

(c) d/D=1.0

Figure 5.5: Pressure at Centerline

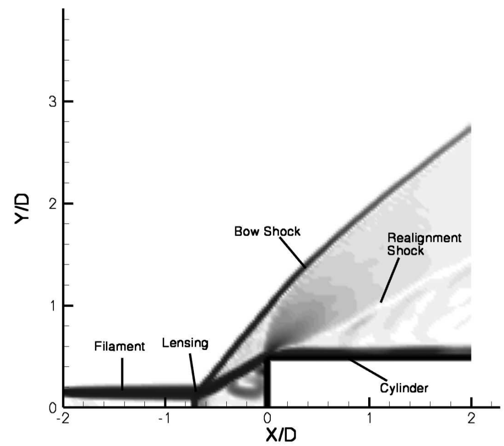

Figure 5.6: Schlieren Images of $d/D = 0.25$ at 34 Nondimensional Time Units

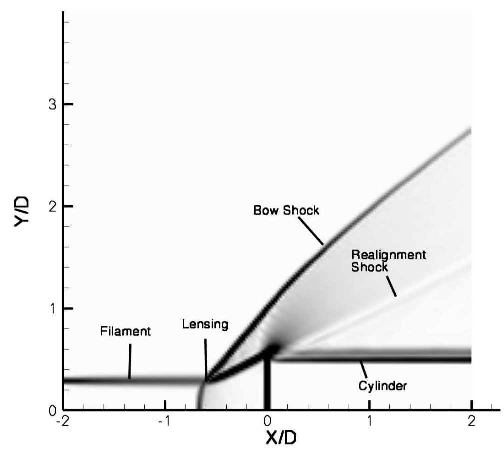

Figure 5.7: Schlieren Images of $d/D = 0.5$ at 34 Nondimensional Time Units

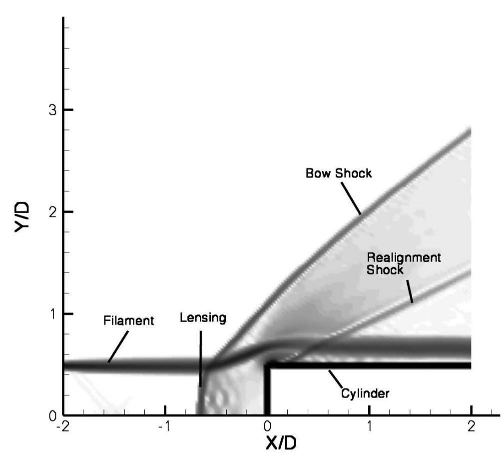

Figure 5.8: Schlieren Images of $d/D = 1.0$ at 47 Nondimensional Time Units

5.1.3 Mean Pressure

The mean pressure on the cylinder face is found with

$$p_{mean} = \frac{\int_0^{\tau} p_{centerline}(t)dt}{\tau} \tag{5.1}$$

where the pressure is non-dimensionalized by $\rho_\infty U_\infty^2$, and τ is the period of integration.

The mean pressures at the centerline are computed for each case and shown in Figure 5.9. It is shown that the mean pressure reaches a steady value after typically 25 nondimensional time units, where time is nondimensionalized by D/U_∞. The mean pressure in cases d/D=0.5 and d/D=1.0 smoothly asymptote to a steady value. The mean pressure in the d/D=0.25 case, however, oscillates at 5 nondimensional time units. This corresponds to the time when the shock lenses upstream due to the interaction with the microwave filament. The d/D=0.25 case has a large eddy that forms behind the shock at this time. The eddy sweeps air into the region in front of the body that is the stagnation region in the steady state case, lowering the pressure at the front of the body.

The mean pressure versus filament diameter is graphed in Figure 5.10. The mean pressure at the front of the cylinder face is uniform for these filament diameters. Because the pressure at the front of the face is not sensitive to a changing filament diameter above $d/D = 0.25$, the drag reduction is not sensitive to filament diameter above $d/D = 0.25$.

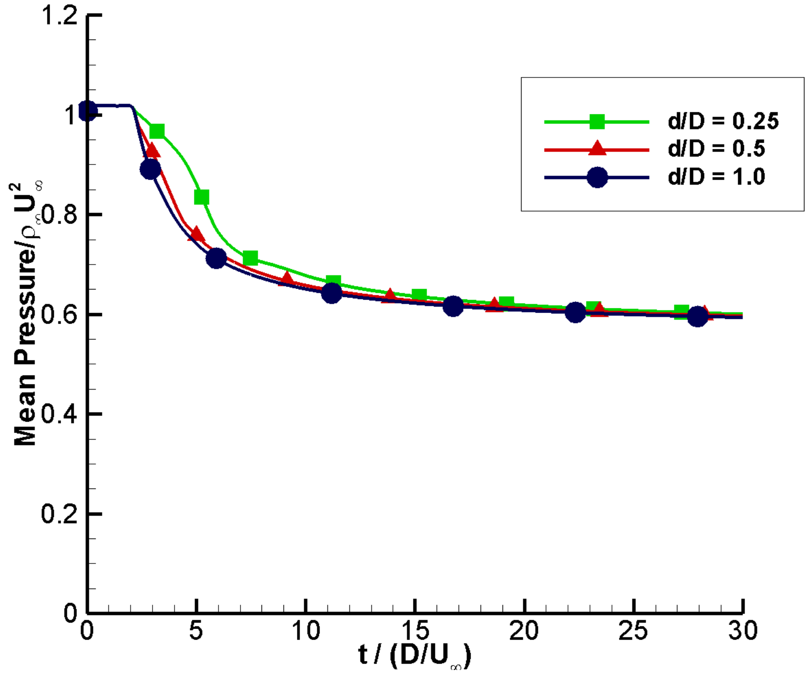

Figure 5.9: Mean Pressure at Centerline Versus Nondimensional Time Units

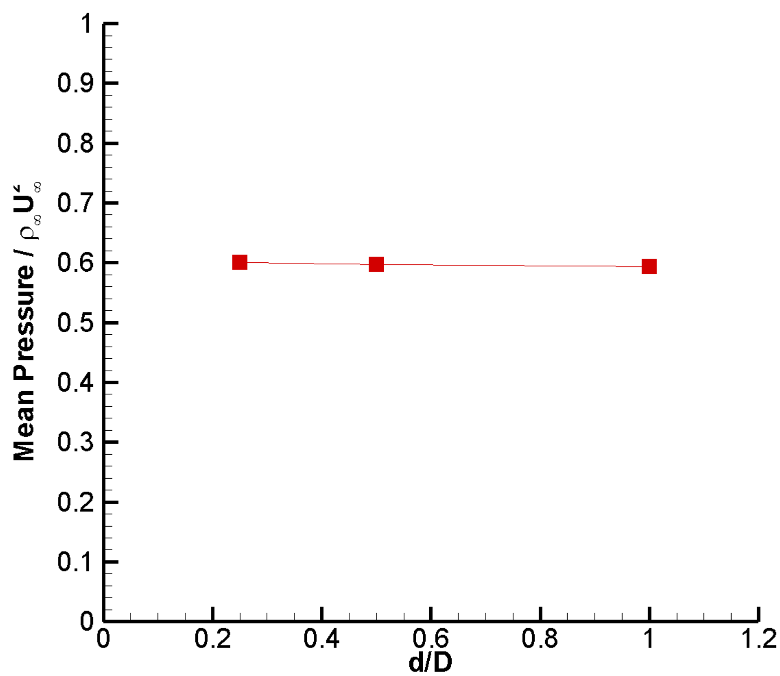

Figure 5.10: Mean Pressure at Centerline Versus d/D

5.1.4 Drag Reduction Efficiency and Effectiveness

The efficiency is the ratio of the power saved due to drag reduction by introduction of the microwave filament to the power necessary to create the microwave filament. Following Farzan *et al* [8] for an infinitely long filament, the efficiency is obtained by dividing the average thrust power saved due to the filament divided by the power used to create the filament. The average power saved due to the presence of the filament is the reduction in work to overcome drag due to the filament over a time period, $\tau *$:

$$\text{dimensional work due to drag} = l^* \cdot \int_{A^*} p^* dA^*$$

$$\text{dimensional thrust power to overcome drag} = \frac{l^*}{\tau^*} \cdot \int_{A^*} p^* dA^*$$

where l^* is the distance that the cylinder moves in time τ^*. The body is moving at the freestream velocity, in the frame of the freestream velocity, and thus $l^*/\tau^* = U_\infty$.

$$\text{dimensional thrust power to overcome drag} = U_\infty \int_{A^*} p^* dA^*$$

The thrust power saved in the presence of the filament is then

$$\begin{aligned} \text{dimensional thrust power saved due to filament} &= U_\infty \int_{A^*} (p^* - p_o^*) dA^* \\ &= U_\infty \int_0^{2\pi} \int_0^{D/2} (p^* - p_o^*) r^* dr^* d\theta^* \end{aligned}$$

The average power saved over time is the power integrated in time, divided by the time period :

$$\text{dimensional average thrust power saved due to filament} = \frac{1}{\tau^*} U_\infty \int_0^{\tau^*} \int_0^{2\pi} \int_0^{D/2} (p^* - p_o^*) r^* dr^* d\theta^* dt^*$$

As the problem is axisymmetric, the azimuthal integration is simplified,

$$\text{dimensional average thrust power saved due to filament} = \frac{1}{\tau^*} U_\infty \int_0^{\tau^*} 2\pi \int_0^{D/2} (p^* - p_o^*) r^* dr^* dt^*$$

Power is nondimensionalized by $\rho_\infty U_\infty^3 D^2$, the nondimensional pressure becomes :

$$\begin{aligned} \text{average thrust power saved due to filament} &= \frac{1}{\rho_\infty U_\infty^3 D^2} \frac{1}{\tau^*} U_\infty \int_0^{\tau^*} 2\pi \int_0^{D/2} (p^* - p_o^*) r^* dr^* dt^* \\ &= \frac{1}{U_\infty} \frac{1}{\tau^*} U_\infty \int_0^{\tau^*} 2\pi \int_0^{1/2} \left(\frac{p^*}{\rho_\infty U_\infty^2} - \frac{p_o^*}{\rho_\infty U_\infty^2} \right) \frac{r^*}{D} d\frac{r^*}{D} dt^* \end{aligned}$$

$$P_s = \frac{2\pi}{\tau} \int_0^{\tau} \int_0^{1/2} (p - p_o) r \, dr \, dt \tag{5.2}$$

The power required to create the filament is determined by the following :

$$P_c = \text{power to create filament}$$

$$\begin{aligned} P_c^* &= \frac{\Delta E}{\tau^*} \\ &= \frac{m^* c_p \Delta T^*}{\tau^*} \\ &= \rho_\infty^* l^* \frac{\pi d^2}{4} \frac{1}{\tau^*} c_p \left(T_f^* - T_\infty^* \right) \end{aligned}$$

To obtain the dimensionless power, the power is divided by $\rho_\infty U_\infty^3 D^2$,

$$\begin{aligned} P_c &= \frac{P^*}{\rho_\infty U_\infty^3 D^2} = \frac{\rho_\infty}{\rho_\infty} \frac{l^*}{D} \frac{\pi}{4} \left(\frac{d}{D} \right)^2 D \frac{1}{\tau^*} \frac{c_p \left(T_f^* - T_\infty^* \right)}{U_\infty^3} \\ &= \frac{l}{D} \left(\frac{d}{D} \right)^2 \frac{\pi}{4} \frac{D}{\tau^*} c_p \left(\alpha - 1 \right) \frac{T_\infty^*}{U_\infty^3} \end{aligned}$$

The Mach number can be written as

$$M_\infty^2 = \frac{U_\infty^2}{\gamma R T_\infty}$$

rearranging,

$$\frac{T_\infty}{U_\infty^2} = \frac{1}{\gamma R M_\infty^2}$$

substituting into the power equation,

$$\begin{aligned} P_c &= \frac{l}{D} \left(\frac{d}{D} \right)^2 \frac{\pi}{4} \frac{D}{\tau^*} c_p (\alpha - 1) \frac{1}{\gamma R M_\infty^2} \frac{1}{U_\infty} \\ &= \left(\frac{d}{D} \right)^2 \frac{\pi}{4} \frac{l}{\tau^*} \frac{c_p}{\gamma R} (\alpha - 1) \frac{1}{M_\infty^2} \frac{1}{U_\infty} \\ &= \left(\frac{d}{D} \right)^2 \frac{\pi}{4} \frac{l}{\tau^*} \frac{1}{\gamma - 1} (\alpha - 1) \frac{1}{M_\infty^2} \frac{1}{U_\infty} \end{aligned}$$

where the τ^* is the time for one period $\tau^* = L/U_\infty$, pluggin in,

$$\begin{aligned} P_c &= \left(\frac{d}{D} \right)^2 \frac{\pi}{4} \frac{l}{L} U_\infty \frac{1}{\gamma - 1} (\alpha - 1) \frac{1}{M_\infty^2} \frac{1}{U_\infty} \\ &= \left(\frac{d}{D} \right)^2 \frac{\pi}{4} \frac{l}{L} \frac{1}{\gamma - 1} (\alpha - 1) \frac{1}{M_\infty^2} \end{aligned}$$

for an infinitely long filament, the length of the filament is equal to the distance between filaments $l = L$,

$$P_c \quad = \quad \left(\frac{d}{D}\right)^2 \frac{\pi}{4} \frac{1}{\gamma - 1} (\alpha - 1) \frac{1}{M_\infty^2}$$

Finally, the efficiency is the ratio of the time averaged power saved due to presence of the filament to the power required to create the filament,

$$\eta = \frac{P_s}{P_c} = \frac{2\pi}{\tau} \int_0^\tau \int_0^{1/2} (p - p_o) r dr dt \left(\frac{D}{d}\right)^2 \frac{4}{\pi} \frac{\gamma - 1}{\alpha - 1} M_\infty^2$$

Switching signs of the pressure term and the density ratio term, the efficiency of drag reduction in terms of dimensionless variables is achieved,

$$\eta = \frac{8(\gamma - 1) M_\infty^2}{1 - \alpha} \left(\frac{D}{d}\right)^2 \frac{1}{\tau_\infty} \int_0^{\tau_\infty} \int_0^{1/2} (p_o - p) r dr dt \tag{5.3}$$

where the pressure is nondimensionalized by ρU_∞^2 and the subscript o indicates the absence of the filament.

The effectiveness is the ratio of the average frontal drag reduction due to the presence of the filament to the frontal drag in the absence of the filament. The dimensional frontal drag reduction is given by

$$\text{dimensional frontal drag reduction} = \int_0^{2\pi} \int_0^{D/2} (p^* - p_o^*) r^* dr^* d\theta^*$$

The time averaged dimensional frontal drag reduction is obtained by integrating over time period, τ^* and dividing by τ^*,

$$\begin{array}{c}\text{time averaged dimensional} \\ \text{frontal drag reduction}\end{array} = \frac{1}{\tau^*} \int_0^{\tau^*} \int_0^{2\pi} \int_0^{D/2} (p^* - p_o^*) r^* dr^* d\theta^* dt^*$$

The dimensionless quantity is obtained by dividing by $\rho_\infty U_\infty^2 D^2$

$$\begin{array}{c}\text{time averaged dimensionless} \\ \text{frontal drag reduction}\end{array} = \frac{1}{\rho_\infty U_\infty^2 D^2} \frac{1}{\tau^*} \int_0^{\tau^*} \int_0^{2\pi} \int_0^{D/2} (p^* - p_o^*) r^* dr^* d\theta^* dt^*$$

$$= \frac{1}{\tau^*} \int_0^{\tau^*} \int_0^{2\pi} \int_0^{D/2} \left(\frac{p^*}{\rho_\infty U_\infty^2} - \frac{p_o^*}{\rho_\infty U_\infty^2}\right) \frac{r^*}{D} d\frac{r^*}{D} d\theta^* dt^*$$

Due to symmetry about its axis, the azimuthal integration is constant

$$= \frac{1}{\tau^*} \int_0^{\tau^*} 2\pi \int_0^{1/2} \left(\frac{p^*}{\rho_\infty U_\infty^2} - \frac{p_o^*}{\rho_\infty U_\infty^2}\right) \frac{r^*}{D} d\frac{r^*}{D} dt^*$$

Simplifying,

$$\begin{array}{c}\text{time averaged dimensionless}\\ \text{frontal drag reduction}\end{array} = \frac{2\pi}{\tau}\int_0^{\tau}\int_0^{1/2}(p - p_o)rdrdt$$

The denominator of the effectiveness is the dimensionless drag in the absense of the filament, which is given by

Simplifying,

$$\begin{array}{c}\text{dimensionless drag in}\\ \text{absense of filament}\end{array} = \frac{2\pi}{\tau}\int_0^{\tau}\int_0^{1/2}p_o rdrdt$$

The effectiveness is

$$\zeta = \frac{\int_0^{\tau_\infty}\int_0^{1/2}(p_o - p)rdrdt}{\tau_\infty\int_0^{1/2}p_o rdr} \tag{5.4}$$

The drag efficiency and effectiveness are computed for the three cases. The effectiveness is shown in Figure 5.11(a). The effectiveness slightly increases with filament diameter. The efficiency is displayed in Figure 5.11(b). It is evident that the efficiency decreases rapidly with increasing filament diameter.

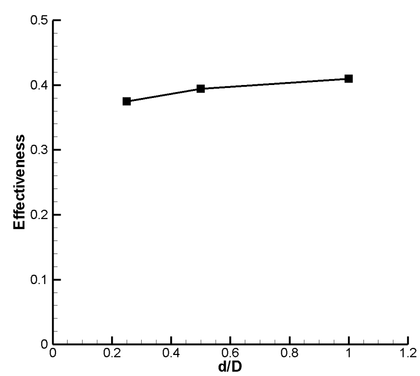

(a) Effectiveness of Drag Reduction

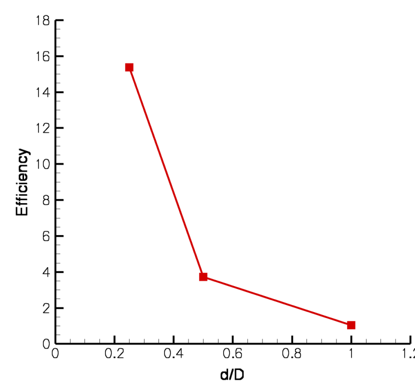

(b) Efficiency of Drag Reduction

Figure 5.11: Effectiveness and Efficiency of Drag Reduction

5.2 Viscous Simulations, Heat Transfer Effects of Pulsed Energy Deposition

The problem of a blunt cylinder in supersonic flow with periodic energy deposition with viscous effects is solved in this section. The flow and energy deposition filament parameters are defined in Table 5.3. The problem dimensions are depicted in Figure 2.1. The pulse period, L/D is varied from 4/3 to infinitely long, as was done in Farzan *et al* [8]. As the pulse period is increased, the length of the pulse remains the same, so the distance between pulses is greater. Thus, the pulsed case with a period of $L/D = 4$ has the largest distance between pulses, and the infinitely long case (which corresponds to a case with $L/D = 1$) has no distance between pulses. The heat transfer to the face of the cylinder is evaluated in the presense of the filament for varying pulse periods.

Table 5.3: Dimensionless Flow Parameters for Heat Transfer Study

Type	Description	Definition	Value
Flow	Mach	M_∞	1.89
	Specific heat ratio	γ	1.4
	Reynolds number	Re	$7.0 \cdot 10^4$
Filament	Density ratio	α	0.5 all cases
	Diameter	$\frac{d}{D}$	0.1 all cases
	Length	$\frac{l}{D}$	1.0, 1.0, 1.0, ∞
	Pulse (Period)	$\frac{L}{D}$	$\frac{4}{3}$, 2.0, 4.0, n/a
Cylinder	Temperature	T_w/T_∞	2.0 all cases

5.2.1 Additional Parameters Calculated

Heat Transfer To Body

The objective of performing the viscous computation is to determine if the heat flux comes with a penalty of additional heat transfer to the body by addition of the microwave filaments. To see this effect, the parameter Φ is studied as defined below. The heat transfer parameter Φ is the average heat transfer over a region of the body divided by the heat transfer in the same region in the absence of the filament. For a Φ value greater than one, the microwave filaments create additional heat transfer to the body. For a Φ less than one, the microwave filaments reduce the heat transfer to the body for the region evaluated.

The heat transfer is studied at the front of the blunt body on the face normal to the oncoming flow.

$$\Phi = \frac{\overline{Q}_{fil}}{\overline{Q}_{nofil}} \tag{5.5}$$

where

$$\overline{Q} = \frac{1}{\tau}\int_0^\tau \int_0^{1/2} q_w r dr dt \tag{5.6}$$

where τ is the dimensionless time at which the integral is taken, and q_w is the dimensionless heat flux at the wall.

Statistically Stationary State

The pulsed filament cases will reach a stochastically stationary state when the variables of interest, primarily the pressure and heat transfer at the front of the body, reach constant mean and root mean square values.

The mean is defined for a variable h as

$$\overline{h} = \frac{1}{\tau}\int_0^\tau \int_0^{D/2} h\, r dr dt \tag{5.7}$$

The root mean square of the perturbation of a variable is defined for an arbitrary variable, h, as

$$h_{rms} = \sqrt{\overline{h'^2}} \tag{5.8}$$

and h' is the perturbation from the mean

$$h' = h - \overline{h} \tag{5.9}$$

where the mean is taken to be the mean at the time the root mean square is taken, and the time period of interest is the period, $\tau = L/D$, for the periodic cases, and the time over which the mean is taken for the infinitely long filament case.

Power Spectrum

The power spectrum is calculated for the heat transfer rate to the front of the face. The power spectrum is analyzed to determine when the flowfield becomes statistically stationary.

When the power spectrum is dominated by only a few peaks, the varying frequencies from the transient associated with the initial interaction have died out and the flow is statistically stationary. The dominant peaks are the frequencies associated with the vortices created in the shear layer changing the heat transfer rate to the front of the cylinder face.

To use the Fast Fourier Transform to obtain the power spectrum, the heat transfer rate is interpolated using a third order polynomial interpolation to even time intervals. An evenly spaced time interval chosen was 0.04 dimensionless time units.

The power spectrum is calculated according to the equation :

$$\text{Power} = \frac{|c_k|^2}{(N/2)^2} \text{ for } k = 1, 2, ..., \left(\frac{N}{2} - 1\right) \tag{5.10}$$

where the c_k are the Fourier coefficients

$$c_k = \sum_{j=0}^{N-1} c_j e^{2\pi ijk/N} \tag{5.11}$$

where $c_j = q(\Delta tj)$ is the heat flux on the face evaluated at the particular time instant.

The frequencies are given by

$$f_n = \frac{n}{N\Delta t} \qquad \text{where} \quad n = 0, ..., \frac{N}{2} \tag{5.12}$$

5.2.2 Infinitely Long Filament

Statistically Stationary State

The heat transfer to the front face, nondimensionalized by $\rho_\infty U_\infty^3$, is analyzed for the infinitely long filament in Figures 5.12 and 5.13. The former is the instantaneous and running time average of the heat transfer integrated over the entire face and the latter is the root mean square of the heat transfer over the cylinder face. The instantaneous value of heat transfer to the cylinder face oscillates in time without decay. These oscillations are attributed to the creation, shedding and subsequent convection past the cylinder face of vortices, generated in the shear layer. The running time average of the face heat transfer is initially high, as the filament and shock wave first interact. After the initial interaction, the running time average of heat transfer then decays to a nearly steady value. The time average shows minor oscillations, due to the oscillating instaneous value. By 30 dimensionless time units, a statistically stationary state has been reached. The root mean square of heat transfer to the front face of the cylinder is also steady and neither increasing nor decreasing by 40 dimensionless time units.

The instantaneous and time averaged centerline pressure and root mean square stagnation pressure are graphed in Figures 5.14 and 5.15, respectively. The pressure is nondimensionalized by $\rho_\infty U_\infty^2$. The stagnation pressure shows continued oscillations due to the creation and convection of vortices from the shear layer just past the bow shock. As the vortices convect past the front face of the cylinder, the pressure on the face is reduced, and restores as the vortices convect over the corner of the cylinder. The local peaks in pressure at time units 22, 32 and 38 are attributed ot a shock wave which moves between the cylinder face and the bow shock. The shock moves back toward the cylinder face and is reflected at the face. The shock then moves toward the bow shock, and is again reflected, as no perturbation can move upstream in the supersonic flow ahead of the bow shock. The shock wave moves back and forth between the bow shock and cylinder face, losing strength in time due to interferences diffusing the strength. The mean of the pressure perturbation is initially high at first interaction of the filament and bow shock, and reduces to a steady value after 30 dimensionless time units. The root mean square of the stagnation pressure also reaches a steady state be 30 dimensionless time units. The stagnation pressure has reached a statistically stationary state by 30 dimensionless time units.

The power spectrum of the heat transfer to the front face of the cylinder is graphed in Figure 5.16. The power spectrum shows most of the energy between a frequency of zero and two. The infinitely long filament case has no frequency associated with the filament; however, there is a frequency associated with the vortex shedding from the shear layer. The vortex shedding frequency is very likely between zero and two, as the vortices convecting past the cylinder face create the periodicity in the heat transfer to the face seen in Figure 5.12. The higher frequencies have powers two to three orders of magnitude smaller than the dominant frequencies. This is a good indication that a statistically stationary state has been reached in the flow.

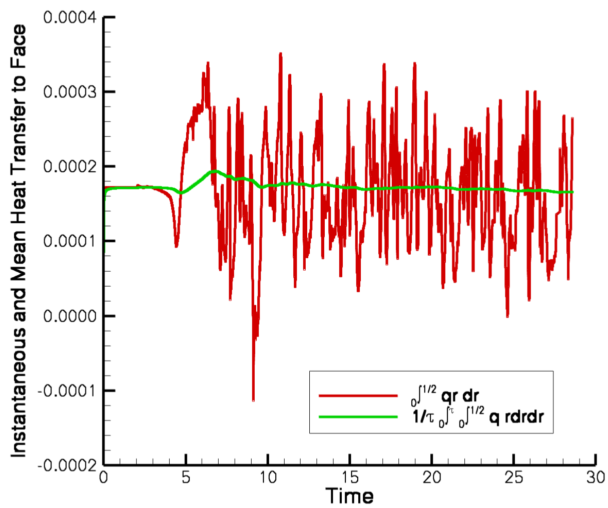

Figure 5.12: Mean and Instantaneous Heat Transfer to Front of Body of the Infinitely Long Filament

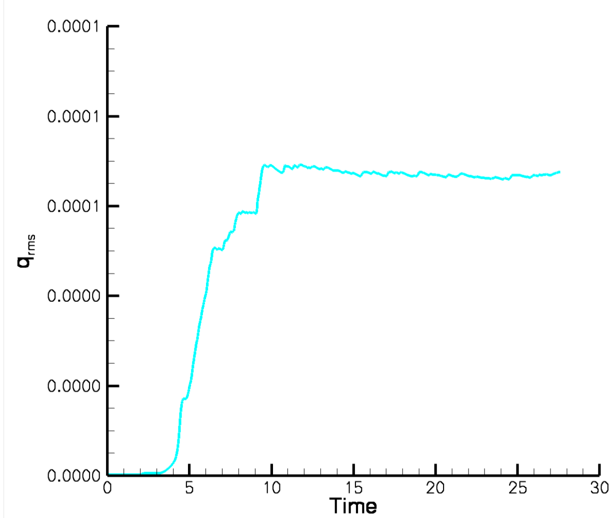

Figure 5.13: Root Mean Square of Heat Transfer to Front of Body of the Infinitely Long Filament

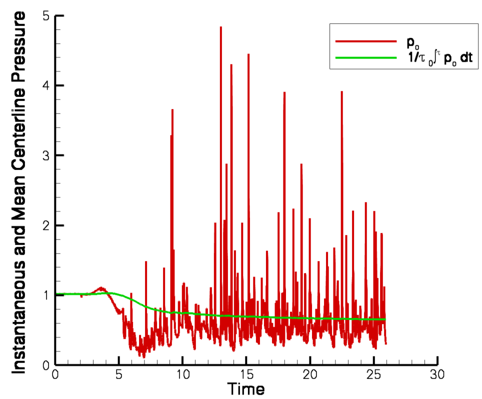

Figure 5.14: Mean and Instantaneous Stagnation Pressure of the Infinitely Long Filament

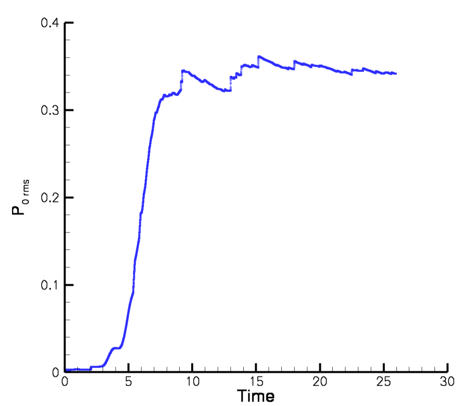

Figure 5.15: Infinite Filament Root Mean Square of Stagnation Pressure

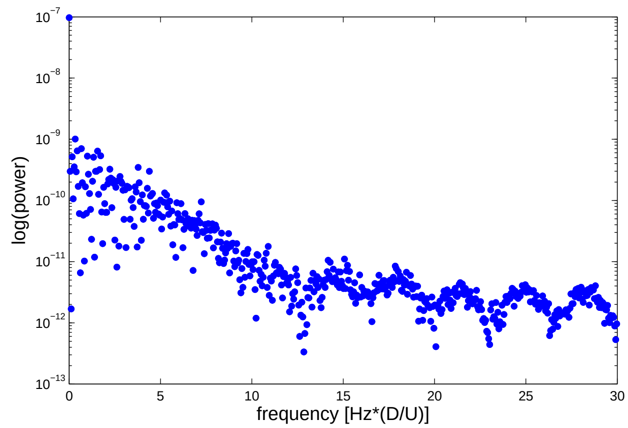

Figure 5.16: Infinite Filament Power Spectrum of Variable q

Efficiency, Effectiveness and Heat Transfer

The efficiency, effectiveness and heat transfer for the cases are graphed in Figures 5.17, 5.18, and 5.19, respectively. The plots of efficiency and effectiveness begin at 10 dimensionless time units to exclude the transient associated with the initial interaction of the heated filament and bow shock. The efficiency of the filament is 108. The infinite filament energy deposition reduces drag on the cylinder body by 40%. The heat transfer rate to the front is reduced by 3%. The vortex structures created by the interaction between the energy filaments and the bow shock reduce the heat transfer. This hypothesis is further explained with the contour graphs in the following subsection.

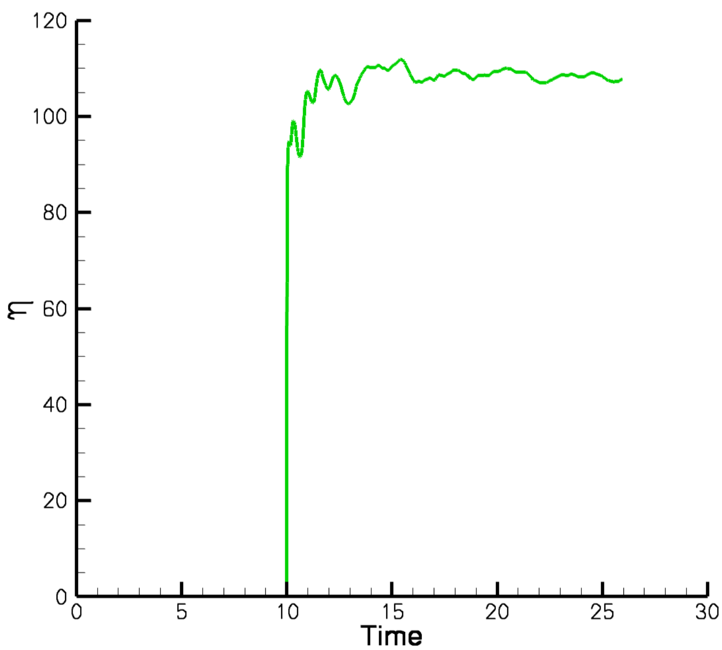

Figure 5.17: Infinite Filament Efficiency Parameter

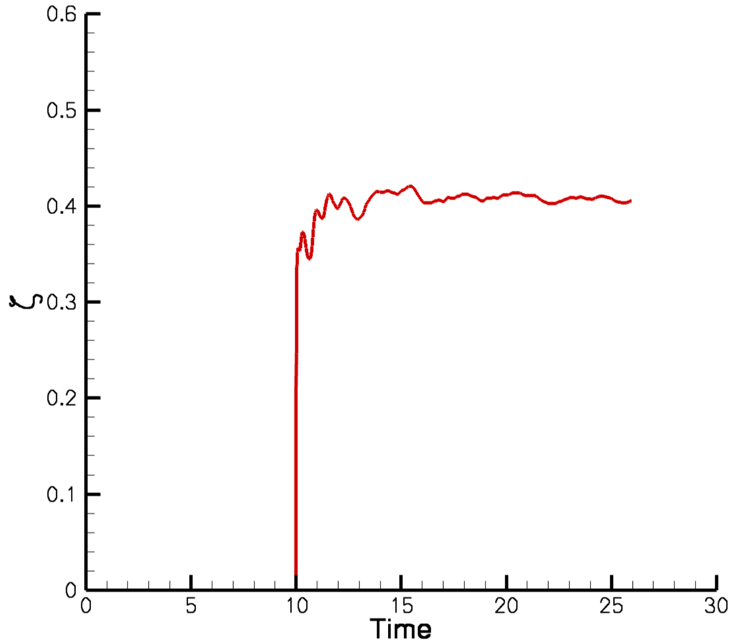

Figure 5.18: Infinite Filament Effectiveness Parameter

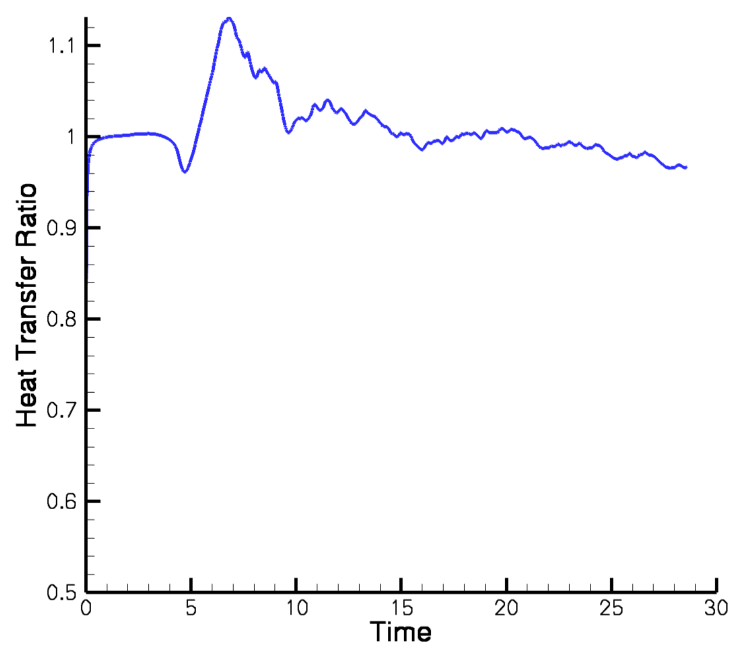

Figure 5.19: Infinite Filament Heat Transfer to Front Face Parameter

Contours of Flow at Stochastically Stationary State

Contours of Flow

The flow contours for the infinitely long filament are presented at the statistically stationary state. Figures 5.20 through 5.22 show a series of images taken over a frame of 1.0 dimensionless time units. The contour plots are used to describe the flow structure, vorticity structure, flow direction and heat transfer rate in the flow in the following paragraphs.

The density gradient contours, Figures 5.20 through 5.22, show gradients in density that occur at contact surfaces and shock waves. The wave structure and contact surfaces are labeled in Figure 5.20(a). The bow shock from the cylinder in the freestream flow is shown. The low density filament is coming into the flow domain from the inflow boundary in Figure 5.20(a). At the intersection of the filament and the bow shock the shock is lensed forward. The contact surface between the heated filament and the freestream flow behind the shock wave can also be seen in the figures. The lower density filament becomes a lower velocity flow downstream from the shock. The lower velocity filament to higher velocity free stream contact surface creates a shear layer. This shear layer is unconditionally unstable to small perturbations; subsequently a vortex sheet is formed at the contact surface. Vortices trailing the vortex sheet are also labeled. An expansion fan appears where the flow accelerates around the corner. Smaller flow structures can be seen in the flow. These are discussed in the paragraphs that follow.

Numerically generated Schlieren images are shown in Figures 5.23 through 5.25. Regions of high density gradients can represent either contact surfaces or shocks waves. Three such high density gradients behind the bow shock are labeled in Figure 5.23(a). These are identified as shocks, due to the jump in pressure that correspond with the sharp density gradient. Shock 1 can be followed through the time progression shown in the contour plots. Shock 1 is shown to convect over the cylinder shoulder. Shock 2 is also followed in time. In Figure 5.24(a) shock 2 has distorted under the influence of the vortices formed after the shear layer. In Figures 5.24(b) through (f), shock 2 moves toward the front face of the cylinder, weakening in strength as it aproaches the bow shock. In Figures 5.25 (a) through (f), shock 2 reflects off the cylinder face towards the symmetry boundary. Shock 3, which is near the center of the flow domain at Figure 5.23 (a), is suspected to be moving in the direction of the axis of symmetry in the first figure because in the subsequent figure, Figure 5.23 (b), the aft portion of shock 3 has reflected off of the axis of symmetry. The front and aft portion of shock 3 then meet each other and move as a stronger shock toward the bow shock. As shock 3 moves toward the bow shock, the density gradient across the shock, or strength of the shock, weakens. This weakening of the shock is likely attributed to the interaction with the vortices near the shear layer. The vortex entrains most of the flow from the shock, diffusing the strength of the shock.

The contact surfaces and shock waves are indistinguishable in the Schlieren images and density gradient contours; the dimensionless pressure contours, Figures 5.26 through 5.28, are used to distinguish the shock waves and contact surfaces. The pressure is nondimensionalized by $\rho_\infty U_\infty^2$. Shock waves exhibit a large pressure jump, while the contact discontinuities can separate regions of the same pressure. In Figure 5.26 (a), the bow shock is seen as a large pressure discontinuity the farthest upstream in the computational domain. Shocks 1, 2 and 3 are seen to have large pressure jumps across them. The pressure contours show that the vortices correspond to regions of low pressure. In Figures 5.27 the vortices reduce the pressure on the front face of the cylinder as they sweep by the cylinder.

The existance of the shear layer is verified by the dimensionless velocity magnitude plots shown in Figures 5.29 through 5.31. The velocity is nondimensionalized by the freestream velocity, U_∞. The lower density filament, upon interaction with the normal shock becomes a lower velocity fluid than the free stream. This shear layer is unstable to any infinitesimally small perturbation and thus a vortex sheet is created.

The vorticity contours are shown in Figures 5.32 through 5.34. The vorticity is generated in Tecplot using the dimensionless velocity vector. Three of the vortices are labeled to track their progression. Vortex 1 becomes entrained in the vortices just ahead of the cylinder, as seen in graph 5.33(a). The vortices ahead of the shock create one larger vortex system, as seen in Figure 5.34(a). Vortex 2 is pulled along the front face of the cylinder face, as is evident if Figure 5.33(c). Vortex 3 is carried over the shoulder of the cylinder, as can be seen in Figure 5.34(f).

The streamlines are plotted with the dimensionless velocity magnitude contours, shown in Figure 5.35 through 5.37. The flow moves in from the inflow boundary parallel to the centerline. The bow shock deflects the flow upward. The region between the bow shock and cylinder face is seen to have a shear layer where the velocity magnitude contours transition sharply from blue (lower velocity) to green (higher velocity). The streamlines show vortices forming at this shear layer. The flow just above the cylinder corner is shown to speed up rapidly. This illustrates the expansion fan around the corner.

Figures 5.38 through 5.40 show the temperature contours. It be seen in Figure 5.38(a) that the individual vortices do not have a significantly lower temperature than the flow in the stagnation region ahead of the cylinder face. As the vortices collect into a larger vortex system, as in Figure 5.39(a), the vortex system has a much lower temperature than the surrounding flow. The presence of the larger vortex system reduces the heat transfer to the face, as this time corresponds to a drop in pressure in Figure 5.12.

The density contours are shown in Figures 5.41 through 5.43. The density contours show spots of reduced density between the intersection of the heated filaments and bow shock and the cylinder corner. These reduced density spots represent the vortices formed at the shear layer which convect toward the cylinder corner. The density contours show a pronounced shock wave just ahead of the cylinder. This is due to the presence of the vortices ahead of the corner. As the vortices collect ahead of the cylinder corner, the flow above the line of vortices is drawn down in the momentum of the vortex system. This is seen in the streamline plot, Figure 5.35(c). A clockwise rotating vortex just ahead of the cylinder corner has pulled the flow above the vortex line down. Just upstream of the cylinder corner, the flow above the vortex line turns upward. A shock wave appears where the flow turns upward.

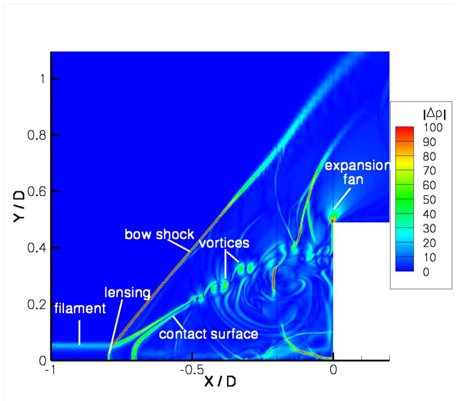

(a) t = 27.42

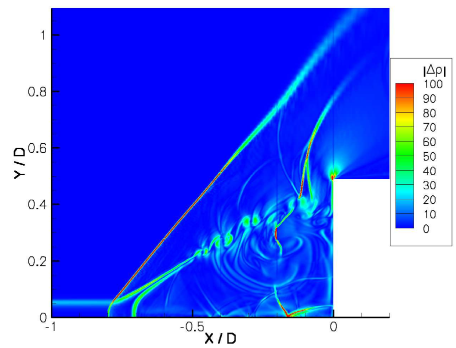

(b) t = 27.47

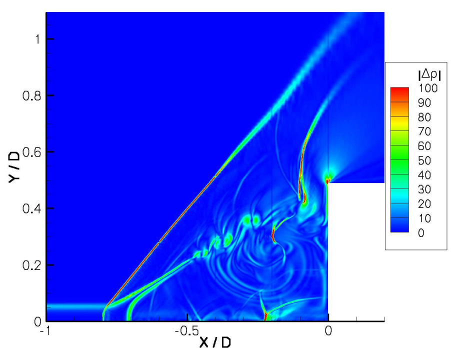

(c) t = 27.53

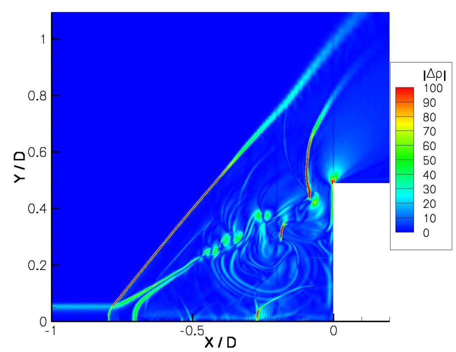

(d) t = 27.58

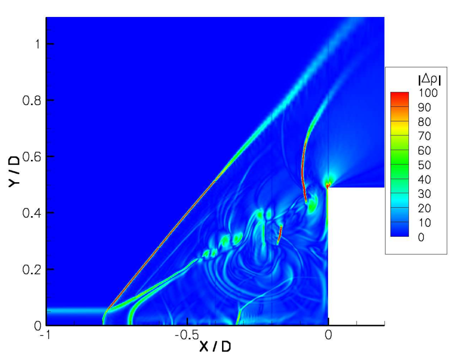

(e) t = 27.64

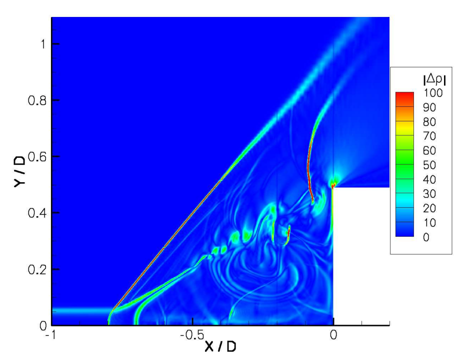

(f) t = 27.70

Figure 5.20: Infinitely Long Filament Density Gradient Contours

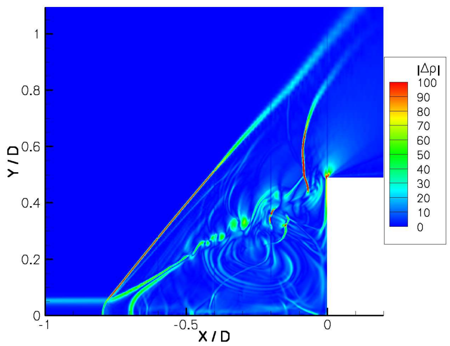

(a) t = 27.77

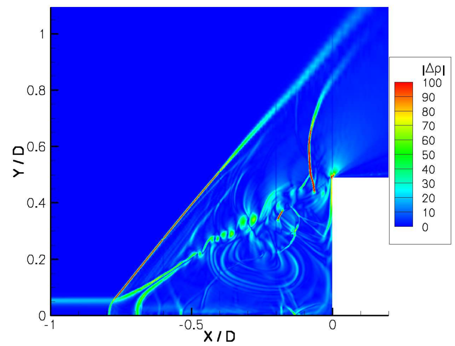

(b) t = 27.83

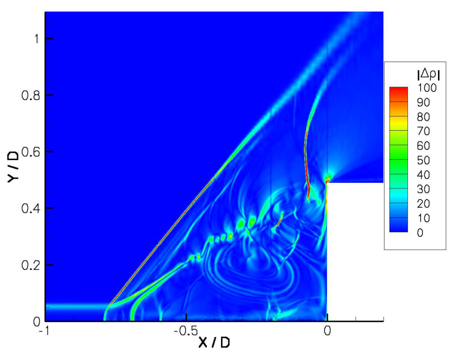

(c) t = 27.88

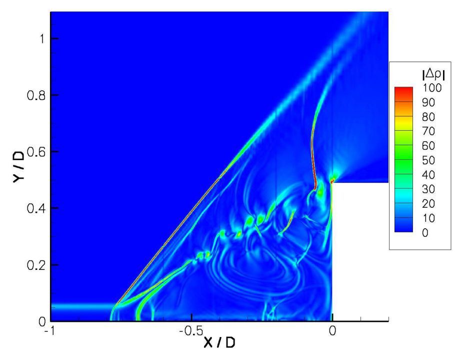

(d) t = 27.94

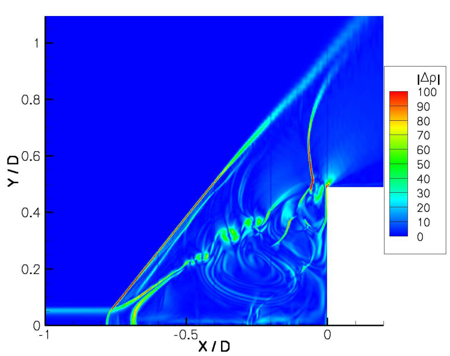

(e) t = 28.00

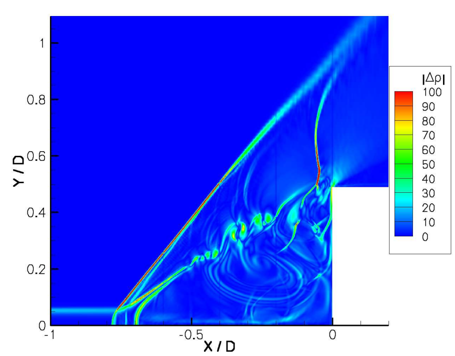

(f) t = 28.06

Figure 5.21: Infinitely Long Filament Density Gradient Contours

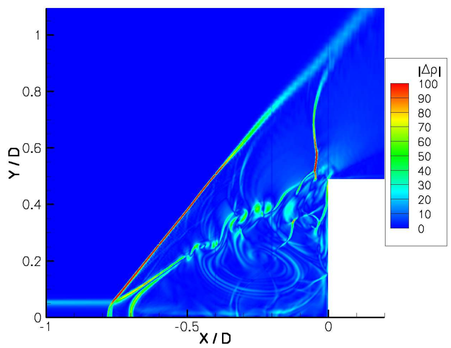

(a) t = 28.11

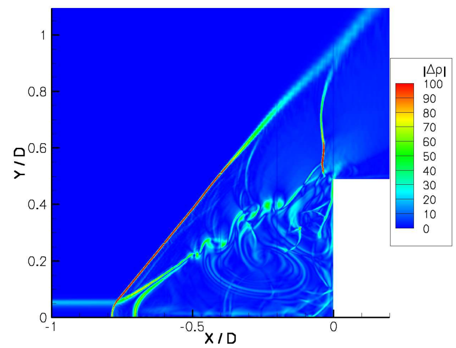

(b) t = 28.17

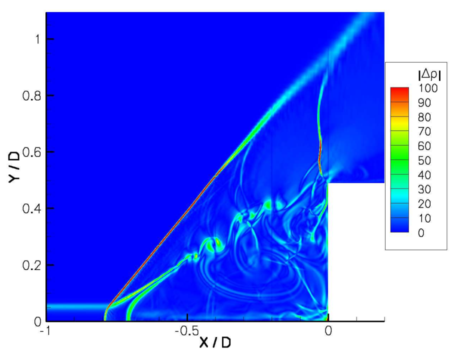

(c) t = 28.23

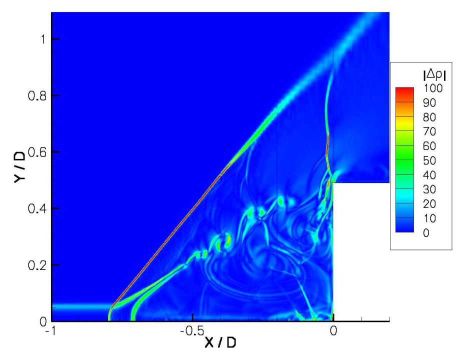

(d) t = 28.29

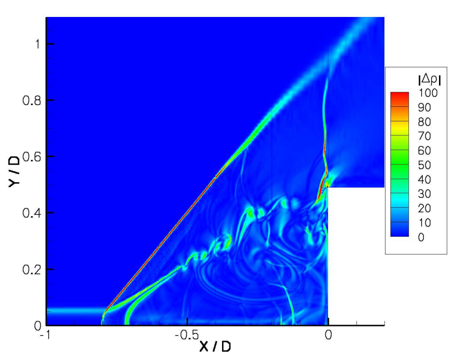

(e) t = 28.35

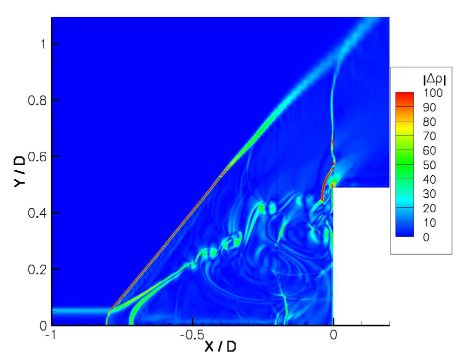

(f) t = 28.41

Figure 5.22: Infinitely Long Filament Density Gradient Contours

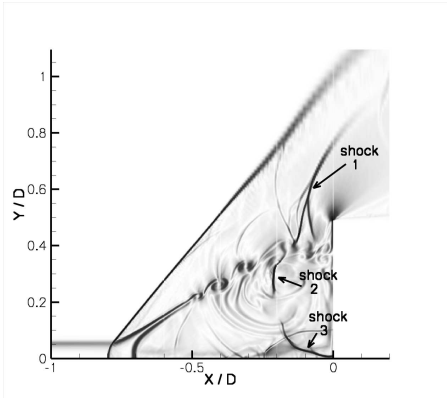

(a) t = 27.42

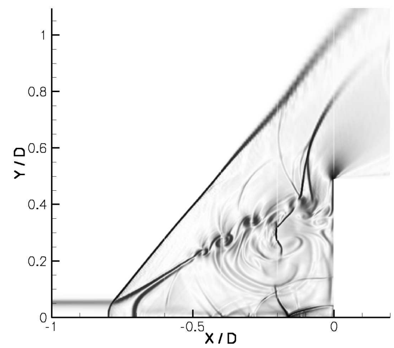

(b) t = 27.47

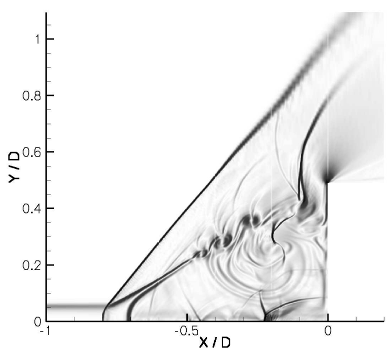

(c) t = 27.53

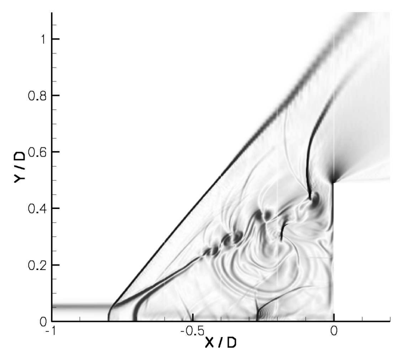

(d) t = 27.58

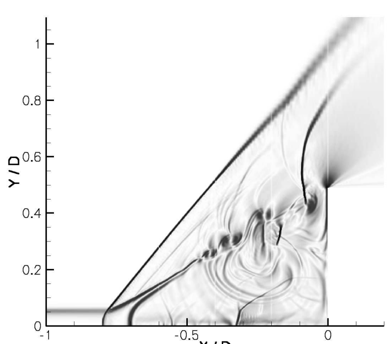

(e) t = 27.64

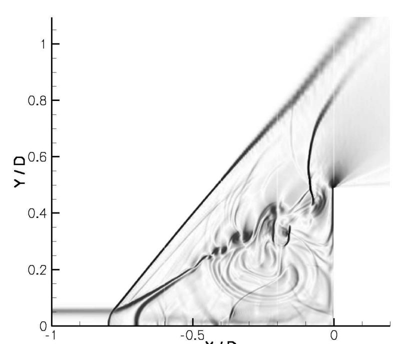

(f) t = 27.70

Figure 5.23: Infinitely Long Filament Numerical Schlieren Images

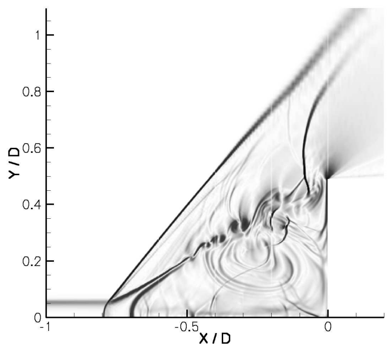

(a) t = 27.77

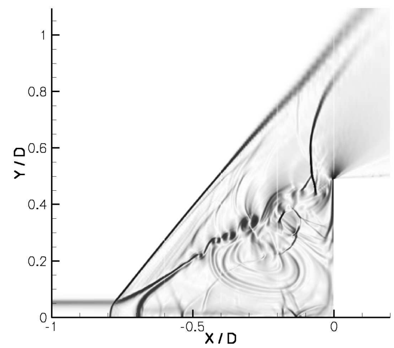

(b) t = 27.83

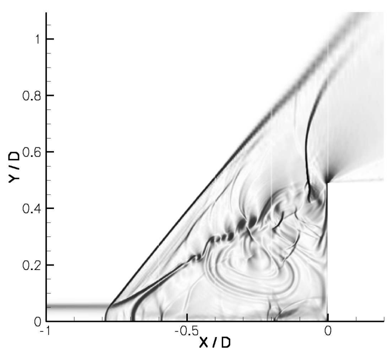

(c) t = 27.88

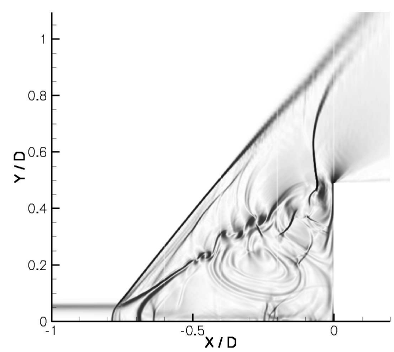

(d) t = 27.94

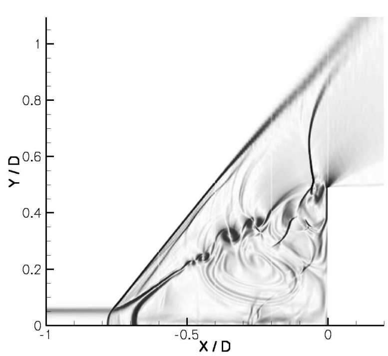

(e) t = 28.00

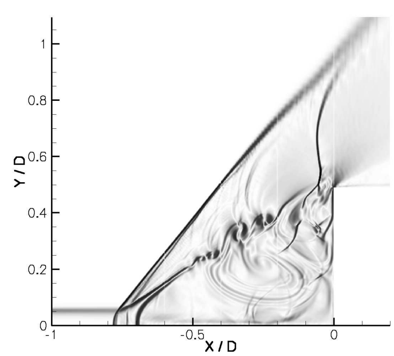

(f) t = 28.06

Figure 5.24: Infinitely Long Filament Numerical Schlieron Images

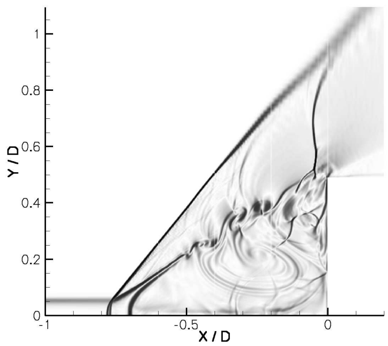

(a) t = 28.11

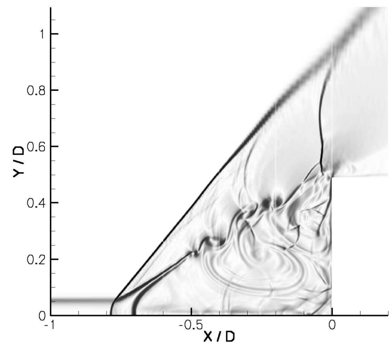

(b) t = 28.17

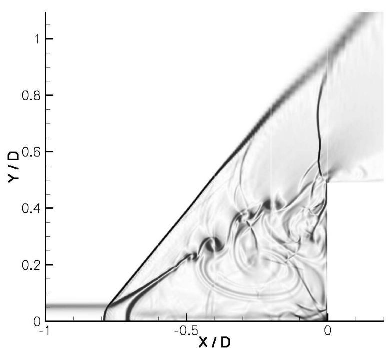

(c) t = 28.23

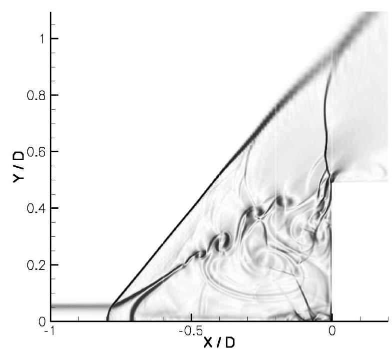

(d) t = 28.29

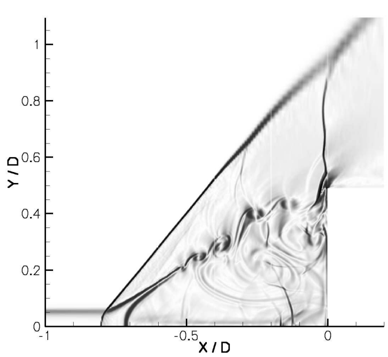

(e) t = 28.35

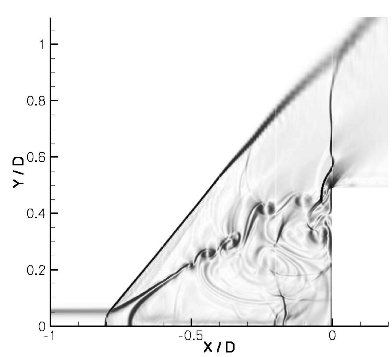

(f) t = 28.41

Figure 5.25: Infinitely Long Filament Numerical Schlieron Images

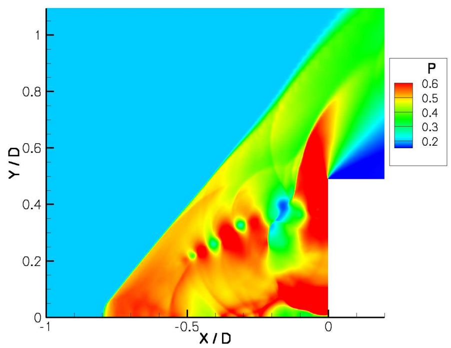

(a) t = 27.42

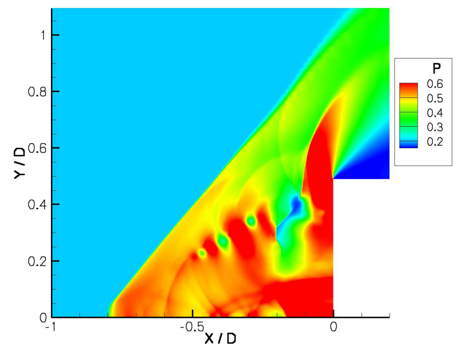

(b) t = 27.47

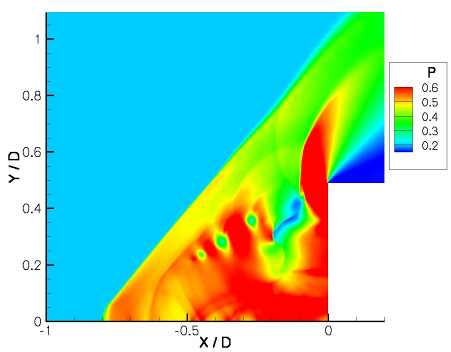

(c) t = 27.53

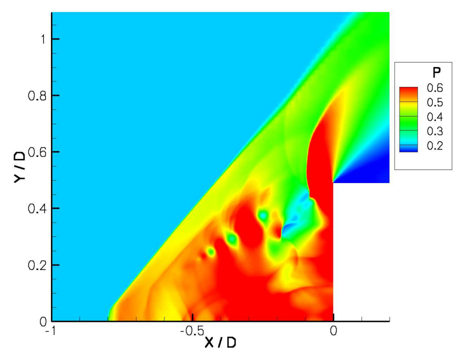

(d) t = 27.58

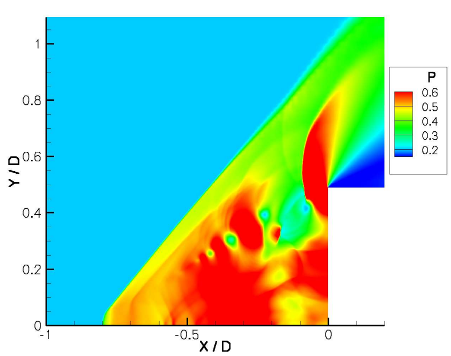

(e) t = 27.64

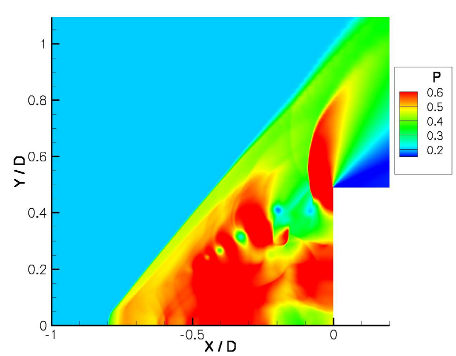

(f) t = 27.70

Figure 5.26: Infinitely Long Filament Pressure Contours

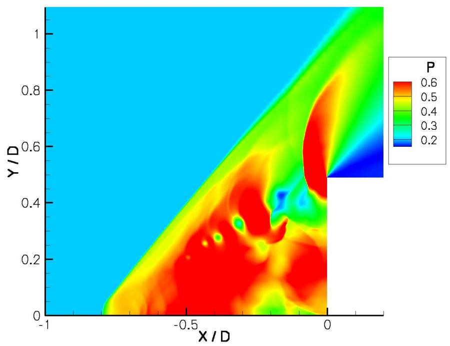

(a) t = 27.77

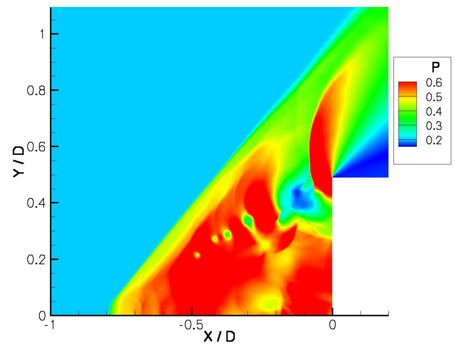

(b) t = 27.83

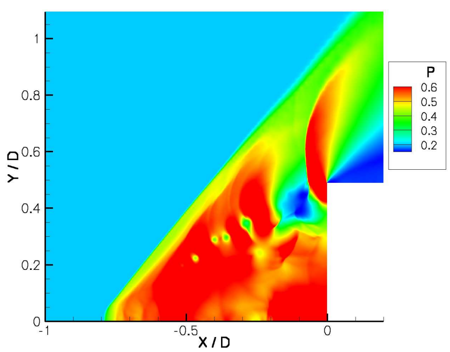

(c) t = 27.88

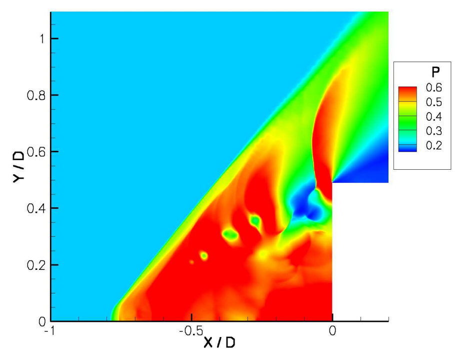

(d) t = 27.94

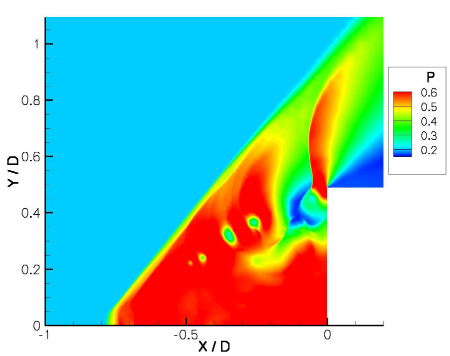

(e) t = 28.00

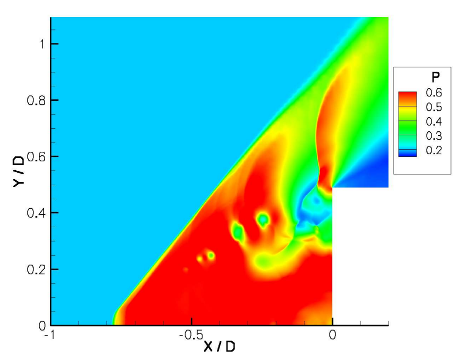

(f) t = 28.06

Figure 5.27: Infinitely Long Filament Pressure Contours

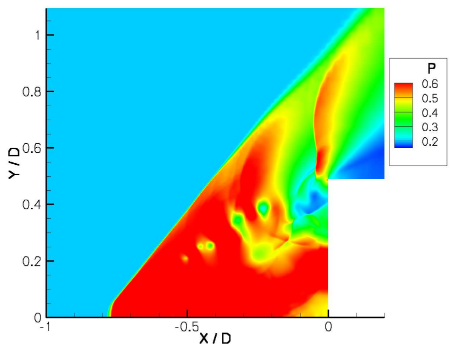

(a) t = 28.11

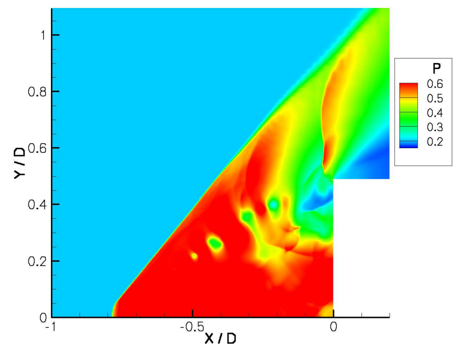

(b) t = 28.17

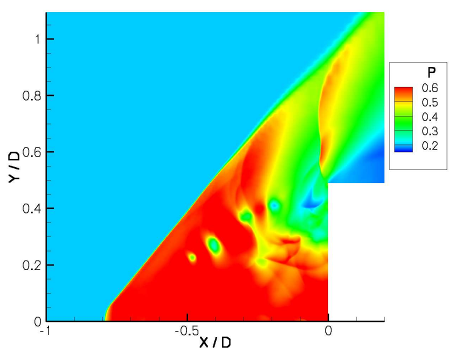

(c) t = 28.23

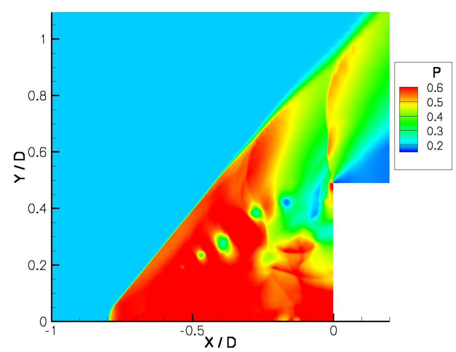

(d) t = 28.29

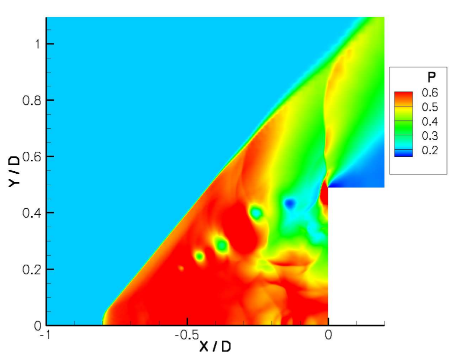

(e) t = 28.35

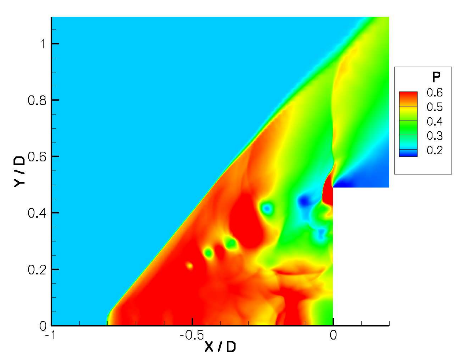

(f) t = 28.41

Figure 5.28: Infinitely Long Filament Pressure Contours

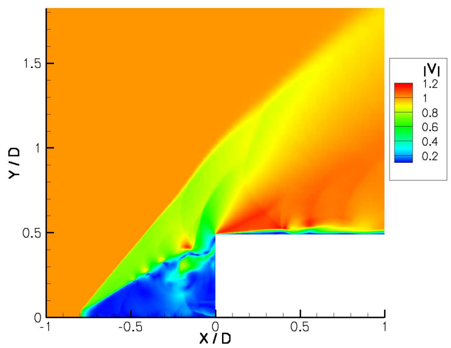

(a) t = 27.42

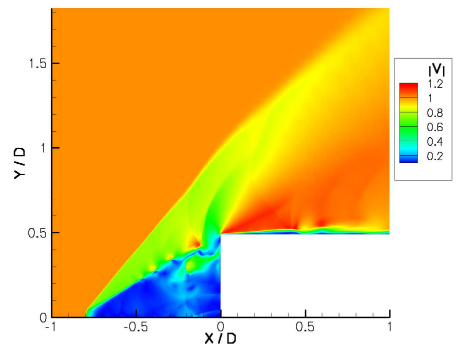

(b) t = 27.47

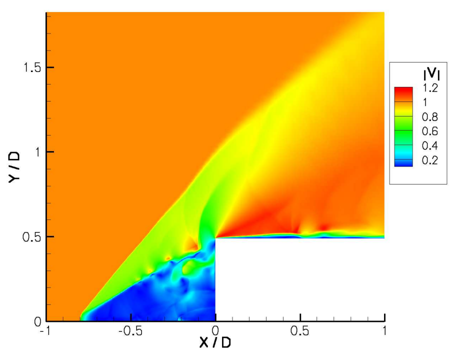

(c) t = 27.53

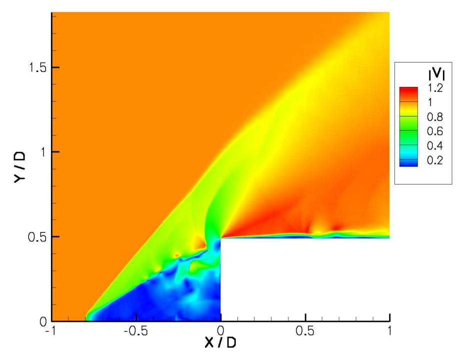

(d) t = 27.58

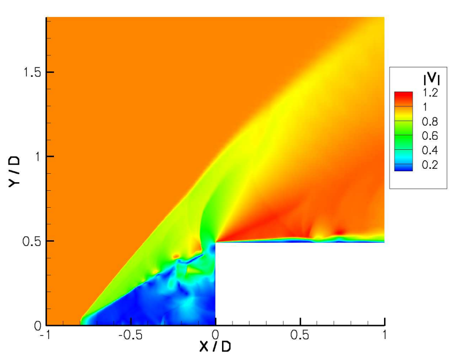

(e) t = 27.64

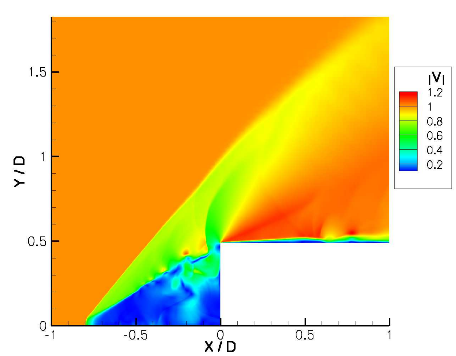

(f) t = 27.70

Figure 5.29: Infinitely Long Filament Velocity Magnitude Contours

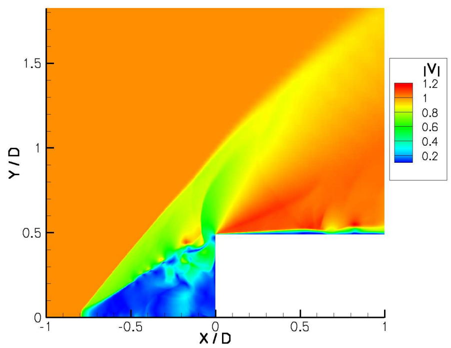

(a) t = 27.77

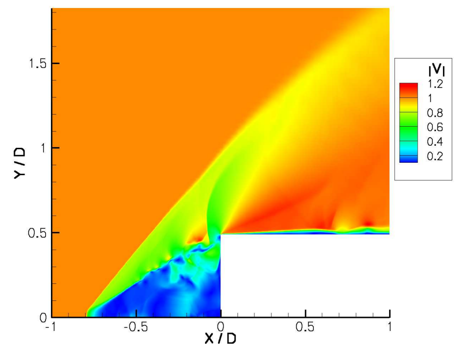

(b) t = 27.83

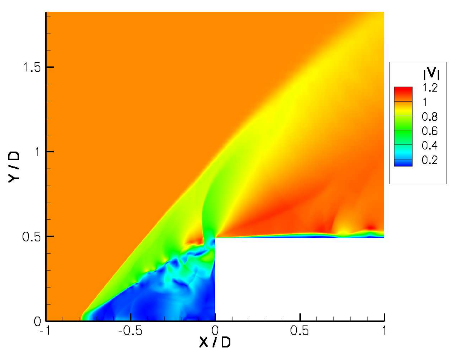

(c) t = 27.88

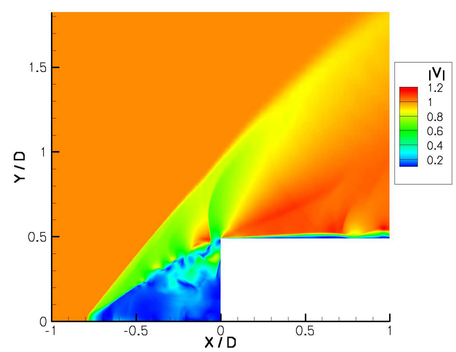

(d) t = 27.94

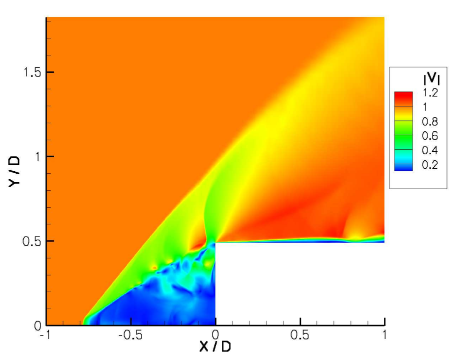

(e) t = 28.00

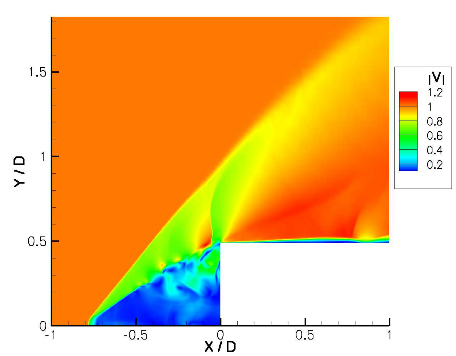

(f) t = 28.06

Figure 5.30: Infinitely Long Filament Velocity Magnitude Contours

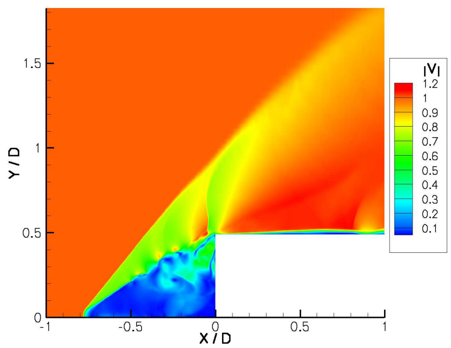

(a) t = 28.11

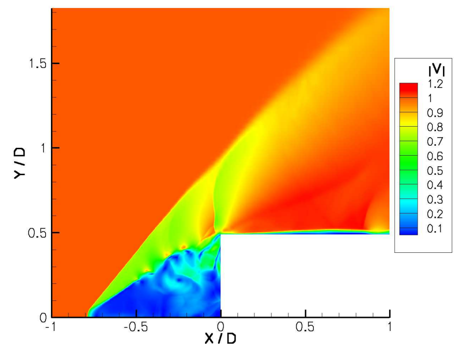

(b) t = 28.17

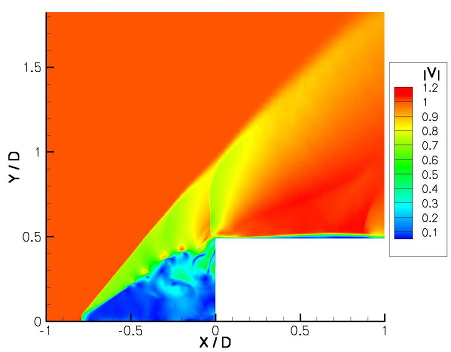

(c) t = 28.23

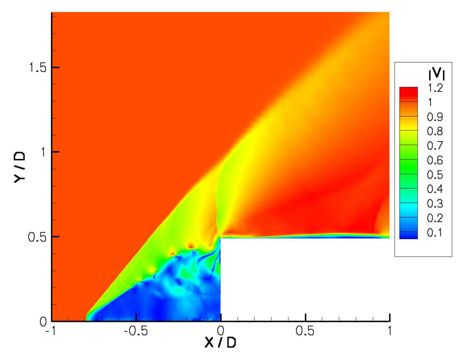

(d) t = 28.29

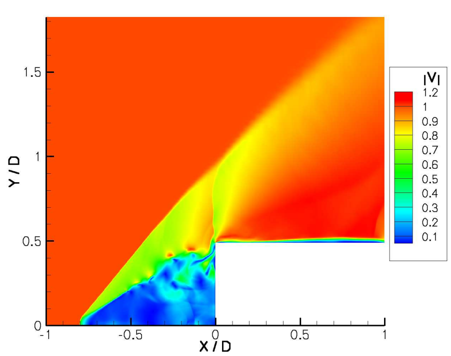

(e) t = 28.35

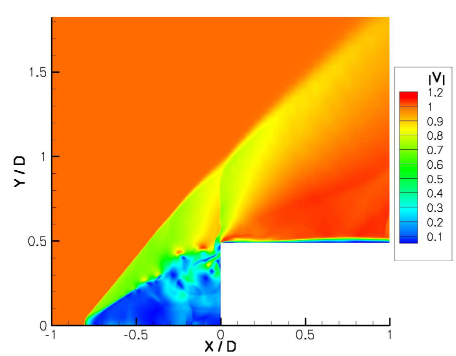

(f) t = 28.41

Figure 5.31: Infinitely Long Filament Velocity Magnitude Contours

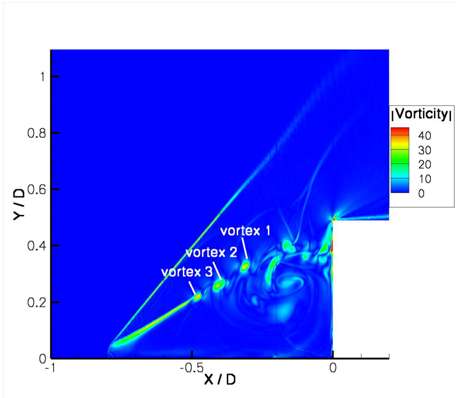

(a) t = 27.42

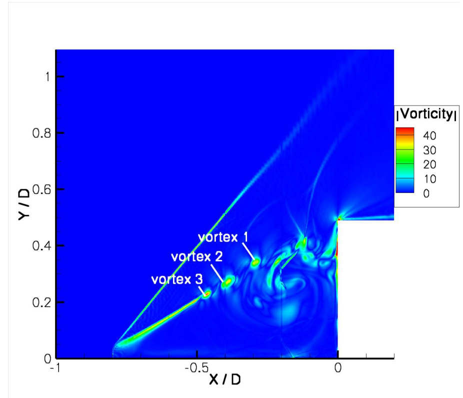

(b) t = 27.47

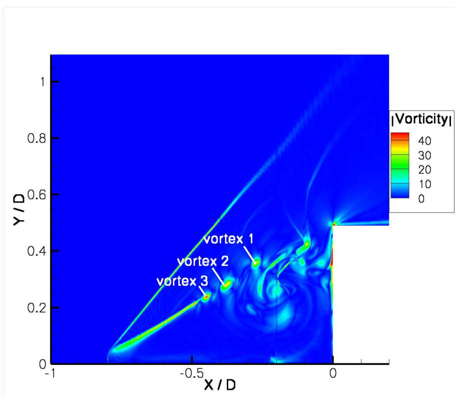

(c) t = 27.53

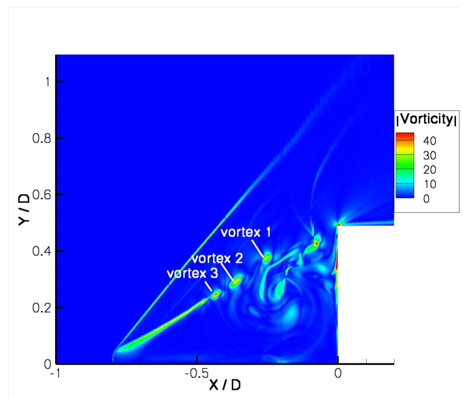

(d) t = 27.58

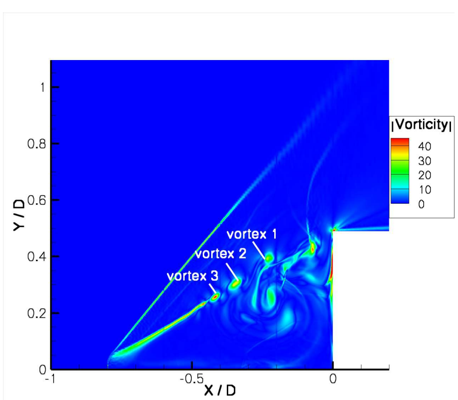

(e) t = 27.64

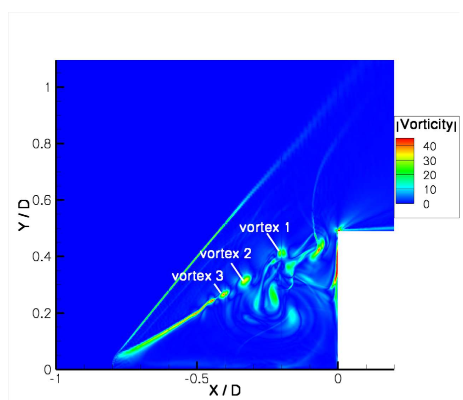

(f) t = 27.70

Figure 5.32: Infinitely Long Filament Vorticity Contours

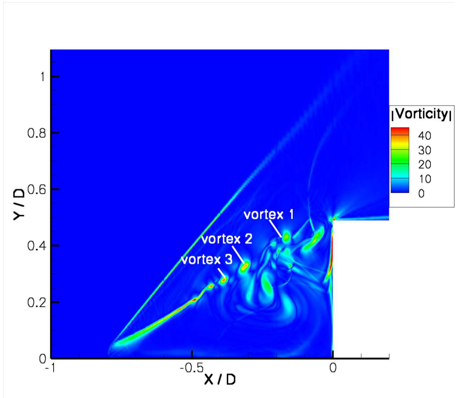

(a) t = 27.77

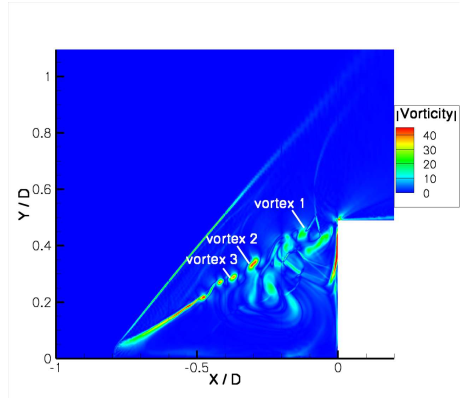

(b) t = 27.83

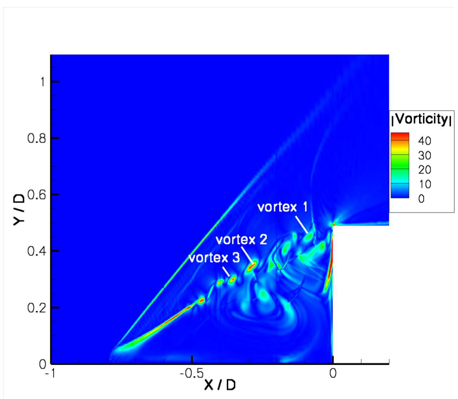

(c) t = 27.88

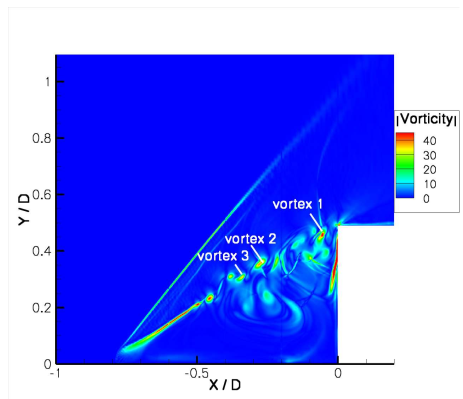

(d) t = 27.94

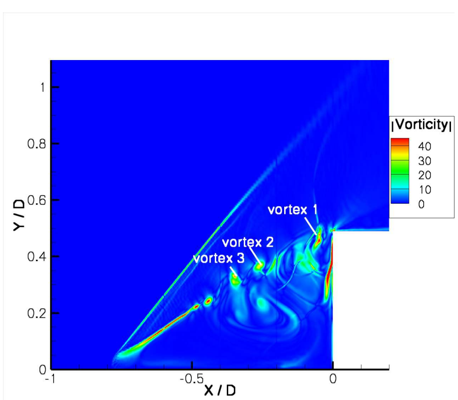

(e) t = 28.00

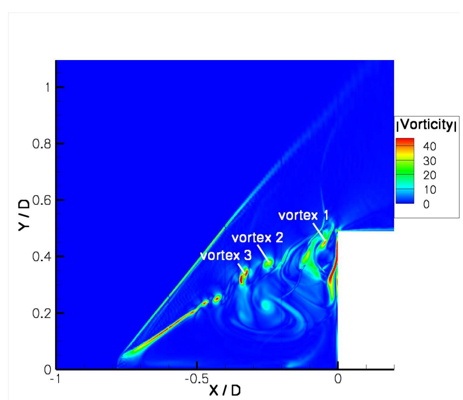

(f) t = 28.06

Figure 5.33: Infinitely Long Filament Vorticity Contours

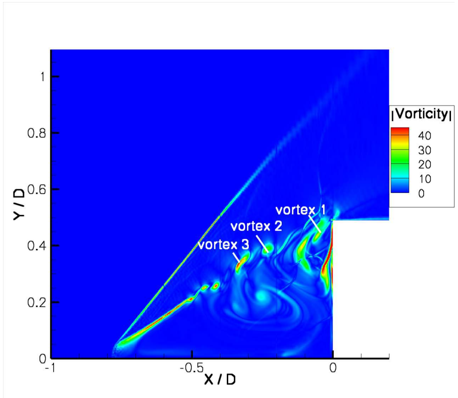

(a) t = 28.11

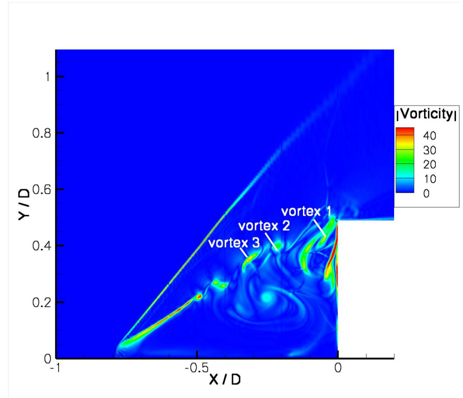

(b) t = 28.17

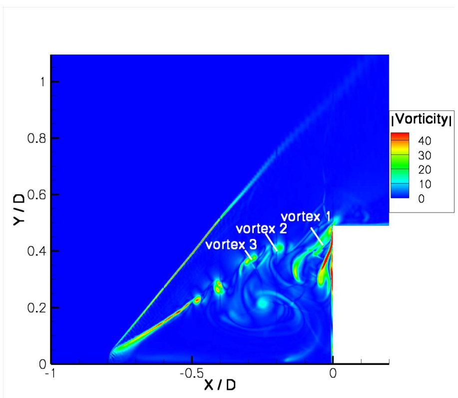

(c) t = 28.23

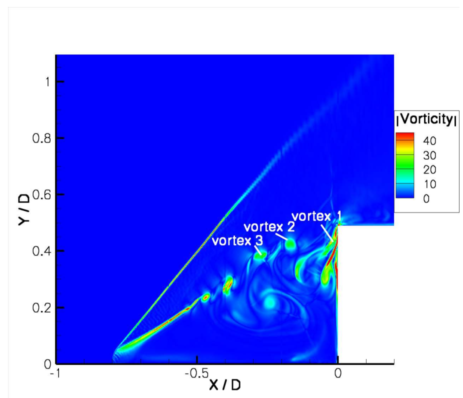

(d) t = 28.29

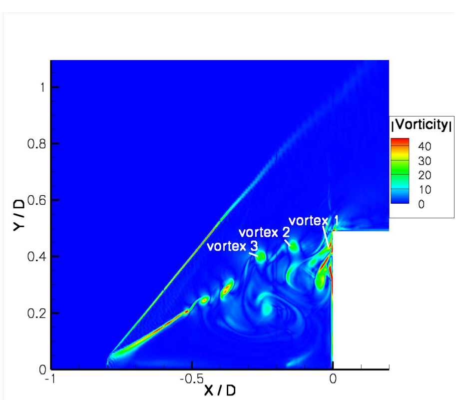

(e) t = 28.35

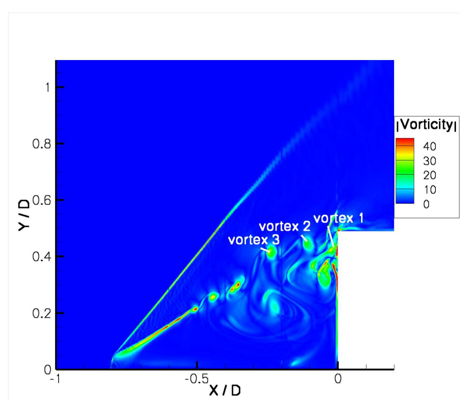

(f) t = 28.41

Figure 5.34: Infinitely Long Filament Vorticity Contours

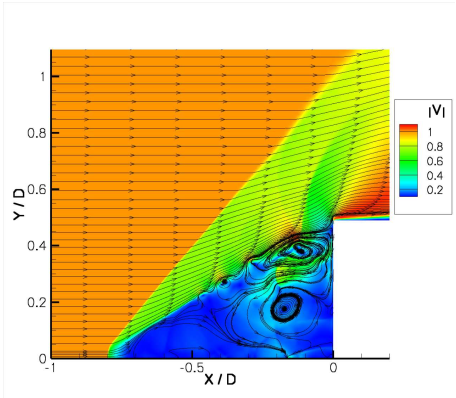

(a) t = 27.42

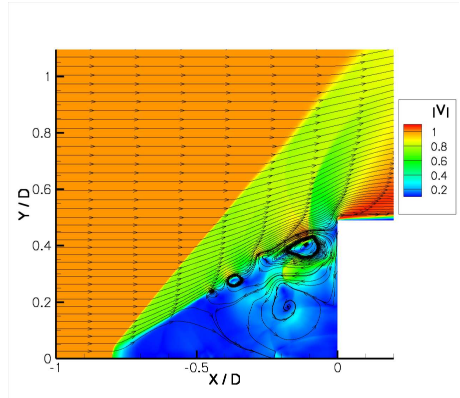

(b) t = 27.47

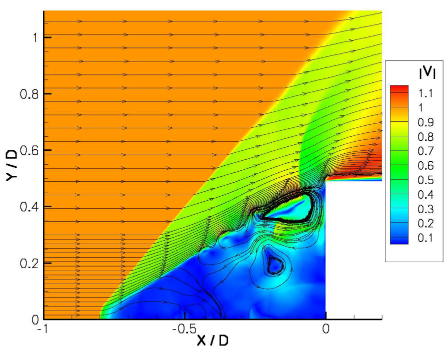

(c) t = 27.53

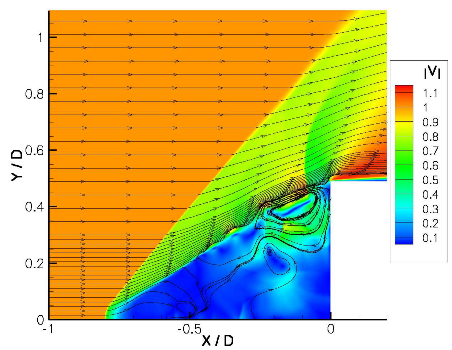

(d) t = 27.58

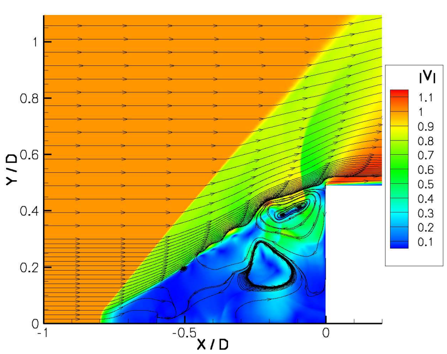

(e) t = 27.64

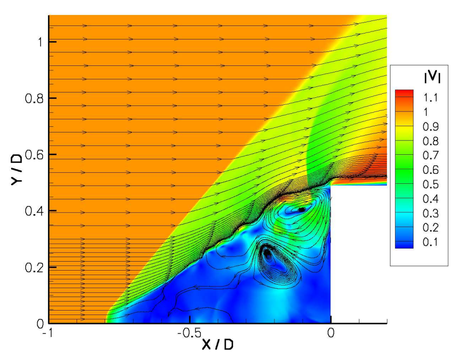

(f) t = 27.70

Figure 5.35: Infinitely Long Filament Streamlines

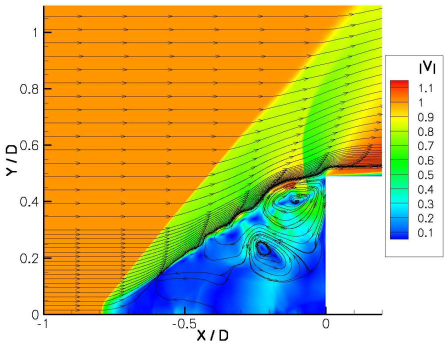

(a) t = 27.77

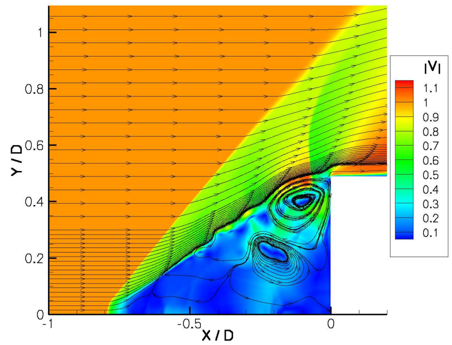

(b) t = 27.83

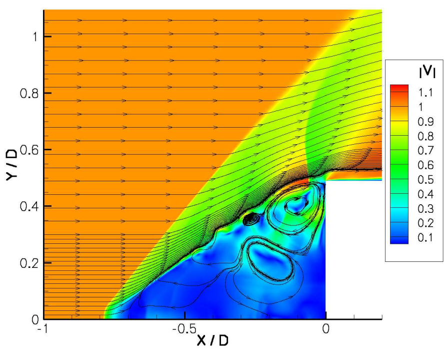

(c) t = 27.88

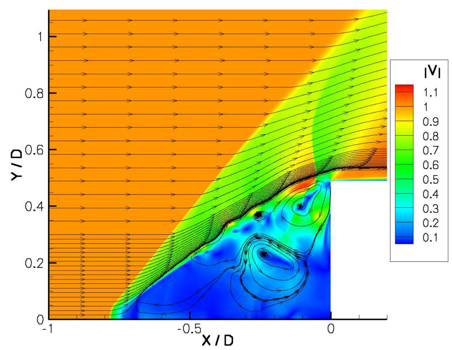

(d) t = 27.94

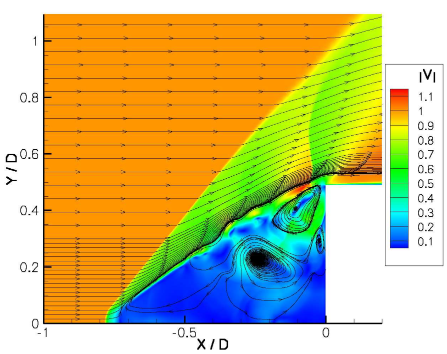

(e) t = 28.00

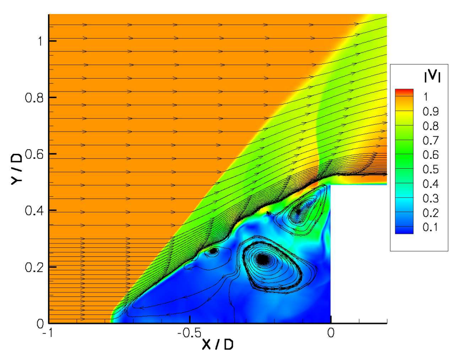

(f) t = 28.06

Figure 5.36: Infinitely Long Filament Streamlines

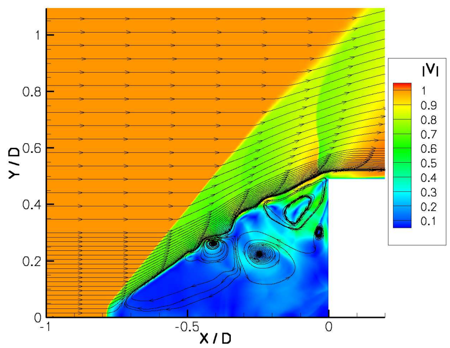

(a) t = 28.11

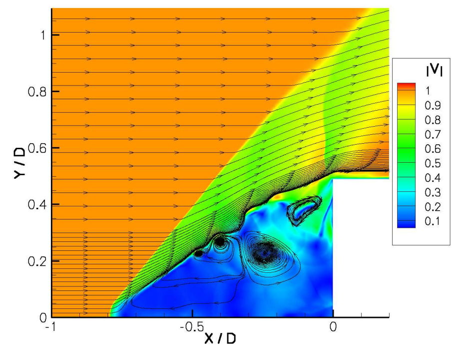

(b) t = 28.17

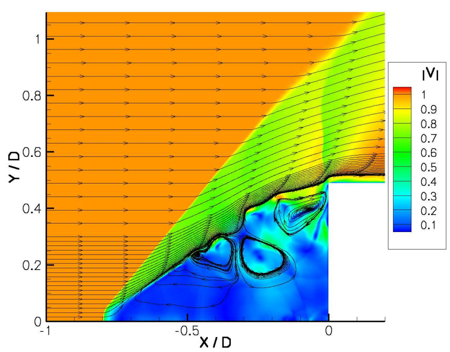

(c) t = 28.23

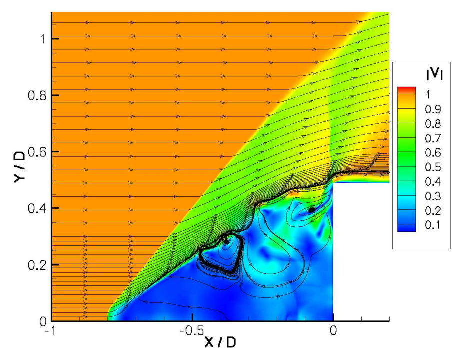

(d) t = 28.29

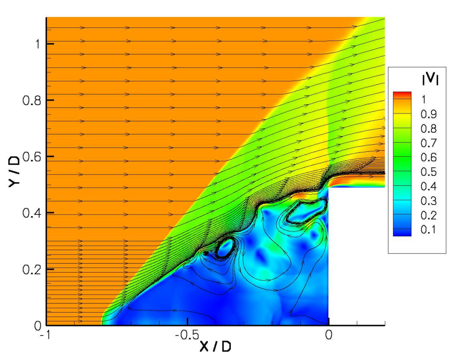

(e) t = 28.35

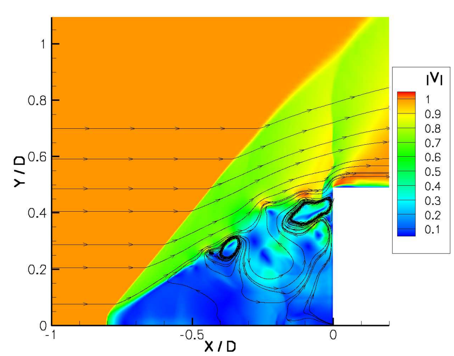

(f) t = 28.41

Figure 5.37: Infinitely Long Filament Streamlines

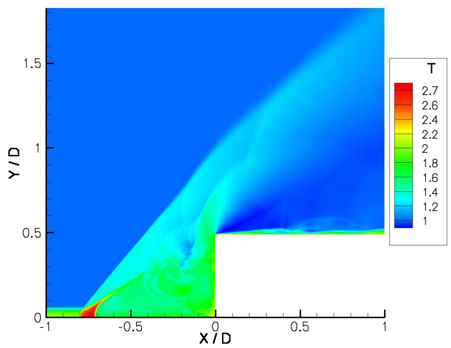

(a) t = 27.42

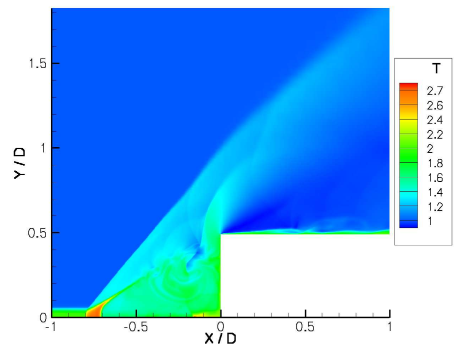

(b) t = 27.47

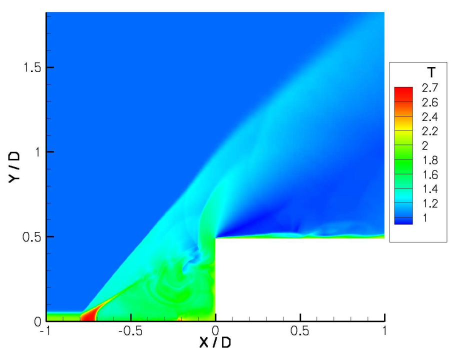

(c) t = 27.53

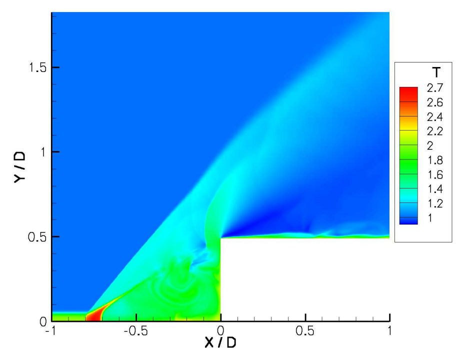

(d) t = 27.58

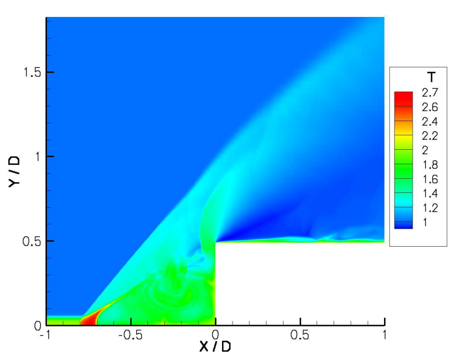

(e) t = 27.64

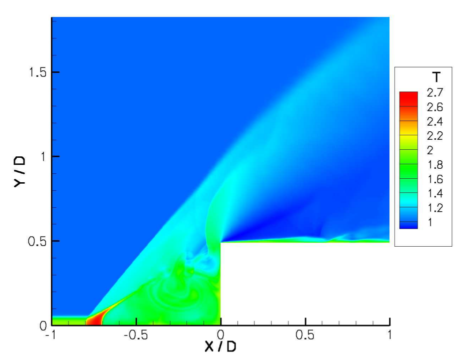

(f) t = 27.70

Figure 5.38: Infinitely Long Filament Temperature Contours

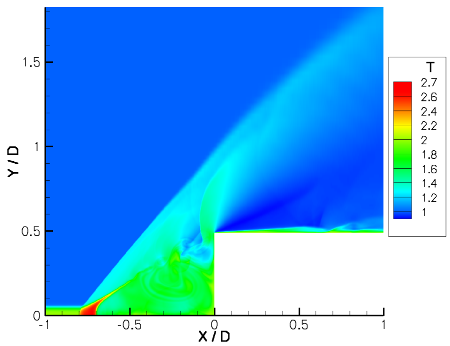

(a) t = 27.77

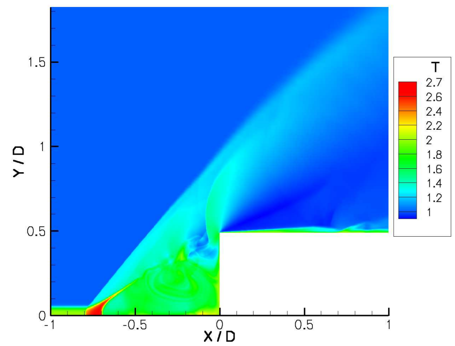

(b) t = 27.83

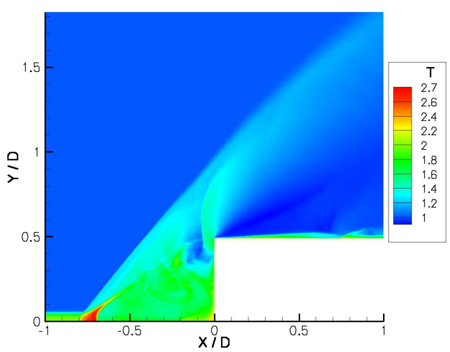

(c) t = 27.88

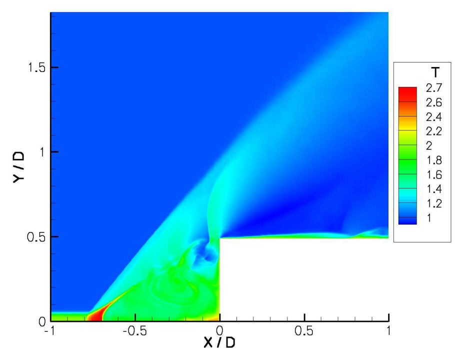

(d) t = 27.94

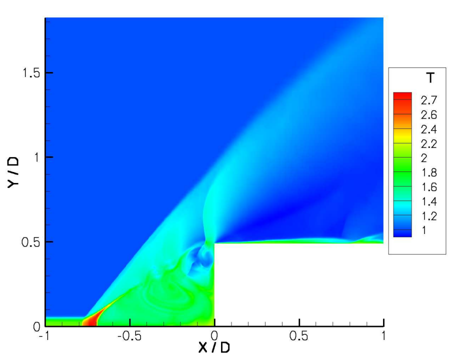

(e) t = 28.00

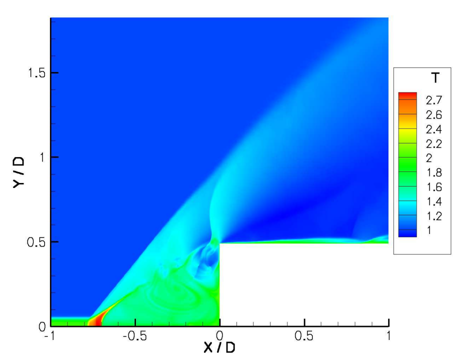

(f) t = 28.06

Figure 5.39: Infinitely Long Filament Temperature Contours

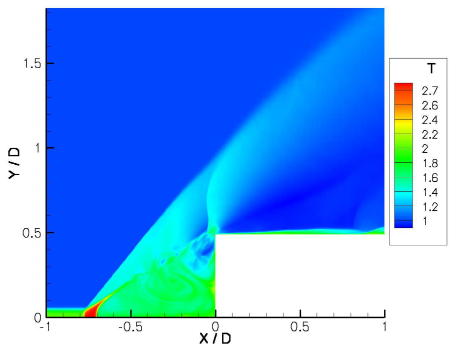

(a) t = 28.11

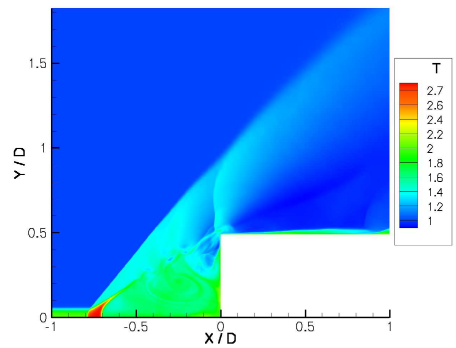

(b) t = 28.17

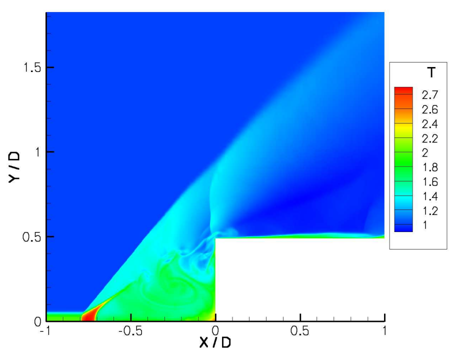

(c) t = 28.23

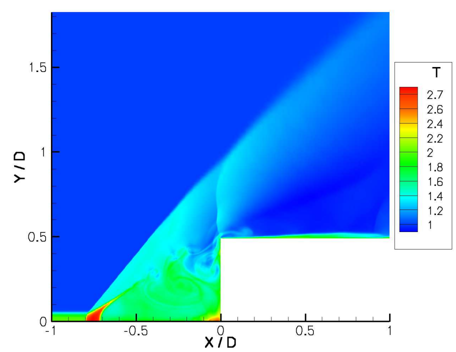

(d) t = 28.29

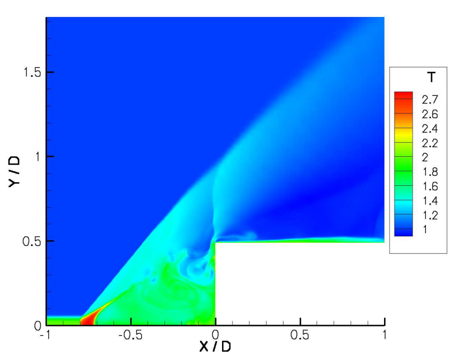

(e) t = 28.35

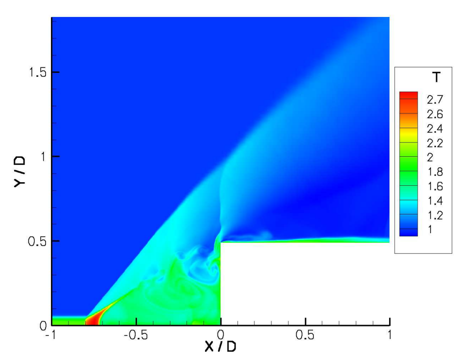

(f) t = 28.41

Figure 5.40: Infinitely Long Filament Temperature Contours

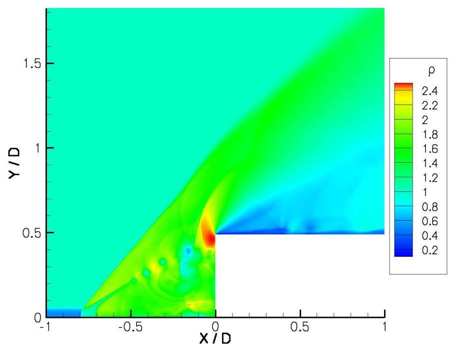

(a) t = 27.42

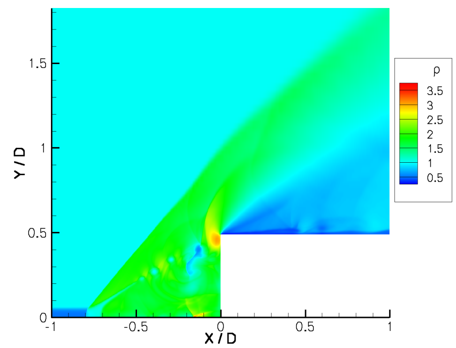

(b) t = 27.47

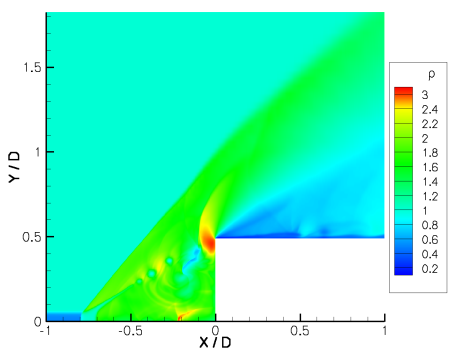

(c) t = 27.53

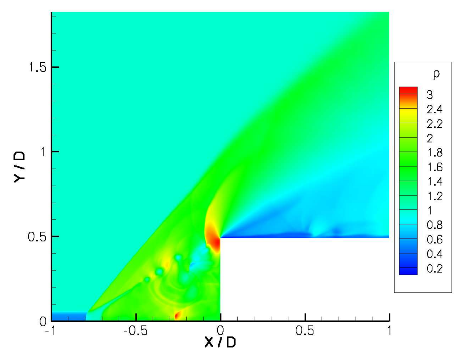

(d) t = 27.58

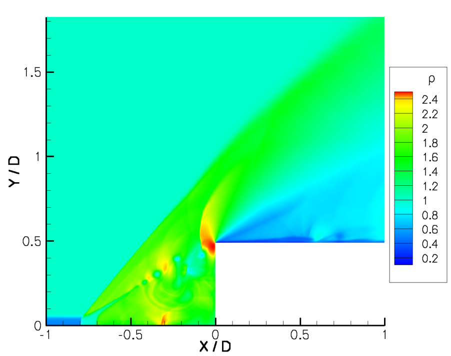

(e) t = 27.64

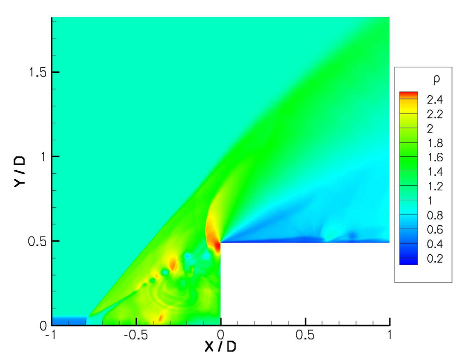

(f) t = 27.70

Figure 5.41: Infinitely Long Filament Density Contours

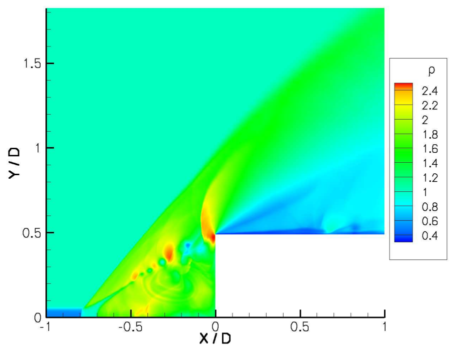

(a) t = 27.77

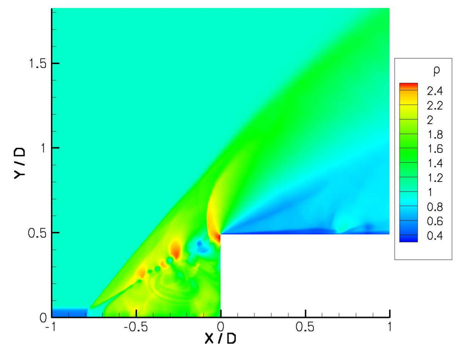

(b) t = 27.83

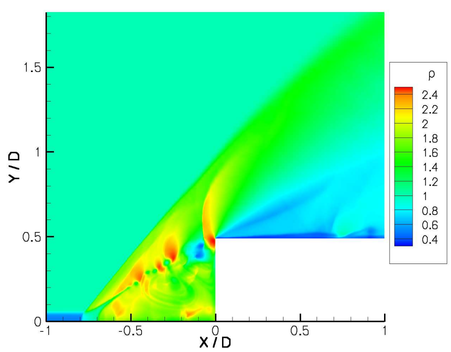

(c) t = 27.88

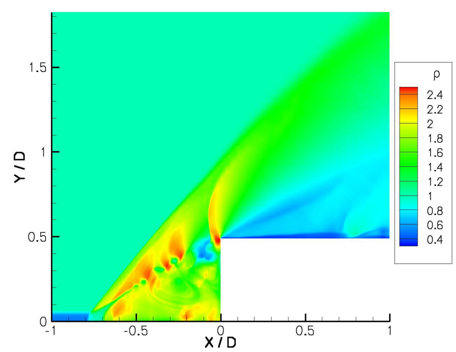

(d) t = 27.94

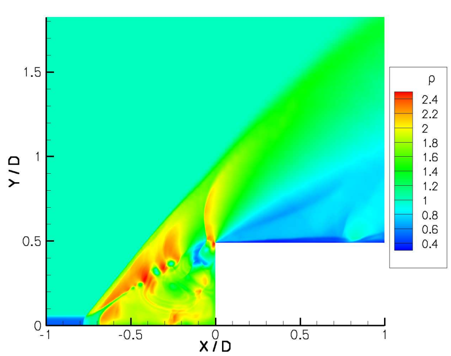

(e) t = 28.00

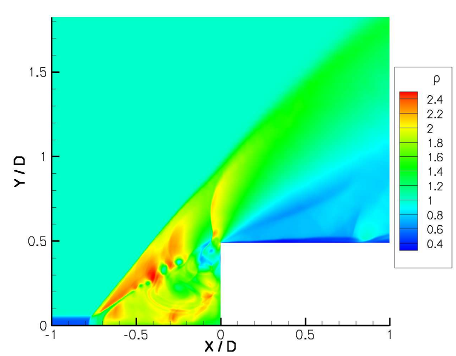

(f) t = 28.06

Figure 5.42: Infinitely Long Filament Density Contours

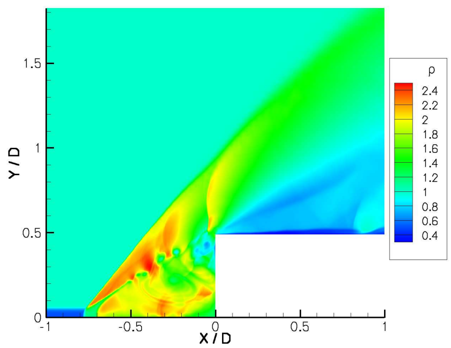

(a) t = 28.11

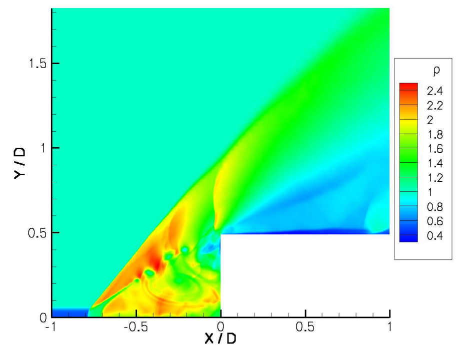

(b) t = 28.17

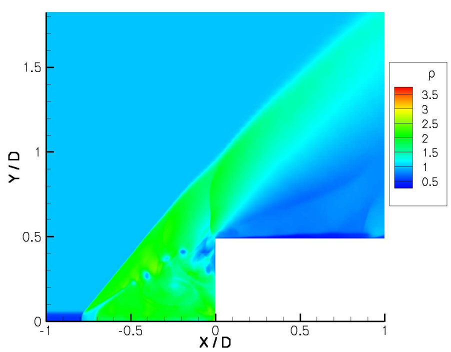

(c) t = 28.23

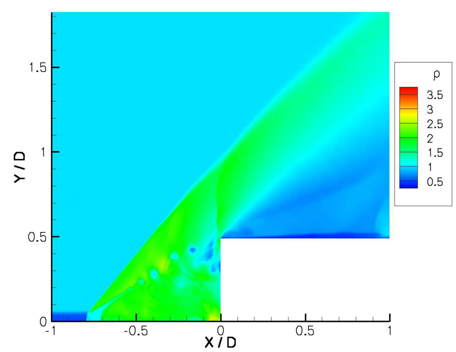

(d) t = 28.29

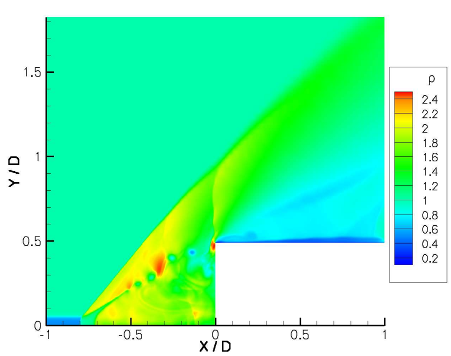

(e) t = 28.35

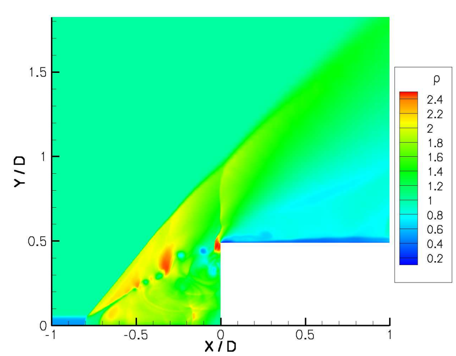

(f) t = 28.41

Figure 5.43: Infinitely Long Filament Density Contours

5.2.3 L = 4/3 Filament

Statistically Stationary State

The instantaneous and running time average of the dimensionless heat transfer to the front face of the cylinder is analyzed in Figure 5.44, and the root mean square of heat transfer to the front of the cylinder face is plotted in Figure 5.45. The instantaneous heat transfer to the face demonstrates periodic behavior. The energy deposition interacts with the bow shock for a duration of 1 dimensionless time units every 4/3 dimensionless time units. Thus, there is an inherent periodicity to the flow. The time average of the heat transfer rate, however, shows a peak upon the initial interaction, but decays to a steady value by 40 dimensionless time units. The root mean square of the heat transfer rate to the front face of the flow has also reached a steady periodicity by 40 dimensionless time units.

The instantaneous and time averaged dimensionless centerline pressure is graphed in Figure 5.46 and the root mean square of the dimensionless centerline pressure is graphed in Figure 5.47. The pressure is nondimensionalized by $\rho_\infty U_\infty^2$. The instantaneous centerline pressure shows a steady periodicity after 35 dimensionless time units and the mean of the centerline pressure has reached a steady value in 30 dimensionless time units. The root mean square has also reached a steady value with slight perturbations. The perturbations exist as the mean is taken over the total time, and not over one period. The centerline pressure is determined to be at the statistically stationary state.

The power spectrum of the dimensionless heat transfer to the face of the cylinder is shown in Figure 5.48. The highest powers occur at the low frequencies, between zero and one. The dimensionless frequency of pulsations is 3/4, so it is expected that the heat transfer frequencies will be near these low frequencies. Higher frequencies have power five orders of magnitude smaller than the lower frequencies. This is a good indicator that the random oscillations from the initial transient have decayed and the steady state frequencies dominate. Thus the heat transfer to the front face of the cylinder has reached a statistically stationary state by 40 dimensionless time units, when the power spectrum was taken.

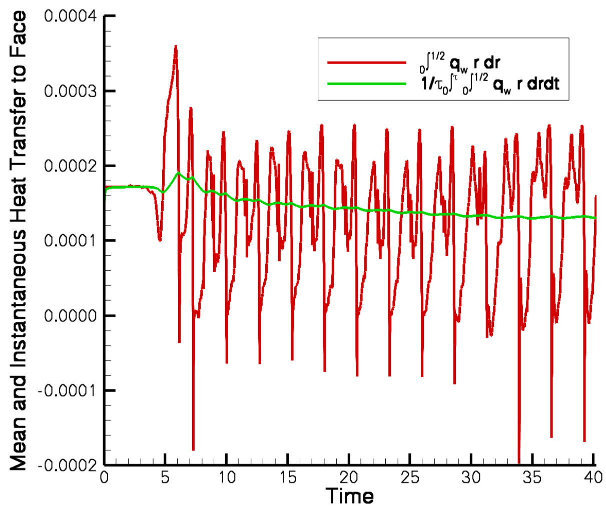

Figure 5.44: $L/D = \frac{4}{3}$ Mean and Instantaneous Heat Transfer to Front of Body

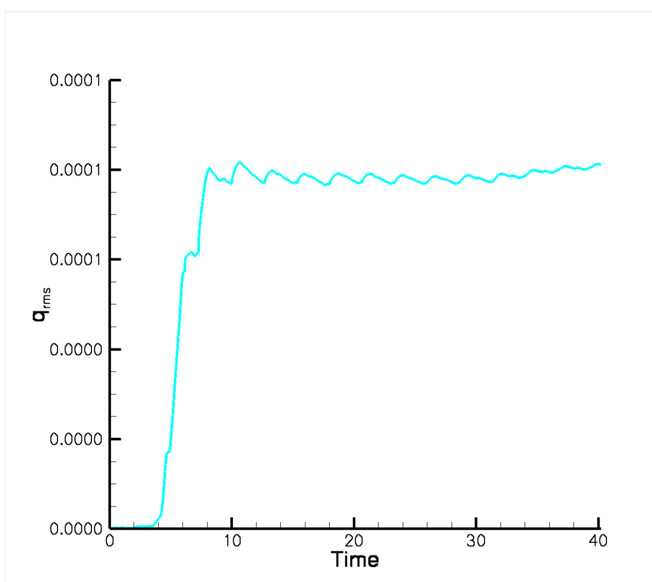

Figure 5.45: $L/D = \frac{4}{3}$ Root Mean Square of Heat Transfer to Front of Body

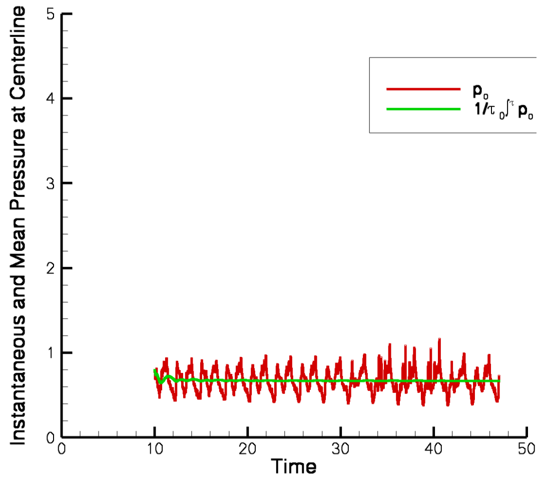

Figure 5.46: $L/D = \frac{4}{3}$ Filament Mean and Instantaneous Stagnation Pressure

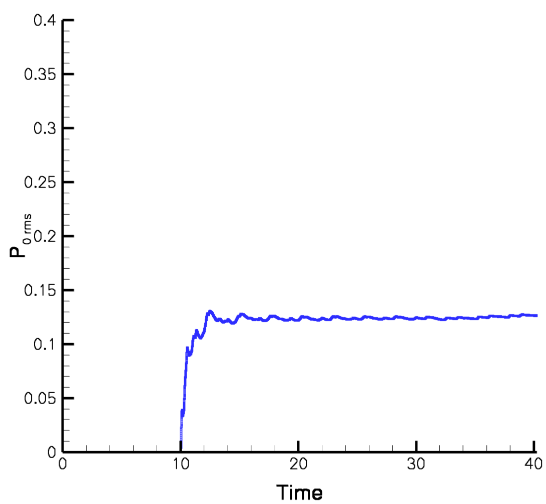

Figure 5.47: $L/D = \frac{4}{3}$ Filament Root Mean Square of Stagnation Pressure

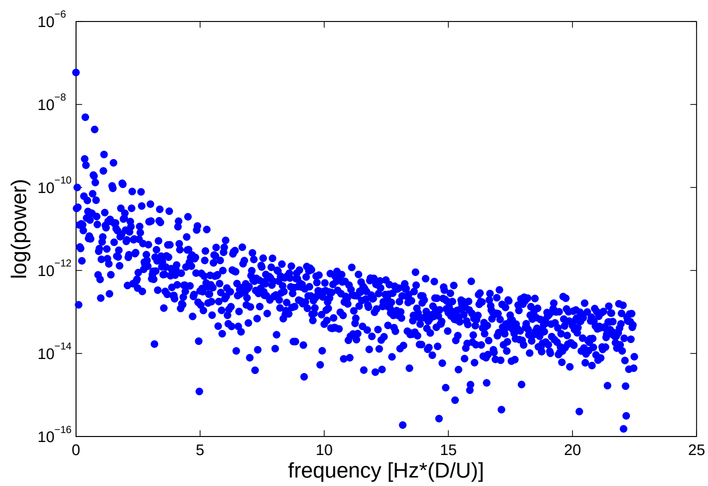

Figure 5.48: $L/D = \frac{4}{3}$ Filament Power Spectrum of Dimensionless q

Efficiency, Effectiveness and Heat Transfer

The pulsed case with a filament period of 4/3 is shown to reduce drag on the cylinder face. The efficiency and effectiveness are 104 and 0.29, as seen in Figures 5.49 and 5.50, respectively. The heat transfer ratio Φ to the front of the cylinder face is 0.71 at the statistically stationary state, as seen in Figure 5.51. The mean heat transfer to the face of the cylinder is reduced with the pulsed energy deposition. The reduction is due to the creation and convection of vortex structures in the shock layer. This phenomenon is explored in detail in this section.

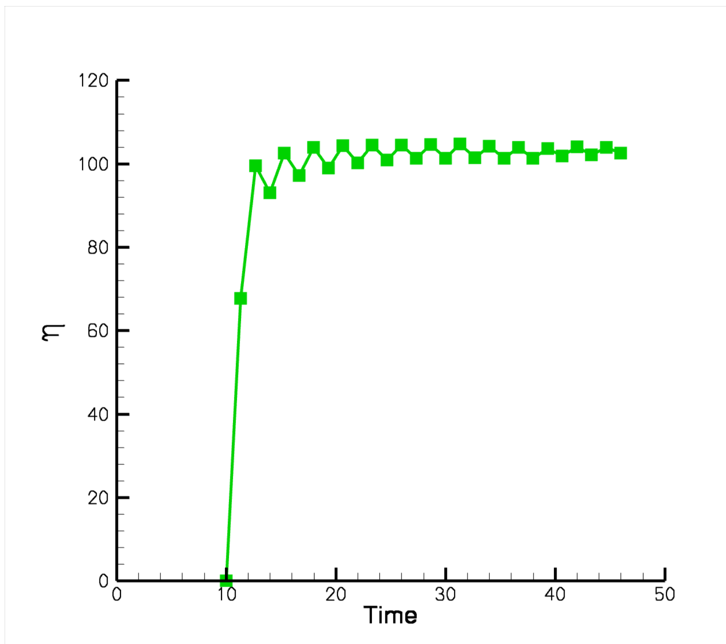

Figure 5.49: $L/D = \frac{4}{3}$ Filament Efficiency Parameter

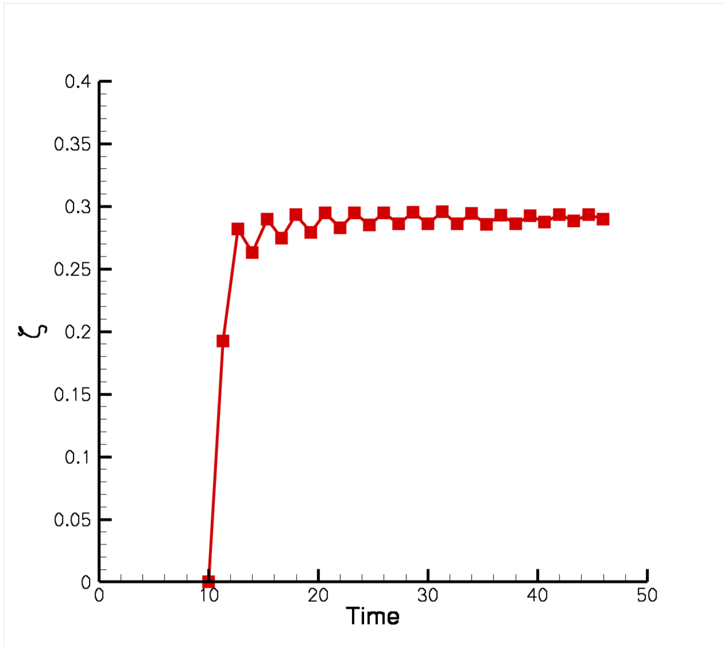

Figure 5.50: $L/D = \frac{4}{3}$ Filament Effectiveness Parameter

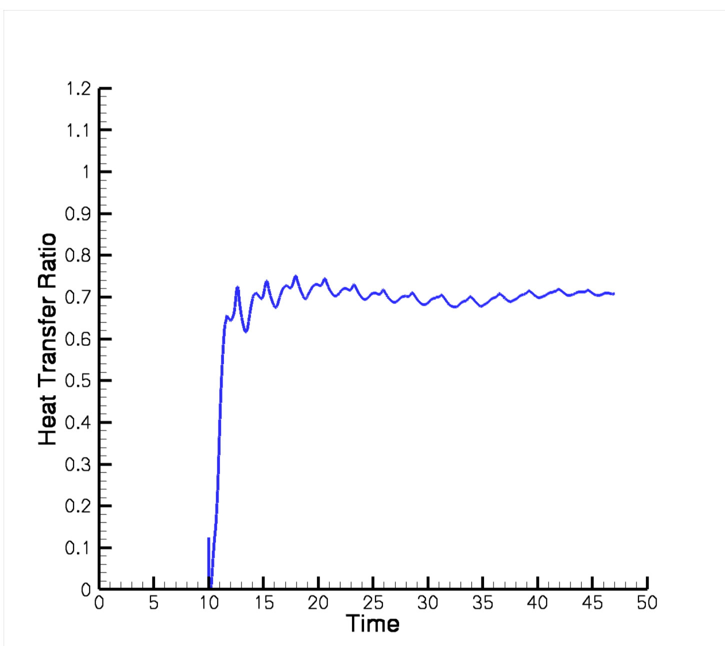

Figure 5.51: $L/D = \frac{4}{3}$ Filament Heat Transfer to Front Face Parameter

Contours of Flow

Flow contours are presented for the pulsed filament case with a pulse period of 4/3. The contours are shown at the statistically stationary state. The images represent fourteen instances of time through one heat transfer cycle. At the statistically stationary state, the heat transfer to the front face is periodic. One heat transfer cycle is taken to be the dimensionless time between peaks in Figure 5.51. The heat transfer cycle is 2.6 dimensionless time units.

The prominent features in the flow structure can be observed in the density gradient and pressure contours, Figures 5.52 through 5.54 and 5.55 through 5.57, respectively. The pressure is nondimensionalized by $\rho_\infty U_\infty^2$, and the density is nondimensionalized by the freestream density. The density gradient contours highlight both shock waves and contact surfaces. The pressure contours distinguish the two flow features, as shock waves are coincident with large pressure jumps and the contact surfaces have uniform pressure. The major flow features are labeled in Figure 5.52(a). The density gradient at the bottom of Figure 5.52(a) has uniform pressure in the pressure contour, Figure 5.55(a). This density gradient is the contact surface between the heated filament and the freestream flow. The bow shock formed by the cylinder body is shown in Figure 5.52(a). The bow shock is confirmed as a shock wave, as it occurs at the same location as a pressure jump in the corresponding pressure graph, Figure 5.55(a). At the intersection of the bow shock and the heated filament, the bow shock lenses upstream. The heated filament is at a lower Mach number than the freestream flow. At lower Mach numbers, bow shocks have larger stand off distances from blunt bodies. Thus, the heated filament induces an upstream lensing of the shock wave. Two contact surfaces emerge at the top and bottom of the filament within the shock layer. The contact surfaces are confirmed by the uniform pressure in Figure 5.55(a). As the heated filament interacts with the shock wave, the lower Mach number flow in the filament becomes a lower velocity flow within the shock layer, as confirmed by the Rankine Hugoniot conditions. Therefore, the contact surfaces between the heated flow and the unheated flow behind the bow shock is a shear layer. The shear layer is unstable and forms clockwise rotating vortices shortly downstream from the bow shock. Two other vortices created by previous heated filaments are seen downstream within the shock layer. As the vortices were generated by the shear layer, they will be referred to as shear layer vortices. As the flow expands around the corner of the cylinder body, it speeds up, creating an expansion fan just above the cylinder corner. The flow must turn to become parallel to the cylinder behind the expansion fan. A recompression shock facilitates the turning of the flow.

The smaller flow features through the heat transfer cycle can be seen in the numerical Schlieren images. The Schlieren images are shown in Figures 5.58 through 5.60. The progression of the filament at the bottom of Figure 5.58(a) is followed through a heat transfer cycle to see how the weaker flow features develop.

Figure 5.58(a) The heated filament lenses the bow shock forward at their intersection. In the shock layer, the filament creates two contact surfaces, each representing a shear layer. The shear layers have initiated a counterclockwise rotating vortex downstream of the shock.

Figure 5.58(b) The lensing at the bow shock and heated filament interaction remains present. The vortex created by the incoming filament has moved toward the cylinder coner.

Figure 5.58(c) The heated filament has moved entirely inside the shock layer. The contact surfaces behind the vortex have become parallel to the bow shock center. The bow shock lensing has subsided. Weak shock waves at the top of the vortex have begun to form. The weak shocks at the top of the vortex are formed because the flow over the top of this vortex is forced to turn upward as it approaches the downstream vortex. Both vortices are counterclockwise so the flow coming off the front of the upstream vortex is moving in the opposite direction as the flow coming from the bottom of the downstream vortex. The opposing flows abruptly change direction, and thus shock waves are formed. Figure 5.61 shows the streamlines at the top of the vortex that has just entered the shock layer. The streamlines wind around downstream over the top of the vortex. As they approach the downstream vortex, they encounter flow moving upward. The weak shock waves facilitate the turning of the flow from downstream, nearly parallel to the symmetry boundary, to upward, nearly parallel to the cylinder face. The flow at the bottom of the vortex is parallel to the symmetry boundary. The vortex, however, is pulling the flow upward around the upstream side of the vortex. Again, the flow makes a 90° turn to move around the upstream side of the cylinder. The weak shock waves at the bottom of the vortex facilitate this turn.

Figure 5.58(d) The vortex has progressed further toward the cylinder corner. The contact surfaces at the back of the vortex remain parallel to the front of the bow shock. The vortex and contact surface is a disk with a circular vortex ring around its outer edge.

The weak shocks at the top and bottom of the vortex structure have become more pronounced. Also, the shape of the bow shock has rounded near the vortex. This is because the flow between the bow shock and the vortex is subsonic. As the vortex induces a circular flow around itself, the bow shock adjusts to turn the upstream flow accordingly. The bow shock exhibits a change in curvature just upstream of the weak shock at the top of the vortex.

Figure 5.58(e) The contact surface behind the vortex remains intact with the symmetry boundary at the bottom of the computational domain. The weak shock at the top of the vortex now extends all the way to the bow shock. A lambda shock has emerged at point where the bow shock changes in radius of curvature. The weak shock at the top of the vortex has stretched between the vortex and the downstream vortex, which can be seen in the corresponding pressure contour, Figure 5.55(e).

Figure 5.58(f) The vortex has convected to 0.2 cylinder diameters above the line of symmetry. The contact surface has become weaker near the vortex, though remains attached to the line of symmetry. The weak shock at the bottom of the vortex is more pronounced. The shock at the top of the vortex has arched upstream toward the lambda shock.

Figure 5.59(a) The vortex forming at the bow shock has begun to entrain the contact discontinuity from the downstream vortex.

Figure 5.59(b) The contact discontinuity has become fully enveloped into the vortex forming upstream. The three-dimensional disk has been broken, leaving the vortex ring, and trailing contact surface which connects to the upstream vortex. The vortex has convected to 0.25 diameters above the line of symmetry. The lambda shock and the shock turning the flow at the top of the vortex have merged, creating one stronger shock. The weak shock at the shock at the bottom of the vortex has increased in strength, as the vortex upstream vortex has influenced the flowfield.

Figure 5.59(c) The vortex has progressed toward the corner of the cylinder. The weak shocks at the top and bottom of the vortex have followed the movement of the vortex.

Figure 5.59(d) - Figure 5.60(b) The vortex has reached the cylinder face by the final frame. One heat transfer cycle is the time it takes for partial forming and convection of a vortex from the bow shock to the cylinder face.

The dimensionless velocity magnitude contours are shown in Figures 5.62 through 5.64. The velocities are nondimensionalized by the freestream velocity, U_∞. In Figure 5.62(a), the contact surfaces are at the bottom of the computed domain, just inside the bow shock. The contact surfaces show sharp velocity gradients. The flow above the top contact surface has a greater velocity than the flow bounded by the contact surfaces. The flow at the bottom of the contact surface has a lower velocity than the flow bounded by the contact surfaces. This velocity gradient creates a clockwise rotating vortex. As the vortex grows and convects toward the cylinder corner in Figures 5.62(b) through 5.62(f), a very low velocity exists at the core of the vortex. The flow on the top of the vortex, however is at a very high velocity. As the flow encounters the weak shock at the top of the vortex, however, the flow is quickly decelerated. The flow accelerates around the downstream side fo the vortex and slows down dramatically at the weak shock at the bottom of the vortex. The flow below the line of shear layer vortices is much slower than the fluid above the vortex line. The low velocity flow at the bottom of the shear layer vortices will be referred to as the stagnation region. The path through which the vortex travels from the bow shock at the bottom of the domain to the cylinder corner will be referred to as the vortex layer.

The vortex structure established by the heated filament and bow shock interaction reduces heat transfer to the cylinder face. The contours of vorticity, streamlines and temperature illustrate this point. These are shown in Figures 5.65 through 5.67, Figures 5.68 through 5.70 and 5.71 through 5.73, respectively. One cycle of heat transfer to the cylinder face is shown in Figure 5.74. Six points of significance to the heat transfer cycle have been labeled in Figure 5.74. The contour plots begin at point 1, the minimum of the heat transfer cycle. These six points are discussed to understand the flow features that contribute to the heat transfer cycle. Three vortices are labeled in Figure 5.65.

Point 1 Point 1 is the minimum for the entire heat transfer cycle. Figure 5.65(a) shows that vortex 0 sits just above the cylinder corner. Vortex 1 is midway between the bow shock and the cylinder face. Vortex 2 is forming as the heated filament enters the shock layer. The streamline plot, Figure 5.68(a), shows that Vortex 1 is sweeping flow from the top of the vortex layer into the stagnation region and up the cylinder face. The corresponding temperature contour, Figure 5.71(a), illustrates that the flow above the vortex layer is much cooler than the flow within the stagnation region. Thus, vortex 1 is sweeping cooler, faster flow from the top of the vortex layer into the stagnation layer and over the face of the cylinder. This increases both advection and conduction of heat from the cylinder face.

Point 2 The heat transfer to the cylinder face begins to increase dramatically at point 2. From the vorticity contour, Figure 5.65(e), it can be seen that vortex 1 has approached the cylinder face. The streamlines, Figures 5.68(b) through 5.68(d), show that the vortex 1 pulls flow from above the vortex layer over the cylinder face. In Figure 5.68(e), however, the flow from the top of the vortex flows over the cylinder corner without sweeping over the cylinder face. At this point, a stagnation region begins to grow at the cylinder face below vortex 1. Thus, advection decreases dramatically from this point on, increasing heat transfer to the cylinder face.

Point 3 Point 3 represents a local peak of heat transfer to the front face of the cylinder. The heat transfer to the front face of the cylinder was previously rising due to the growing stagnation region below vortex 1. At point 3, the expansion fan at the downstream side of the vortex begins to interact with the wall. From Figure 5.66(a), the vortex is just upstream of the cylinder face. The high velocity region downstream of the vortex begins to interact with the cylinder face, as shown in Figure 5.69(a). The expansion fan is a region of decreased temperature, which begins to contact the cylinder face in Figure 5.72(a).

Point 4 Between points 3 and 4, the expansion fan at the downstream side of vortex 1 moves toward the cylinder corner, continually decreasing heat transfer to the cylinder face. At point 4, however, vortex 1 convects over the cylinder corner. The position of the vortex can be tracked toward the cylinder corner in Figures 5.66(b) through 5.66(d) where it finally convects over the corner. The streamlines and velocity magnitude contour plots show evidence of this as well, in Figures 5.69(b) through 5.69(d). Finally, the low temperature region downstream of the vortex is seen to convect over the corner just ahead of vortex 1, in Figures 5.66(b) through 5.66(d). After vortex 1 has moved over the cylinder corner, vortex 2 is the primary means of heat transfer reduction at the cylinder face. As vortex 2 approaches the face, however, it tends to convect heat away from a smaller and smaller portion of the cylinder face and a stagnation region grows at the cylinder face below it. Thus, the heat transfer to the front of the face increases after point 4.

Point 5 Finally, at point 5, the expansion fan at the front of vortex 2 begins to interact with the cylinder face. This is seen in the streamline/velocity magnitude plot in Figure 5.69(e). The increasing heat transfer to the cylinder face ends when the expansion fan intersects the cylinder face. The gradient of dimensionless heat transfer to the cylinder face changes from positive (increasing) to negative (decreasing) at point 5 and thus point 5 is a peak in heat transfer. As the expansion fan moves closer to the cylinder corner, it increases convection, reducing heat transfer to the corner of the cylinder. The cylinder corner exhibits peak heating at the steady state and the expansion fan has the greatest effect of cooling the cylinder from the corner.

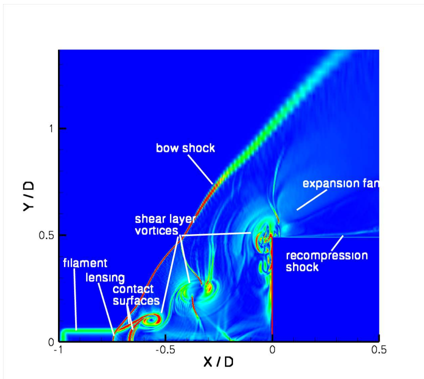

(a) t = 42.0

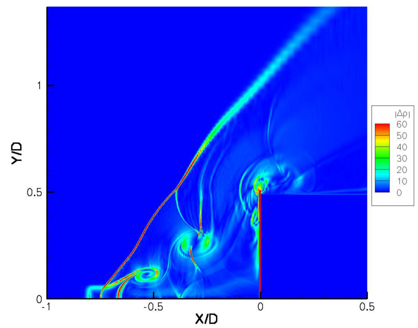

(b) t = 42.2

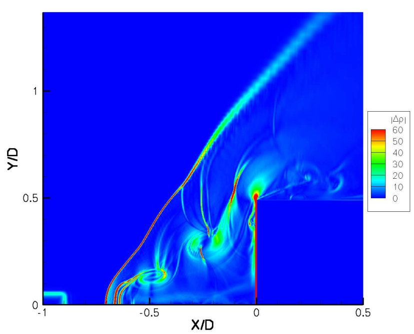

(c) t = 42.4

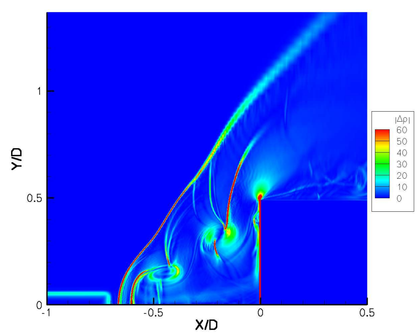

(d) t = 42.6

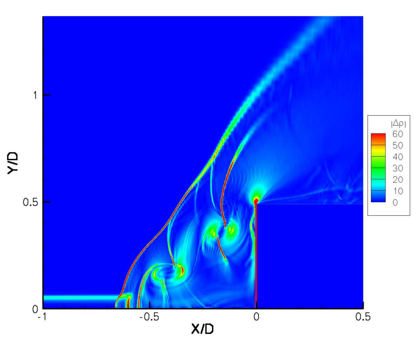

(e) t = 42.8

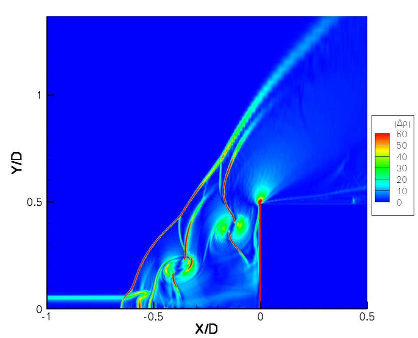

(f) t = 42.9

Figure 5.52: $L/D = \frac{4}{3}$ Filament Density Gradient Contours

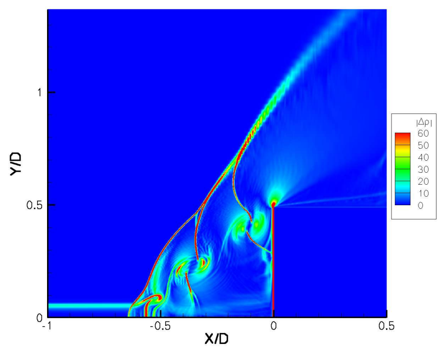

(a) t = 43.2

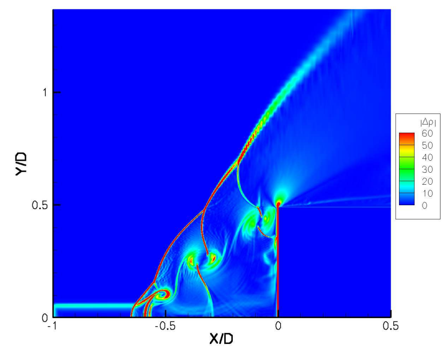

(b) t = 43.4

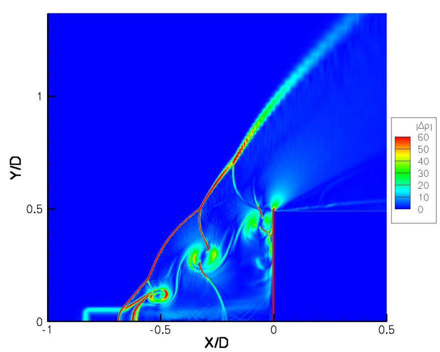

(c) t = 43.5

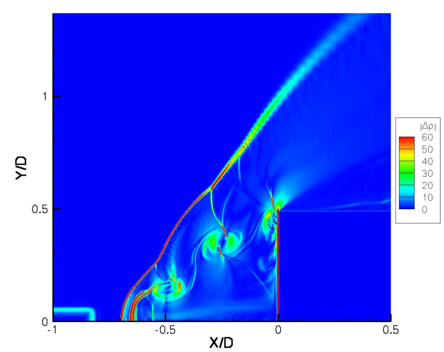

(d) t = 43.8

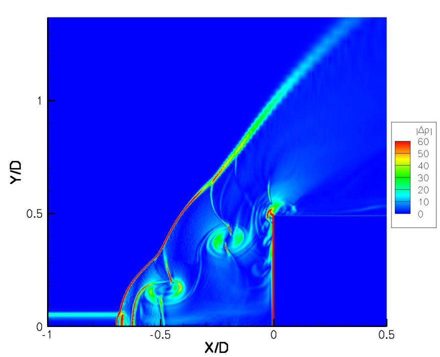

(e) t = 44.0

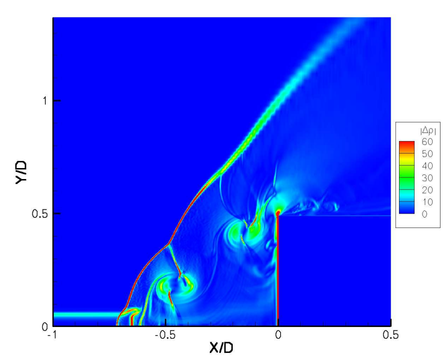

(f) t = 44.2

Figure 5.53: $L/D = \frac{4}{3}$ Filament Density Gradient Contours

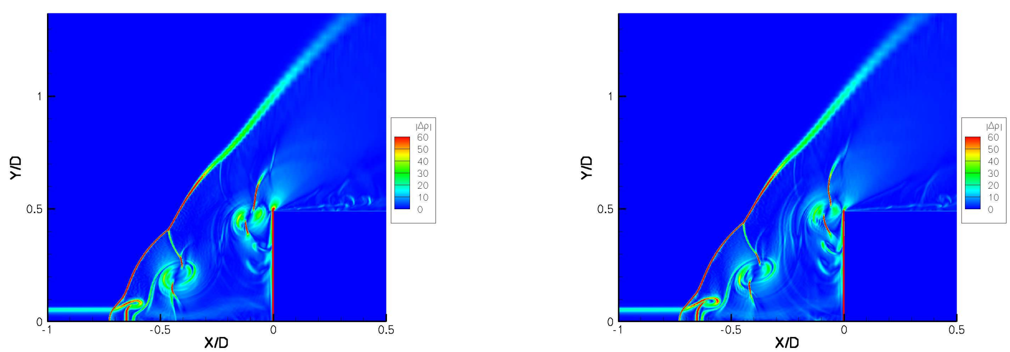

(a) t = 44.4

(b) t = 44.5

Figure 5.54: $L/D = \frac{4}{3}$ Filament Density Gradient Contours

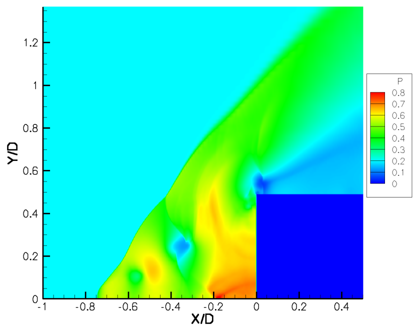

(a) t = 42.0

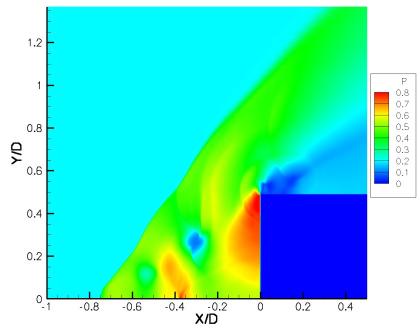

(b) t = 42.2

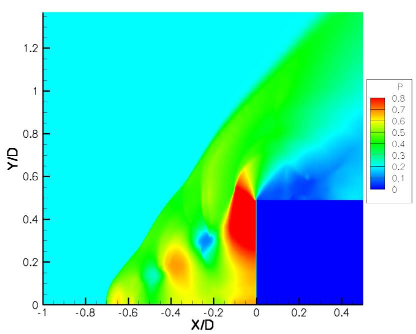

(c) t = 42.4

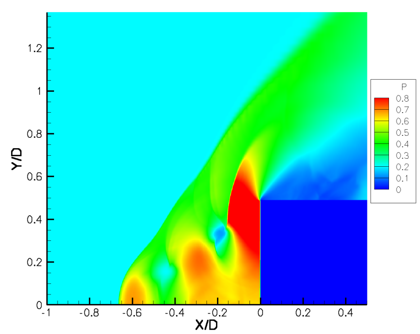

(d) t = 42.6

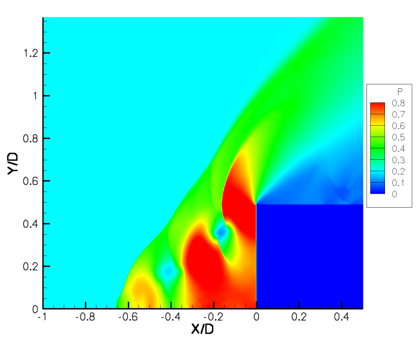

(e) t = 42.8

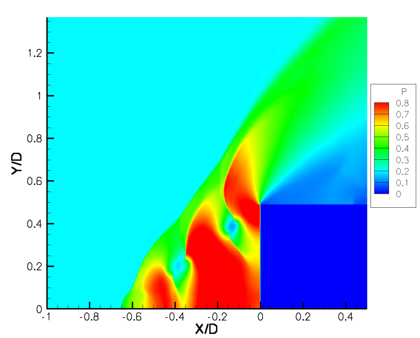

(f) t = 42.9

Figure 5.55: $L/D = \frac{4}{3}$ Pressure Contours

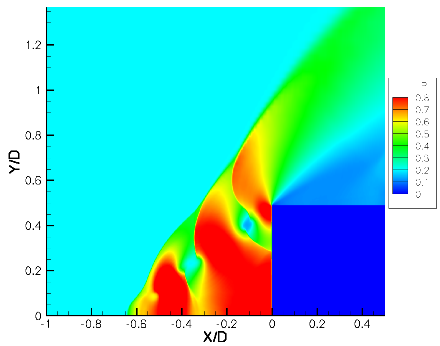

(a) t = 43.2

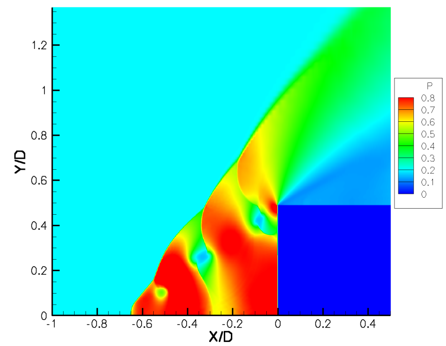

(b) t = 43.4

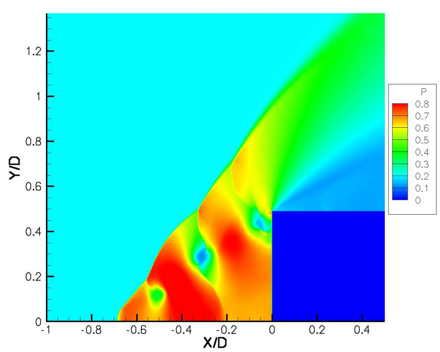

(c) t = 43.5

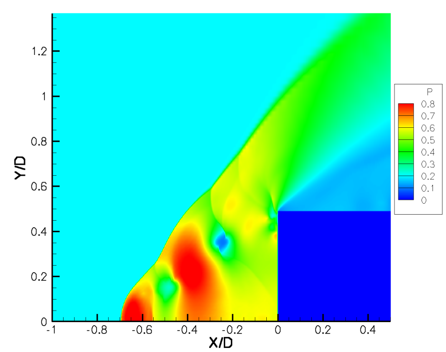

(d) t = 43.8

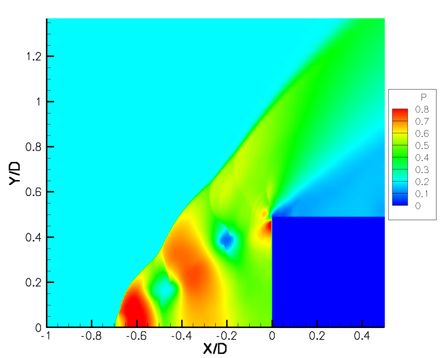

(e) t = 44.0

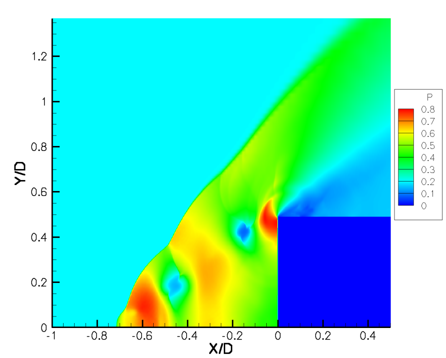

(f) t = 44.2

Figure 5.56: $L/D = \frac{4}{3}$ Pressure Contours

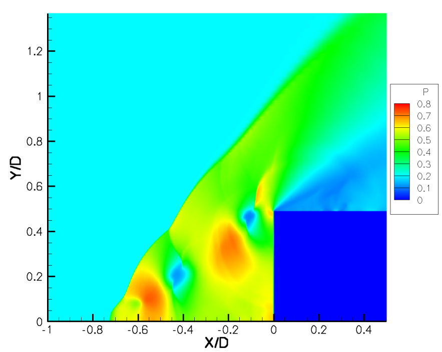

(a) t = 44.4

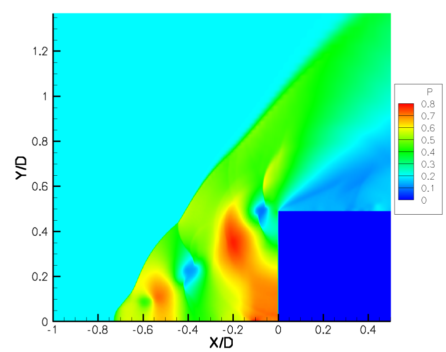

(b) t = 44.5

Figure 5.57: $L/D = \frac{4}{3}$ Pressure Contours

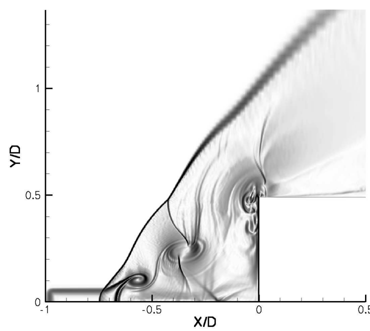

(a) t = 42.0

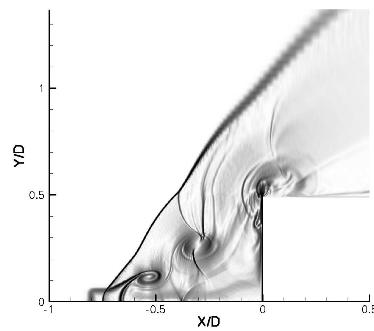

(b) t = 42.2

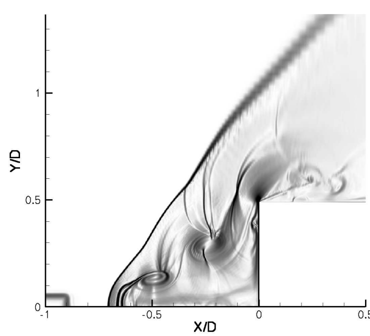

(c) t = 42.4

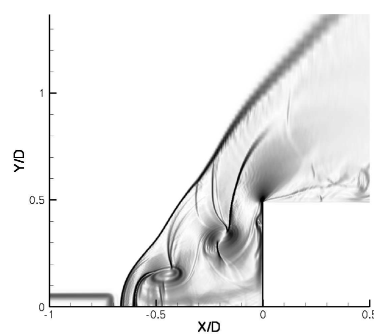

(d) t = 42.6

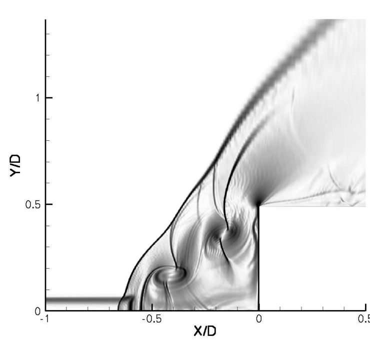

(e) t = 42.8

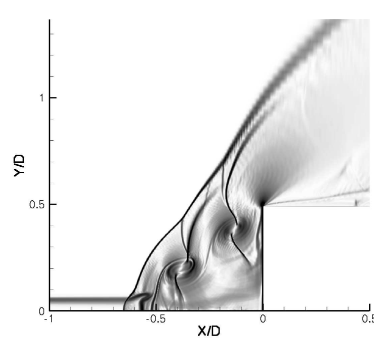

(f) t = 42.9

Figure 5.58: $L/D = \frac{4}{3}$ Numerical Schlieren Images

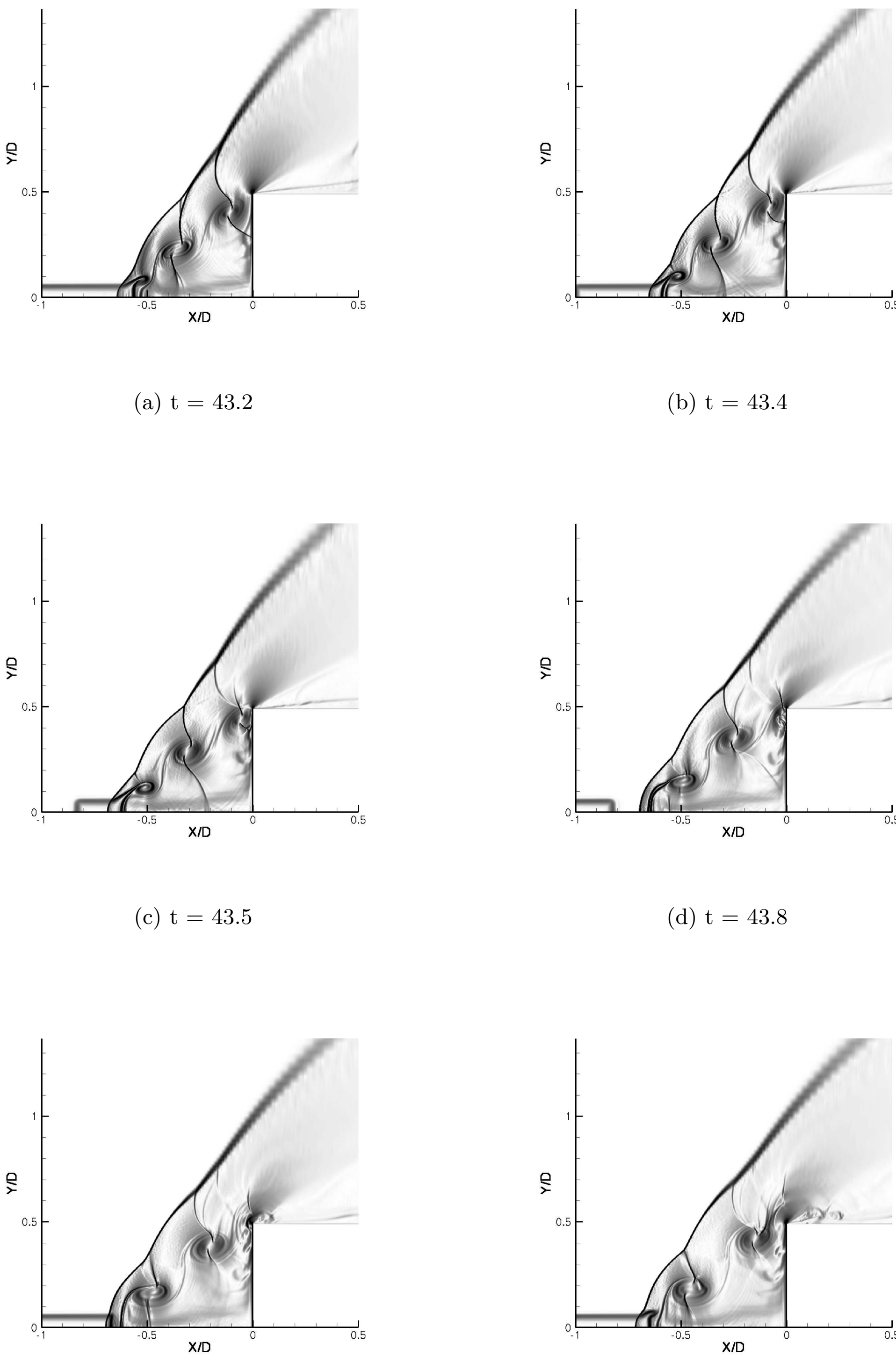

(a) t = 43.2

(b) t = 43.4

(c) t = 43.5

(d) t = 43.8

(e) t = 44.0, point 5

(f) t = 44.2

Figure 5.59: $L/D = \frac{4}{3}$ Numerical Schlieren Images

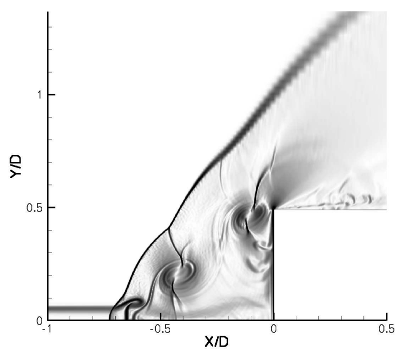

(a) t = 44.4

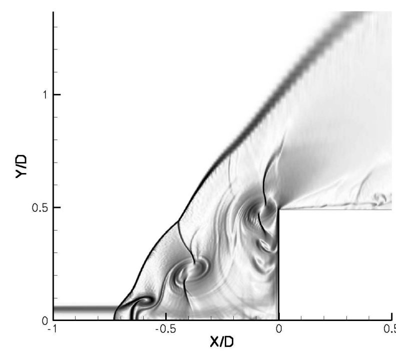

(b) t = 44.5, point 6

Figure 5.60: $L/D = \frac{4}{3}$ Numerical Schlieren Images

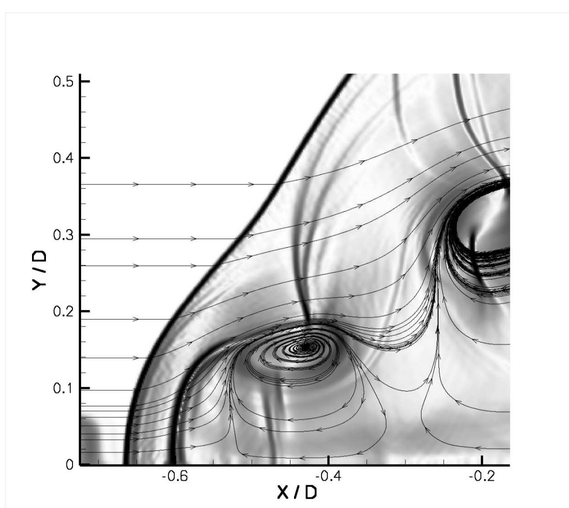

Figure 5.61: Streamlines Between Two Vortices

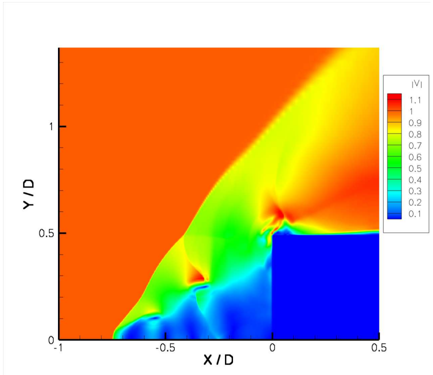

(a) t = 42.0

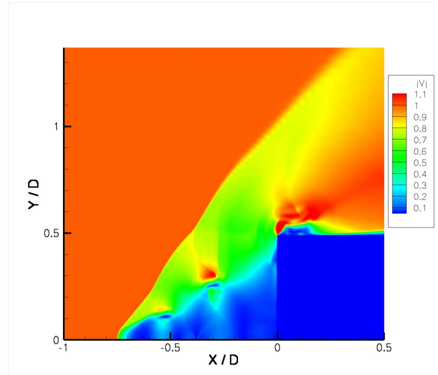

(b) t = 42.2

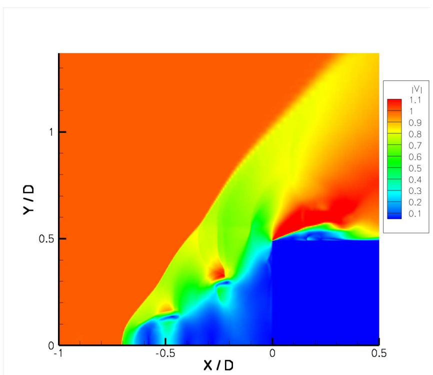

(c) t = 42.4

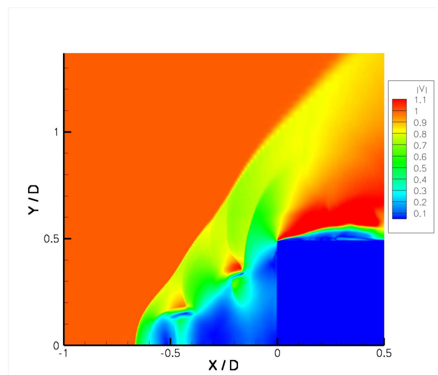

(d) t = 42.6

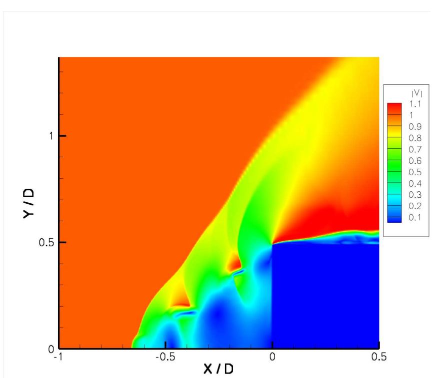

(e) t = 42.8

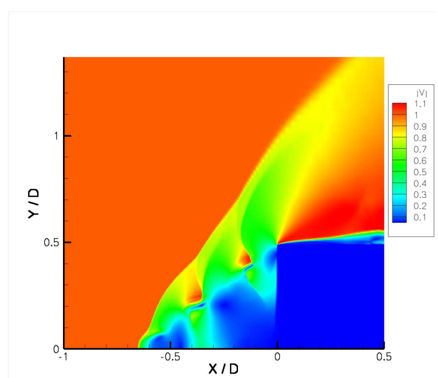

(f) t = 42.9

Figure 5.62: $L/D = \frac{4}{3}$ Velocity Magnitude Contours

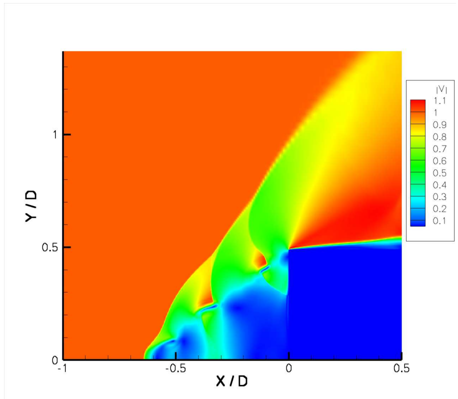

(a) t = 43.2

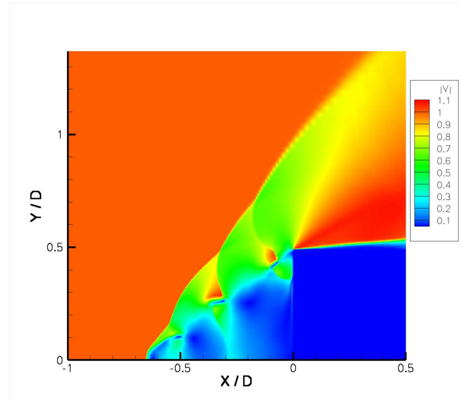

(b) t = 43.4

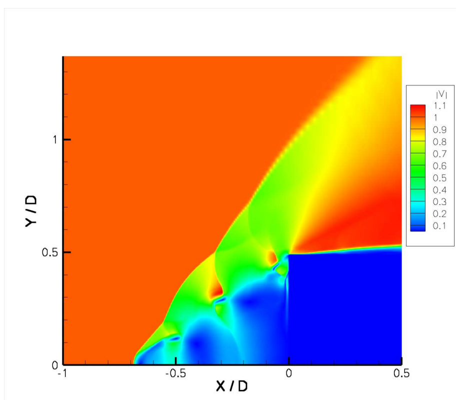

(c) t = 43.5

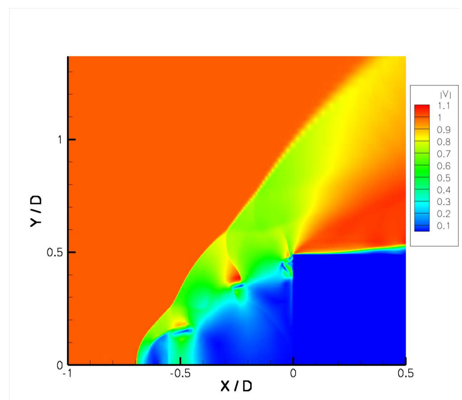

(d) t = 43.8

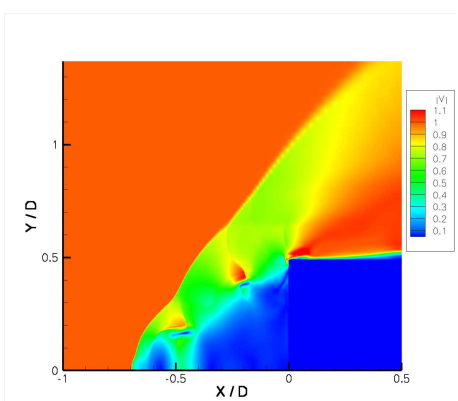

(e) t = 44.0

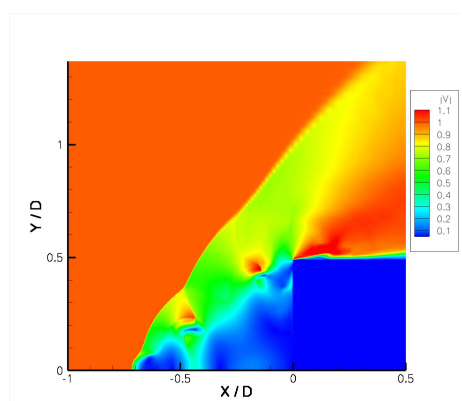

(f) t = 44.2

Figure 5.63: $L/D = \frac{4}{3}$ Velocity Magnitude Contours

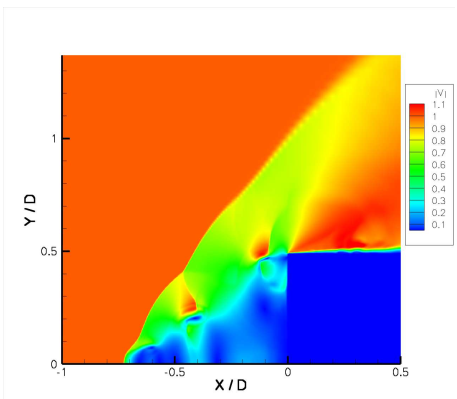

(a) t = 44.4

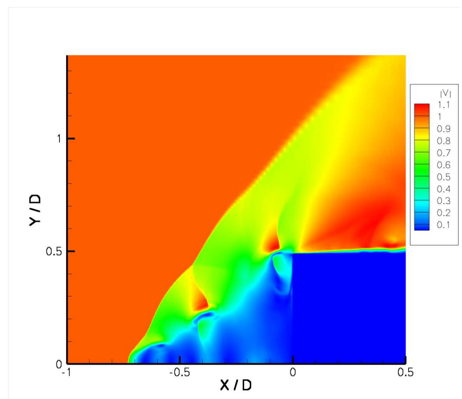

(b) t = 44.5

Figure 5.64: $L/D = \frac{4}{3}$ Velocity Magnitude Contours

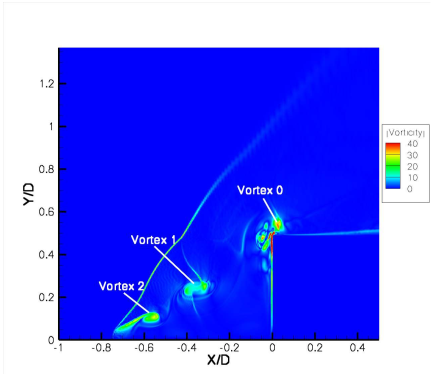

(a) t = 42.0, point 1

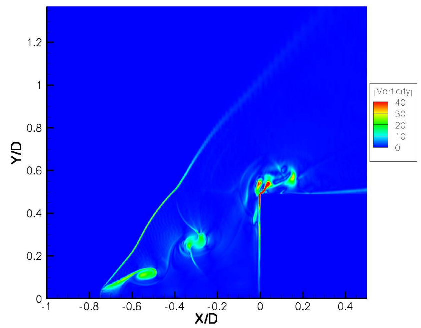

(b) t = 42.2

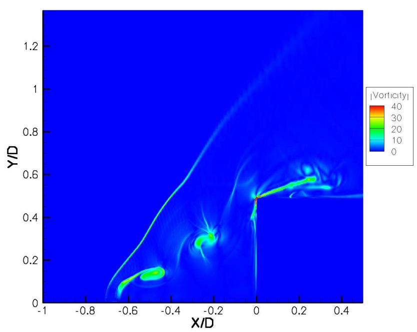

(c) t = 42.4

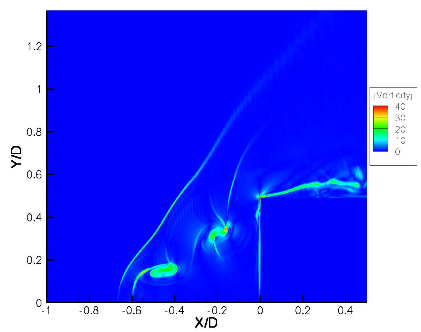

(d) t = 42.6, point 2

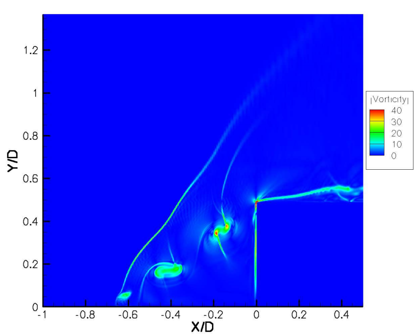

(e) t = 42.8, point 2

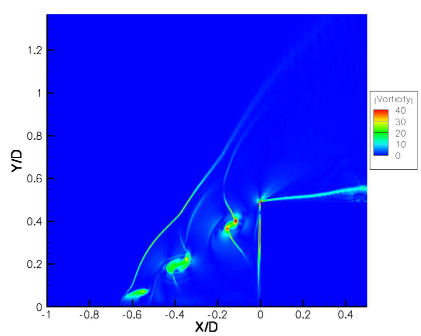

(f) t = 42.9

Figure 5.65: $L/D = \frac{4}{3}$ Vorticity Magnitude Contours

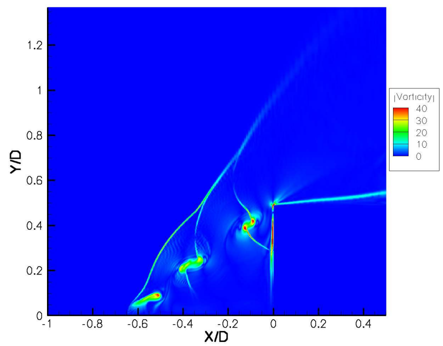

(a) t = 43.2

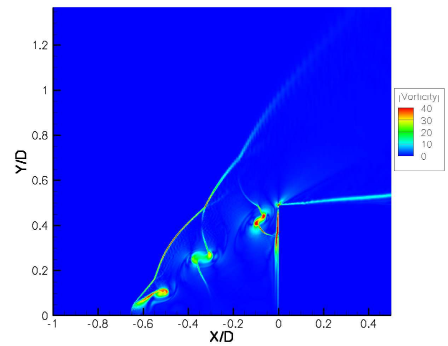

(b) t = 43.4, point 3

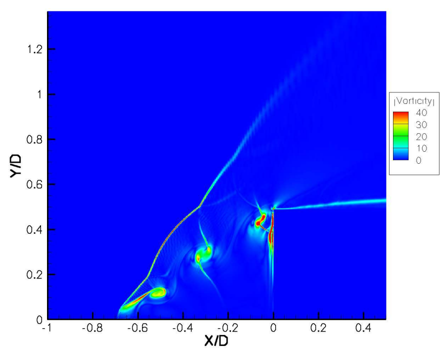

(c) t = 43.5

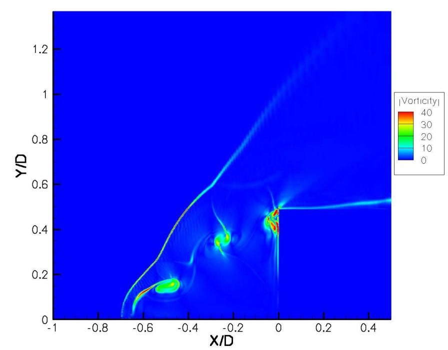

(d) t = 43.8

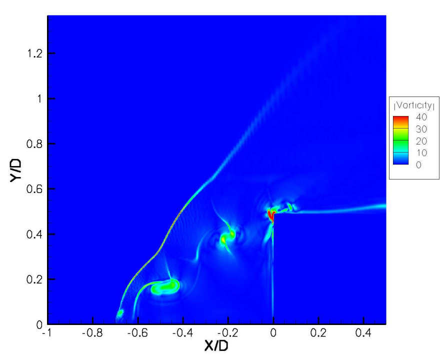

(e) t = 44.0, point 4

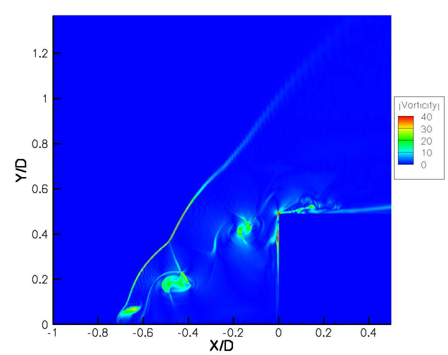

(f) t = 44.2

Figure 5.66: $L/D = \frac{4}{3}$ Vorticity Magnitude Contours

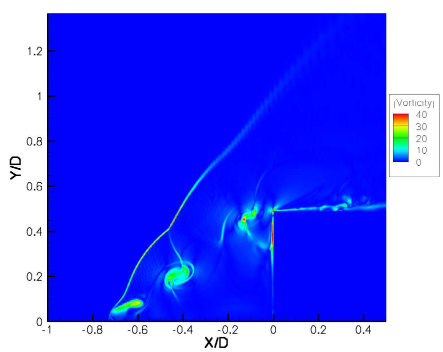

(a) t = 44.4, point 5

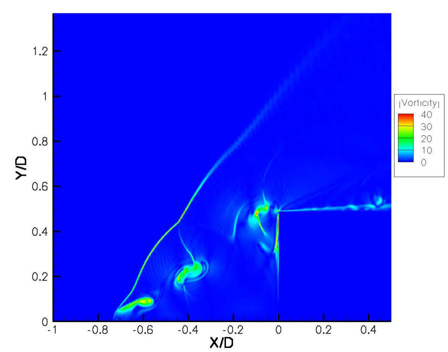

(b) t = 44.5

Figure 5.67: $L/D = \frac{4}{3}$ Vorticity Magnitude Contours

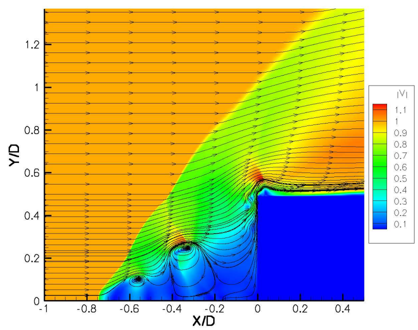

(a) t = 42.0, point 1

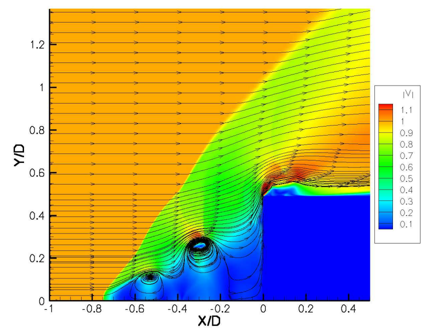

(b) t = 42.2

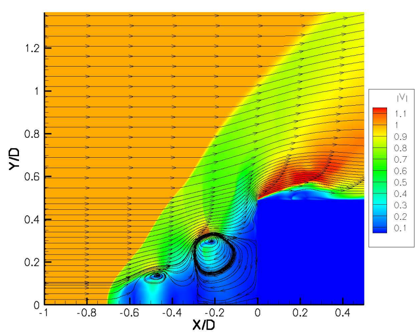

(c) t = 42.4

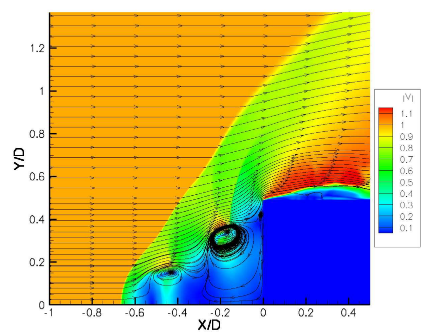

(d) t = 42.6, point 2

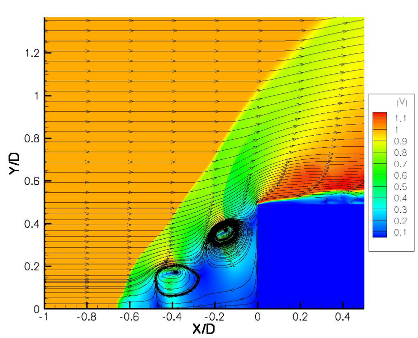

(e) t = 42.8

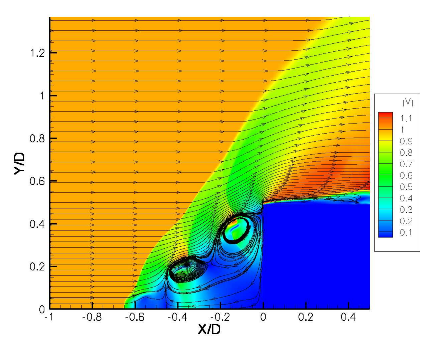

(f) t = 42.9

Figure 5.68: $L/D = \frac{4}{3}$ Streamlines of Flow

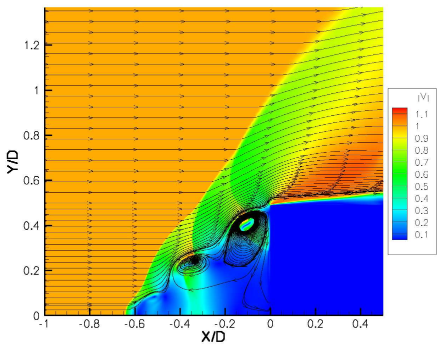

(a) t = 43.2

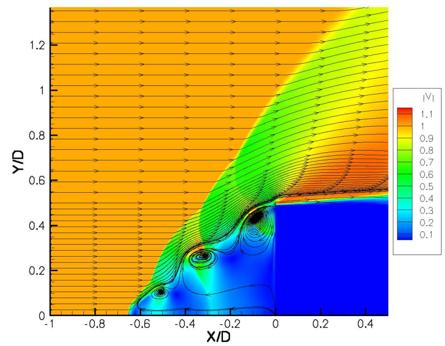

(b) t = 43.4, point 3

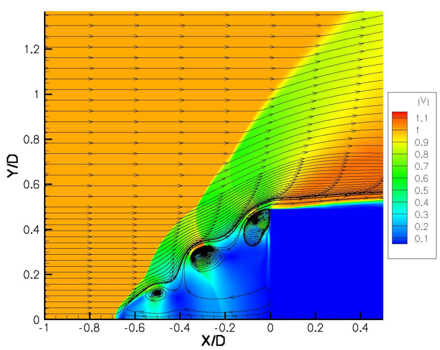

(c) t = 43.5

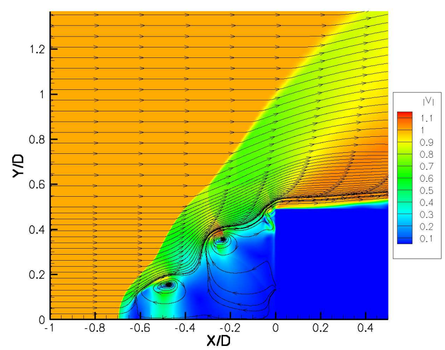

(d) t = 43.8

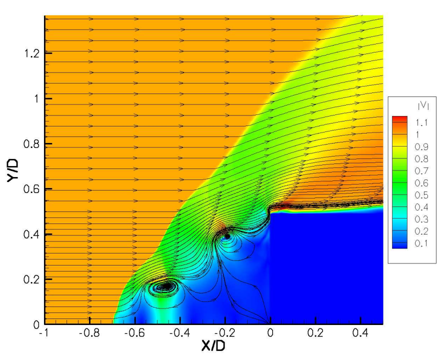

(e) t = 44.0, point 4

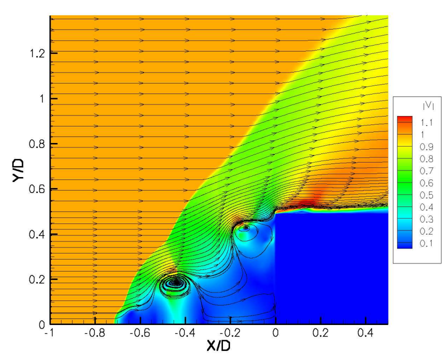

(f) t = 44.2

Figure 5.69: $L/D = \frac{4}{3}$ Streamlines of Flow

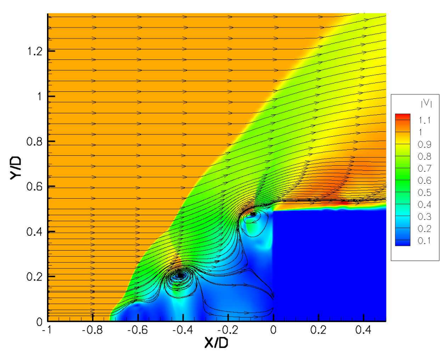

(a) t = 44.4, point 5

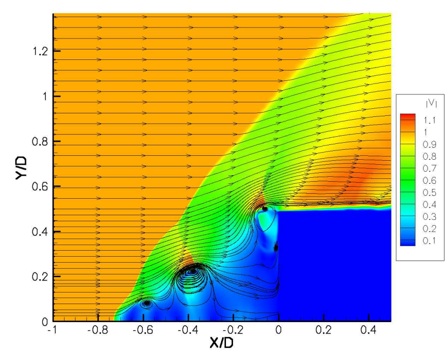

(b) t = 44.5

Figure 5.70: $L/D = \frac{4}{3}$ Streamlines of Flow

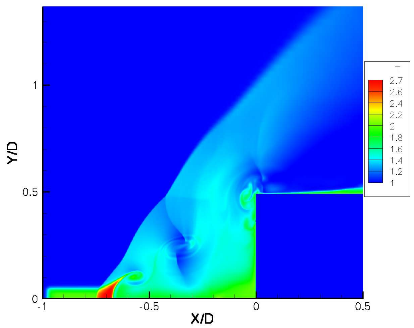

(a) t = 42.0, point 1

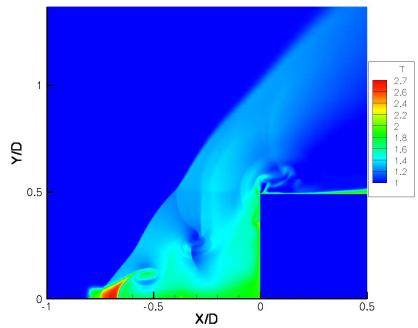

(b) t = 42.2

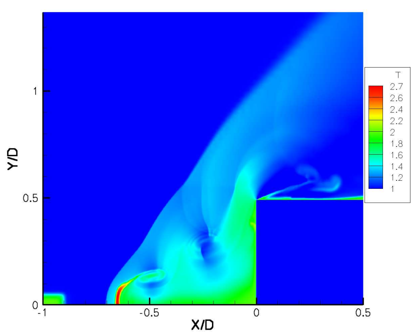

(c) t = 42.4

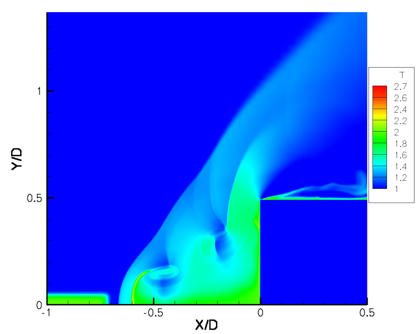

(d) t = 42.6, point 2

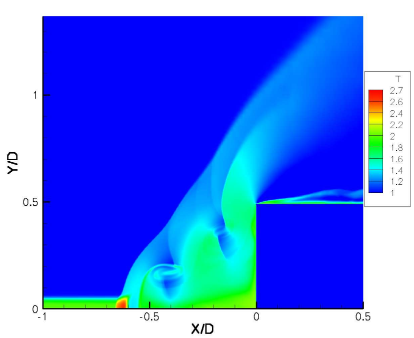

(e) t = 42.8

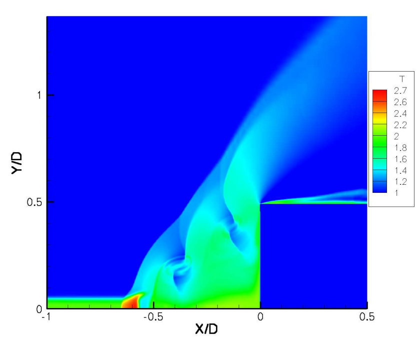

(f) t = 42.9

Figure 5.71: $L/D = \frac{4}{3}$ Filament Temperature Contours

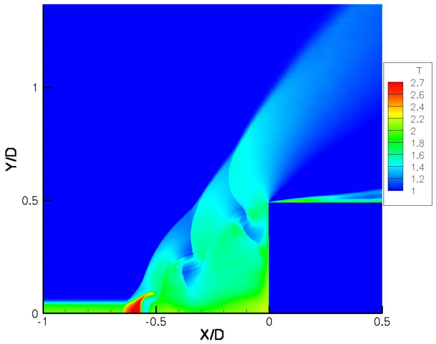

(a) t = 43.2

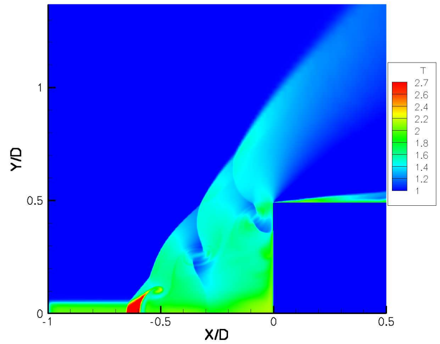

(b) t = 43.4, point 3

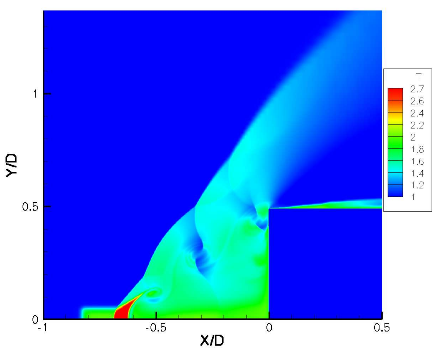

(c) t = 43.5

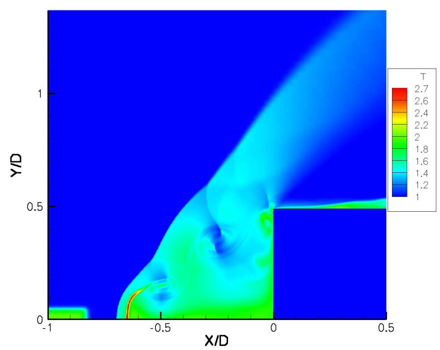

(d) t = 43.8

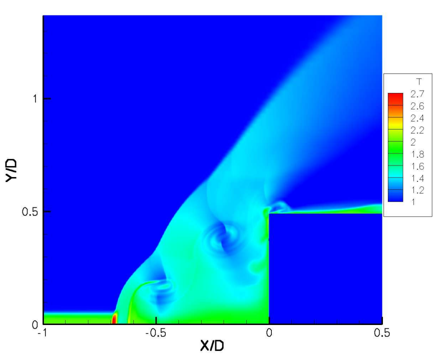

(e) t = 44.0, point 4

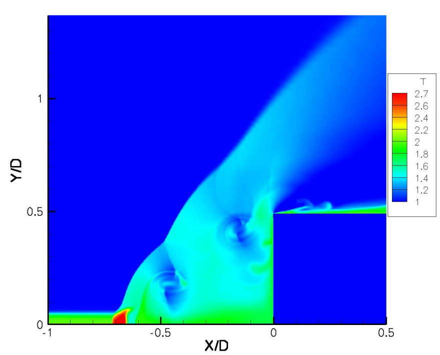

(f) t = 44.2

Figure 5.72: $L/D = \frac{4}{3}$ Filament Temperature Contours

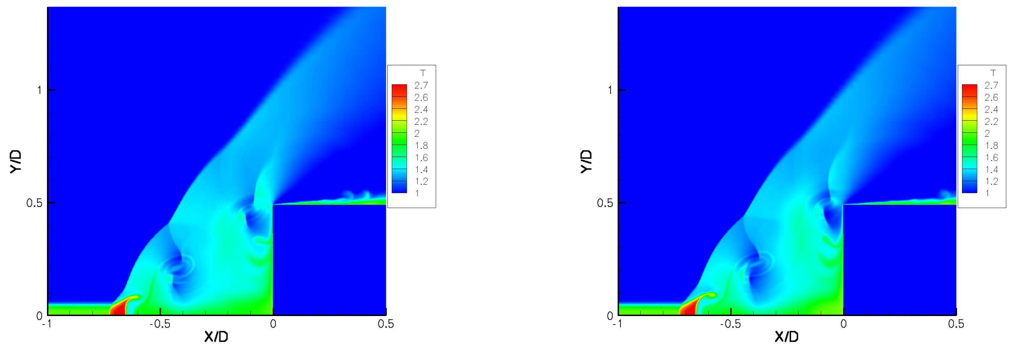

(a) t = 44.4, point 5

(b) t = 44.5

Figure 5.73: $L/D = \frac{4}{3}$ Filament Temperature Contours

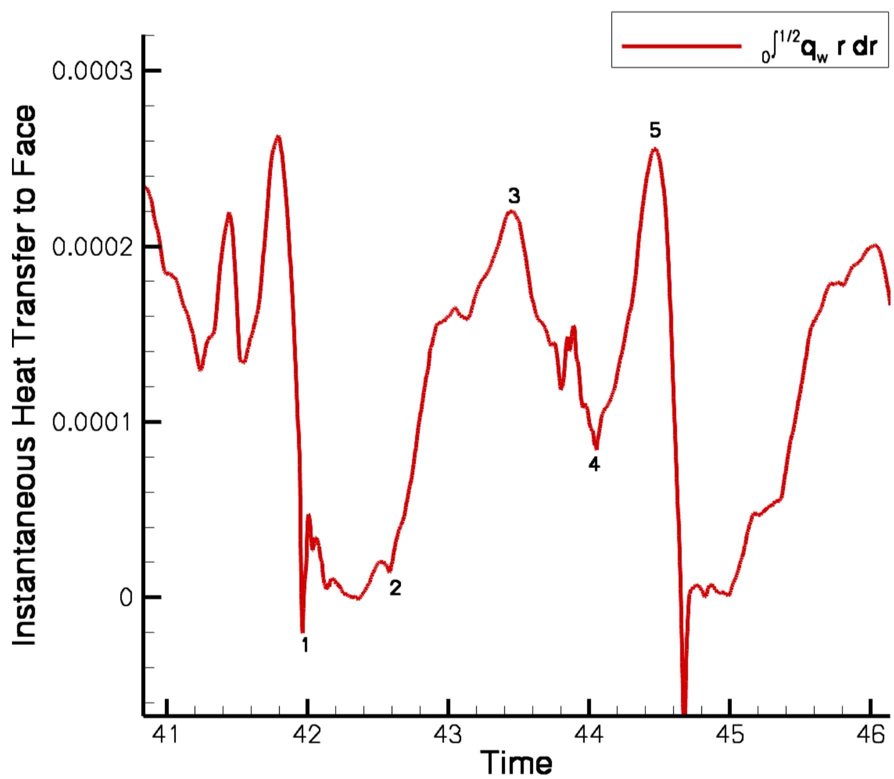

Figure 5.74: $L/D = \frac{4}{3}$ Heat Transfer Over One Period

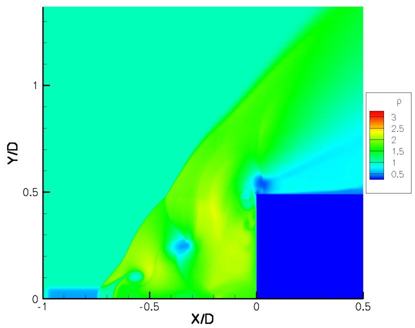

(a) t = 42.0, point 1

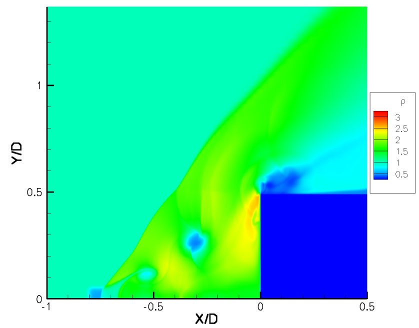

(b) t = 42.2

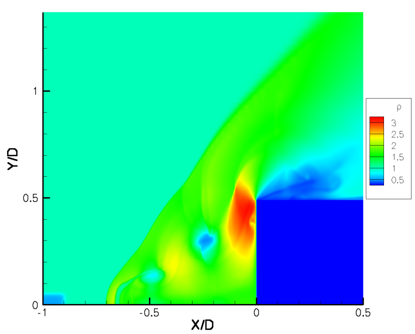

(c) t = 42.4

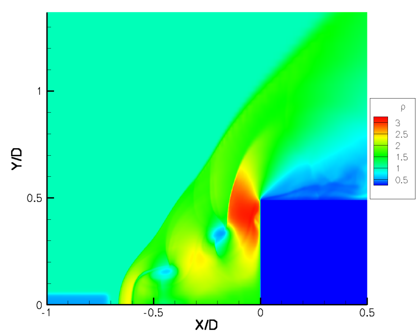

(d) t = 42.6

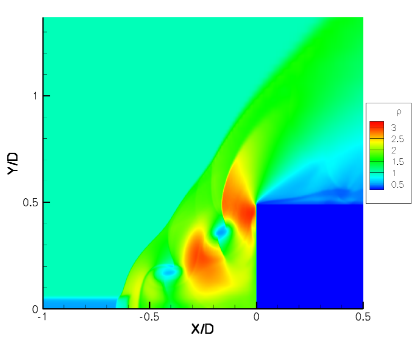

(e) t = 42.8, point 2

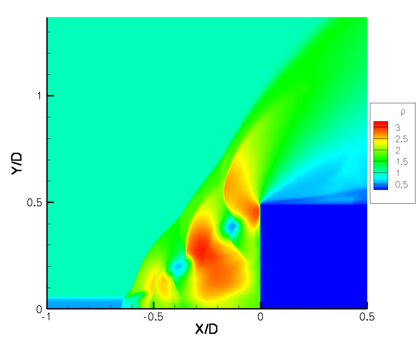

(f) t = 42.9, point 3

Figure 5.75: $L/D = \frac{4}{3}$ Filament Density Contours

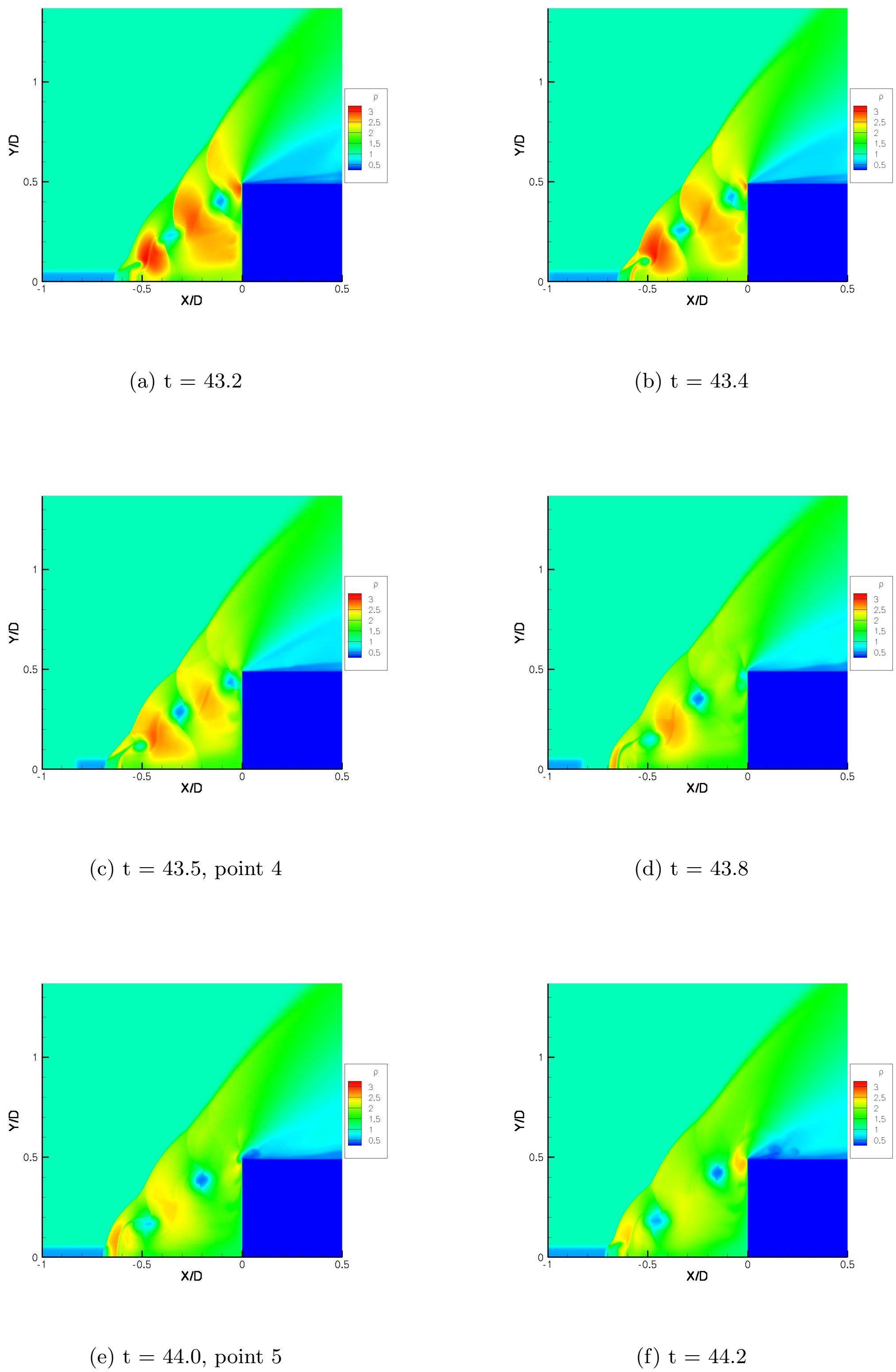

(a) t = 43.2

(b) t = 43.4

(c) t = 43.5, point 4

(d) t = 43.8

(e) t = 44.0, point 5

(f) t = 44.2

Figure 5.76: $L/D = \frac{4}{3}$ Filament Density Contours

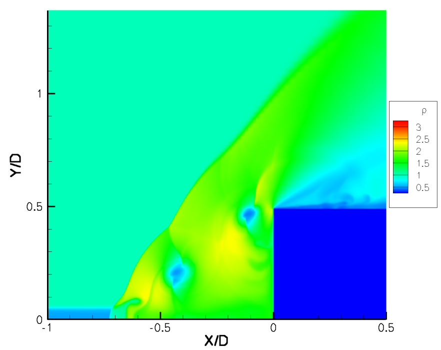

(a) t = 44.4

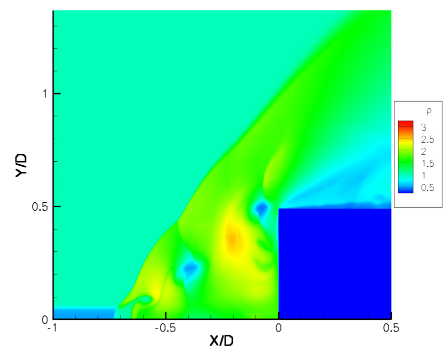

(b) t = 44.5, point 6

Figure 5.77: $L/D = \frac{4}{3}$ Filament Density Contours

5.2.4 L/D = 2 Filament

Statistically Stationary State

The heat transfer to the front face of the cylinder is plotted in Figures 5.78 and 5.79. Figure 5.78 shows the mean and instantaneous heat transfer to the front face of the cylinder. The instantaneous heat transfer to the front face of the cylinder are periodic after 30 dimensionless time units. The root mean square of the heat transfer to the front face of the cylinder, graphed in Figure 5.79, is periodic after 35 dimensionless time units. These two parameters are good evidence that the case has reached a statistically stationary state by $t = 35$.

The instantanous, mean and root mean square of dimensionless centerline pressure are graphed in Figures 5.80 and 5.81. The instantaneous pressure is oscillatory. The mean of the centerline pressure in time has reached a steady state value, with minor oscillations about a stable mean, in 40 dimensionless time units. The root mean square of the dimensionless centerline pressure also reaches a statistically stationary point by 45 dimensionless time units. The statistically stationary state for the dimensionless centerline pressure has been reached in 45 dimensionless time units.

The power spectrum of the dimensionless heat transfer is shown in Figure 5.82. Two peak frequencies are seen. The highest frequency occurs at zero because the power spectrum was performed on the dimensionless heat transfer variable and not of the perturbation. The mean frequency is represented at the zero frequency. The other peak frequncy occurs at 0.25, which is the vortex shedding frequency behind the shock layer. This number is confirmed later in this section.

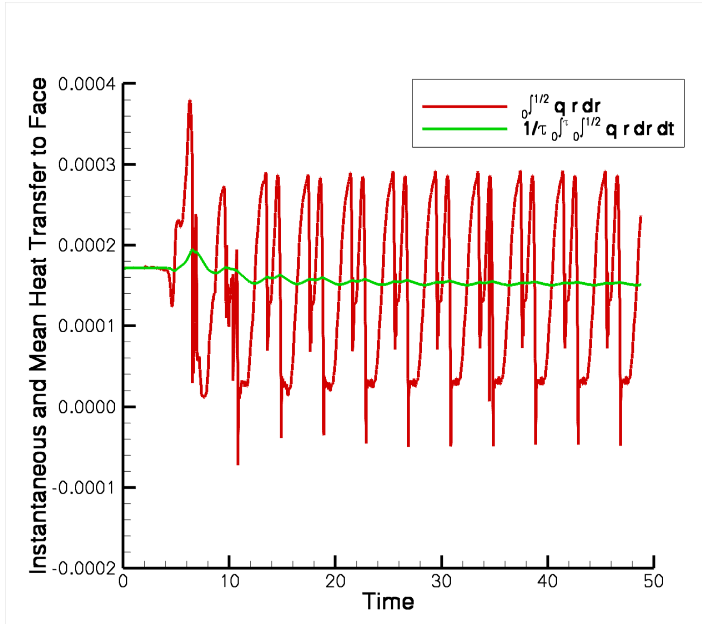

Figure 5.78: $L/D = 2$ Mean and Instantaneous Heat Transfer to Front of Body

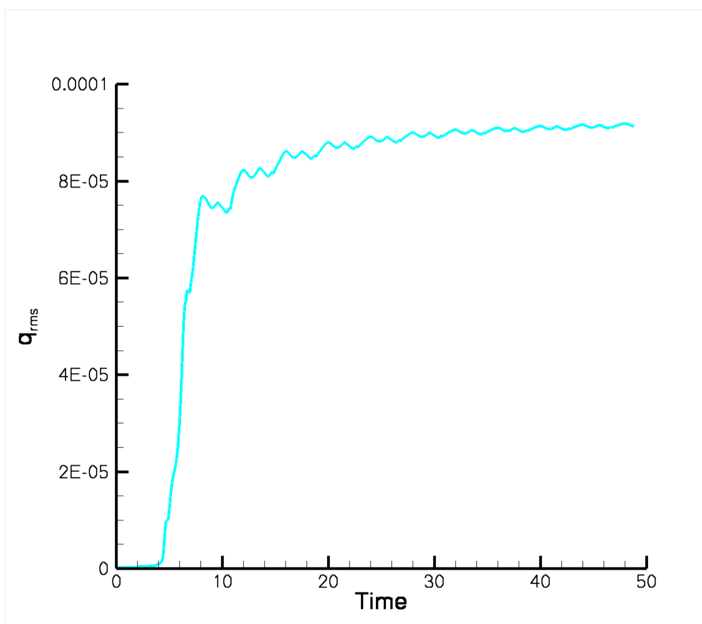

Figure 5.79: $L/D = 2$ Root Mean Square of Heat Transfer to Front of Body

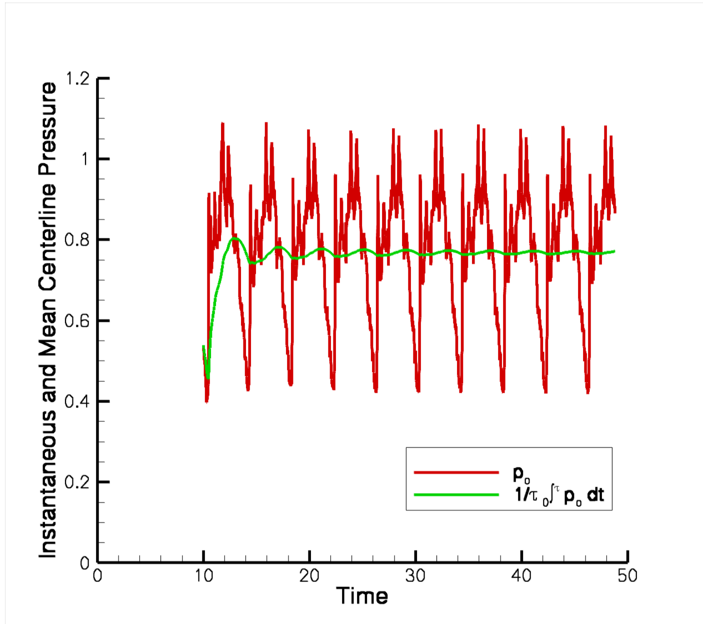

Figure 5.80: $L/D = 2$ Mean and Instantaneous Stagnation Pressure

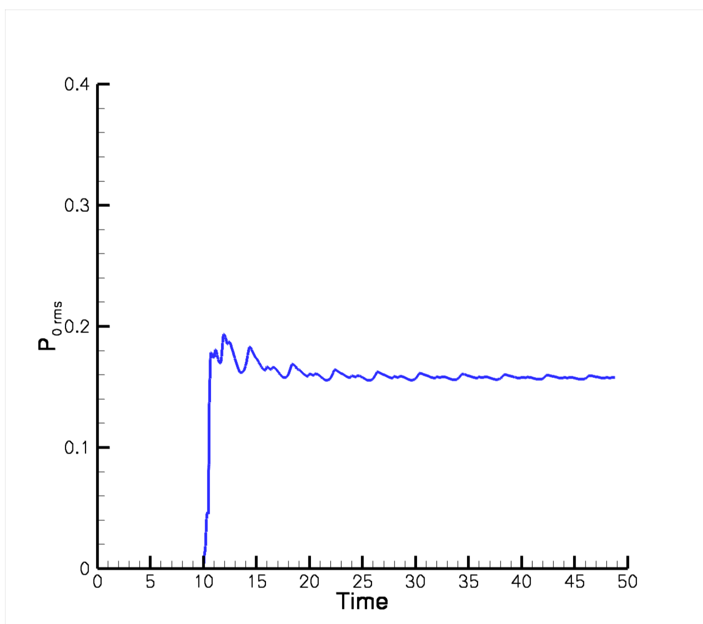

Figure 5.81: $L/D = 2$ Root Mean Square of Stagnation Pressure

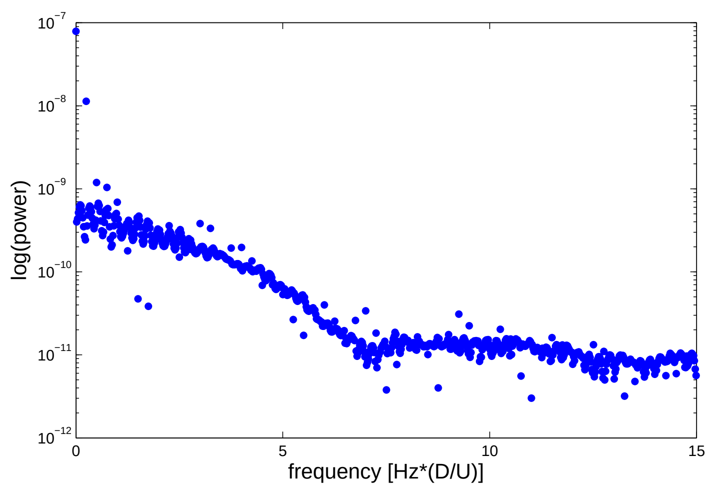

Figure 5.82: $L/D = 2$ Filament Power Spectrum of Dimensionless q

Efficiency, Effectiveness and Heat Transfer

The drag reduction efficiency, effectiveness and heat transfer to cylinder face parameters are graphed in Figures 5.83, 5.84 and 5.85, respectively. The total drag is reduced by 20%. The effectiveness of the drag reduction is lower than the $L/D = 4/3$ case and the efficiency is 111, higher than the $L/D = 4/3$ case. The heat transfer to the front face is reduced by 12%. The heated filament reduces the heat transfer to the front face of the cylinder. This result is explained further in the analysis of the flow contours.

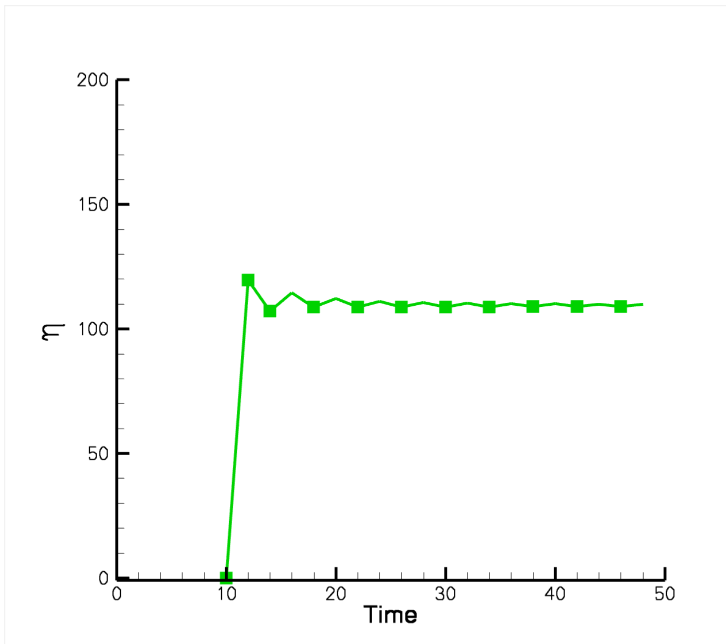

Figure 5.83: $L/D = 2$ Filament Efficiency Parameter

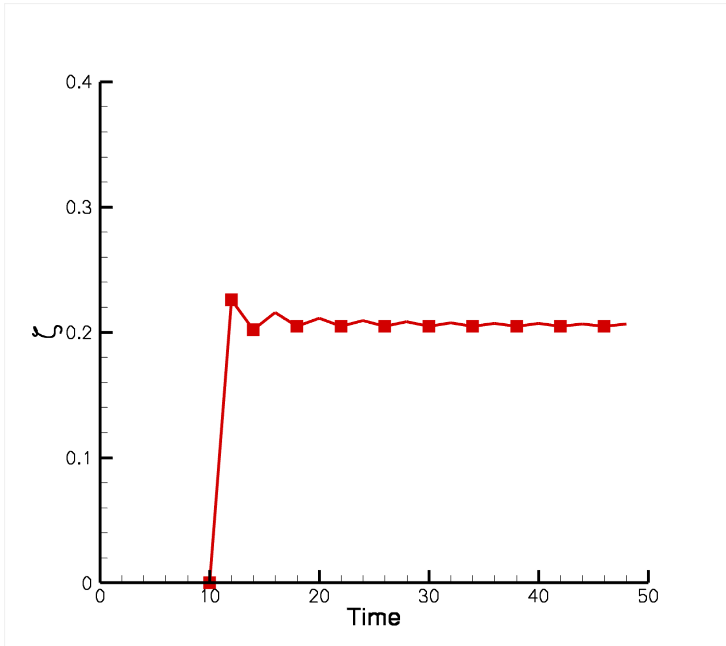

Figure 5.84: $L/D = 2$ Filament Effectiveness Parameter

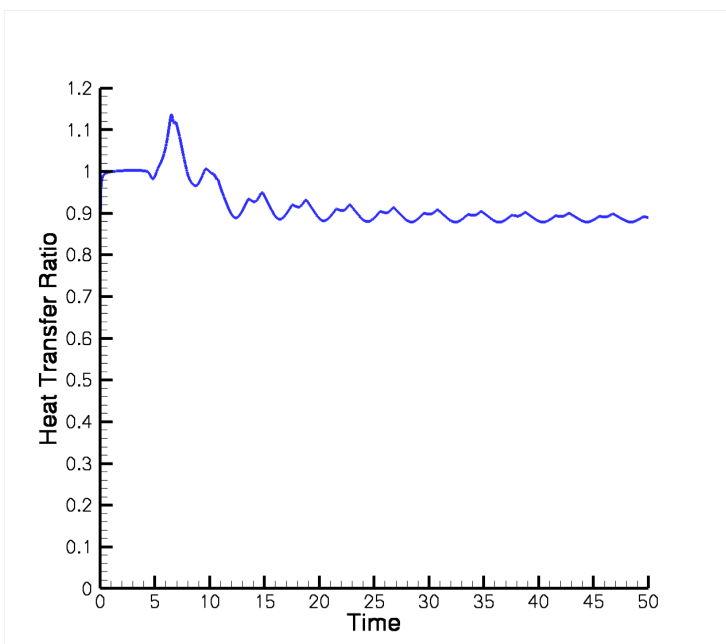

Figure 5.85: $L/D = 2$ Filament Heat Transfer to Front Face Parameter

Contours of Flow

The contours for the pulsed case of period 2 are displayed in Figures 5.86 through 5.107. The contours over one heat transfer cycle are shown at the statistically stationary state. One cycle of heat transfer is determined by the graph of heat transfer versus time. One heat transfer cycle for this case is 4 dimensionless time units.

The major flow features are depicted in the density gradient and pressure contours, Figures 5.86 through 5.88 and 5.89 through 5.91, respectively. Shock waves and contact surfaces are visible in the density gradient contours. The major flow features at the beginning of the heat transfer cycle are labeled in Figure 5.86(a). The heated filament is entering from the inflow boundary. Where the heated filament intersects the bow shock, an upstream lensing of the bow shock occurs. Behind the bow shock, the contact surfaces between the heated filament and surrounding flow are shown. According to the Rankine Hugoniot conditions, because the heated filament is at a reduced Mach number, its velocity behind the bow shock is lower than the surrounding flow. The contact surface at the top of the heated filament within the shock layer is, therefore, a shear layer. The shear layer is unstable to small perturbations and create a vortex downstream of the bow shock. This is seen in Figures 5.86(a) through 5.86(f). Each filament generates a vortex with a trailing contact surface in the shear layer. The vortices convect toward the cylinder corner. Two such vortices from previous heated filaments are seen in Figure 5.86(a). As the flow passes over the cylinder corner, it accelerates, and an expansion fan is created at the top of the cylinder corner. Downstream of the expansion fan a recompression shock is formed to turn the flow parallel to the cylinder.

The flow features can be seen in the numerical Schlieren images in Figures 5.92 through 5.94. The progression in time of the heated filament entering the shock layer seen in Figure 5.92(a) is followed through one heat transfer cycle, 4 dimensionless time units, to understand how the flow features develop. One heat transfer cycle is defined as the dimensionless time between peaks in the heat transfer to the front face of the cylinder or Φ (Figure 5.85).

Figure 5.92(a) The heated filament approaches the cylinder from the left boundary. As the heated filament contacts the bow shock, the bow shock lenses forward.

Figure 5.92(c) As the heated filament progresses into the shock layer, the contact surfaces within the shock layer begin to roll into a vortex. A small lambda shock stems from the bow shock at the point where the lensed part of the shock meets the unlensed shock.

Figure 5.92(f) A vortex has formed behind the shock layer at the downstream side of the contact surface. The contact surface meets the symmetry boundary. This represents a disk with a vortex ring at its outer edge. A shock wave between the new vortex and the downstream vortex is shown. This shock turns the flow coming off the front (downstream side) of the new vortex upward, to progress over the back (upstream side) of the downstream vortex. A weak shock at the bottom of the new vortex begins to form. Because the flow near the symmetry boundary is parallel to the symmetry boundary, the flow must turn to flow over the upstream side of the new vortex. A weak shock appears where the flow turns.

Figure 5.93(b) The new vortex has convected toward the cylinder corner. The shock between the vortices has progressed upstream and is now sitting atop the new vortex. This weak shock at the top of the vortex turns the flow at top of the vortex to progress down over the front side of the vortex. The flow at the front of the vortex expands into a lower pressure area, thus an expansion fan sits at the front of the vortex. The contact surface that trails the vortex remains attached to the symmetry boundary. The density gradient across the contact surface weakens as the vortex convects away from the symmetry boundary. The contact surface from the downstream vortex remains in the flow after the vortex has convected over the cylinder corner.

Figure 5.93(c) The contact surface from the vortex that has passed over the cylinder corner remains ahead of the cylinder face. A weak shock wave forms just ahead of the cylinder corner, where clockwise rotating flow from the upstream vortex must turn to progress over the cylinder corner.

Figure 5.93(d) The weak shock turning flow over the cylinder corner has retracted and now sits on top of the vortex approaching the corner. The vortex forces the flow around it to curve in a clockwise motion. The direction of the flow influences the shape of the bow shock around the vortex. The bow shock curves in the vicinity of the vortex. Where the curved part of the bow shock meets the uncurved part of the bow shock, a lambda shock forms. The lambda shock is seen stemming from the bow shock above the vortex.

Figure 5.94(b) The vortex has progressed toward the cylinder corner. The weak shock at the top of the vortex has merged with the lambda shock stemming from the bow shock. The contact surface trailing the vortex has become entrained in the upstream vortex.

Figure 5.94(f) Finally, the vortex contacts the cylinder corner. The weak shock at the bottom of the vortex can be seen interacting with the corner. The trailing contact surface has become very weak, mostly sucked in to the vortex upstream. The contact surface does not remain ahead of the cylinder face, as was the case with the previous vortex.

The velocity magnitude contours are shown in Figures 5.95 through 5.97. It can be seen in Figure 5.95(a), that the vortices form a line between the lensed part of the bow shock and the cylinder corner. This will be referred to as the vortex layer. The region below the vortex layer is a very low velocity region. This will be referred to as the stagnation region. A vortex sits at the center of the vortex layer in Figure 5.95(a). The core of the vortex is at a very low velocity. The top of the vortex has a high velocity. The high velocity flow decelerates immediately just ahead of the downstream side of the vortex. This is the location of the contact surface from the downstream vortex. Below the contact surface is low velocity flow, which accelerates as it winds around the bottom of the vortex. The flow quickly decelerates again at the bottom upstream side of the vortex, as it encounters the weak shock at the bottom of the vortex. The contact surface at the upstream side of the vortex separates the low velocity flow from the higher velocity flow at the top of the vortex.

The formation and convection of vortices over the cylinder corner reduce the heat transfer to the front face of the cylinder. This is seen through one period of the heat transfer cycle. The major points in a heat transfer cycle are labeled in Figure 5.98. The relation of heat transfer cycle to the vortex formation and convection is illustrated through the contour plots of vorticity magnitude, streamlines of flow and temperature contours, shown in Figures 5.99 through 5.101, Figures 5.102 through 5.104 and Figures 5.105 through 5.107, respectively. Vortices labeled in Figure 5.99(a) are referred to in the descriptions that follow.

Point 1 Point 1 represents a maximium point of heat transfer to the cylinder face. Previously, vortex 0 had been approaching the cylinder face. As vortex 0 approached the face, the area of influence of the convection by vortex 0 on the cylinder face was reducing and a stagnation region was growing below vortex 0 at the cylinder face. Point 1 represents the maximum heat transfer, which occurs just before the expansion fan that sits in front of vortex 0 contacts the cylinder face. As the expansion fan interacts with the cylinder face, it dramatically increases conduction and advection of heat away from the cylinder face. At point 1 vortex 0 is just ahead of the cylinder corner, this can be seen in Figure 5.99(a). The graph of streamlines and velocity magnitude show that the area of high velocity in front of the corner begins to interact with the cylinder corner at this instant in Figure 5.102(a). The temperature plot shows that an area of reduced pressure sits just downstream of the vortex. At point 1, the reduced temperature region, the expanion fan, intersects the cylinder face. This is seen in Figure 5.105(a).

Point 2 As vortex 0 moves up and over the corner, the expansion fan approaches the point of maximum heat transfer, the cylinder corner. Thus, point 2 is the point where the expansion fan is at the cylinder corner. The vortex is seen sitting at the edge of the corner in Figure 5.99(b). The streamlines around vortex 0 have ceased to interact with the cylinder face, as seen in Figure 5.102(b). The low temperature region is no longer in front of the cylinder face in Figure 5.105(b)

Point 3 Point 3 is a minor jump in the heat transfer to the cylinder. This is due to the weak shock from the top of vortex 0 interacting with the cylinder corner.

Point 4 After vortex 0 convects over the cylinder corner, vortex 1 is the primary influence on heat transfer to the front face of the cylinder. It pulls flow from above the vortex layer down to the region ahead of the cylinder face. In Figure 5.102(b), the streamlines from the top of vortex 0 sweep across 15% of the total diameter of the cylinder.

By Figure 5.102(d), however, the streamlines pulling flow from above the vortex layer only interact with 5% of the cylinder face. A stagnation region is growing over the cylinder face. The temperature contours show an increasing temperature at the cylinder face over the period of time in Figures 5.105(b) through 5.105(d). The increase in temperature across the face ceases when the expansion fan just downstream of vortex 1 contacts the cylinder face. Evidence of this is seen in the streamline and velocity magnitude plot, as the high velocity aread upstream of vortex 1 contacts the cylinder face in Figure 5.102(e). The temperature profile confirms this in Figure 5.105(e). The low temperature region just downstream of vortex 0 is at the cylinder face.

Point 5 As the expansion fan convects up and over the cylinder corner, it approaches the peak heating on the cylinder. Thus, as the expansion fan convects over the corner, the maximum cooling of the face occurs. This corresponds to point 5 in the graph. The vortex is seen just above the cylinder corner in Figure 5.100(a).

Point 6 Point 6 begins the climb in heat transfer to the front face of the cylinder. No significant flow structure is seen in the velocity magnitude, streamline or temperature graph at point 6. However, the density gradient contour shows that this is the point where the contact surface interacts with the cylinder face, Figure 5.87(e). This figure is at a time just before point 6 occurs. The contact surface is seen just ahead of the cylinder face. The contact surface separates regions of different density. The density following vortex 1 is less than the density ahead of vortex 2. Thus, the climb in heat transfer begins again after the contact discontinuity has contacted the cylinder face.

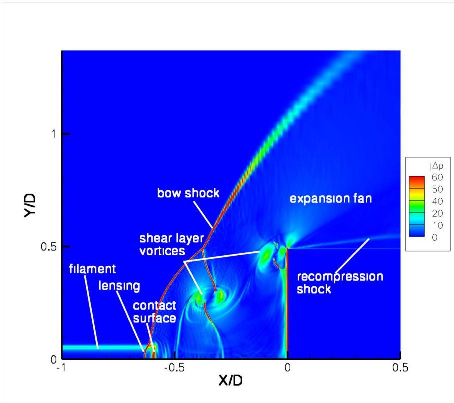

(a) t = 49.5

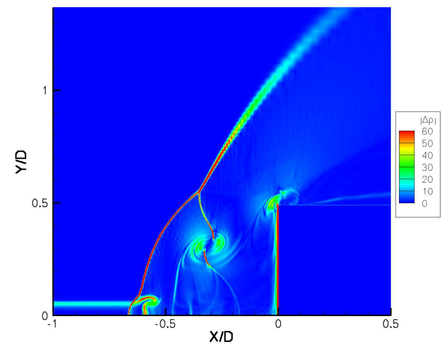

(b) t = 49.7

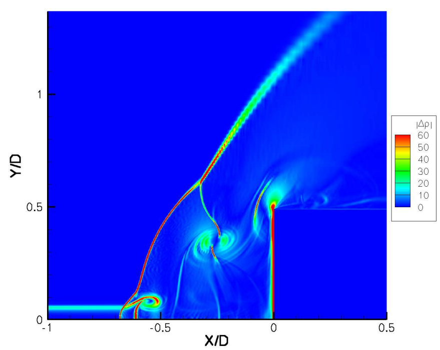

(c) t = 49.9

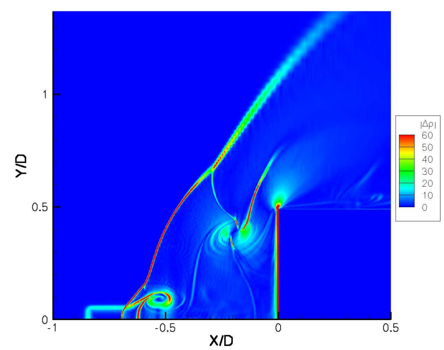

(d) t = 50.2

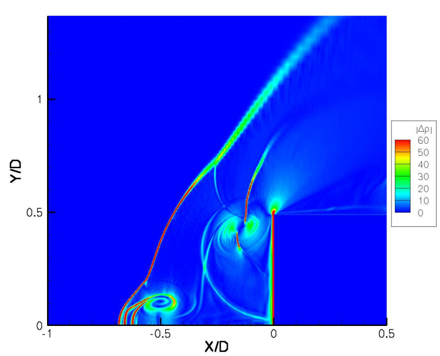

(e) t = 50.4

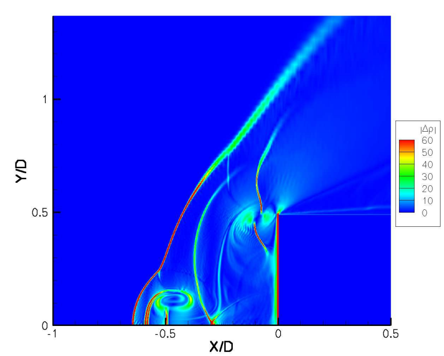

(f) t = 50.6

Figure 5.86: $L/D = 2$ Filament Density Gradient Contours

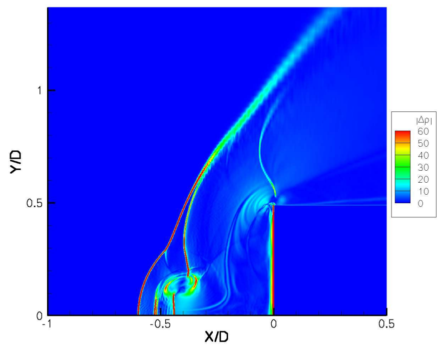

(a) t = 50.9

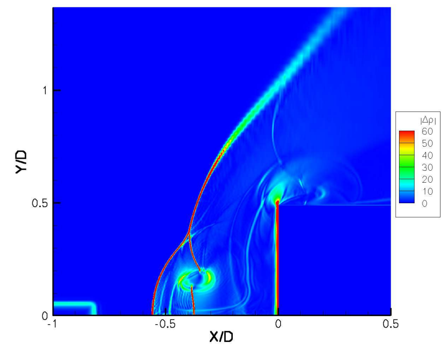

(b) t = 51.2

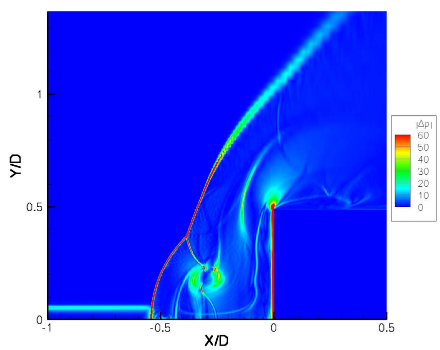

(c) t = 51.5

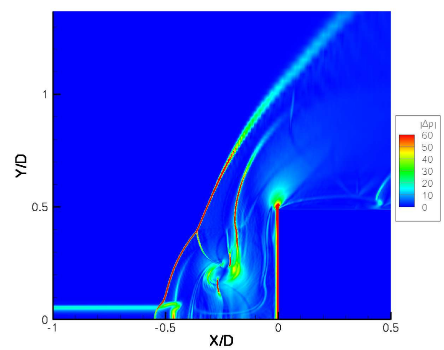

(d) t = 51.7

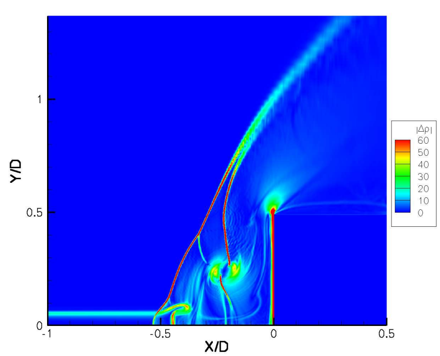

(e) t = 51.9

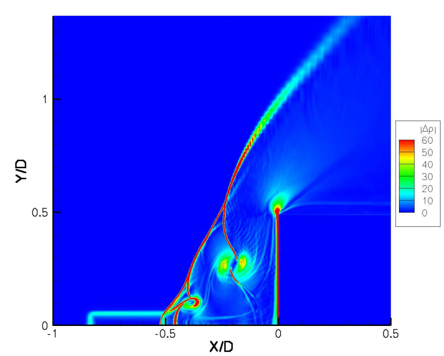

(f) t = 52.2

Figure 5.87: $L/D = 2$ Filament Density Gradient Contours

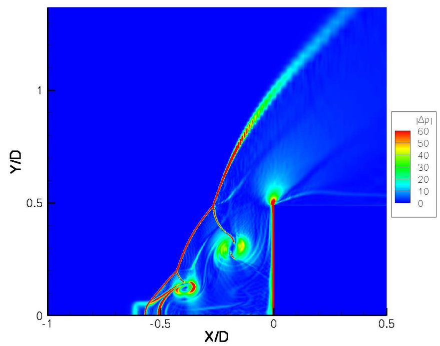

(a) t = 52.4

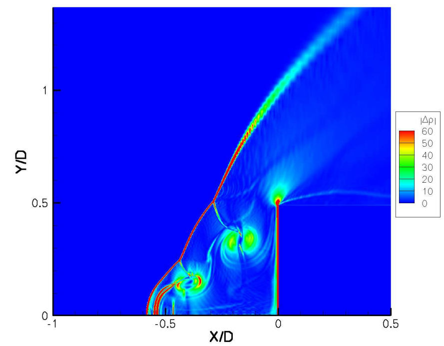

(b) t = 52.6

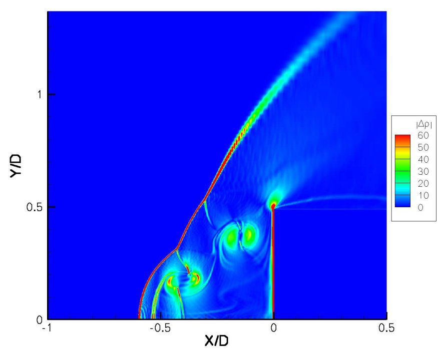

(c) t = 52.9

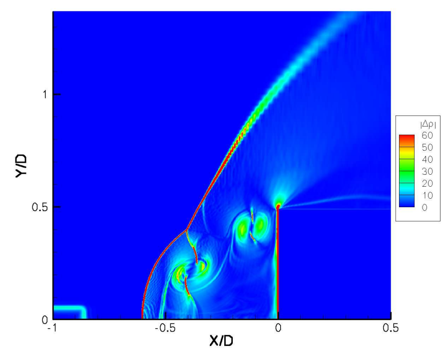

(d) t = 53.1

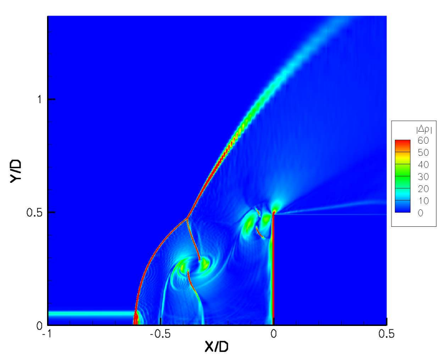

(e) t = 53.4

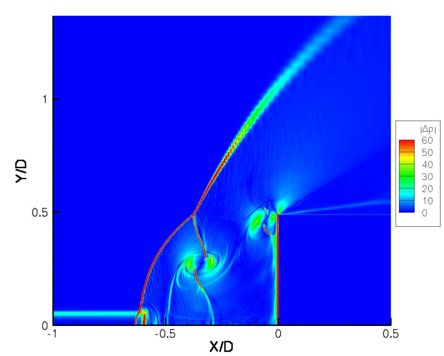

(f) t = 53.5

Figure 5.88: $L/D = 2$ Filament Density Gradient Contours

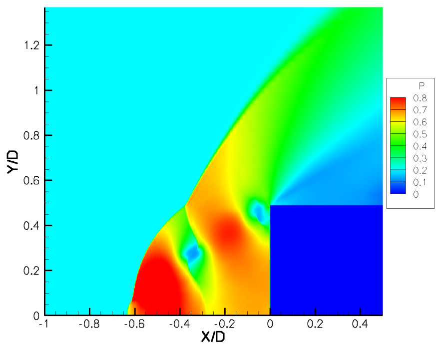

(a) t = 49.5

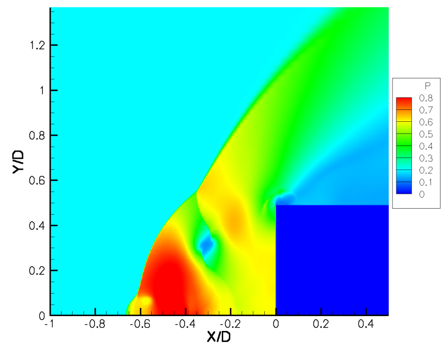

(b) t = 49.7

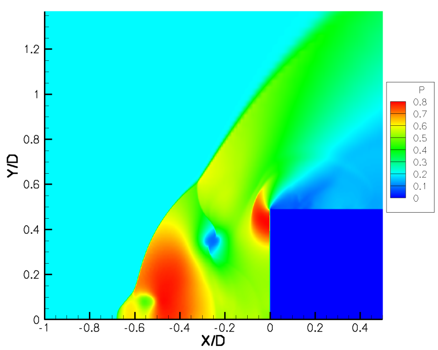

(c) t = 49.9

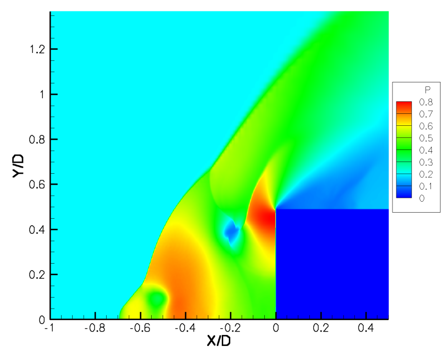

(d) t = 50.2

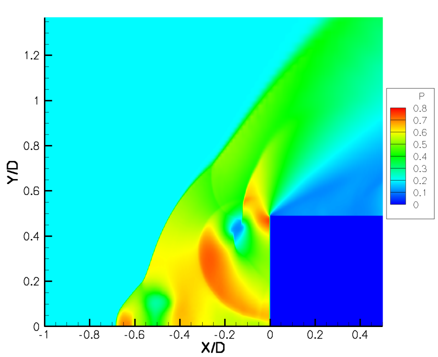

(e) t = 50.4

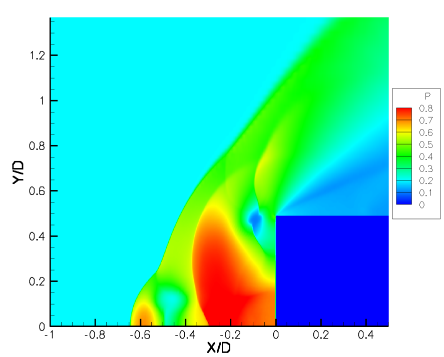

(f) t = 50.6

Figure 5.89: $L/D = 2$ Pressure Contours

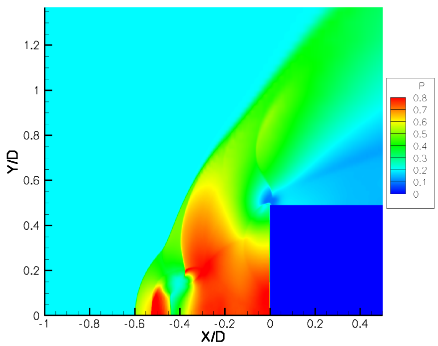

(a) t = 50.9

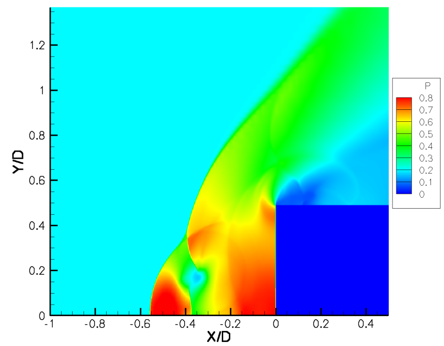

(b) t = 51.2

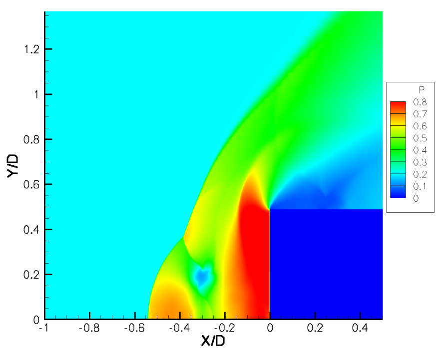

(c) t = 51.5

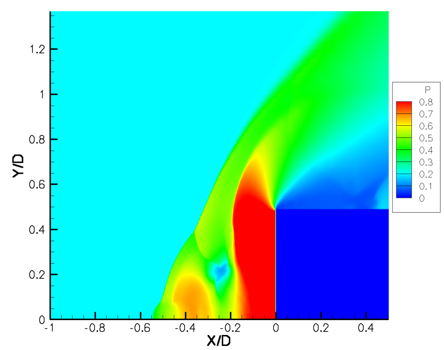

(d) t = 51.7

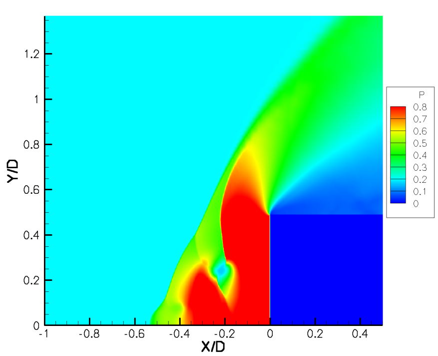

(e) t = 51.9

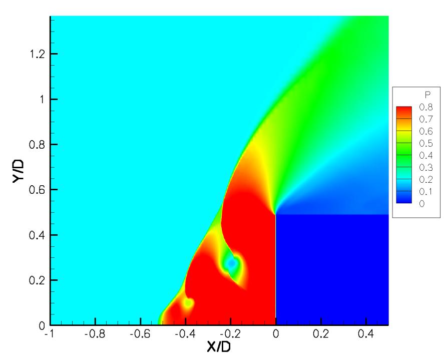

(f) t = 52.2

Figure 5.90: $L/D = 2$ Filament Pressure Contourss

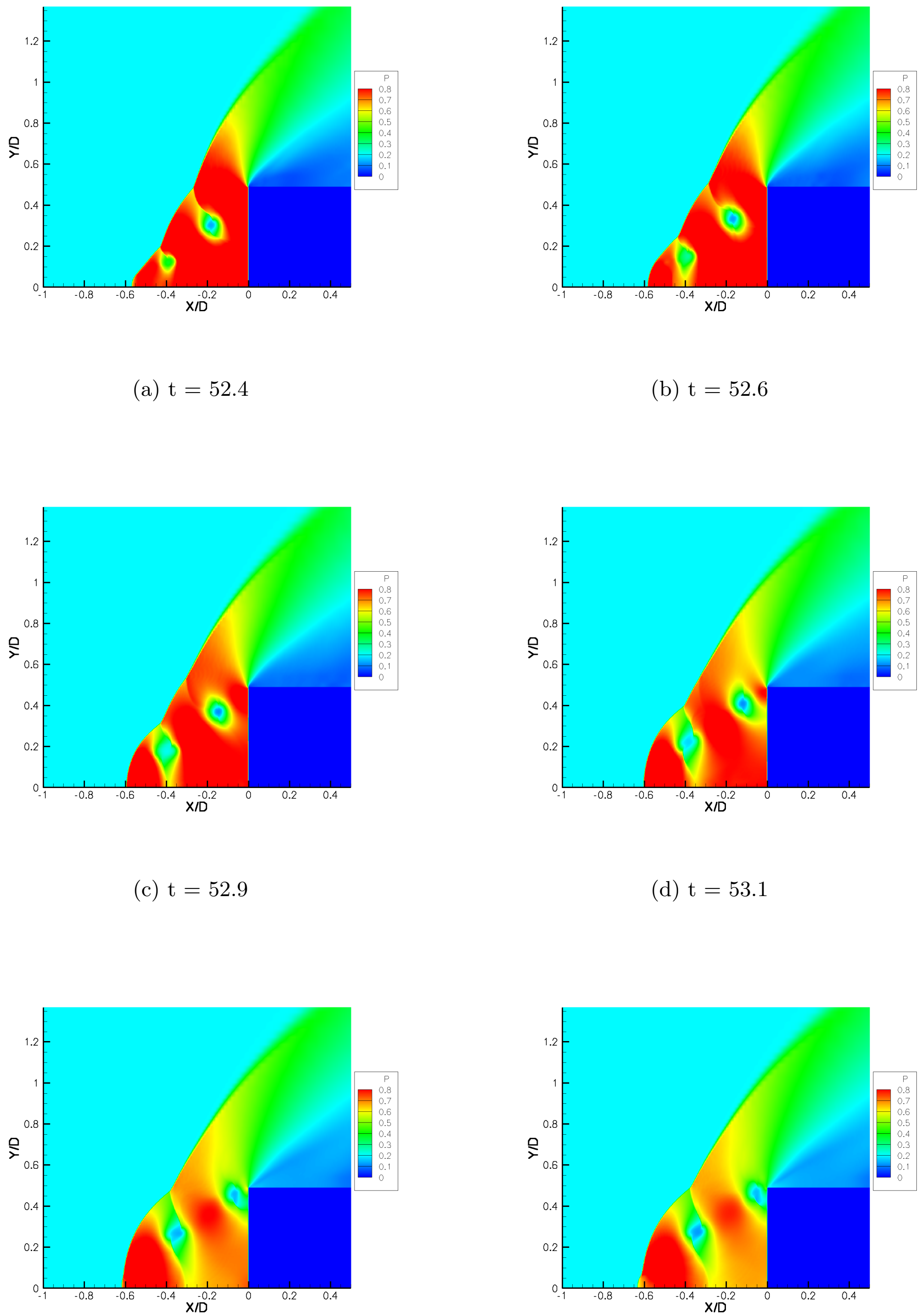

(a) t = 52.4

(b) t = 52.6

(c) t = 52.9

(d) t = 53.1

(e) t = 53.4

(f) t = 53.5

Figure 5.91: $L/D = 2$ Filament Pressure Contours

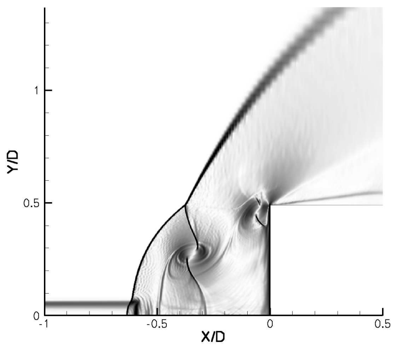

(a) t = 49.5

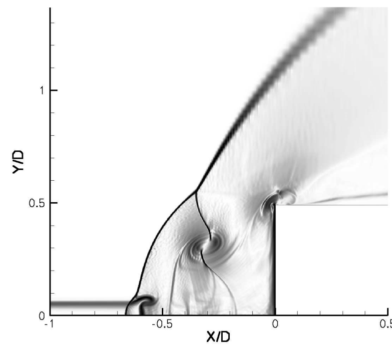

(b) t = 49.7

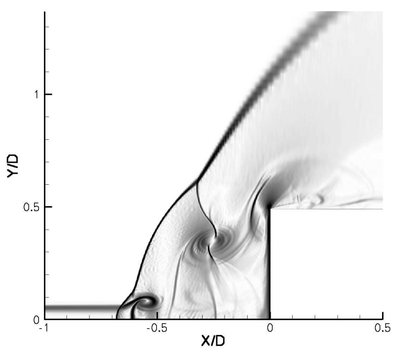

(c) t = 49.9

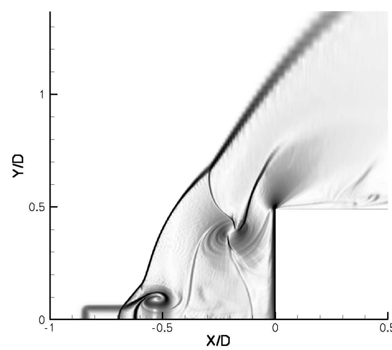

(d) t = 50.2

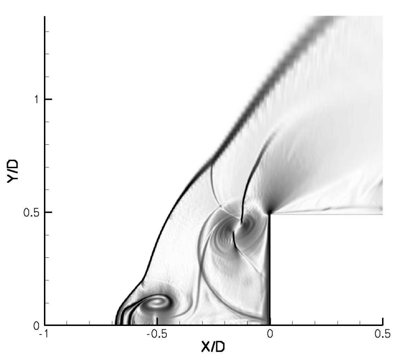

(e) t = 50.4

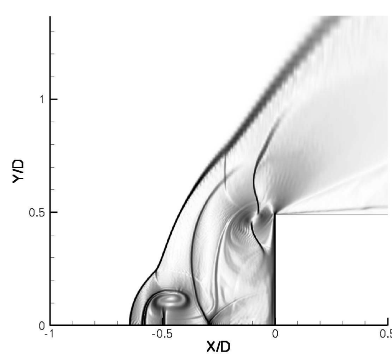

(f) t = 50.6

Figure 5.92: $L/D = 2$ Numerical Schlieren Images

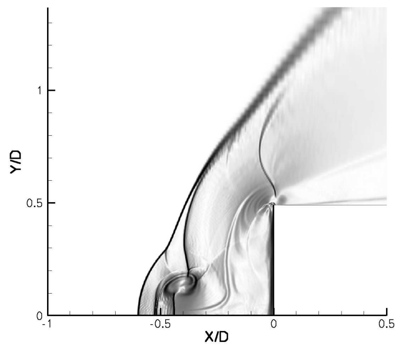

(a) t = 50.9

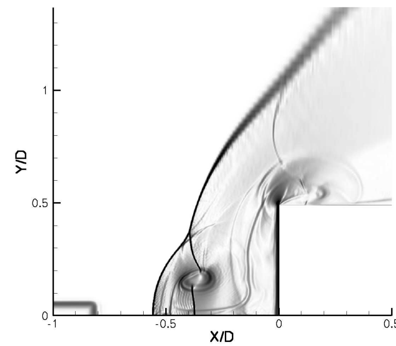

(b) t = 51.2

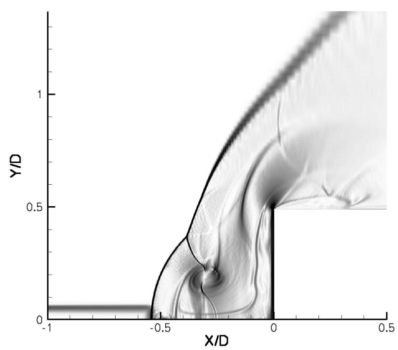

(c) t = 51.5

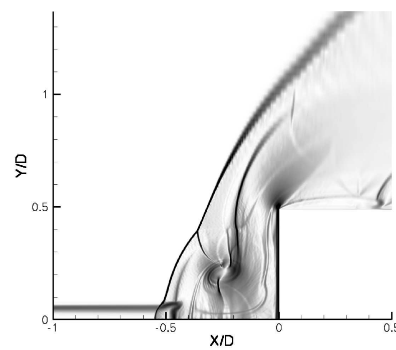

(d) t = 51.7

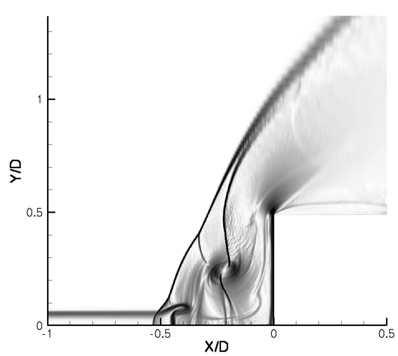

(e) t = 51.9

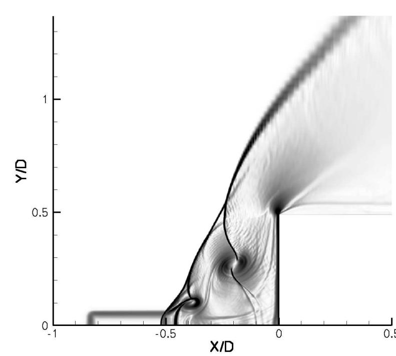

(f) t = 52.2

Figure 5.93: $L/D = 2$ Filament Numerical Schlieren Images

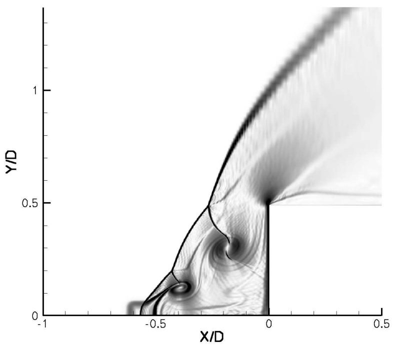

(a) t = 52.4

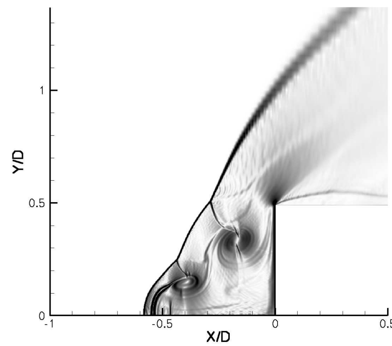

(b) t = 52.6

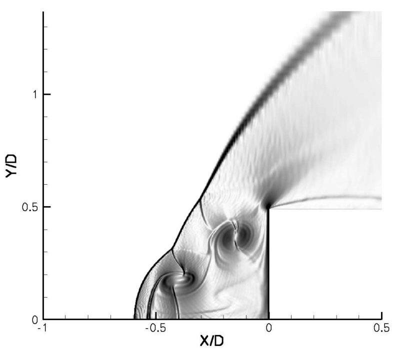

(c) t = 52.9

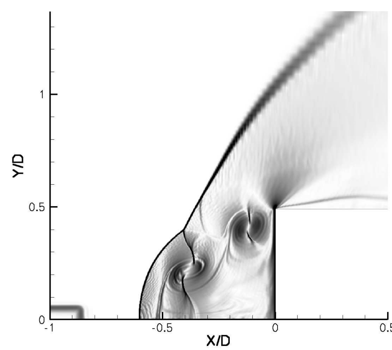

(d) t = 53.1

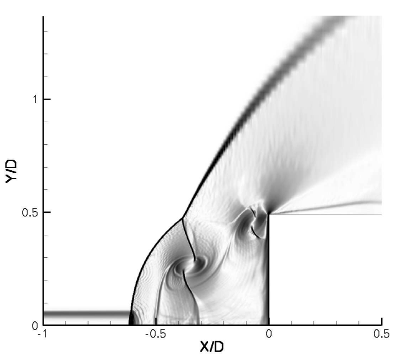

(e) t = 53.4

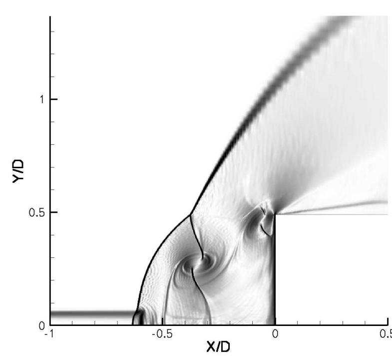

(f) t = 53.5

Figure 5.94: $L/D = 2$ Filament Numerical Schlieren Images

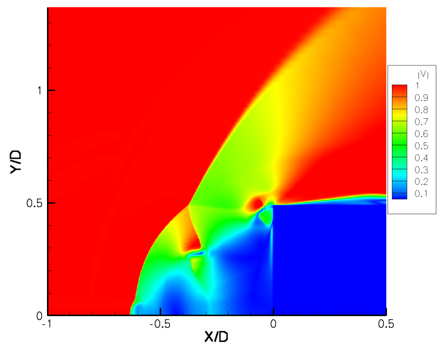

(a) t = 49.5

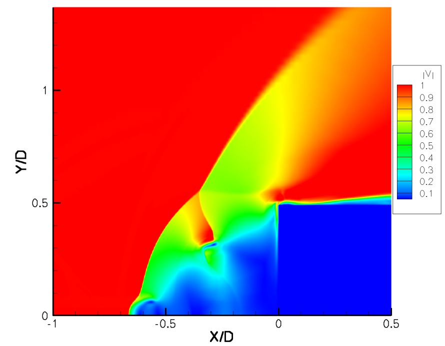

(b) t = 49.7

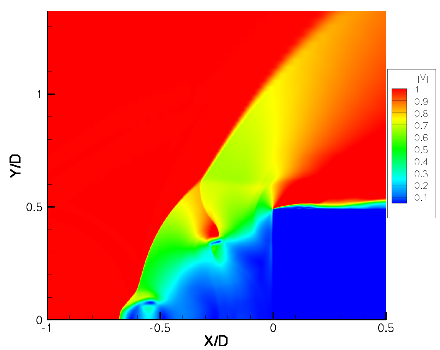

(c) t = 49.9

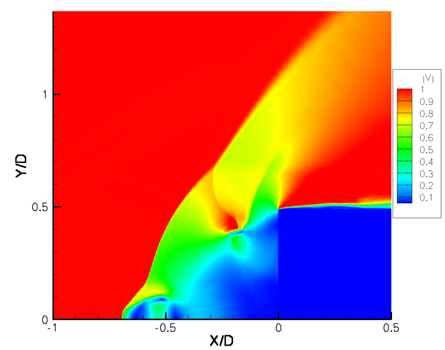

(d) t = 50.2

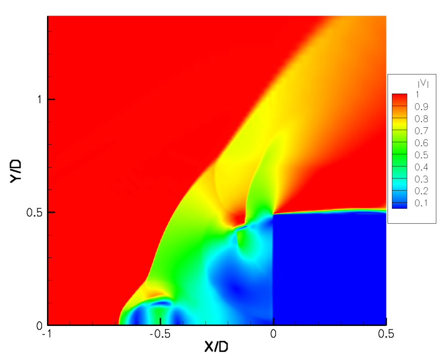

(e) t = 50.4

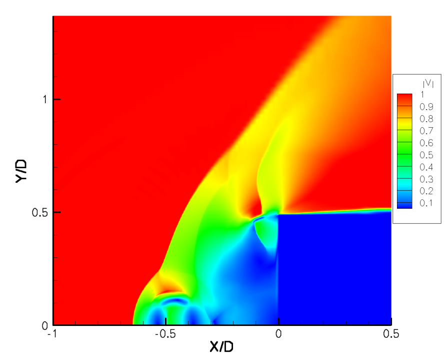

(f) t = 50.6

Figure 5.95: $L/D = 2$ Velocity Magnitude Contours

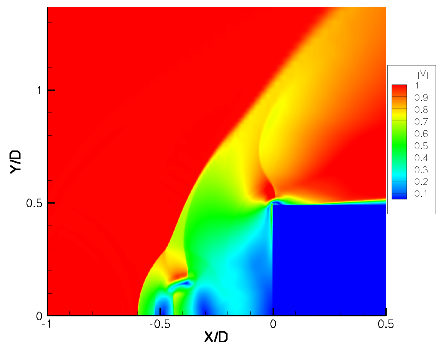

(a) t = 50.9

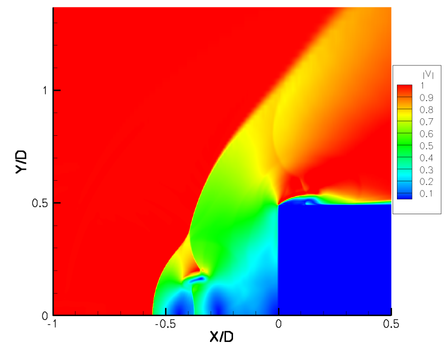

(b) t = 51.2

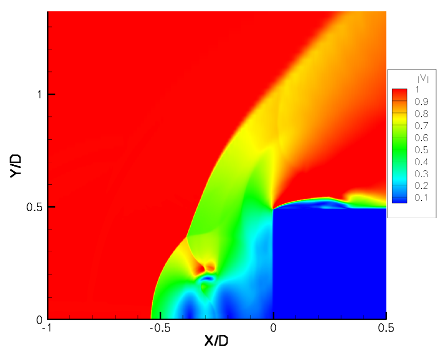

(c) t = 51.5

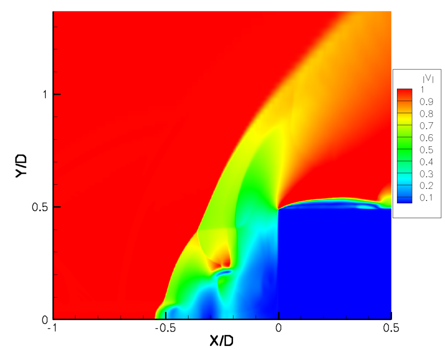

(d) t = 51.7

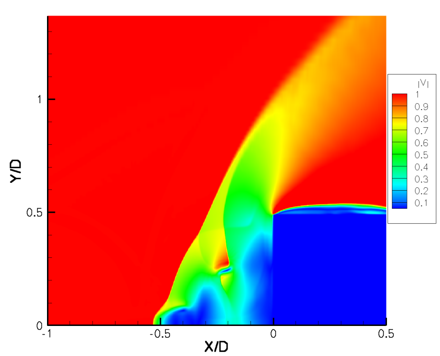

(e) t = 51.9

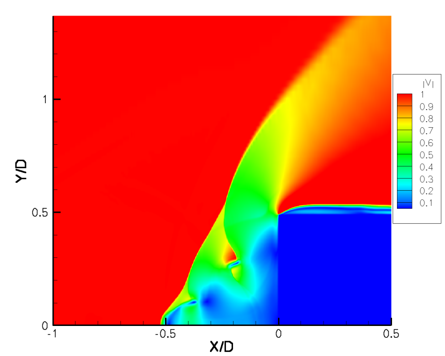

(f) t = 52.2

Figure 5.96: $L/D = 2$ Filament Velocity Magnitude Contourss

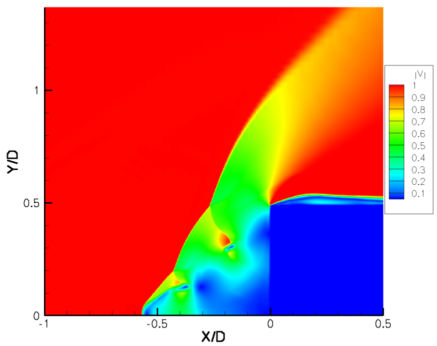

(a) t = 52.4

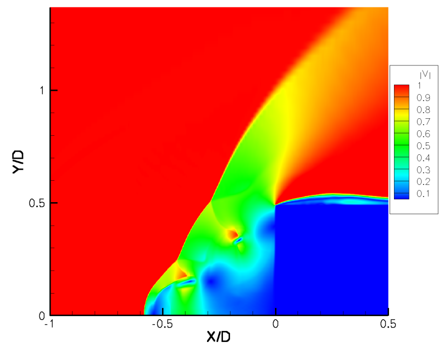

(b) t = 52.6

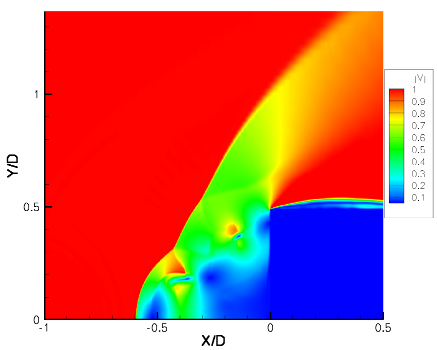

(c) t = 52.9

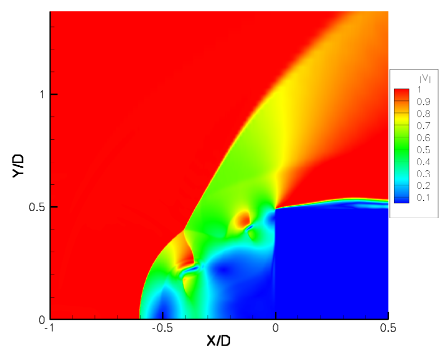

(d) t = 53.1

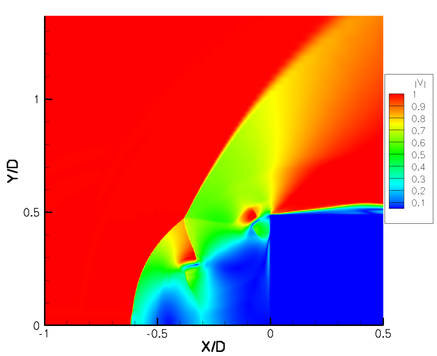

(e) t = 53.4

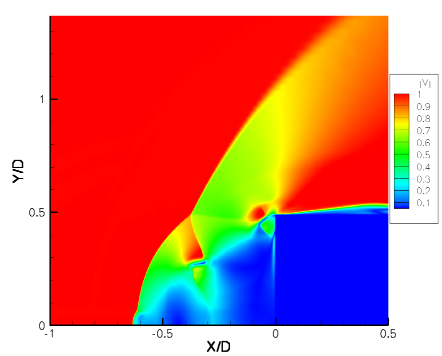

(f) t = 53.5

Figure 5.97: $L/D = 2$ Filament Velocity Magnitude Contours

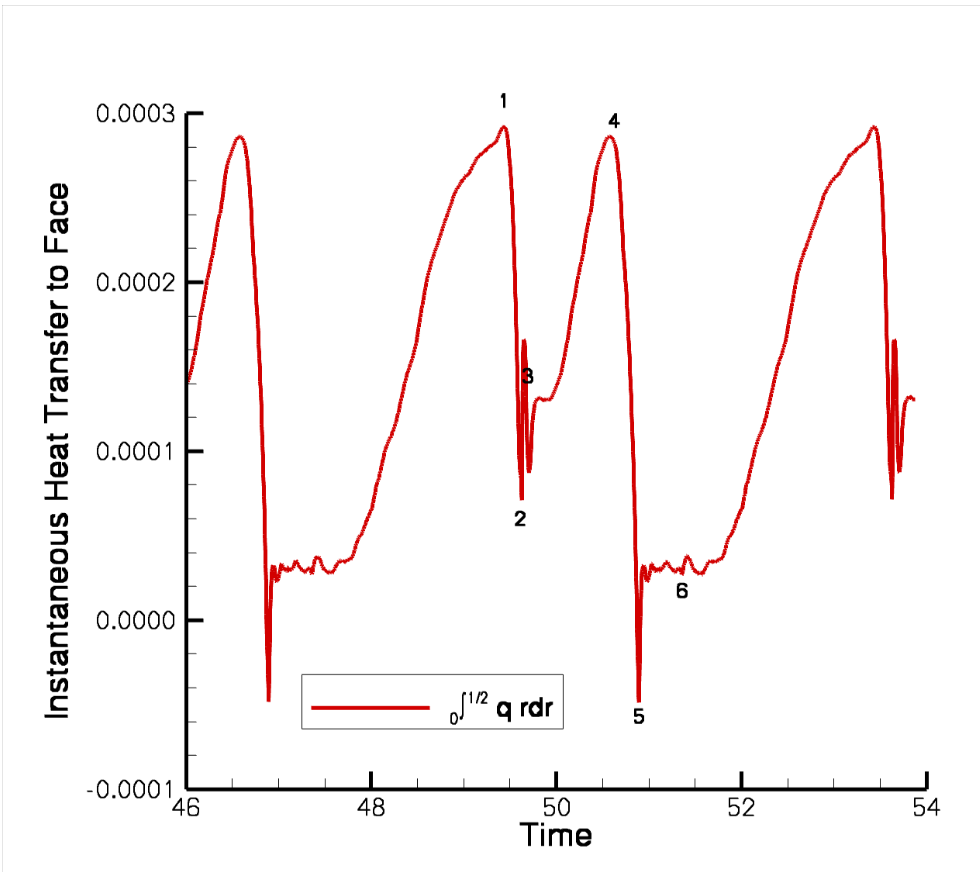

Figure 5.98: $L/D = 2$ Heat Transfer to Cylinder Face

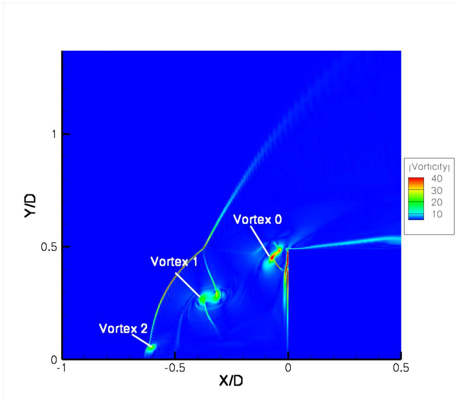

(a) t = 49.5, point 1

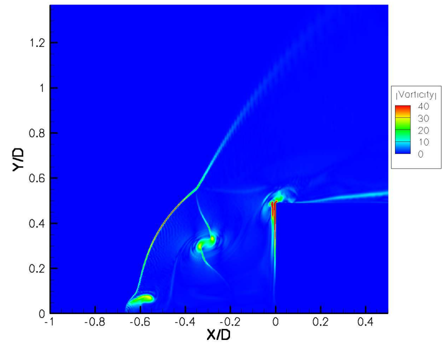

(b) t = 49.7, point 2

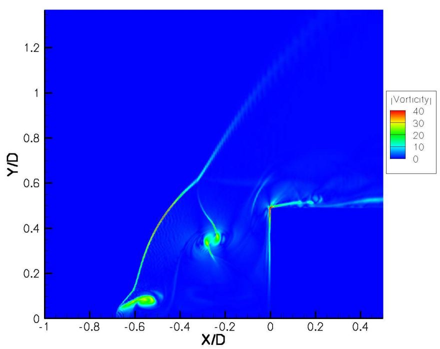

(c) t = 49.9, point 3

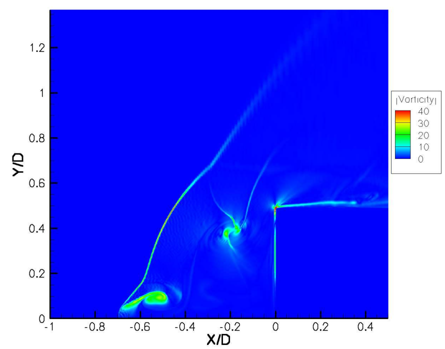

(d) t = 50.2

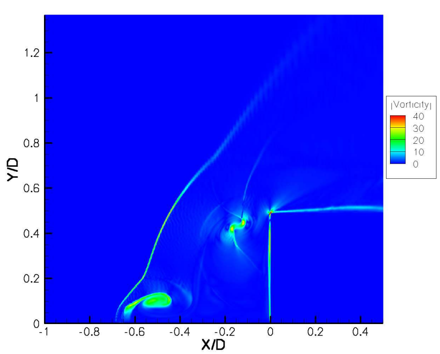

(e) t = 50.4, point 4

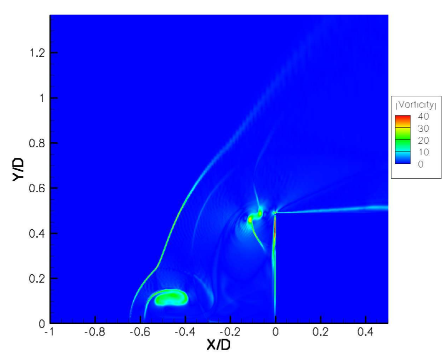

(f) t = 50.6

Figure 5.99: $L/D = 2$ Vorticity Contours

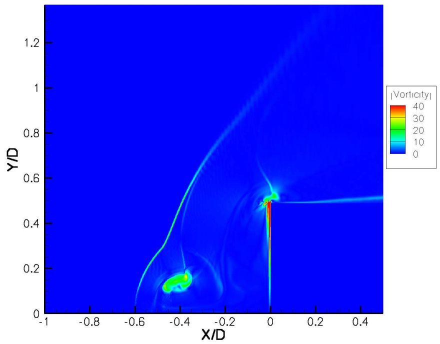

(a) t = 50.9, point 5

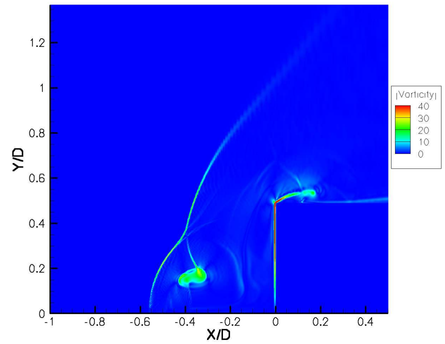

(b) t = 51.2

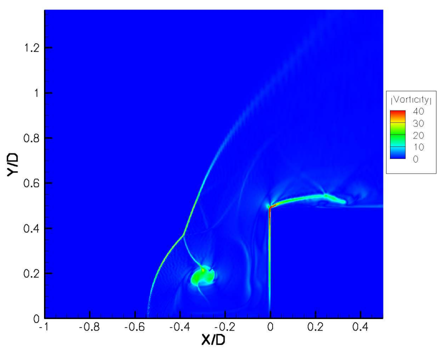

(c) t = 51.5

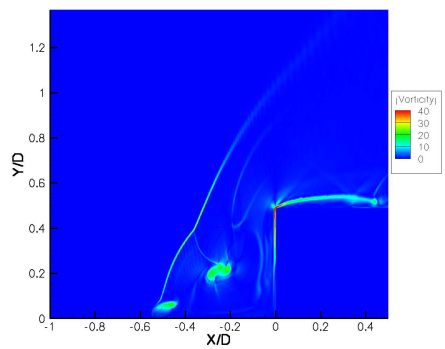

(d) t = 51.7

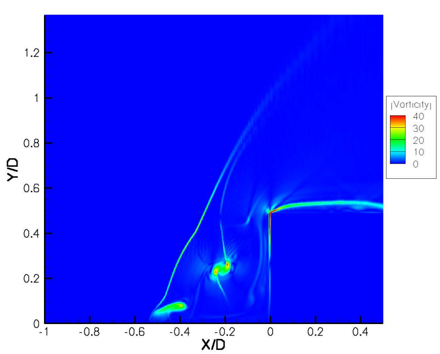

(e) t = 51.9, point 6

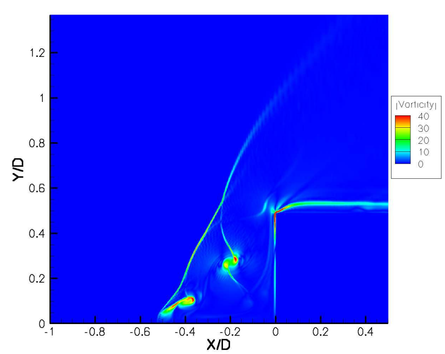

(f) t = 52.2

Figure 5.100: $L/D = 2$ Filament Vorticity Contours

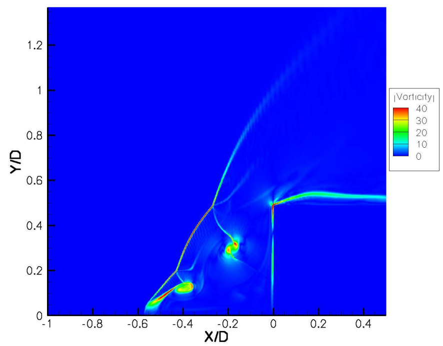

(a) t = 52.4

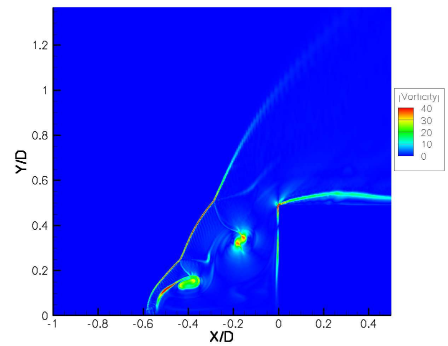

(b) t = 52.6

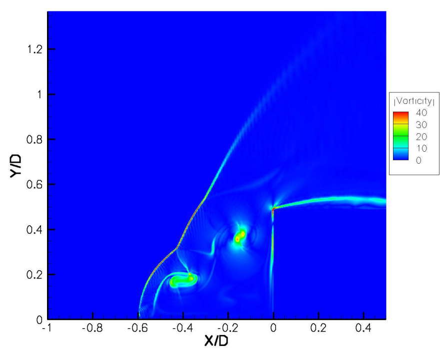

(c) t = 52.9

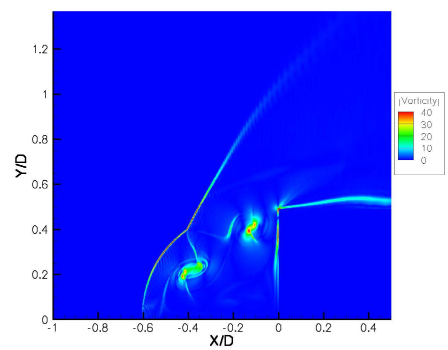

(d) t = 53.1

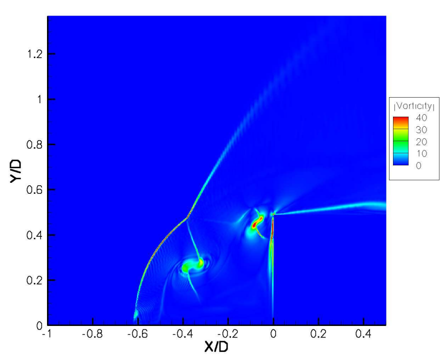

(e) t = 53.4

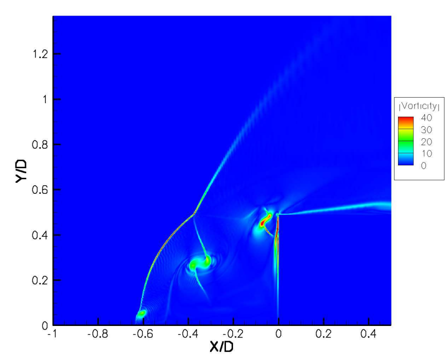

(f) t = 53.5

Figure 5.101: $L/D = 2$ Filament Vorticity Contours

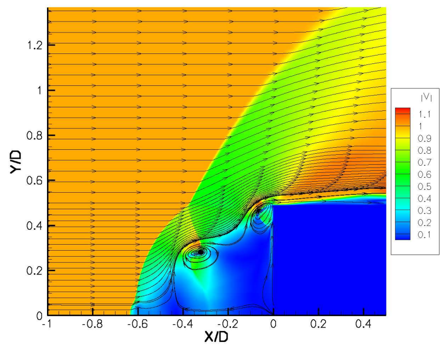

(a) t = 49.5, point 1

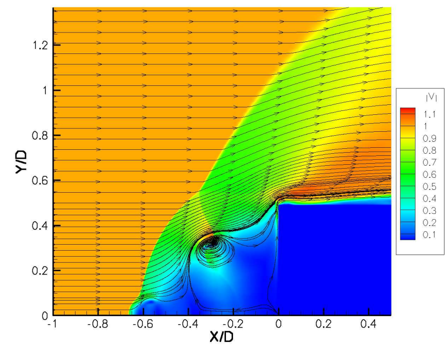

(b) t = 49.7, point 2

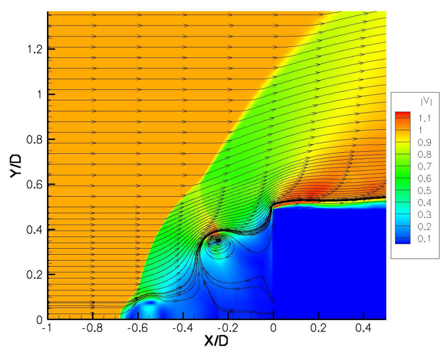

(c) t = 49.9, point 3

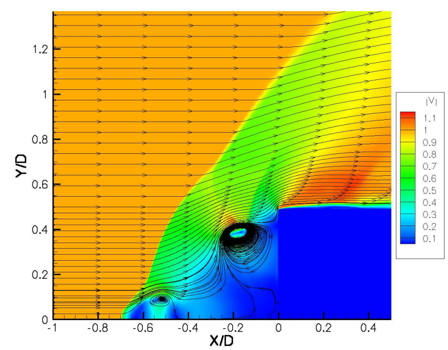

(d) t = 50.2

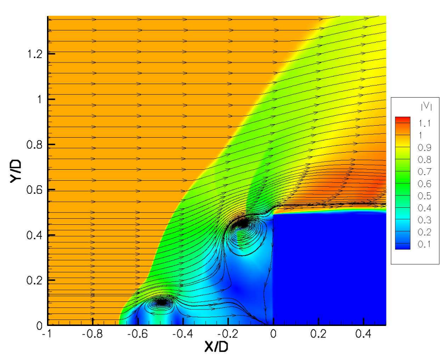

(e) t = 50.4

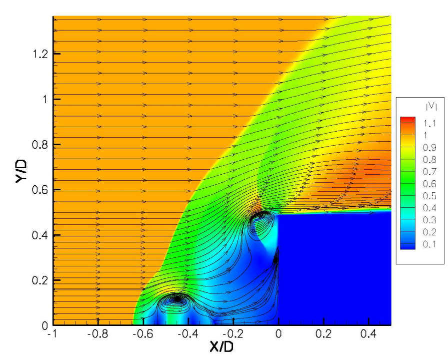

(f) t = 50.6

Figure 5.102: $L/D = 2$ Streamlines

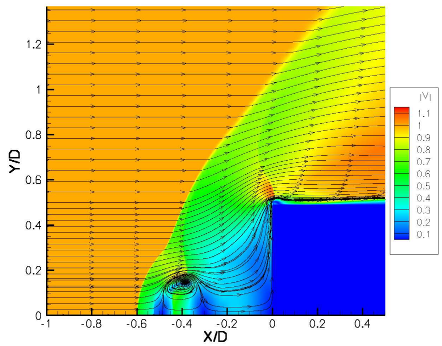

(a) t = 50.9

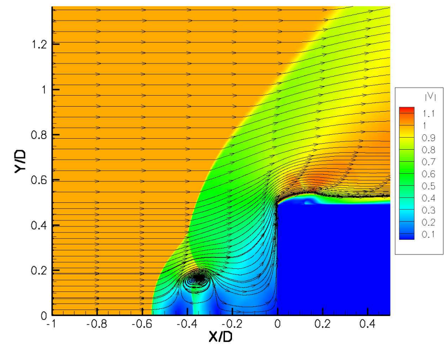

(b) t = 51.2

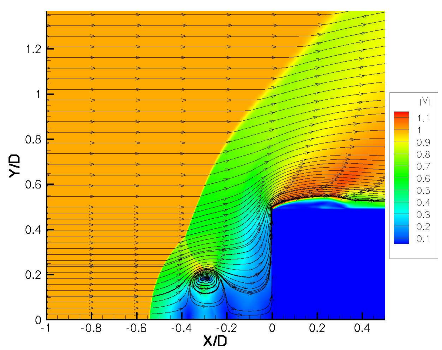

(c) t = 51.5

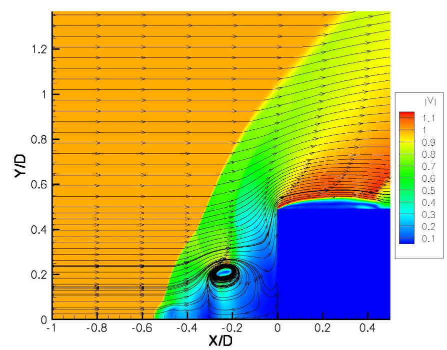

(d) t = 51.7

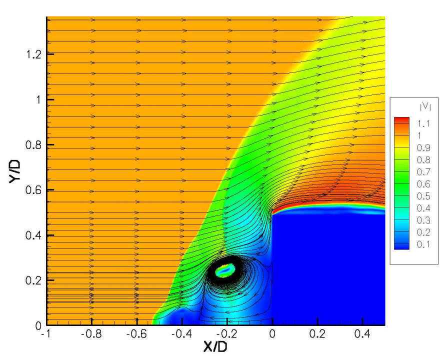

(e) t = 51.9, point 6

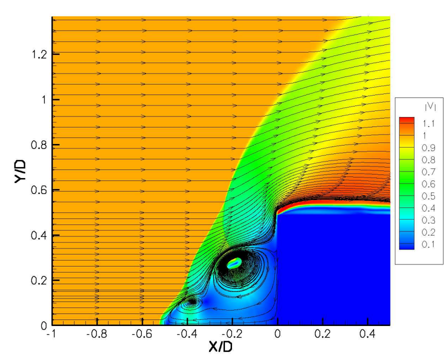

(f) t = 52.2

Figure 5.103: $L/D = 2$ Filament Streamlines

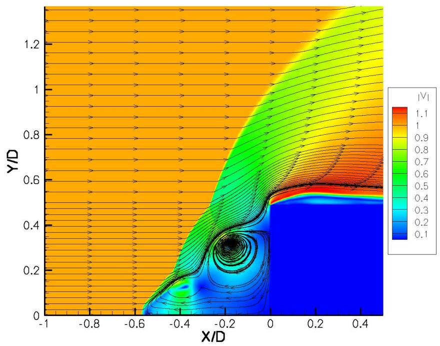

(a) t = 52.4

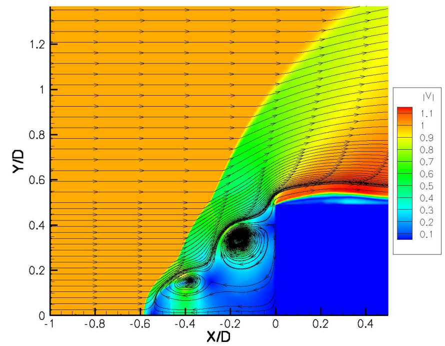

(b) t = 52.6

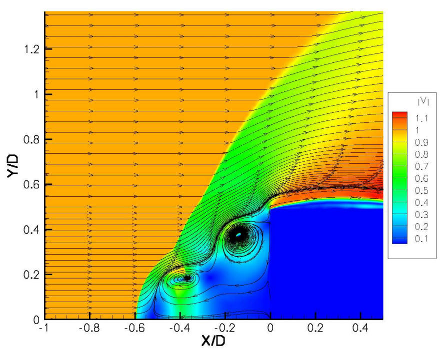

(c) t = 52.9

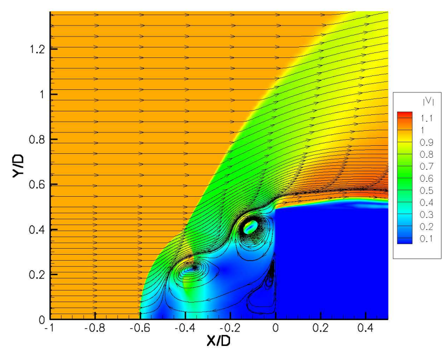

(d) t = 53.1

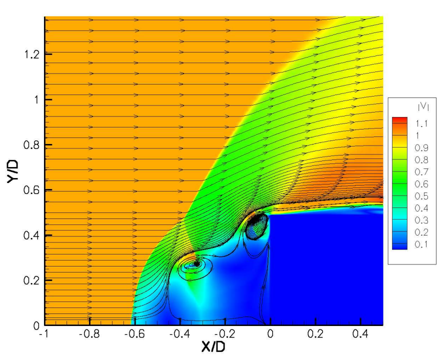

(e) t = 53.4

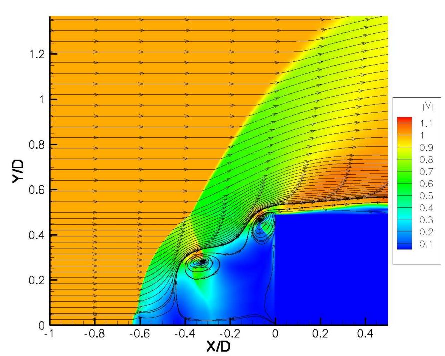

(f) t = 53.5

Figure 5.104: $L/D = 2$ Filament Streamlines

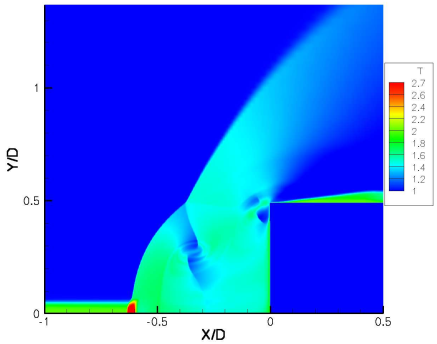

(a) t = 49.5, point 1

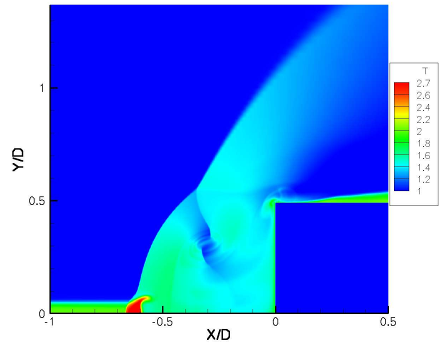

(b) t = 49.7, point 2

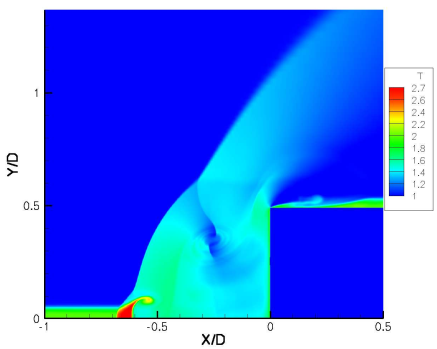

(c) t = 49.9, point 3

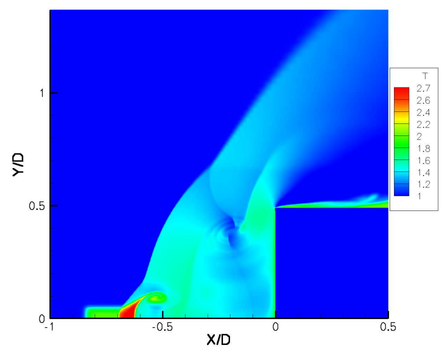

(d) t = 50.2

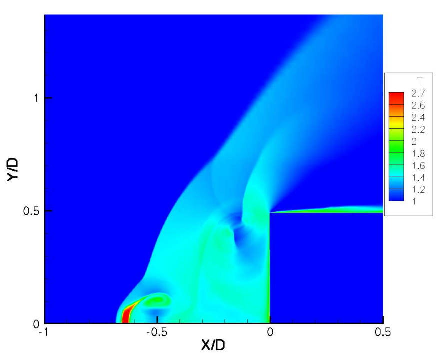

(e) t = 50.4, point 4

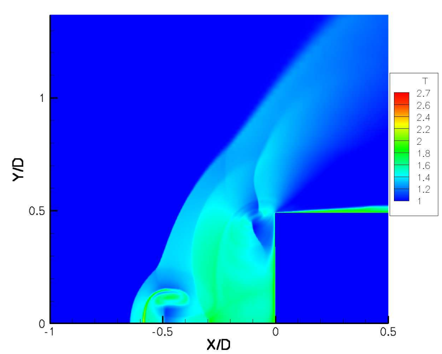

(f) t = 50.6, point 5

Figure 5.105: $L/D = 2$ Temperature Contours

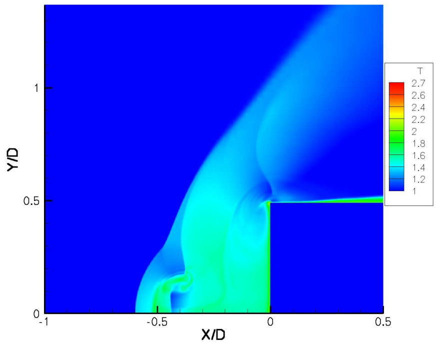

(a) t = 50.9

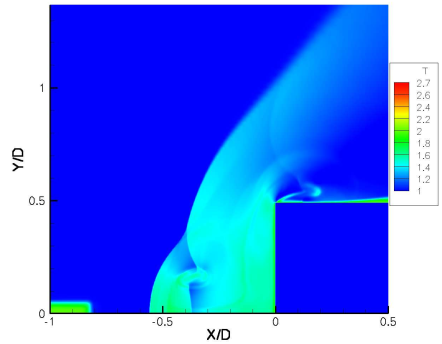

(b) t = 51.2

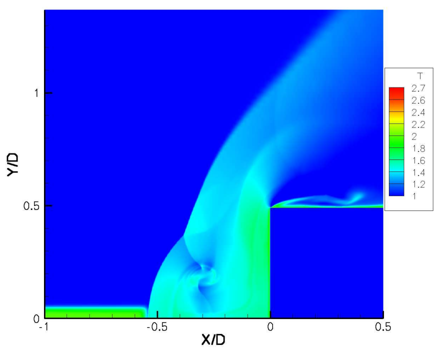

(c) t = 51.5

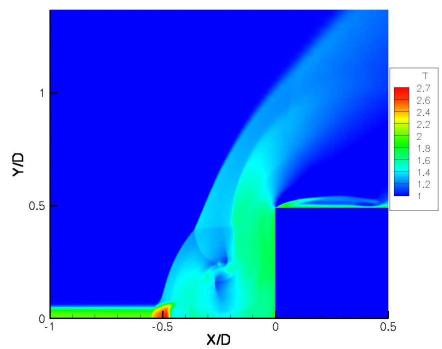

(d) t = 51.7

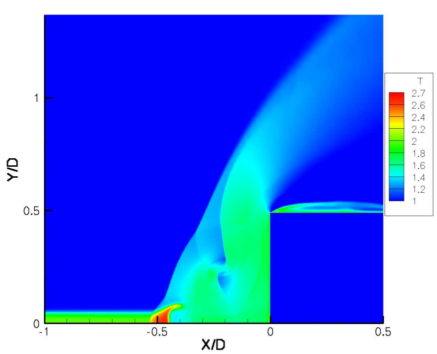

(e) t = 51.9, point 6

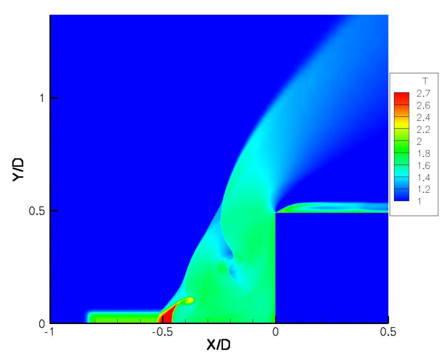

(f) t = 52.2

Figure 5.106: $L/D = 2$ Filament Temperature Contours

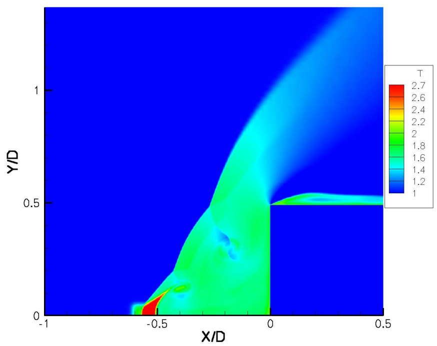

(a) t = 52.4

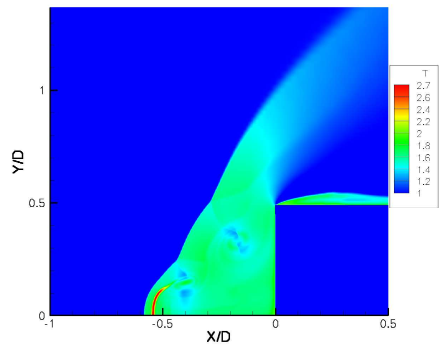

(b) t = 52.6

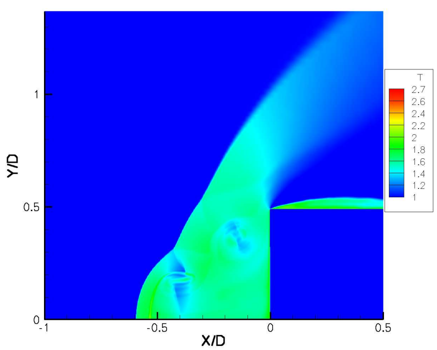

(c) t = 52.9

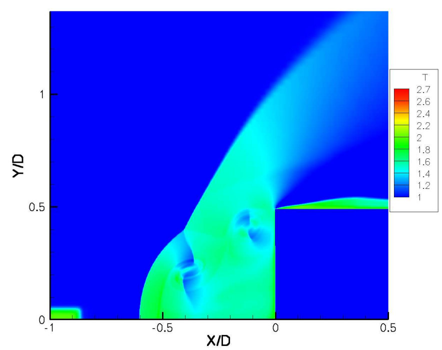

(d) t = 53.1

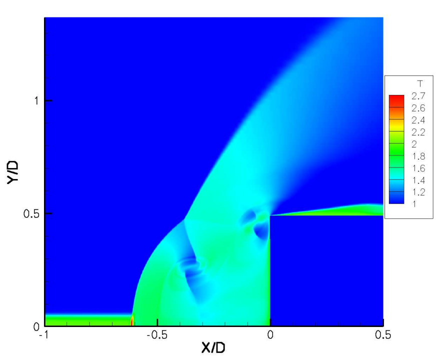

(e) t = 53.4

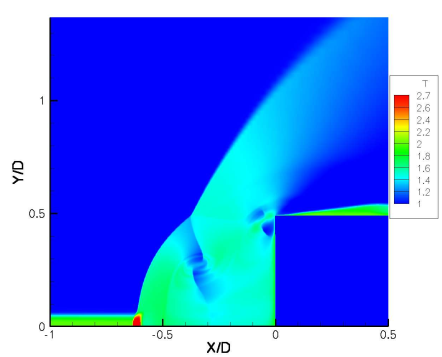

(f) t = 53.5

Figure 5.107: $L/D = 2$ Filament Temperature Contours

5.2.5 $L/D = 4$ Filament

Statistically Stationary State

The dimensionless heat transfer to the front face of the cylinder and its root mean square are plotted in Figures 5.108 and 5.109. Figure 5.108 shows the mean and instantaneous heat transfer to the front face of the cylinder. The instantaneous heat transfer to the front face of the cylinder are periodic at 20 dimensionless time units. The root mean square of the heat transfer to the front face of the cylinder, graphed in Figure 5.109, is periodic at 30 dimensionless time units. These two parameters are good evidence that the case has reached a statistically stationary state by a dimensionless time of 30.

The instantanous, mean and root mean square of dimensionless centerline pressure are graphed in Figures 5.110 and 5.111. The instantaneous pressure is periodic in time. The mean of the centerline pressure in time has reached a steady value in 40 dimensionless time units. The root mean square of the dimensionless centerline pressure also reaches a statistically stationary point by 40 dimensionless time units. The statistically stationary state for the dimensionless centerline pressure has been reached in 40 dimensionless time units.

The power spectrum of the dimensionless heat transfer is shown in Figure 5.112. Two peak frequencies are seen. The highest frequency occurs at zero because the power spectrum was performed on the dimensionless heat transfer variable and not of the perturbation. The mean frequency is represented at the zero frequency. The other peak frequncy occurs at 0.25, which is the vortex shedding frequency behind the shock layer. This implies that each filament pulse consitutes one cycle of heat transfer to the front face of the cylinder.

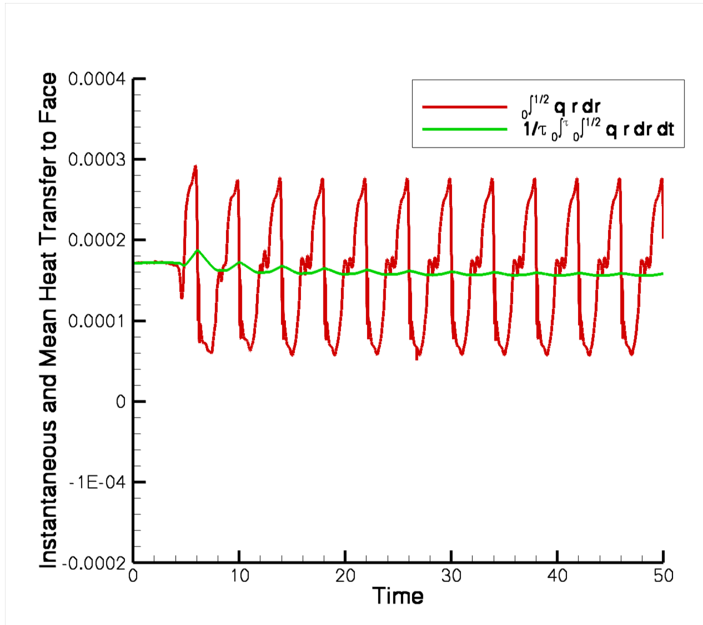

Figure 5.108: $L/D = 4$ Mean and Instantaneous Heat Transfer to Front of Body

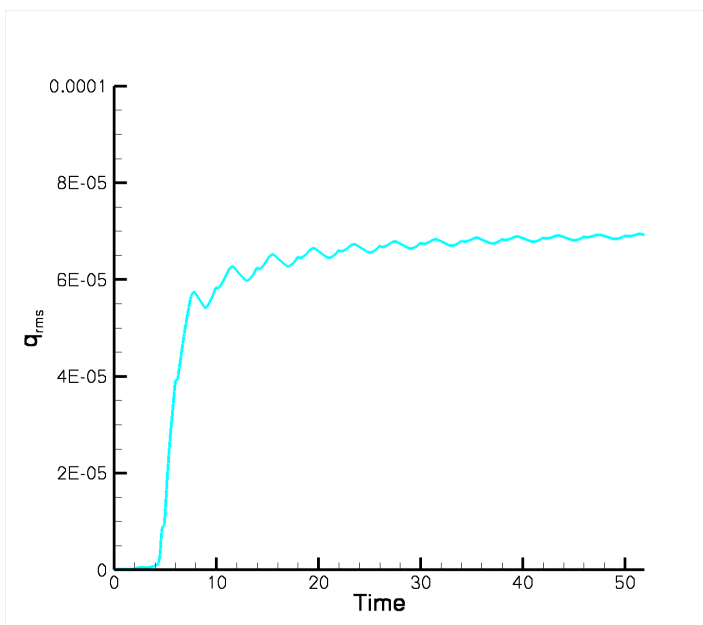

Figure 5.109: $L/D = 4$ Root Mean Square of Heat Transfer to Front of Body

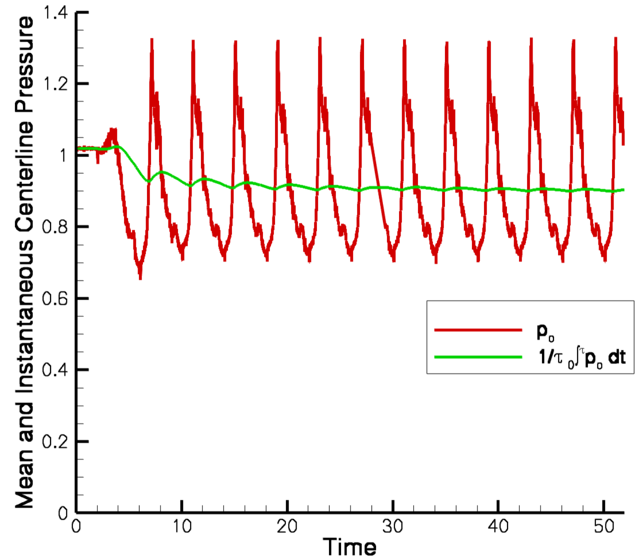

Figure 5.110: $L/D = 4$ Filament Mean and Instantaneous Stagnation Pressure

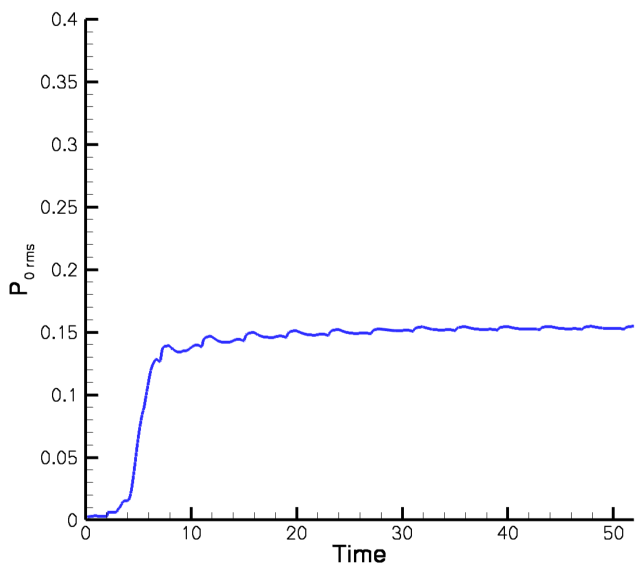

Figure 5.111: $L/D = 4$Filament Root Mean Square of Stagnation Pressure

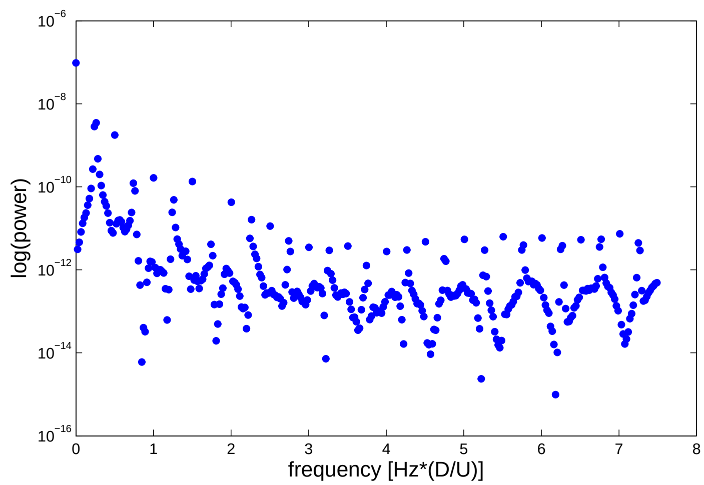

Figure 5.112: $L/D = 4$ Filament Power Spectrum of Dimensionless q

Efficiency, Effectiveness and Heat Transfer

The drag reduction efficiency, effectiveness and heat transfer to cylinder face parameters are graphed in Figures 5.113, 5.114 and 5.115, respectively. The total drag is reduced by 10%. The effectiveness of the drag reduction is lower than the previous cases and the efficiency is 104, lower than the $L/D = 2$ case. The heat transfer to the front face is reduced by 9%. The heated filament reduces the heat transfer to the front face of the cylinder. This result is explained further in the analysis of the flow contours.

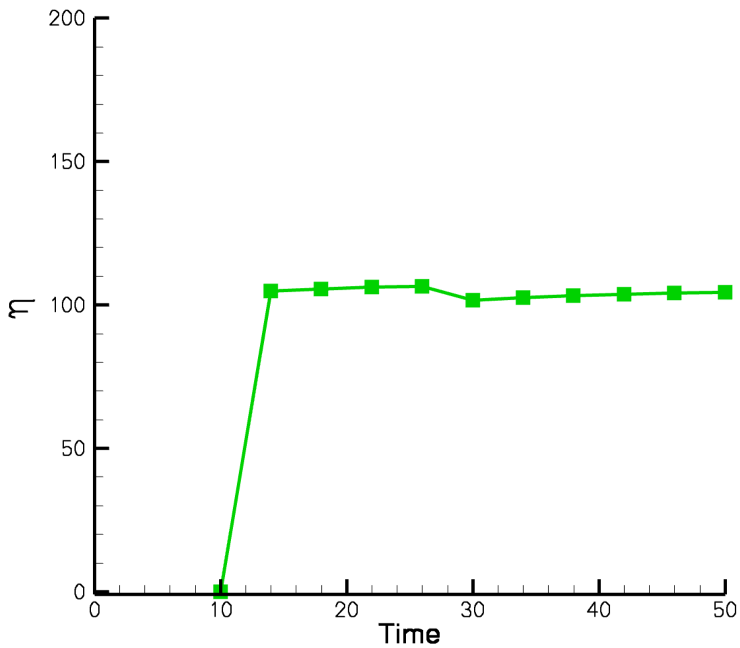

Figure 5.113: $L/D = 4$ Filament Efficiency Parameter

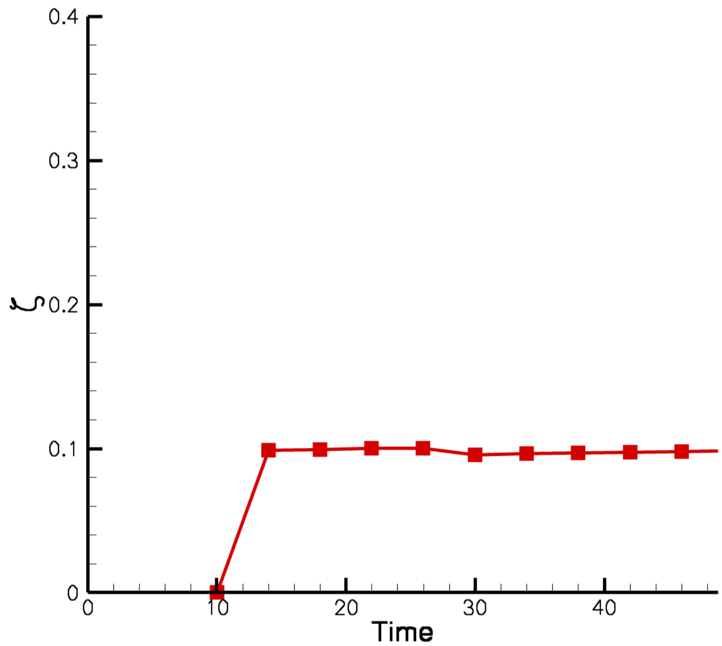

Figure 5.114: $L/D = 4$ Filament Effectiveness Parameter

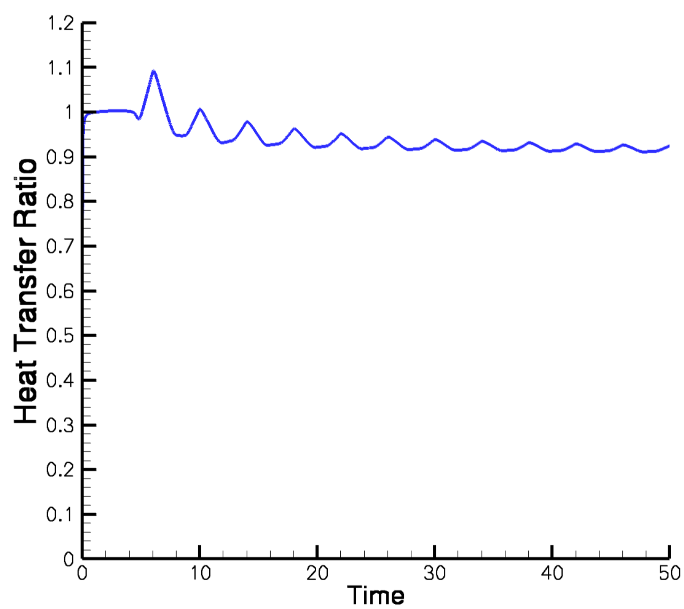

Figure 5.115: $L/D = 4$ Filament Heat Transfer to Front Face Parameter

Contours of Flow

The contours for the pulsed case of period 4 are shown in Figures 5.116 through 5.130. The contours over one heat transfer cycle are shown at the statistically stationary state. One cycle of heat transfer is determined by the graph of heat transfer versus time. One heat transfer cycle for this case is 4 dimensionless time units.

The major flow features are depicted in the density gradient and pressure contours, Figures 5.116 through 5.117 and 5.118 through 5.119, respectively. Shock waves and contact surfaces are both visible in the density gradient contours. The pressure contours distinguish the two flow features. The major flow features at the beginnning of the heat transfer cycle are labeled in Figure 5.116(a). The heated filament can be seen entering from the inflow boundary at the centerline. An upstream lensing of the bow shock occurs where the heated filament intersects the bow shock. Behind the bow shock, the contact surfaces between the heated filament and surrounding flow are shown. Because the heated filament is at a reduced Mach number, its velocity behind the bow shock is lower than the surrounding flow, which makes the contact surface at the top of the heated filament a shear layer within the shock layer. This can be verified with the Rankine Hugoniot conditions. The shear layers create a vortex downstream of the bow shock. This is seen in Figures 5.116(a) through 5.116(f). Each filament becomes a vortex with a trailing contact surface behind the bow shock. These vortices convect with the surrounding flow toward the cylinder corner. A vortex from the previous fillament is near the cylinder corner in Figure 5.116(a). The flow accelerates as it passes over the cylinder corner. An expansion fan sits at the top of the cylinder corner. Downstream of the expansion fan a recompression shock is formed. The recompression shock turns the flow parallel to the cylinder.

The minor flow features can be seen in the numerical Schlieren images in Figures 5.120 through 5.121. The progression in time of the heated filament entering the shock layer seen in Figure 5.120(a) is followed through a cycle to understand how minor flow features develop.

Figure 5.120(a) The heated filament encounters the the bow shock. Because of the reduced Mach number within the heated filament, the shock wave lenses forward upon contact.

Figure 5.120(c) The shear layer contact surface is unstable and creates a vortex downstream of the bow shock. A small lambda shock is seen where the lensed shock meets the unlensed shock.

Figure 5.120(f) The end of the filament has entered the shock layer. The filament has become a vortex trailed by a contact boundary from the end of the filament. The lensing of the bow shock has decreased. The bow shock has not yet returned to its undisturbed state. The bow shock is curved around the area surrounding the vortex just downstream of the bow shock. A small shock appears ahead of the cylinder corner. To explore how this shock is created, the same image is shown with the steady state bow shock location and streamlines in Figure 5.122. The bow shock of the current case is upstream of the steady state bow shock location. The streamlines of the current case are shown in black and the steady state streamlines emanating from the same locations are shown in white. Compared to the steady state streamlines, the streamlines of this case are less inclinded after the bow shock. The current streamlines near the corner bend upward just ahead of the expansion fan. At the same location the steady state streamlines smoothly expand in the vicinity of the corner. The shock appears just ahead of the cylinder corner where the streamlines turn.

Figure 5.121(a) The new vortex has convected toward the cylinder corner. The bow shock lensing has reduced and the entire bow shock has moved downstream. The shock ahead of the corner has grown and moved upstream toward the bow shock. A weak shock has formed at the bottom of the vortex downstream of the contact boundary. This is due to the flow under the vortex meeting the flow coming in through the bow shock.

Figure 5.121(b) The shock ahead of the corner has moved upstream and merged with the bow shock. The bottom of the shock has become entrained in the vortex.

Figure 5.121(c) The vortex has convected toward the cylinder corner. The vortex influences the direction of the flow behind the bow shock. Because the bow shock determines the amount of turning of the flow, the direction of the flow behind the bow shock influences the shape of the bow shock. Thus, as the vortex convects toward the corner, the bow shock changes shape. The circular nature of the flow behind the bow shock has created a curved bow shock in the vicinity of the vortex. The most prominent shock downstream of the bow shock is the lambda shock between the curved part of the bow shock and the vortex. The contact discontinuity remaining from the heated filament trails the vortex, remaining attached to the symmetry boundary and weakening as it grows.

Figure 5.121(f) By this time the vortex has convected half way to the cylinder face from the bow shock. The shocks at the top and the bottom of the vortex have weakend significantly and the bow shock has begun to restore to its steady state shape. There are some residual density gradients around the vortex, however, the vortex is largely independent of the vortex that preceeded it in the flow domain. Each heat transfer cycle represents the convection of one vortex across the shock layer.

The velocity magnitude contours are shown in Figures 5.123 through 5.124. The core of the vortex is at a very low velocity. The top of the vortex has a high velocity. The high velocity flow decelerates immediately just before the downstream side of the vortex. This is the location of the contact surface from the downstream vortex. Below the contact surface is low velocity flow, which accelerates as it winds around the bottom of the vortex. The flow quickly decelerates again at the bottom upstream side of the vortex, as it encounters the weak shock at the bottom of the vortex. The contact surface at the upstream side of the vortex separates the low velocity flow from the higher velocity flow at the top of the vortex.

Reduction of heat transfer to the front face of the cylinder is due to the formation and convection of vortices over the cylinder corner. This can be seen by evaluating the vorticity magnitude, streamlines of flow and temperature contours, as graphed in Figures 5.125 through 5.126, Figures 5.127 through 5.128 and Figures 5.129 through 5.130, respectively. The major points in a heat transfer cycle are labeled in Figure 5.131.

Point 1 Point 1 represents a maximium point of heat transfer to the cylinder face. Previously, vortex 0 had been approaching the cylinder face. As vortex 0 approached the face, the area of influence of the convection by vortex 0 on the cylinder face was reducing and a stagnation region was growing at the center of the cylinder face. Point 1 represents the time of maximum heat transfer, which occurs just before the expansion fan that sits in front of vortex 0 contacts the cylinder face. As the expansion fan interacts with the cylinder face, it dramatically increases conduction and advection of heat away from the face. Point 1 is when vortex 0 is just ahead of the cylinder corner, as seen in Figure 5.125(a). The graph of streamlines and velocity magnitude show that the area of high velocity in front of the corner begins to interact with the cylinder corner at this instant in Figure 5.127(a).

Point 2 As the expansion fan just ahead of vortex contacts the cylinder face, the heat transfer to the cylinder face drops dramatically. The heat transfer reduces more as the vortex and expansion fan move closer to the corner, as the corner is the point of maximum heat transfer to the cylinder face. At point 2, however, there is a temporary increase in heat transfer rate to the cylinder face, as the shock wave at the bottom of the vortex contacts the cylinder face. This is best seen in the density gradient graph 5.120(b).

Point 3 As vortex 0 convected over the cylinder, vortex 1 was just downstream of the bow shock. Vortex 1 increased the velocity of the flow just ahead of the cylinder face by forcing air down at the front of the vortex (the downstream side). The flow was then forced to sweep over the entire front of the cylinder face. This is seen in Figures 5.127(c) through 5.127(f). At point 3, however, vortex 1 begins to convect upward toward the cylinder corner. At point 3, the streamlines pulled down in front of the vortex sweep up a small fraction of the cylinder face. This is seen in Figure 5.128(a). After point 3, a stagnation region builds across the cylinder face, starting at the center of the face. This is seen in Figures 5.128(b) through 5.128(c).

Point 4 The stagnation region continues to build, decreasing advection of heat away from the face and increasing heat transfer to the front of the face until just after point 4.

At point 4, a small counterclockwise rotating vortex builds just ahead of the cylinder face. This can be seen in Figure 5.128(d). The counterclockwise vortex moves toward the center of the cylinder, which temporarily increases advection of heat away from the center of the cylinder.

Point 5 Though the streamlines of Figure 5.128(f) don't capture the counterclockwise vortex near the cylinder wall, it shows up in Figure 5.126(f). The larger vortex, vortex 1, has drawn the smaller vortex away from the wall. The smaller vortex no longer exerts an influence on the heat transfer rate to the cylinder away from the cylinder face. Thus, as vortex 1 moves upward and the stagnation region below it continues to grow, the heat transfer to the front face of the cylinder increases.

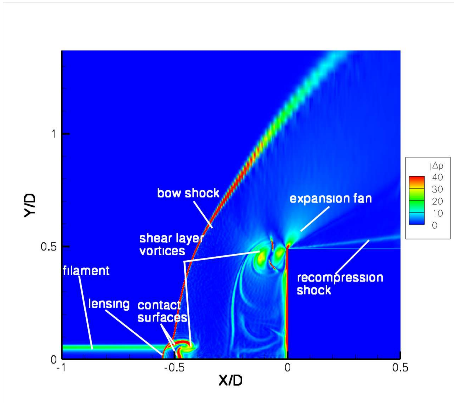

(a) t = 45.84

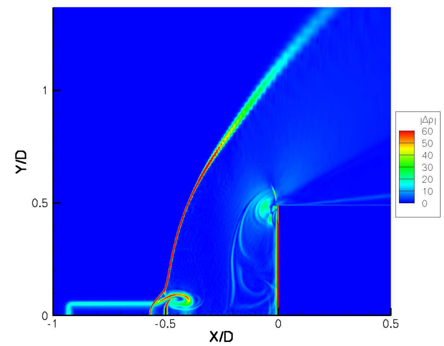

(b) t = 46.07

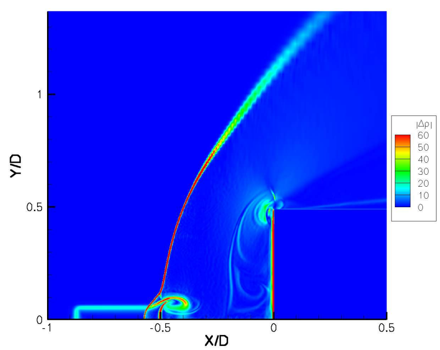

(c) t = 46.17

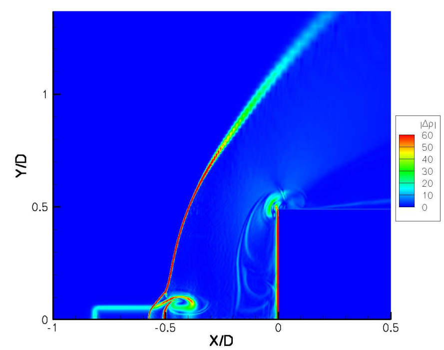

(d) t = 46.18

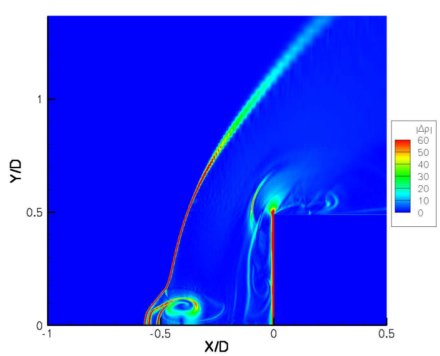

(e) t = 46.48

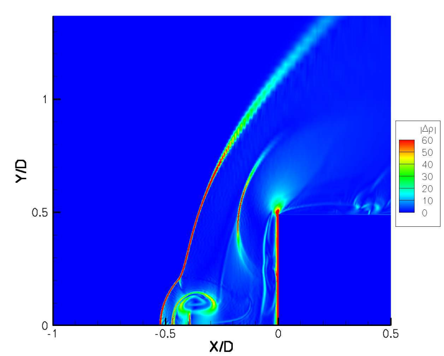

(f) t = 46.79

Figure 5.116: $L/D = 4$ Filament Density Gradient Contours

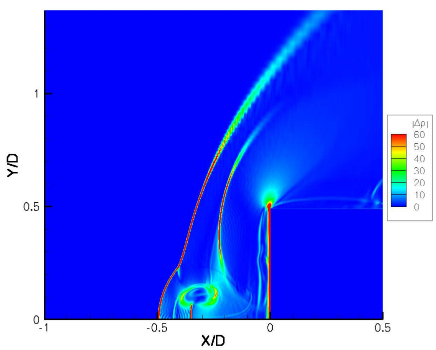

(a) t = 46.99

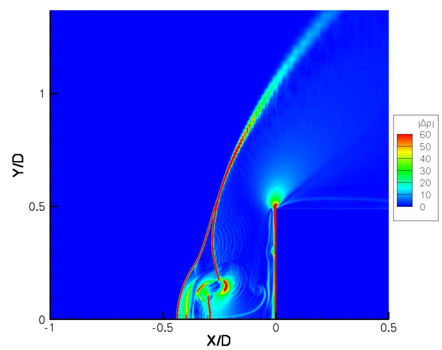

(b) t = 47.34

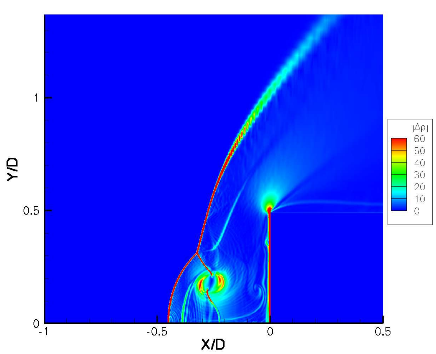

(c) t = 47.68

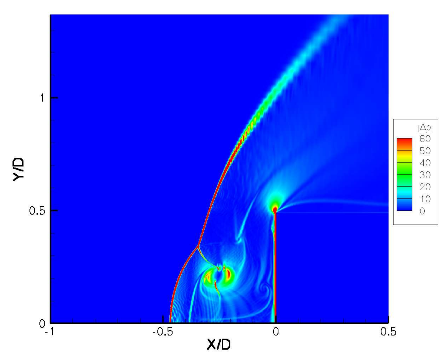

(d) t = 47.96

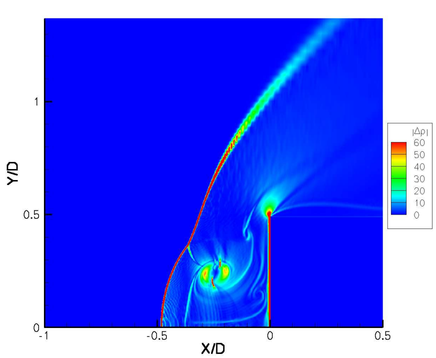

(e) t = 48.23

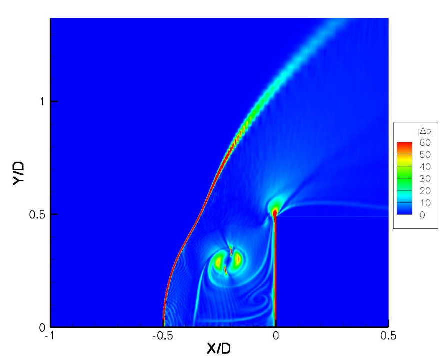

(f) t = 48.58

Figure 5.117: $L/D = 4$ Filament Density Gradient Contours

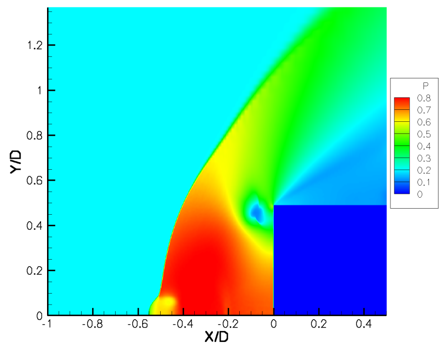

(a) t = 45.84

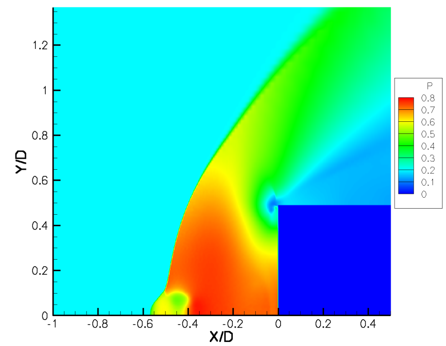

(b) t = 46.07

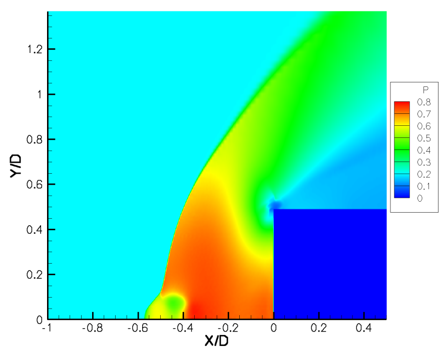

(c) t = 46.17

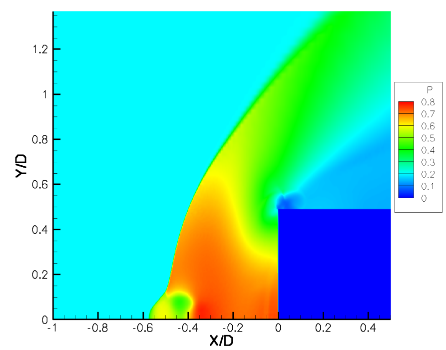

(d) t = 46.18

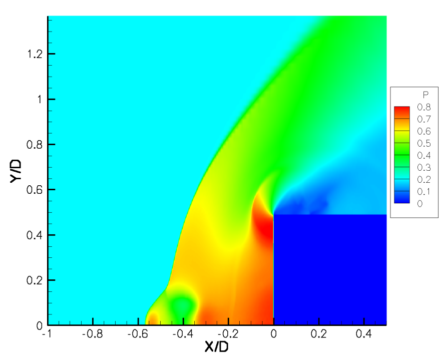

(e) t = 46.48

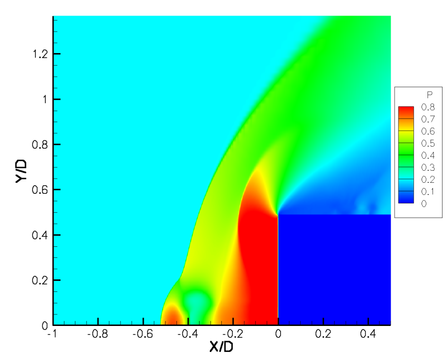

(f) t = 46.79

Figure 5.118: $L/D = 4$ Filament Pressure Contours

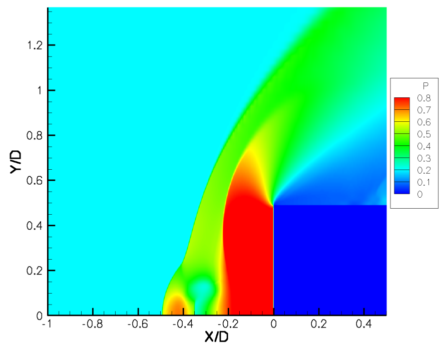

(a) t = 46.99

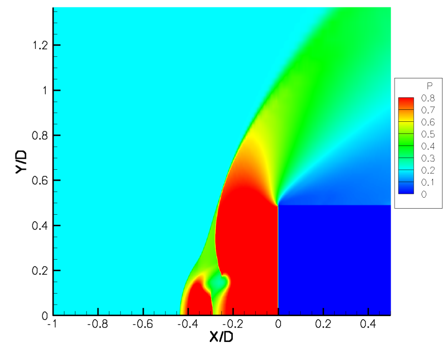

(b) t = 47.34

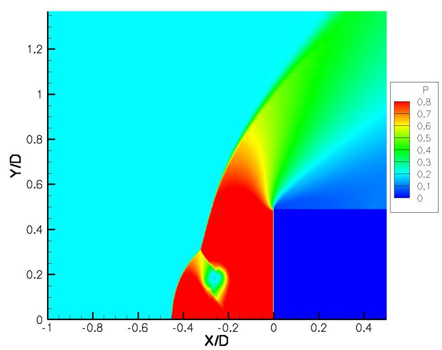

(c) t = 47.68

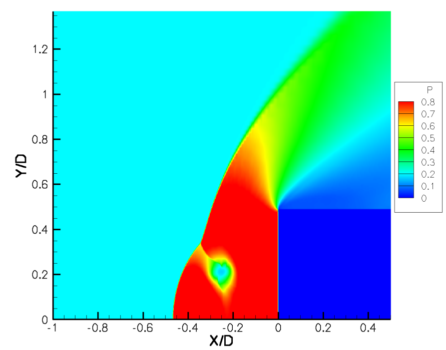

(d) t = 47.96

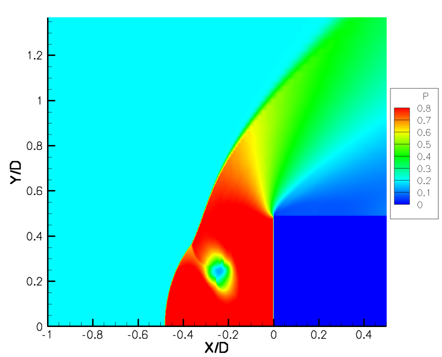

(e) t = 48.23

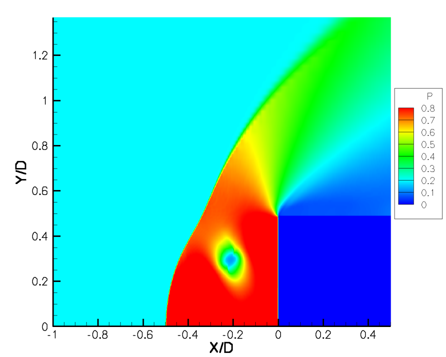

(f) t = 48.58

Figure 5.119: $L/D = 4$ Filament Pressure Contours

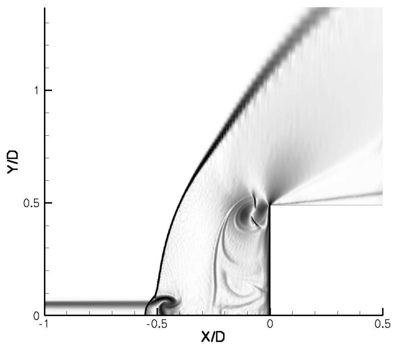

(a) t = 45.84

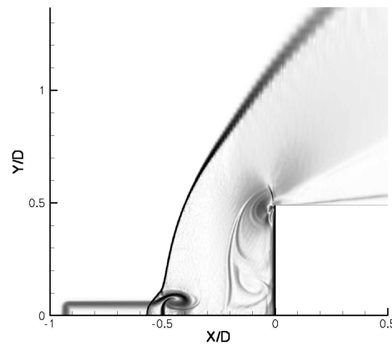

(b) t = 46.07

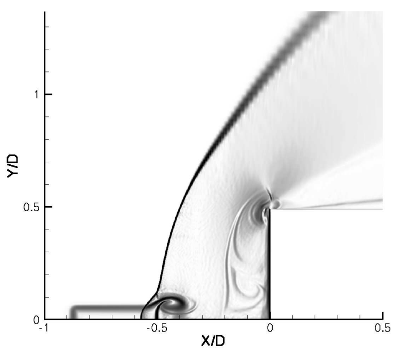

(c) t = 46.17

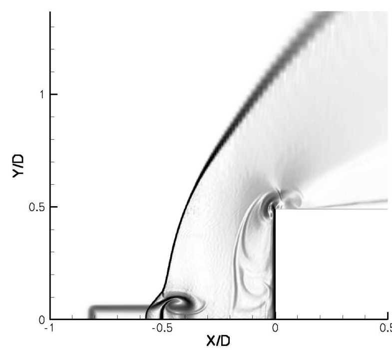

(d) t = 46.18

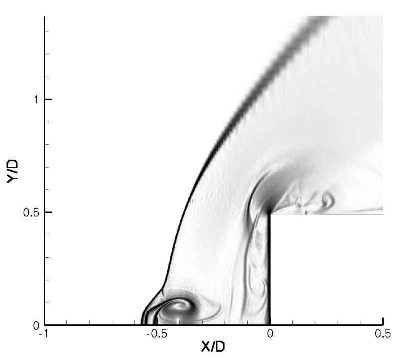

(e) t = 46.48

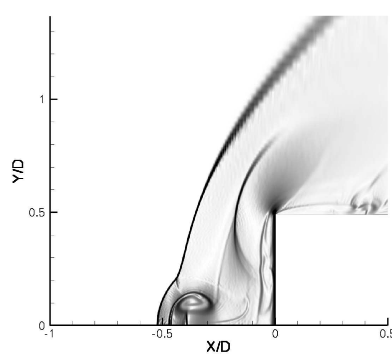

(f) t = 46.79

Figure 5.120: $L/D = 4$ Filament Numerical Schlieren Images

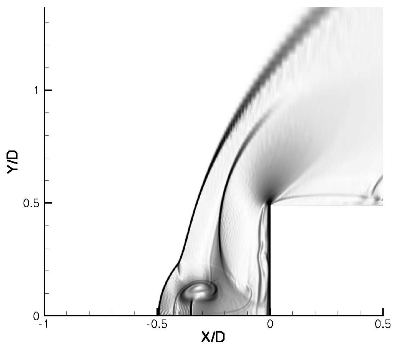

(a) t = 46.99

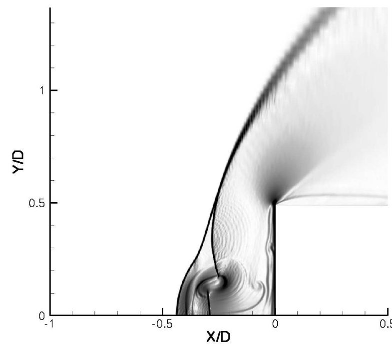

(b) t = 47.34

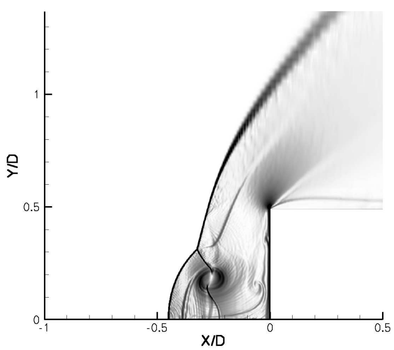

(c) t = 47.68

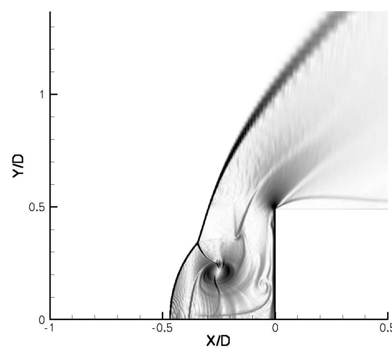

(d) t = 47.96

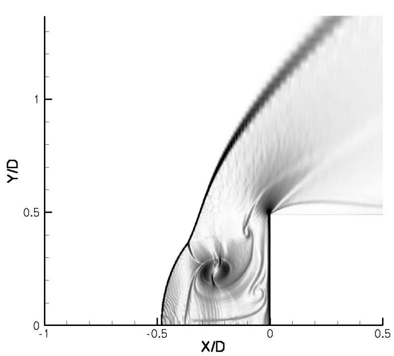

(e) t = 48.23

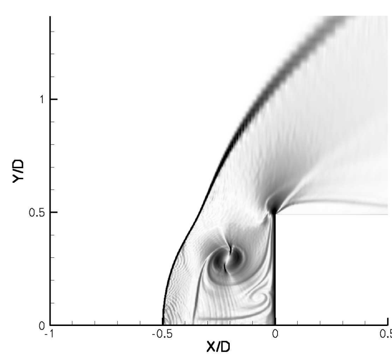

(f) t = 48.58

Figure 5.121: $L/D = 4$ Filament Numerical Schlieren Images

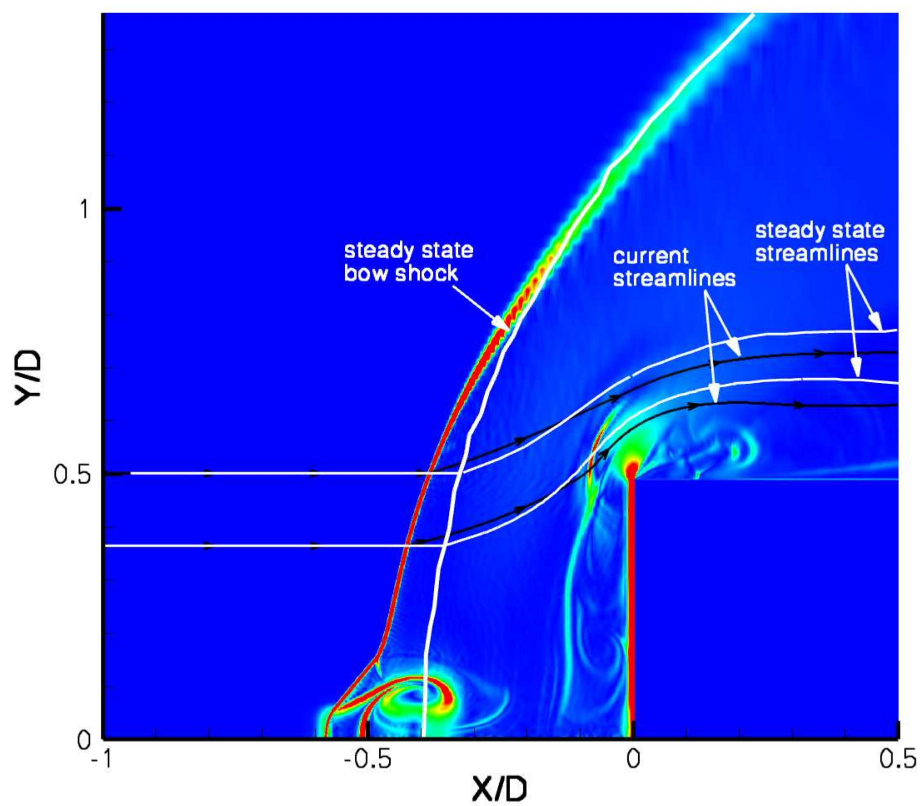

Figure 5.122: Density Gradient Magnitude Plot at $t = 46.48$ with Steady State Streamline and Bow Shock Location Shown

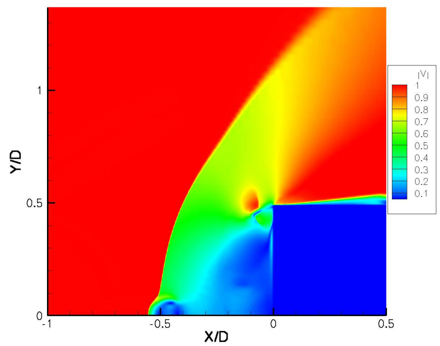

(a) t = 45.84

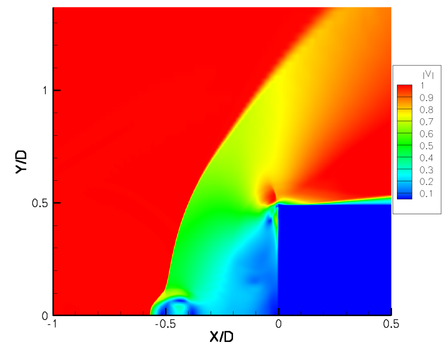

(b) t = 46.07

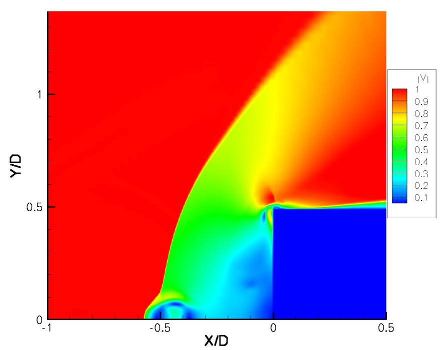

(c) t = 46.17

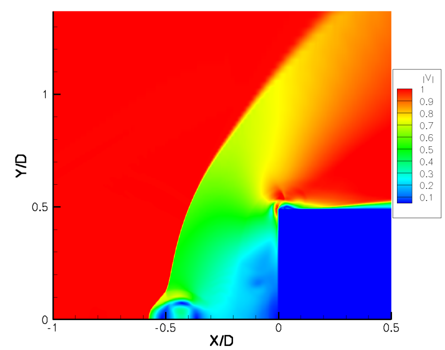

(d) t = 46.18

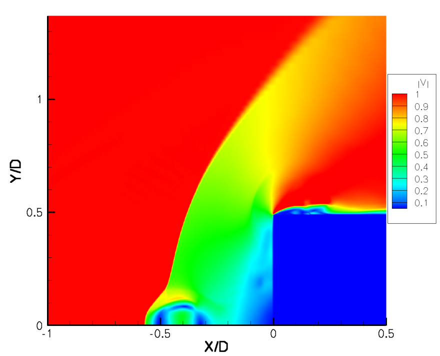

(e) t = 46.48

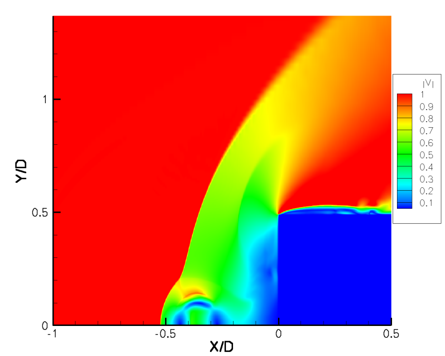

(f) t = 46.79

Figure 5.123: $L/D = 4$ Filament Velocity Magnitude Contours

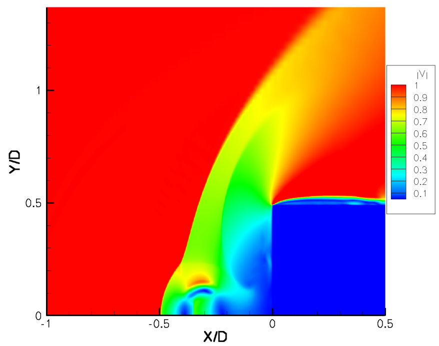

(a) t = 46.99

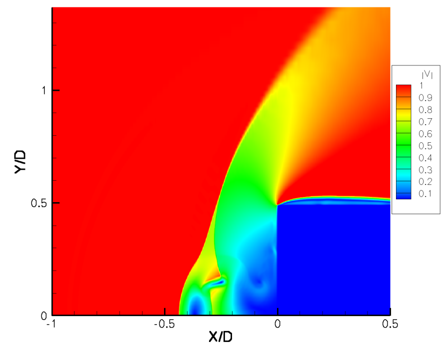

(b) t = 47.34

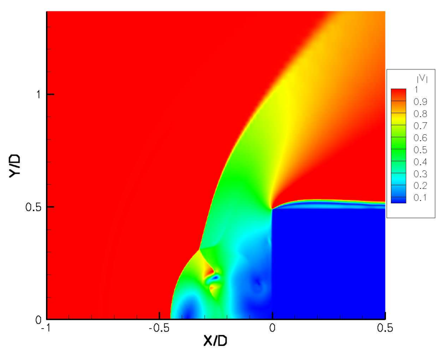

(c) t = 47.68

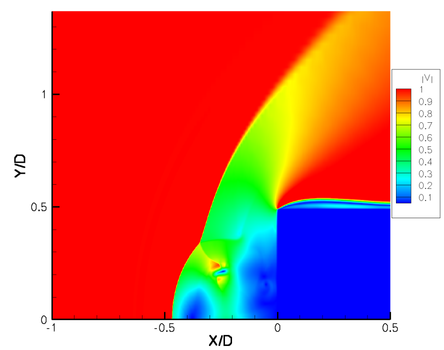

(d) t = 47.96

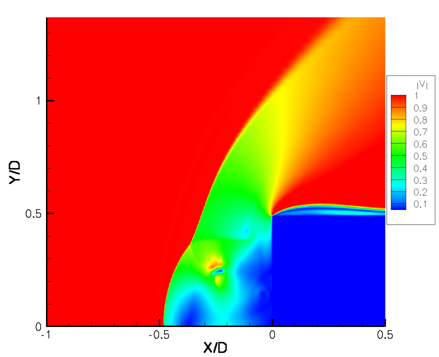

(e) t = 48.23

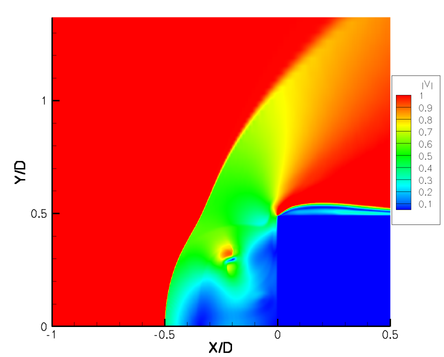

(f) t = 48.58

Figure 5.124: $L/D = 4$ Filament Velocity Magnitude Contours

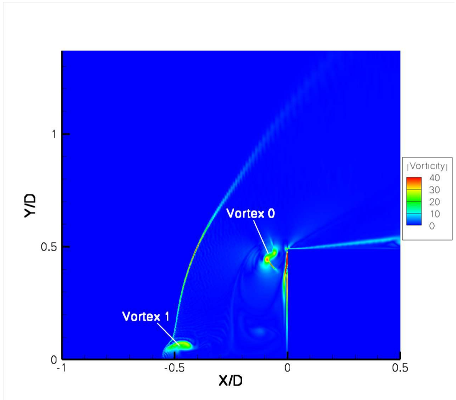

(a) t = 45.84, point 1

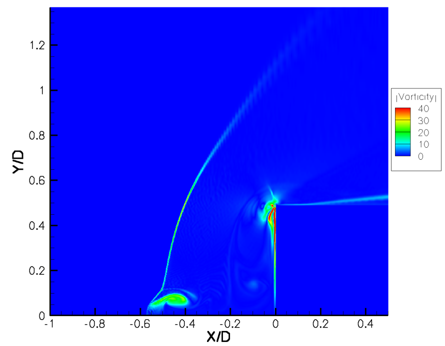

(b) t = 46.07, point 2

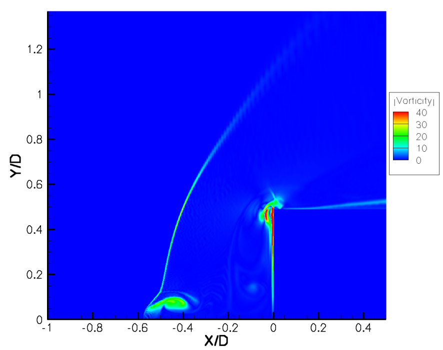

(c) t = 46.17

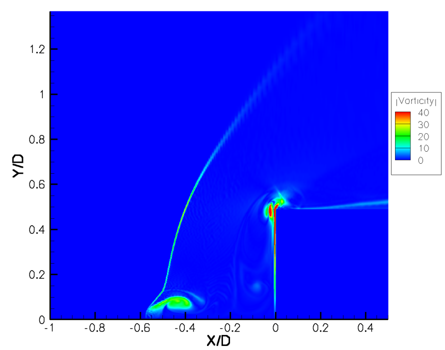

(d) t = 46.18

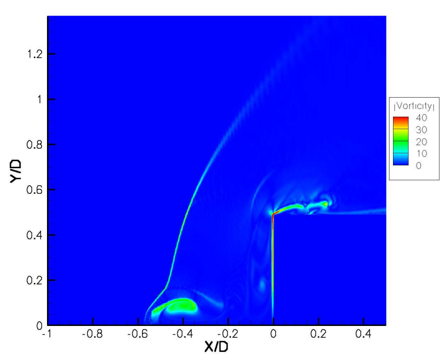

(e) t = 46.48

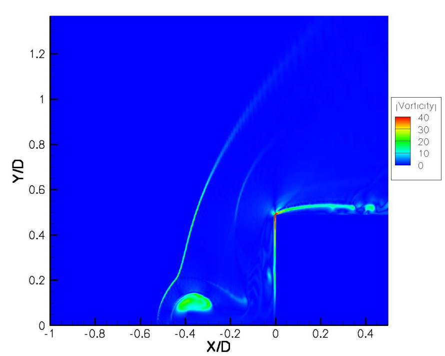

(f) t = 46.79

Figure 5.125: $L/D = 4$ Filament Vorticity Contours

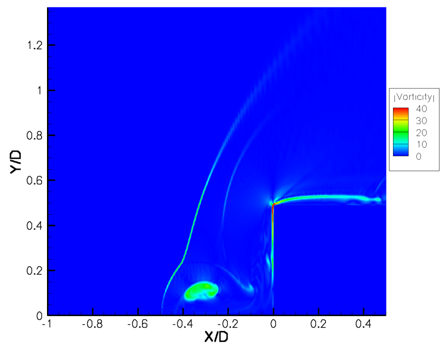

(a) t = 46.99, point 3

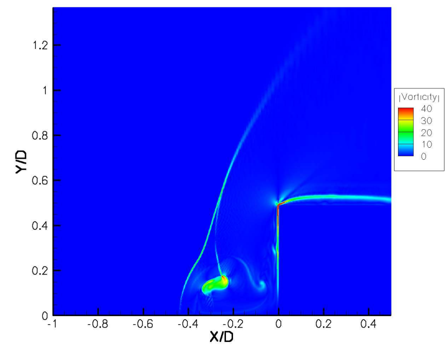

(b) t = 47.34

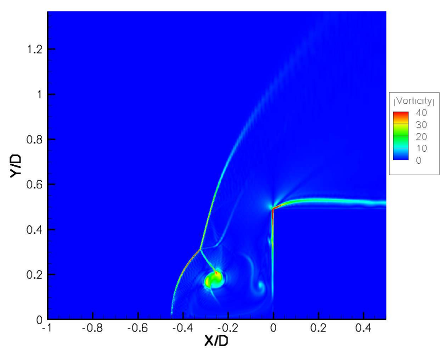

(c) t = 47.68

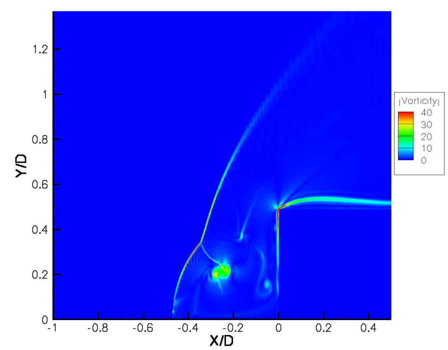

(d) t = 47.96, point 4

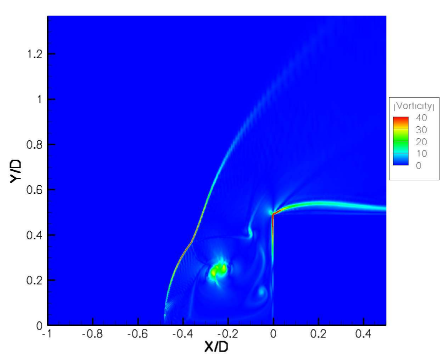

(e) t = 48.23

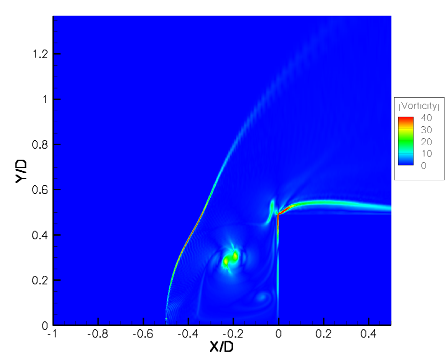

(f) t = 48.58

Figure 5.126: $L/D = 4$ Filament Vorticity Contours

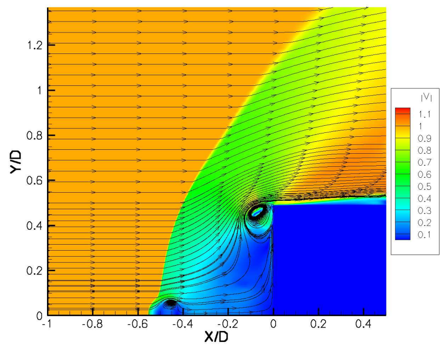

(a) t = 45.84, point 1

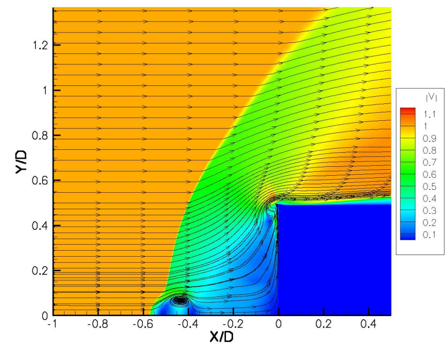

(b) t = 46.07, point 2

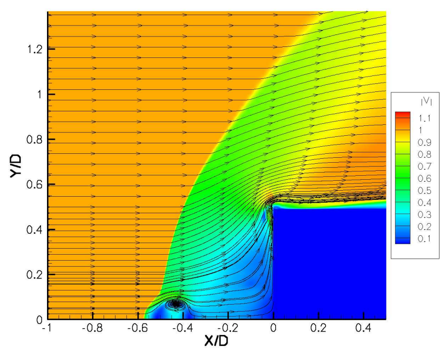

(c) t = 46.17

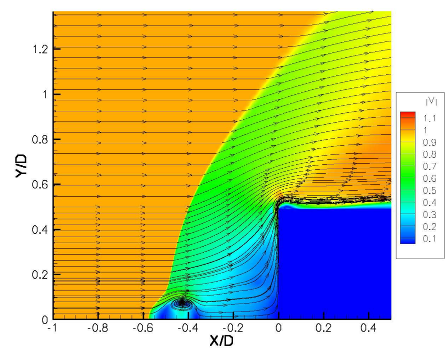

(d) t = 46.18

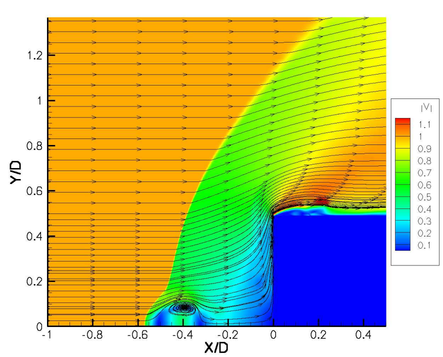

(e) t = 46.48

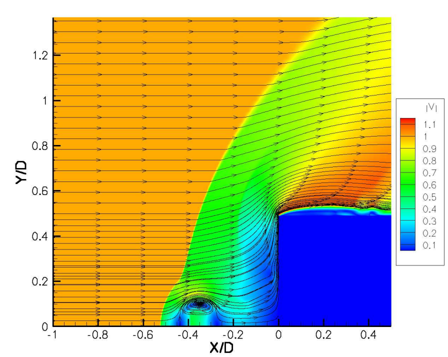

(f) t = 46.79

Figure 5.127: $L/D = 4$ Filament Streamlines

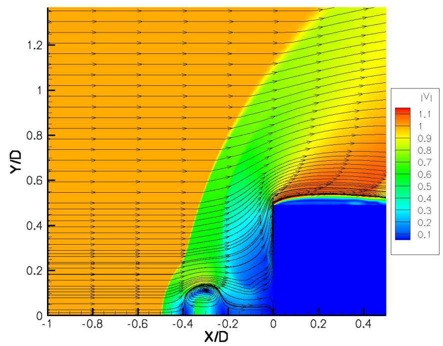

(a) t = 46.99, point 3

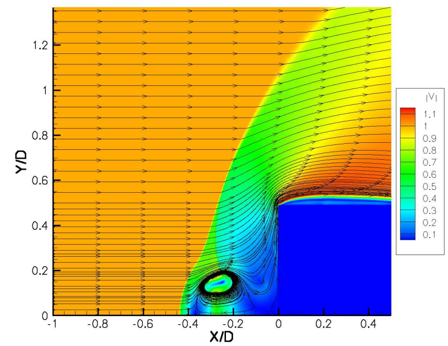

(b) t = 47.34

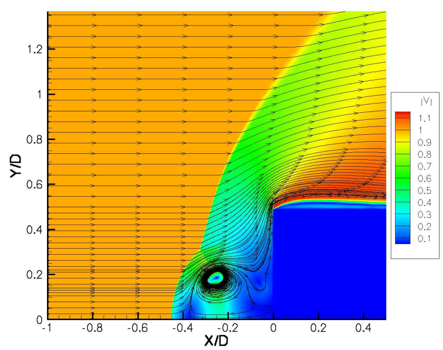

(c) t = 47.68

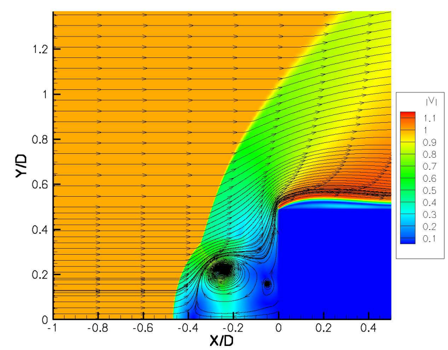

(d) t = 47.96, point 4

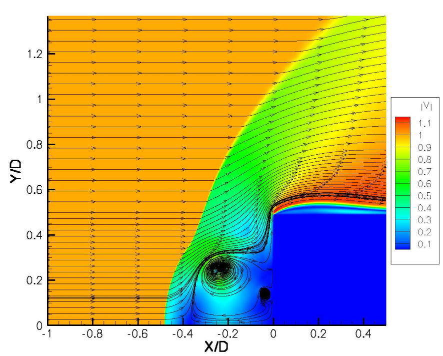

(e) t = 48.23

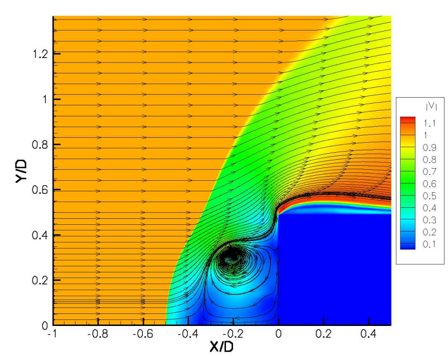

(f) t = 48.58

Figure 5.128: $L/D = 4$ Filament Streamlines

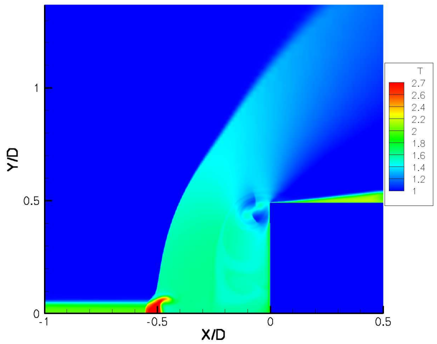

(a) t = 45.84, point 1

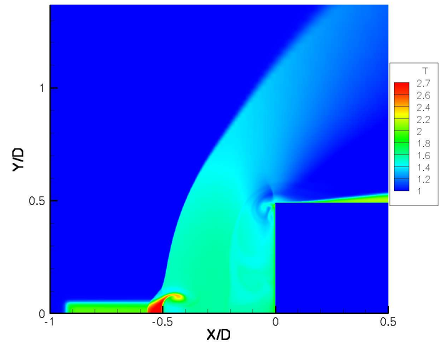

(b) t = 46.07, point 2

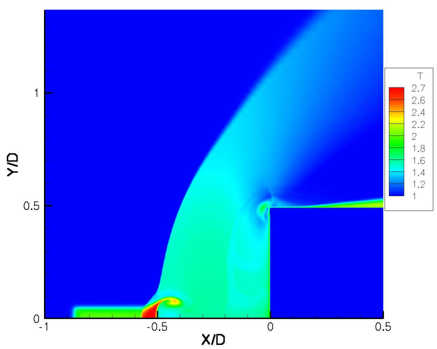

(c) t = 46.17

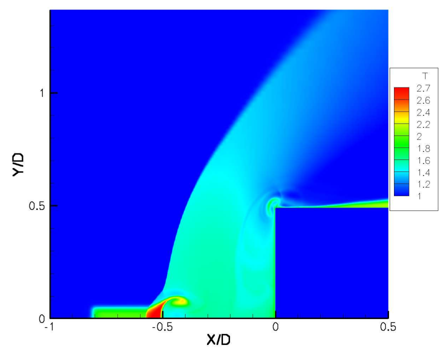

(d) t = 46.18

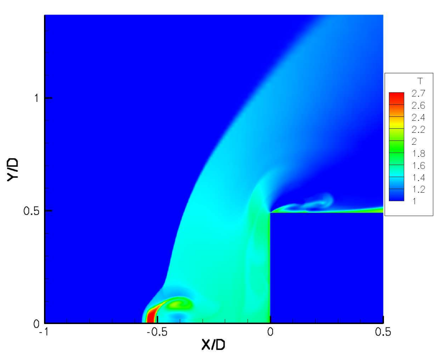

(e) t = 46.48

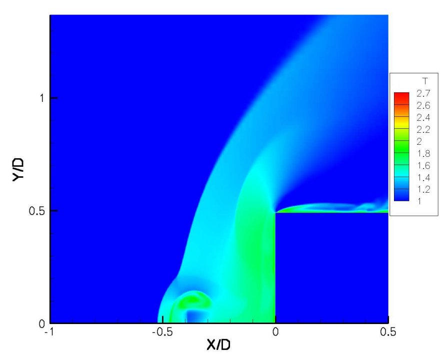

(f) t = 46.79

Figure 5.129: $L/D = 4$ Filament Temperature Contours

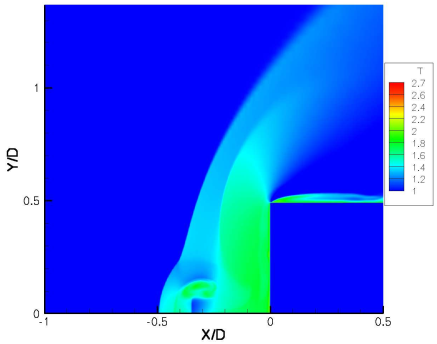

(a) t = 46.99, point 3

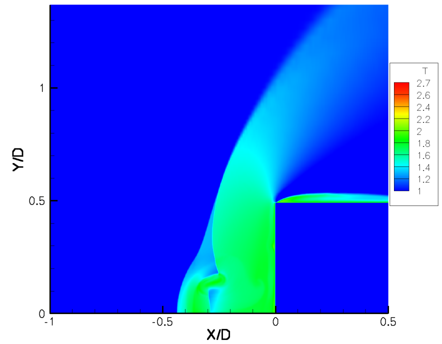

(b) t = 47.34

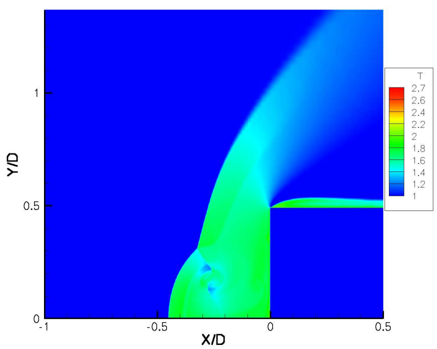

(c) t = 47.68

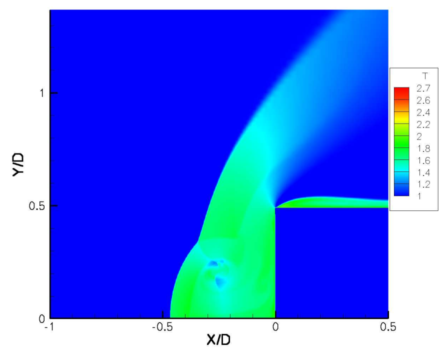

(d) t = 47.96, point 4

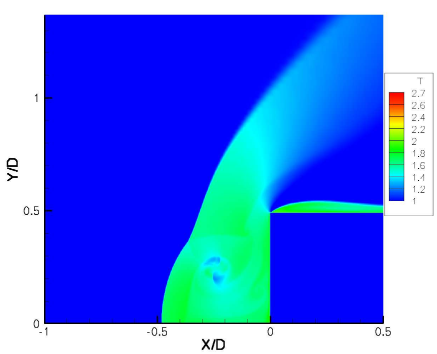

(e) t = 48.23

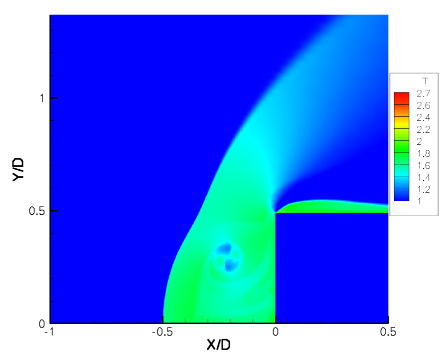

(f) t = 48.58

Figure 5.130: $L/D = 4$ Filament Temperature Contours

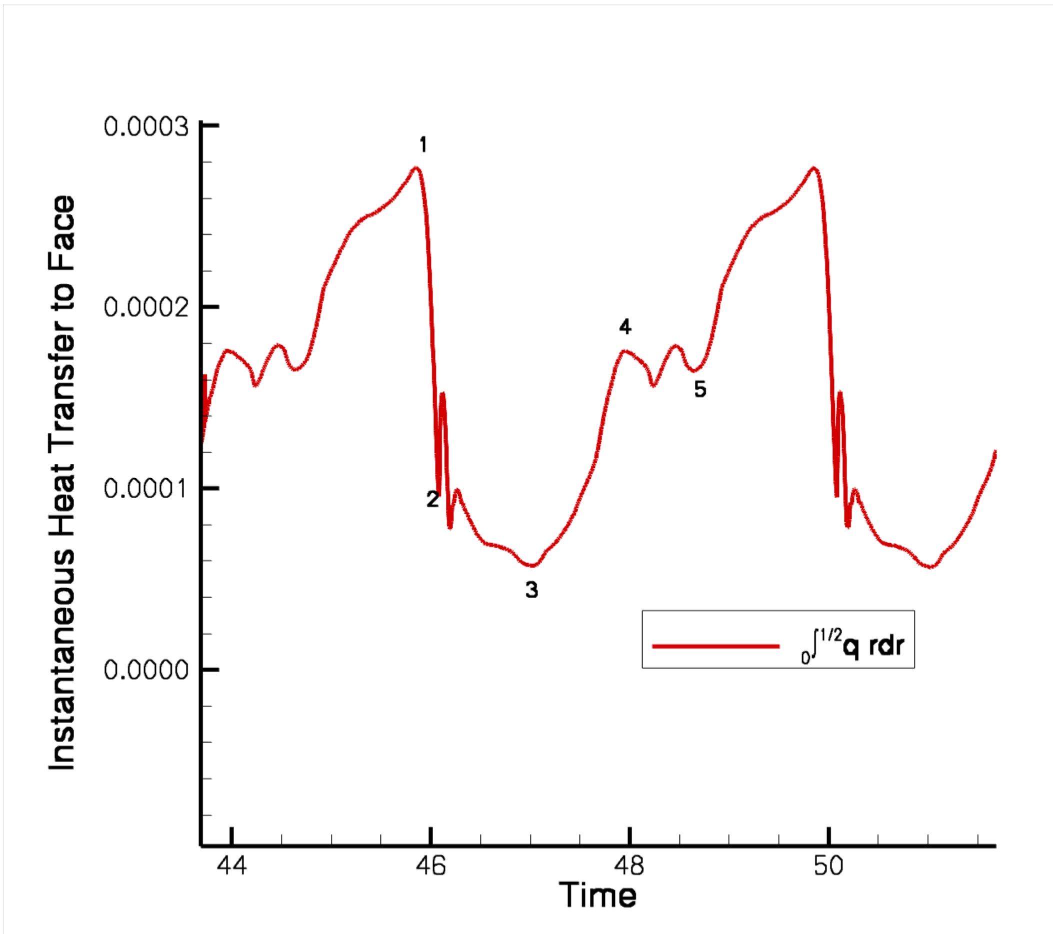

Figure 5.131: $L/D = 4$ Dimensionles Heat Transfer to Cylinder Face Over One Cycle

5.2.6 Summary of Results

The effect of varying the period of the pulsed heated filaments on drag efficiency, effectiveness and heat transfer are evaluated. The efficiency, effectiveness and heat transfer parameter are graphed on three axes in Figure 5.132. The numbers in the figure correspond to the different period of pulsation of heated filaments, as shown in Table 5.4. The efficiency has a peak value for $L/D = 2$. The effectiveness decreases with increasing period. The heat transfer parameter increases with increasing filament pulsation period, as seen in Figure 5.133. However, the heat transfer ratio seems to level off between L/D of 2 and 4. The $L/D = 2$ and 4 cases have the same heat transfer cycle, thus a similar heat transfer reduction is plausible. The distance between filaments is larger for larger periods, as the length of the filaments are the same due to a coupling of the vortices in the $L/D = 2$ case and total independence of vortices in the $L/D = 4$ case. The larger the distance between filaments, the less effective the vortices are at cooling the cylinder face. This levels off where the vortices cease to interact with one another ahead of the cylinder face. The exception to this is the infinitely long filament, which is not as effective at cooling the cylinder face. The effectiveness of drag reduction is plotted against the filament period in Figure 5.134. The effectiveness decreases with increasing period. The larger gaps in between the filaments create large gaps between vortices within the shock layer, which translates to a larger stagnation region in front of the cylinder face. The stagnation region increases the drag. Finally, the efficiency is graphed against the heated filament pulsation period in Figure 5.135. The efficiency exhibits a nonlinear relation with filament pulsation period. The maximum efficiency occurs for a filament period of two.

Table 5.4: Cases Index to Figures

Number in Figure	$\frac{L}{D}$	Color
1	4.0	Red
2	2.0	Red
3	1.33	Red
	∞	Green

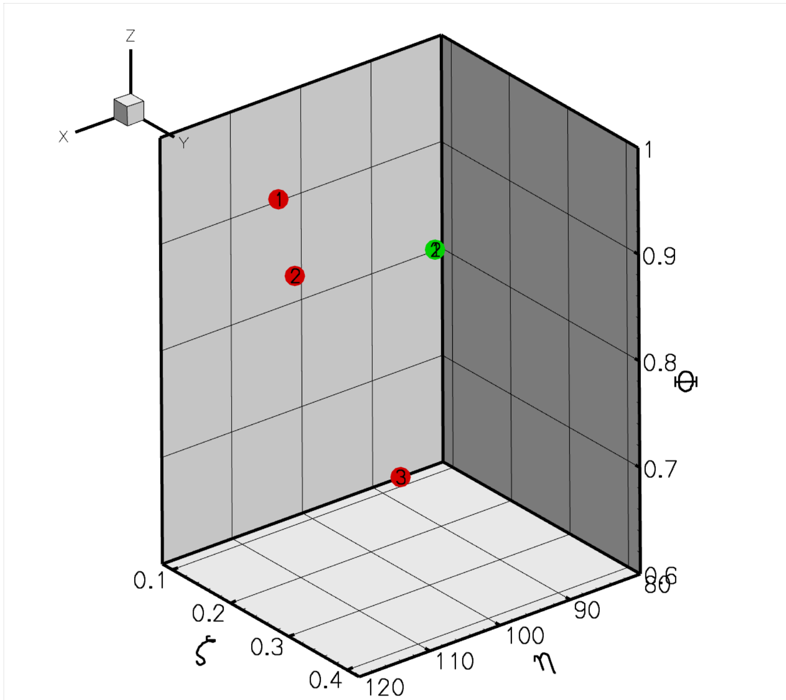

Figure 5.132: Efficiency, Effectiveness Versus Heat Transfer Parameter

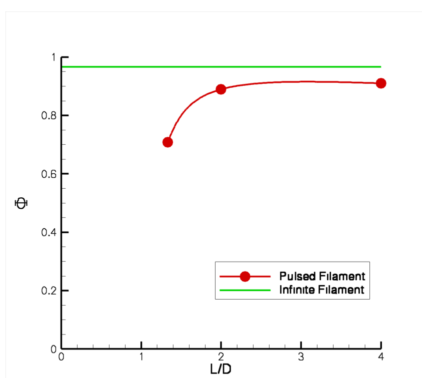

Figure 5.133: Heat Transfer Parameter Versus Period, $\frac{L}{D}$

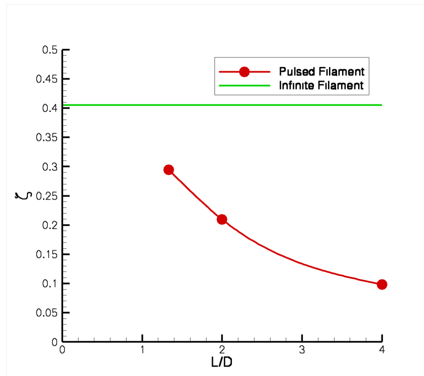

Figure 5.134: Effectiveness Versus Period, $\frac{L}{D}$

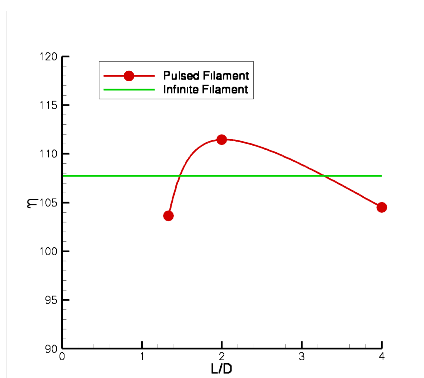

Figure 5.135: Efficiency Versus Period, $\frac{L}{D}$

Chapter 6

Conclusions

Two cases of energy deposition to a cylinder in supersonic flow have been evaluated. The first case was an inviscid simulation, in which energy deposition filament diameters are evaluated. The second case was a viscous simulation which varied the period of pulses of energy deposition to evaluate the effect on heat transfer to the body.

6.1 Effect of Large Filament Diameter on Drag

The objective of the analysis was to determine the effect of varying the nondimensional microwave filament diameter to the drag savings in terms of effectiveness and efficiency. The case of a cylinder in inviscid supersonic flow at Mach 1.89 was solved. Three cases were computed with nondimensional filament diameters d/D=0.25, 0.5 and 1.0. It was shown that an increase in nondimensional filament diameter slightly increases the drag effectiveness. The drag effectiveness, defined as the ratio of drag savings to the drag in the absence of the energy deposition, is nearly constant for all three cases and varies from 0.37 to 0.40. The drag efficiency, defined as the ratio of the energy saved to the energy required to created the filament decreased from 15.4 at d/D=0.25 to 1.0 at d/D=1.0.

6.2 Heat Transfer to Blunt Body with Energy Deposition

The objective of this analysis was to the study the heat transfer to a blunt body in which energy deposition is applied to the flow ahead of the shock wave. It was shown that for the four cases studied, the heat transfer to the body was not greater than without the energy deposition applied to the flow. In face, due to eddies generated behind the shock wave, the heat transfer to the body was reduced in all of the cases. The greatest reduction in heat transfer was for a pulse period of two times the cylinder diameter. The least reduction in heat transfer to the front face of the blunt body was for the largest pulse period, $L/D = 4$.

Appendix A

Compressible Flat Plate Boundary Layer Solution Derivation

We begin with the dimensional steady compressible laminar boundary layer equations

$$\frac{\partial \rho u}{\partial x} + \frac{\partial \rho v}{\partial y} = 0 \tag{A.1}$$

$$\rho u \frac{\partial u}{\partial x} + \rho v \frac{\partial u}{\partial y} = -\frac{\partial p}{\partial x} + \frac{\partial}{\partial y}\left(\mu \frac{\partial u}{\partial y}\right) \tag{A.2}$$

$$0 = -\frac{\partial p}{\partial y} \tag{A.3}$$

$$\rho u c_p \frac{\partial T}{\partial x} + \rho v c_p \frac{\partial T}{\partial y} = u \frac{\partial p}{\partial x} + \frac{\partial}{\partial y}\left(k \frac{\partial T}{\partial y}\right) + \mu \left(\frac{\partial u}{\partial y}\right)^2 \tag{A.4}$$

Assume

$$\frac{\mu}{\mu_0} = C \frac{T}{T_0} \tag{A.5}$$

We require $\mu(T_\infty) = \mu_\infty$ as $y \to \infty$. Then,

$$\frac{\mu_\infty}{\mu_0} = C \frac{T_\infty}{T_0} \tag{A.6}$$

$$C = \frac{\mu_\infty}{\mu_0} \frac{T_0}{T_\infty} \tag{A.7}$$

Then, substituting into equation (A.5),

$$\frac{\mu}{\mu_0} = \left(\frac{\mu_\infty}{\mu_0} \frac{T_0}{T_\infty}\right) \frac{T}{T_0} \tag{A.8}$$

$$\frac{\mu}{\mu_\infty} = \frac{T}{T_\infty} \tag{A.9}$$

We introduce a transformation to scale the y direction with density,

$$\tilde{x} = x \tag{A.10}$$

$$\tilde{y} = \int_0^y \frac{\rho(x, y')}{\rho_\infty} dy' \tag{A.11}$$

$$\tilde{u} = u \tag{A.12}$$

$$\tilde{v} = \text{to be determined} \tag{A.13}$$

For any function $f(x,y)$, where $\tilde{x}(x,y)$ and $\tilde{y}(x,y)$,

$$\frac{\partial f}{\partial x} = \frac{\partial f}{\partial \tilde{x}}\frac{\partial \tilde{x}}{\partial x} + \frac{\partial f}{\partial \tilde{y}}\frac{\partial \tilde{y}}{\partial x} \tag{A.14}$$

$$= \frac{\partial f}{\partial \tilde{x}} + \frac{\partial f}{\partial \tilde{y}}\frac{\partial \tilde{y}}{\partial x} \tag{A.15}$$

and

$$\frac{\partial f}{\partial y} = \frac{\partial f}{\partial \tilde{x}}\frac{\partial \tilde{x}}{\partial y} + \frac{\partial f}{\partial \tilde{y}}\frac{\partial \tilde{y}}{\partial y} \tag{A.16}$$

and since $\partial \tilde{x}/\partial y = 0$

$$\frac{\partial f}{\partial y} = \frac{\partial f}{\partial \tilde{y}}\frac{\rho}{\rho_\infty} \tag{A.17}$$

$$\tag{A.18}$$

Evaluating the differentials,

$$dx = \frac{\partial x}{\partial \tilde{x}}d\tilde{x} + \frac{\partial x}{\partial \tilde{y}}d\tilde{y} \tag{A.19}$$

$$dx = d\tilde{x} + 0 \tag{A.20}$$

$$dx = d\tilde{x} \tag{A.21}$$

$$dy = \frac{\partial y}{\partial \tilde{x}}d\tilde{x} + \frac{\rho_\infty}{\rho}\left(\frac{\partial \tilde{y}}{\partial x}dx + \frac{\rho}{\rho_\infty}dy\right) \tag{A.22}$$

$$dy = \left(\frac{\partial y}{\partial \tilde{x}} + \frac{\rho_\infty}{\rho}\frac{\partial \tilde{y}}{\partial x}\right)dx + dy \tag{A.23}$$

$$\tag{A.24}$$

thus, in order to satisfy the requirement that $dy = dy$, the first term on the right hand must vanish,

$$\left(\frac{\partial y}{\partial \tilde{x}} + \frac{\rho_\infty}{\rho}\frac{\partial \tilde{y}}{\partial x}\right)dx = 0 \tag{A.25}$$

$$\frac{\partial y}{\partial \tilde{x}} + \frac{\rho_\infty}{\rho}\frac{\partial \tilde{y}}{\partial x} = 0 \tag{A.26}$$

and finally,

$$\frac{\partial \tilde{y}}{\partial x} = -\frac{\rho}{\rho_\infty}\frac{\partial y}{\partial \tilde{x}} \tag{A.27}$$

Therefore, for a given function, f,

$$\begin{aligned}
\frac{\partial f}{\partial x} &= \frac{\partial f}{\partial \tilde{x}} + \frac{\partial f}{\partial \tilde{y}}\left(-\frac{\rho}{\rho_\infty}\frac{\partial y}{\partial \tilde{x}}\right) \\
\frac{\partial f}{\partial y} &= \frac{\rho}{\rho_\infty}\frac{\partial f}{\partial \tilde{y}}
\end{aligned}$$

Consider, first the x-momentum equation, Equation (A.2),

$$\begin{aligned}
\rho u\frac{\partial u}{\partial} + \rho v\frac{\partial u}{\partial} &= -\frac{dp}{dx} + \frac{\partial}{\partial y}\left(\mu\frac{\partial u}{\partial y}\right) \\
(\rho\tilde{u})\frac{\partial \tilde{u}}{\partial \tilde{x}} - \frac{\rho}{\rho_\infty}\frac{\partial y}{\partial \tilde{x}}\frac{\partial \tilde{u}}{\partial \tilde{y}} + \left(\rho_\infty\tilde{v} + \rho\tilde{u}\frac{\partial u}{\partial \tilde{x}}\right)\frac{\rho}{\rho_\infty}\frac{\partial \tilde{u}}{\partial \tilde{y}} &= -\frac{dp}{d\tilde{x}} - \frac{\rho}{\rho_\infty}\frac{\partial y}{\partial \tilde{y}}\frac{\partial p}{\partial \tilde{y}} + \frac{\rho}{\rho_\infty}\frac{\partial}{\partial \tilde{y}}\left(\frac{\mu\rho}{\rho_\infty}\frac{\partial \tilde{u}}{\partial \tilde{y}}\right) \\
\rho\tilde{u}\frac{\partial \tilde{u}}{\partial \tilde{x}} + \rho\tilde{v}\frac{\partial \tilde{u}}{\partial \tilde{y}} &= -\frac{dp}{d\tilde{x}} + \frac{\rho}{\rho_\infty}\frac{\partial}{\partial \tilde{y}}\left(\frac{\mu\rho}{\rho_\infty}\frac{\partial \tilde{u}}{\partial \tilde{y}}\right)
\end{aligned}$$

With the assumption that $\rho\mu = \rho_\infty\mu_\infty$, and Equation (A.9), $\rho T = \rho_\infty T_\infty$, and

$$\begin{aligned}
\frac{dp}{d\tilde{x}} &= \frac{d\rho RT}{d\tilde{x}} \\
&= R\frac{d\rho T}{d\tilde{x}} \\
&= R\frac{d\rho_\infty T_\infty}{d\tilde{x}} \\
&= 0
\end{aligned}$$

Then, the x-momentum equation becomes,

$$\begin{aligned}
\rho\tilde{u}\frac{\partial \tilde{u}}{\partial \tilde{x}} + \rho\tilde{v}\frac{\partial \tilde{u}}{\partial \tilde{y}} &= \frac{\rho}{\rho_\infty}\left(\frac{\mu_\infty\rho_\infty}{\rho_\infty}\right)\frac{\partial^2 \tilde{u}}{\partial \tilde{y}^2} \\
\tilde{u}\frac{\partial \tilde{u}}{\partial \tilde{x}} + \tilde{v}\frac{\partial \tilde{u}}{\partial \tilde{y}} &= \nu_\infty\frac{\partial^2 \tilde{u}}{\partial \tilde{y}^2} \qquad \text{(A.28)}
\end{aligned}$$

The energy equation becomes

$$\begin{aligned}
\rho\tilde{u}c_p\left(\frac{\partial T}{\partial \tilde{x}} - \frac{\rho}{\rho_\infty}\frac{\partial y}{\partial \tilde{x}}\frac{\partial T}{\partial \tilde{y}}\right) + \left(\rho_\infty\tilde{v} + \rho\tilde{u}\frac{\partial y}{\partial \tilde{x}}\right)c_p\frac{\rho}{\rho_\infty}\frac{\partial T}{\partial \tilde{y}}& \\
= \tilde{u}\frac{dp}{d\tilde{x}} + \frac{\rho}{\rho_\infty}\frac{\partial}{\partial \tilde{y}}\left(k\frac{\rho}{\rho_\infty}\frac{\partial T}{\partial \tilde{y}}\right) + \mu\left(\frac{\rho}{\rho_\infty}\right)^2\left(\frac{\partial \tilde{u}}{\partial \tilde{y}}\right)^2&
\end{aligned}$$

$$\rho c_p\left(\tilde{u}\frac{\partial T}{\partial \tilde{x}} + \tilde{v}\frac{\partial T}{\partial \tilde{y}}\right) = \frac{\rho}{\rho_\infty^2}\frac{\partial}{\partial \tilde{y}}\left(\frac{c_p}{Pr}\rho_\infty\mu_\infty\frac{\partial T}{\partial \tilde{y}}\right) + \mu_\infty\left(\frac{\rho}{\rho_\infty}\right)\left(\frac{\partial \tilde{u}}{\partial \tilde{y}}\right)^2$$

where $Pr = \mu c_p/k$. Introduce $\kappa_\infty = k_\infty/c_p\rho_\infty$,

$$\begin{aligned}
c_p\rho\left(\tilde{u}\frac{\partial T}{\partial \tilde{x}} + \tilde{v}\frac{\partial T}{\partial \tilde{y}}\right) &= \mu_\infty\frac{\rho c_p}{Pr}\frac{\partial^2 T}{\partial \tilde{y}^2} + \kappa_\infty\frac{Pr\rho^2 c_p}{c_p\rho_\infty}\left(\frac{\partial \tilde{u}}{\partial \tilde{y}}\right)^2 \\
\tilde{u}\frac{\partial T}{\partial \tilde{x}} + \tilde{v}\frac{\partial T}{\partial \tilde{y}} &= \frac{\nu_\infty}{Pr}\frac{\partial^2 T}{\partial \tilde{y}^2} + \frac{\kappa_\infty Pr}{c_p}\left(\frac{\partial \tilde{u}}{\partial \tilde{y}}\right)^2 \\
\tilde{u}\frac{\partial T}{\partial \tilde{y}}\tilde{v}\frac{\partial T}{\partial \tilde{y}} &= \frac{\nu_\infty}{Pr}\frac{\partial^2 T}{\partial \tilde{y}^2} + \frac{\kappa_\infty Pr}{c_p}\left(\frac{\partial \tilde{u}}{\partial \tilde{y}}\right)^2 \qquad \text{(A.29)}
\end{aligned}$$

The similarity solution is of the following form

$$\tilde{u} = \frac{\partial \psi}{\partial \tilde{y}} \quad \& \quad \tilde{v} = \frac{\partial \psi}{\partial \tilde{x}} \tag{A.30}$$

where

$$\psi = \sqrt{\nu_\infty U_\infty \tilde{x}} f(\eta) \quad \& \quad \eta = \tilde{y}\sqrt{\frac{U_\infty}{\nu_\infty \tilde{x}}} \tag{A.31}$$

The mass equation, is automatically satisfied with this transformation. From the transformed variable, $\tilde{u}$,

$$\begin{aligned} u &= \frac{\partial \psi}{\partial y}\frac{\rho_\infty}{\rho} \\ \rho u &= \rho_\infty \frac{\partial \psi}{\partial y} \end{aligned} \tag{A.32}$$

From the transformed variable, $\tilde{v}$,

$$\begin{aligned} \tilde{v} &= -\frac{\partial f}{\partial x} - \frac{\partial y}{\partial \tilde{x}}\frac{\partial \psi}{\partial y} \\ \frac{\rho}{\rho_\infty} v - \frac{\rho}{\rho_\infty}\frac{\partial y}{\partial \tilde{x}} u &= -\frac{\partial f}{\partial x} - \frac{\partial y}{\partial \tilde{x}}\frac{\rho u}{\rho_i nfty} \\ \rho v &= -\rho_\infty \frac{\partial f}{\partial x} \end{aligned} \tag{A.33}$$

Plugging Equations (A.32) and (A.33) into the mass equation, (A.1),

$$\rho_\infty \left(\frac{\partial^2 \psi}{\partial x \partial y} - \frac{\partial^2 \psi}{\partial y \partial y} \right) = 0 \tag{A.34}$$

Thus, the similarity variables and the transformation identically satisfy the mass equation.

$$\begin{aligned} \frac{\partial \eta}{\partial \tilde{y}} &= \sqrt{\frac{U_\infty}{\nu_\infty \tilde{x}}} \\ \frac{\partial \eta}{\partial \tilde{y}} &= -\frac{1}{2}\sqrt{\frac{U_\infty}{\nu_\infty \tilde{x}^3}}\tilde{y} \\ &= -\frac{1}{2}\frac{1}{\tilde{x}}\eta \\ \tilde{v} &= \frac{1}{2}\sqrt{\frac{\nu_\infty U_\infty}{\tilde{x}}} f - \frac{1}{2}\frac{U_\infty}{\sqrt{\tilde{x}}} f' \\ \frac{\partial \tilde{u}}{\partial \tilde{x}} &= -\frac{1}{2}\frac{U_\infty \eta}{\tilde{x}} f'' \\ \frac{\partial \tilde{u}}{\partial \tilde{y}} &= \sqrt{\frac{U_\infty^3}{\nu_\infty \tilde{x}}} f'' \\ \frac{\partial^2 \tilde{u}}{\partial \tilde{y}^2} &= \frac{U_\infty^2}{\nu_\infty \tilde{x}} f''' \end{aligned}$$

The x-momentum equation, is transformed with the similarity variables,

$$\begin{aligned}
u_\infty^2 f' \left(-\frac{1}{2}\right) \frac{\eta}{\tilde{x}} f'' + \left(-\frac{1}{2}\right) \sqrt{\nu_\infty u_\infty \tilde{x}} \left(f - \eta f'\right) \sqrt{\frac{u_\infty^2}{\nu_\infty \tilde{x}}} f'' &= \nu_\infty \frac{u_\infty^2}{\nu_\infty \tilde{x}} f''' \\
-\frac{1}{2} \frac{u_\infty^2}{\tilde{x}} \eta f'' f' + \frac{1}{2} \frac{u_\infty^2}{\tilde{x}} \eta f'' f' - \frac{1}{2} \frac{u_\infty^2}{\tilde{x}} f f'' &= \frac{u_\infty^2}{\tilde{x}} f''' \\
f''' + \frac{1}{2} f f'' &= 0 \\
2 f''' + f f'' &= 0 \qquad \text{(A.35)}
\end{aligned}$$

with boundary conditions

$$f(0) = 1 \qquad \text{(A.36)}$$

$$f'(0) = 0 \qquad \text{(A.37)}$$

$$f'(\infty) = 1 \qquad \text{(A.38)}$$

Equations (A.35) through (A.38) are exactly the Blasius equations. The solution to this transformed system is the same as the solution to the Blasius equations.

Appendix B

Crocco Solution and Reynolds Analogy

Crocco Solution

Starting with the boundary layer equations for compressible flow,

$$\frac{\partial \rho u}{\partial x} + \frac{\partial \rho v}{\partial y} = 0 \tag{B.1}$$

$$\rho u \frac{\partial u}{\partial x} + \rho v \frac{\partial u}{\partial y} = -\frac{dp}{dx} + \frac{\partial}{\partial y}\left(\mu \frac{\partial u}{\partial y}\right) \tag{B.2}$$

$$0 = -\frac{\partial p}{\partial y} \tag{B.3}$$

$$\rho u c_p \frac{\partial T}{\partial x} + \rho v c_p \frac{\partial T}{\partial y} = u\frac{\partial p}{\partial x} + \frac{\partial}{\partial y}\left(k\frac{\partial T}{\partial y}\right) + \mu\left(\frac{\partial u}{\partial y}\right)^2 \tag{B.4}$$

If it assumed that the (i) Prandtl number is constant, and (ii) the specific heat at constant pressure are constant, the energy equation, equation B.4, becomes

$$\rho u c_p \frac{\partial T}{\partial x} + \rho v c_p \frac{\partial T}{\partial y} = u\frac{dP}{dx} + \frac{\partial}{\partial y}\left(k\frac{\partial T}{\partial y}\right) + \mu\left(\frac{\partial u}{\partial y}\right)^2$$

Seeking an expression of temperature that is solely a function of streamwise velocity $T(u)$, and plugging in,

$$\begin{aligned}
\rho u c_p \frac{dT}{du}\frac{\partial u}{\partial x} + \rho v c_p \frac{dT}{du}\frac{\partial u}{\partial y} &= u\frac{dp}{dx} + \frac{dT}{du}\frac{\partial}{\partial y}\left(k\frac{\partial u}{\partial y}\right) + k\frac{\partial u}{\partial y}\frac{\partial}{\partial y}\left(\frac{dT}{du}\right) + \mu\left(\frac{\partial u}{\partial y}\right)^2 \\
&= u\frac{dp}{dx} + \frac{dT}{du}\frac{\partial}{\partial y}\left(k\frac{\partial u}{\partial y}\right) + k\left(\frac{\partial u}{\partial y}\right)^2\left(\frac{d^2T}{du^2}\right) + \mu\left(\frac{\partial u}{\partial y}\right)^2 \\
&= u\frac{dp}{dx} + \frac{1}{Pr}\frac{dT}{du}\frac{\partial}{\partial y}\left(Prk\frac{\partial u}{\partial y}\right) + \left(\frac{\partial u}{\partial u}\right)^2\mu\left(1 + \frac{k}{\mu}\frac{d^2T}{du^2}\right) \\
&= u\frac{dp}{dx} + \frac{1}{Pr}\frac{dT}{du}\frac{\partial}{\partial y}\left(\mu c_p\frac{\partial u}{\partial y}\right) + \left(\frac{\partial u}{\partial y}\right)^2\mu\left(1 + \frac{c_p}{Pr}\frac{d^2T}{du^2}\right) \\
&= u\frac{dp}{dx} + \frac{c_p}{Pr}\frac{dT}{du}\frac{\partial}{\partial y}\left(\mu\frac{\partial u}{\partial y}\right) + \left(\frac{\partial u}{\partial y}\right)^2\mu\left(1 + \frac{c_p}{Pr}\frac{d^2T}{du^2}\right) \\
c_p\frac{dT}{du}\left(\rho u\frac{\partial u}{\partial x} + \rho v\frac{\partial u}{\partial y}\right) &= u\frac{dp}{dx} + \frac{c_p}{Pr}\frac{dT}{du}\frac{\partial}{\partial y}\left(\mu\frac{\partial u}{\partial y}\right) + \left(\frac{\partial u}{\partial y}\right)^2\mu\left(1 + \frac{c_p}{Pr}\frac{d^2T}{du^2}\right)
\end{aligned}$$

Using the x-momentum equation, equation B.2, on the left hand side,

$$c_p \frac{dT}{du}\left(-\frac{dp}{dx} + \frac{\partial}{\partial y}\left(\mu \frac{\partial u}{\partial y}\right)\right) = u\frac{dp}{dx} + \frac{c_p}{Pr}\frac{dT}{du}\frac{\partial}{\partial y}\left(\mu\frac{\partial u}{\partial y}\right) + \left(\frac{\partial u}{\partial y}\right)^2 \mu \left(1 + \frac{c_p}{Pr}\frac{d^2T}{du^2}\right)$$

Finally,

$$\frac{dp}{dx}\left(u + c_p\frac{dT}{du}\right) + \left(\frac{c_p}{Pr} - c_p\right)\frac{dT}{du}\frac{\partial}{\partial y}\left(\frac{c_p}{Pr}\frac{\partial u}{\partial y}\right) + \left(\frac{c_p}{Pr}\frac{\partial^2 T}{\partial u^2} + 1\right)\mu\left(\frac{\partial u}{\partial y}\right)^2 = 0 \qquad \text{(B.5)}$$

Now, if we assume

$$\begin{aligned}
&\text{(iii)} \quad Pr = 1 \\
&\text{(iv)} \quad c_p\frac{d^2T}{du^2} + 1 = 0 \\
&\text{(v)} \quad u + c_p\frac{dT}{du} = 0 \\
&\qquad\quad \text{or } \frac{dp}{dx} = 0
\end{aligned}$$

Then the mass equation, equation B.1, is exactly satisfied, and we evaluate the momentum and energy equations, equations B.2 and B.4, respectively, to see if $T(u)$ is a solution. There are two possible boundary conditions at the wall,

$$\begin{array}{llll}
\text{(I)} & \text{adiabatic wall} & \text{(II)} & \text{isothermal wall} \\
 & dT_w/dy = 0 & & T_w = \text{constant}
\end{array}$$

(I) Adiabatic Wall Integrating assumption (iv),

$$\begin{aligned}
\frac{d^2T}{du^2} &= -\frac{1}{c_p} \\
\frac{dT}{du} &= -\frac{u}{c_p} + A
\end{aligned}$$

$$T(u) = -\frac{u^2}{2c_p} + Au + B \qquad \text{(B.6)}$$

Using the adiabatic wall condition (I),

$$\frac{dT}{dy}|_{y=0} = \frac{dT}{du}\frac{\partial u}{\partial y}|_{y=0,u=0} = 0 \qquad \text{(B.7)}$$

Since, the velocity gradient at the wall is not zero,

$$\frac{\partial u}{\partial y} \neq = 0 \qquad \text{(B.8)}$$

Then dT/du must be equal to zero at the wall, where $y = 0$ and $u = 0$.

$$\frac{dT}{du} = -\frac{u}{c_p} + A = 0 \Rightarrow A = 0 \tag{B.9}$$

Thus,

$$T(u) = -\frac{u}{c_p} + B \tag{B.10}$$

At $y \to \infty$, $T \to T_\infty$ and $u \to U_\infty$. Thus,

$$B = T_\infty + \frac{U_\infty^2}{2c_p} = \text{total temperature at edge of boundary layer} \tag{B.11}$$

Then, the temperature becomes

$$T(u) = T_\infty(x, y) + \frac{1}{2c_p}\left(U_\infty^2 - u^2\right) \tag{B.12}$$

$$T + \frac{u^2}{2c_p} = T_\infty + \frac{U_\infty^2}{2c_p} \tag{B.13}$$

$$T_t(x, y) = T_{te}(x) \tag{B.14}$$

where T_{te} is the total temperature at the edge of the boundary layer. equation B.14 demonstrates that the total temperature, T_t, is constant across the boundary layer. To satisfy Assumption (v), for a nonzero dp/dx,

$$\begin{aligned} \frac{dT}{dx} &= \left(\frac{dT_\infty}{dx} + \frac{1}{2c_p}\frac{dU_\infty^2}{dx}\right)\frac{\partial x}{\partial u} - \frac{1}{2c_p}2u \\ &= \frac{dT_{te}(x)}{dx} - \frac{u}{c_p} \end{aligned}$$

Plugging in to Assumption (v) for an arbitrarty dp/dx,

$$c_p\frac{dT}{dx} + u = c_p\frac{dT_{te}}{dx}\frac{\partial x}{\partial u} - u + u = 0 \tag{B.15}$$

The last equality follows if T_t is constant in x. Thus, for an adiabatic wall, equation B.12 is a solution to equations B.1, B.2, B.3 and B.4 if

(i) $Pr = 1$

(ii) $c_p\frac{d^2T}{du^2} + 1 = 0$

(iii) $dT_{te}/dx = 0$

(II) Isothermal Wall : $T_w =$ constant For the case of an isothermal wall, we again integrate assumption (iv) :

$$T(u) = -\frac{u^2}{2c_p} + Au + B \tag{B.16}$$

At $y = 0$, $u = 0$ adn $T = T_w$, which gives us $B = T_w$. At $y \to \infty$, $u \to U_\infty$, $T \to T_\infty(x)$, thus

$$T_\infty + \frac{U_\infty^2}{2c_p} - T_w = AU_\infty \tag{B.17}$$

Thus,

$$A = \frac{T_\infty - T}{U_\infty} + \frac{U_\infty}{2c_p} \tag{B.18}$$

Finally,

$$T(u) = -\frac{u^2}{2c_p} + \frac{u}{U_\infty}(T_\infty - T_w) + \frac{uU_\infty}{2c_p} + T_w \tag{B.19}$$

If we wish to satisfy (v) for an arbitrary dp/dx,

$$u + c_p \frac{dT}{du} = 0 \tag{B.20}$$

$$u + c_p \left(-\frac{u}{c_p} + \frac{(T_\infty - T_w)}{U_\infty} + \frac{U_\infty}{2c_p} \right) = 0 \tag{B.21}$$

and

$$T_w = T_\infty + \frac{U_\infty^2}{2c_p} \tag{B.22}$$

which is the adiabatic wall temperature. Thus, if $T =$constant and $T \neq T_\infty$, then $dp/dx = 0$ must be true for B.19 to be a solution to equations B.1, B.2, B.3, B.4.

Reynolds Analogy

Define the Stanton number

$$St = \frac{q_w}{\rho_e U_e c_p (T_w - T_a)} \tag{B.23}$$

where

$$q_w = -k\frac{\partial T}{\partial y} = -k\frac{dT}{du}\frac{\partial u}{\partial y} \tag{B.24}$$

for an isothermal wall, from equation B.19,

$$\frac{\partial T}{\partial u} = \frac{-u}{c_p} + \frac{T_\infty - T_w}{U_\infty} + \frac{U_\infty}{2c_p} = -\frac{U}{c_p} - \frac{T_w}{U_\infty} + \frac{T_a}{U_\infty} \tag{B.25}$$

where the adiabatic wall temperature is $T_a = T_\infty + U_\infty^2/2c_p$ from equation B.12. At the wall,

$$\begin{aligned} u &= 0 \Rightarrow \frac{dT}{du} = -\frac{1}{U_\infty}\left(T_w - T_a\right) \\ q_w &= k\frac{\partial u}{\partial y}\frac{T_w - T_a}{U_\infty} \end{aligned}$$

$$\begin{aligned} St &= \frac{-k\frac{\partial u}{\partial y}\left(T_a - T_w\right)}{\rho_\infty U_\infty^2 c_p \left(T_w - T_a\right)} \\ &= \frac{k\frac{\partial u}{\partial y}}{\rho_\infty U_\infty^2 c_p} \end{aligned}$$

where

$$\tau_w = \tau_{12} = \mu\left(\frac{\partial u}{\partial y} = \frac{\partial v}{\partial x}\right)0\frac{2}{3}(0) = \mu\frac{\partial u}{\partial y} \tag{B.26}$$

the last equation follows from the fact that the vertical velocity, v, is zero at the wall. Thus,

$$St = \frac{\tau_w}{\mu}\frac{k}{\rho_\infty U_\infty^2 c_p} \tag{B.27}$$

and

$$Pr = \frac{c_p \mu}{k} = 1 \tag{B.28}$$

where skin friction is defined as

$$C_f = \frac{\tau_w}{\frac{1}{2}\rho_e U_e^2} \tag{B.29}$$

it follows that

$$\frac{\tau_w}{\rho_\infty U_\infty^2} = \frac{C_f}{2} \tag{B.30}$$

and finally

$$St = \frac{C_f}{2} \tag{B.31}$$

which is the Reynolds analogy.

References

[1] Shang, J. S., "Validation of Injection for Hypersonic Blunt Body Drag Reduction," *TWO AVT Symposium on 'Reduction of Military Vehicle Acquisition Time and Cost Through Advanced Modeling and Virtual Simulation*, 2002.

[2] Knight, D., Kuchinskiy, V., Kuranov, A., and Sheikin, E., "Survey of Aerodynamic Flow Control at High Speed Using Energy Addition," *AIAA Paper No. 2003-0525*, 2003.

[3] Knight, D., Kuchinskiy, V., Kuranov, A., and Sheikin, E., "Aerodynamic Flow Control at High Speed Using Energy Deposition," *Fourth Workshop on Magneto-Plasma Aerodynamics for Aerospace Applications*, Institute for High Temperatures, Moscow, Russia, 2002.

[4] Jacobis van den Donker, M., *Modeling Microwave Plasmas for Deposition Purposes : Exploring the Freedom in Space and Chemistry*, Ph.D. thesis, Eindhoven University of Technology, 2008.

[5] Zheltovodov, A., Pimonov, E., and Knight, D., "Energy Deposition Influence on Supersonic Flow Over Axisymmetric Bodies," *AIAA Paper No. 2007-1230*, 2007.

[6] Azarova, O., Grudnitsky, V., and Kolesnichenko, Y., "Some Gas Dynamic Aspects of Flow Control by MW Energy Deposition," *Sixth Workshop on Magneto-Plasma Aerodynamics for Aerospace Applications*, Institute for High Temperatures, Moscow, Russia, 2005.

[7] Georgievskii, P. and Levin, V., "Unsteady Interaction of a Sphere with Atmospheric Temperature Inhomogeneity at Supersonic Speed," *Mekhanika Zhidkosti i Gaza*, 1993, pp. 174–183.

[8] Farzan, F., Knight, D., Azarova, O., and Kolesnichenko, Y., "Interaction of Microwave Filament and Blunt Body in Supersonic Flows," *AIAA Paper No. 2008-1356*, 2008.

[9] Fomin, V., Tretyakov, P., and Taran, J. P., "Flow Control Using Various Plasma and Aerodynamic Approaches," *Aerospace Science and Technology*, Vol. 8, No. 5, 2004, pp. 411–421.

[10] Knight, D., "Survey of Magneto-Gasdynamic Local Flow Control at High Speeds," *AIAA Paper No. 2004-1191*, 2004.

[11] Bletzinger, P., Ganguly, B., Van Wie, D., and Garscadden, A., "Plasmas in High Speed Aerodoynamics," *Journal Physics D: Applied Physics*, Vol. 38, No. 4, 2005, pp. 33–57.

[12] Knight, D., "Survey of Aerodynamic Drag Reduction at High Speed by Energy Deposition," *Journal of Propulsion and Power*, Vol. 24, No. 6, 2006, pp. 1153–1167.

[13] Adelgren, R., Elliott, G., Knight, D., Zheltovodov, A., and Beutner, T., "Energy Deposition in Supersonic Flows," *AIAA Paper No. 2001-0885*, 2001.

[14] Exton, R. J., Balla, R. J., Shirinzadeh, B., Brauckmann, G. J., Herring, G. C., Kelliher, W. C., Fugitt, J., Lazard, C. J., and Khodataev, K. V., "On-Board Projection of a Microwave Plasma Upstream of a Mach 6 Bow Shock," *Physics of Plasmas*, Vol. 8, No. 11, 2001, pp. 5013–5017.

[15] Adelgren, R., Yan, H., Elliott, G., Knight, D., Beutner, T., Zheltovodov, A., Ivanov, M., and Khotyanovsky, D., "Localized Flow Control by Laser Energy Deposition Applied to Edney IV Shock Impingement and Intersecting Shocks," *AIAA Paper No. 2003-0031*, 2003.

[16] Zaidi, S. H., Shneider, M. N., and Miles, R. B., "Shock-Wave Mitigation Through Off-Body Pulsed Energy Deposition," *AIAA Journal*, Vol. 42, No. 2, 2004, pp. 326–331.

[17] Kolesnichenko, Y., Khmara, D., Brovkin, V., and Afanas'ev, S., "Optimization of Laser-Pulse Controlled Microwave Energy Deposition," *AIAA Paper No. 1228*, 2007.

[18] Lashkov, V., Mashek, I., Anisimov, Y., Ivanov, V., Kolesnichenko, Y., and Azarova, O., "Gas-dynamic Effects Around the Body Under Energy Deposition in Supersonic Flow," *AIAA Paper No. 2007-1231*, 2007.

[19] Knight, D., Azarova, O., and Kolesnichenko, Y., "On Details of Flow Control Via Characteristics and Location of Microwave Filament During Its Interaction with Supersonic Blunt Body," *AIAA Paper No. 2009-847*, 2009.

[20] Kolesnichenko, Y., Brovkin, V., Azarova, O., Grudnitsky, V., Lashkov, V., and Mashek, I., "Microwave Energy Deposition for Aerodynamic Application," *AIAA Paper No. 2003-0361*, 2003.

[21] Schlichting, H., Gersten, K., Mayes, K., and Oertel, H., *Boundary Layer Theory*, Springer-Verlag Berlin Heidelberg New York, 2000.

[22] van Leer, B., "Flux-Vector Splitting for the Euler Equations," *Lecture Notes in Physics*, Vol. 170, No. 82-30, 1982, pp. 507–512.

[23] AeroSoft, Inc., *Aerosoft GASP 3 User Manual*, May 1996.

[24] Harten, A. and Chakravarthy, S., "Multi-Dimensional ENO Schemes for General Geometries," Tech. Rep. 91-76, Institue for Computer Applications in Science and Engineering, 1991.

[25] Hirsch, C., *Numerical Computation of Internal and External Flows*, Vols. I and II, John Wiley and Sons, New York, 1988.

[26] Anderson, W., Thomas, J., and Van Leer, B., "Comparison of Finite Volume Flux Vector Splittings for the Euler Equations," *AIAA Journal*, Vol. 24, No. 9, 1986, pp. 1453–1460.

[27] Knight, D., *Elements of Numerical Methods for Compressible Flows*, Cambridge University Press, New York, 2006.

[28] Abramowitz, M. and Stegun, I., *Handbook of Mathematical Functions*, Vol. 55, National Bureau of Standards, Washington, DC, 1971.

[29] Colella, P. and Woodward, P., “The Numerical Simulation of Two-Dimensional Fluid Flow with Strong Shocks,” *Journal of Computational Physics*, Vol. 54, No. 1, 1984, pp. 115–173.

[30] Donat, R. and Marquina, A., “Capturing Shock Reflections: An Improved Flux Formula,” *Journal of Computational Physics*, Vol. 125, No. 78, 1996, pp. 42–58.

[31] White, F. M., *Viscous Fluid Flow*, Mc-Graw Hill, 1974.

[32] Hirschel, E., *Basics of Aerothermodynamics*, Springer, New York, 2005.